

1-1-2013

Exploring Molecular Systems From Chemical Physics To Biochemistry Using Classical And Quantum Mechanics

Brian Thomas Psciuk
Wayne State University,

Follow this and additional works at: http://digitalcommons.wayne.edu/oa_dissertations



Part of the [Physical Chemistry Commons](#)

Recommended Citation

Psciuk, Brian Thomas, "Exploring Molecular Systems From Chemical Physics To Biochemistry Using Classical And Quantum Mechanics" (2013). *Wayne State University Dissertations*. Paper 688.

This Open Access Dissertation is brought to you for free and open access by DigitalCommons@WayneState. It has been accepted for inclusion in Wayne State University Dissertations by an authorized administrator of DigitalCommons@WayneState.

**EXPLORING MOLECULAR SYSTEMS FROM CHEMICAL PHYSICS TO
BIOCHEMISTRY USING CLASSICAL AND QUANTUM MECHANICS**

by

BRIAN THOMAS PSCIUK

DISSERTATION

Submitted to the Graduate School

of Wayne State University,

Detroit, Michigan

in partial fulfillment of the requirements

for the degree of

DOCTOR OF PHILOSOPHY

2013

MAJOR: CHEMISTRY (Physical)

Approved by:

Advisor

Date

DEDICATION

*This volume would not have been feasible without the two that are both the embodiment
and source of my motivation, my ambition, and my dreams*

To Jennifer and Landon

ACKNOWLEDGMENTS

The effort and work put into this thesis officially began in the fall of 2007. Since then and even prior, there have been numerous people that have helped and supported my career in so many ways.

First, I would like to start by thanking my advisor Professor H. Bernhard Schlegel. I am not sure how I would have been able to reach such a monumental goal without the seemingly unconditional patience, help, and guidance that he has offered me. He never stopped believing in my scientific abilities and pushed me to persevere even when I felt that things had become too overwhelming to continue. His lessons not only in science, but in life, will stay with me forever.

In the eight years that I have been a part of the Schlegel group, I have accumulated an enormous amount of unpaid debts that I owe to many fellow students and post docs. Professors Jason Sonnenberg, Peng Tao, and Richard Lord have each been a mentor, psychotherapist, confidant, and friend to me over my graduate years. Among my colleagues, they have been the most critical in my development and growth into the scientist that I am today. Professor Barbara Munk and Dr. Jason Sonk have been very close friends as well as colleagues helping me both scientifically and being there for me many times personally. Professor Smriti Anand, and Drs. Stanley Smith and Jie Li were senior graduate students who were kind enough to take the time to help me as an undergraduate intern at the beginning of my understanding of quantum mechanics. I would also like to acknowledge all of the other Schlegel group members that I have spent many fond hours working, collaborating, and procrastinating with: Adam Birkholz, Dr. Pascal Krause, Dr. Michael Cato, Dr. Suk Young Lee, Dr. Jia Zhou,

Xuetao Shi, and Bishnu Thapa. I need to make one last special mention of a Schlegel group member, Professor Hrant Hratchian, who was willing to put his name on the line and recommend a lost, naïve chemistry undergraduate for a position in his former research group.

I would like to thank all of my graduate committee members: Professors Vladimir Chernyak, G. Andres Cisneros, John Santalucia Jr., Ashok Bhagwat, and Caroline Morgan for their collaborations, mentoring, and guidance through all of my graduate years. I need to make special mention of the scientific collaborators that helped in the scientific foundations of this thesis including Professor Charles Winter, Professor Victor Benderskii, Dr. Raviprasad Aduri, and Laura Visger. Many thanks and great appreciation go out to all of the Wayne State University Chemistry department and Wayne State Computing Grid staff with special mentions to Melissa Barton, Sharon Kelly, Erin Bachert, Nestor Ocampo, Michael Thompson, and Aragorn Steiger. Additionally, I would like to thank influential instructors from my undergraduate education Professors Mark Paulsen, Thomas Getman, Leslie Putman, Frankie Ann McCormick, Heather Holmes, and Dr. Lakshmi Narasimhan for preparing me for my career in chemistry.

I would like to give many thanks and appreciation to the providers of my financial support from the Thomas C. Rumble graduate research fellowship, the Paul A. and Carol Schaap graduate research fellowship, and Professor Schlegel's research grants from the National Science Foundation, Department of Energy, and Gaussian Inc. I would also like to thank the Wayne State computing grid for the generous use of their computational resources.

Going all the way back to my childhood and through the present, I want to thank my wonderful parents, Mark and Karen. Although their career paths were quite different from the sciences, they were always encouraging and supportive of my dreams and ambitions. They didn't have all the answers to my endless inquiries about the physical world, but always made me feel like my questions were deserving of answers. They believed in my abilities and encouraged me to become what I am today. I want to thank my mother, individually, for showing me how to incorporate creativity and balance in my life, while being my shelter whenever I felt scared and overburdened. My father pushed me to strive for excellence and perfection in everything I do, and had never ending pride and confidence in my abilities. Also, I have to acknowledge his frequent "Polish updates" that kept me informed on worldly news whenever I spent long periods of time studying. Certainly, Scott and Sue Hawley are to be included as parents also. Without Scott and Sue, I may not have been afforded the time to work on and complete my thesis. Sue literally retired from her job to allow me to finish graduate school after the arrival of Landon. They have been very generous and supportive over the years, and they even shared their home with my family for well over a year.

I want to thank my sister, Alicia, for inspiring me to follow my dreams and to be confident and unyielding toward a career with great challenges and tall odds. I would like to acknowledge my grandparents past and present: Donald and Diana Peterson and Reginald and Helene Psciuk. Additionally, I am lucky to have so many loving family members that have been very understanding and completely supportive even during my absences from holidays, birthdays, and get-togethers: Becca, Kevin, Brayden, Nate, Kelsey, Kate, Dave, AJ, Vanessa, Eric, Jennie, Ken, Kenny, Maggie, Linda, Matt,

Matthew, Erika, Erin, Sean, Gene, Deb, Dale, Steven, Diana, Carol, Matt, Dave, Randy, Mary, Justin, Bree, Pauline, Ken, Sarah, Chris, and Katie. I want to thank Karen Donoughe for helping me with my perspective and outlook through my graduate years. I have been very fortunate to have some very close friends that have been around with me for many years helping to keep my sanity through graduate school and playing a big role in shaping who I am today: Rob, Jordan, Matt, and Armen.

Lastly, I would like to thank Jennifer and Landon. Here, I have to acknowledge all of the sacrifices that you have made for me while completing this work. The expectations and obligations that come with the completion of graduate school and a thesis such as this are stressful and sometimes unpredictable. There is nothing that I am able to write that can express all the love and appreciation that I have for you and everything you do. The work within this volume is as much yours as it is my own.

TABLE OF CONTENTS

Dedication	ii
Acknowledgements	iii
Table of Contents	vii
List of Tables	xii
List of Figures	xvi
List of Schemes	xxiii
CHAPTER 1 INTRODUCTION	1
1.1 References	7
CHAPTER 2 AB INITIO CLASSICAL TRAJECTORY STUDY OF THE FRAGMENTATION OF C ₃ H ₄ DICATION ON THE SINGLET AND TRIPLET SURFACES	14
2.1 Introduction	14
2.2 Methods	16
2.3 Structure and Energetics	17
2.4 Dynamics of the Dication Fragmentation	19
2.5 Summary	23
2.6 References	38

CHAPTER 3	ASSESSING THE ACCURACY OF TD-DFT TRANSITION ENERGIES AND INTENSITIES FOR EXCITED STATE CHARGE TRANSFER BANDS IN INORGANIC COMPLEXES	44
3.1	Introduction.....	44
3.2	Computation Details	45
3.3	Inorganic Complex Results and Discussions.....	47
3.4	Summary	50
3.5	References	62
CHAPTER 4	CAN METALLAPYRIMIDINES BE AROMATIC? A COMPUTATIONAL STUDY INTO A NEW CLASS OF METALLACYCLES	69
4.1	Introduction.....	69
4.2	Computational Details	71
4.3	Niobapyrimidine Formation.....	72
4.4	Natural Chemical Shielding for $[(pz)_2(Nb-pyr)]^0$	75
4.5	$d^0 [(pz)_2(M^{n+}-pyr)]^{(n-5)+}$ Complexes ($M = Y^{III}, Zr^{IV}, Nb^V, Mo^VI, Tc^{VII}$) .	79
4.6	$M^V [(pz)_2(M-pyr)]^0$ Complexes ($M = Nb^V, Mo^V, Tc^V, Ru^V, Rh^V$).....	82
4.7	Conclusions.....	85
4.8	References	115
CHAPTER 5	PROTONATION AND GEOMETRY EFFECTS ON THE AROMATICITY OF METALLAPYRIMIDINE COMPLEXES CONTAINING 2ND ROW TRANSITION METALS	121

5.1	Introduction.....	121
5.2	Computational Details	122
5.3	Results and Discussions	124
5.4	Summary.....	131
5.5	References	153

CHAPTER 6 AMBER FORCE FIELD PARAMETERS FOR MODIFIED DNA

NUCLEOSIDES AND NATURALLY OCCURRING MODIFIED RNA

	NUCLEOSIDES.....	157
6.1	Introduction.....	157
6.2	Parameterization Strategy	159
6.3	Naming Convention	163
6.4	Generating the Parameters	164
6.5	Electrostatic Potential Calculations	165
6.6	Testing the Parameters	166
6.7	References	183

CHAPTER 7 THEORETICAL DETERMINATION OF ONE-ELECTRON OXIDATION

POTENTIALS FOR NUCLEIC ACID BASES

7.1	Introduction.....	191
7.2	General Description of a Reduction Potential.....	194
7.3	Gas and Solution Phase Calculations	196

7.4	Accounting for Multiple Tautomers	198
7.5	Calculating pK_a and E_7	199
7.6	Results and Discussion	202
7.7	Gas Phase Energies.....	203
7.8	Solvent Scaling Parameters	205
7.9	Calculated pK_a Values.....	206
7.10	Redox Potentials in Acetonitrile	207
7.11	Redox Potentials in Water	209
7.12	Summary	213
7.13	References	237

CHAPTER 8 COMPUTATIONAL PREDICTION OF ONE-ELECTRON REDUCTION POTENTIALS AND ACID DISSOCIATION CONSTANTS FOR GUANINE OXIDATION PRODUCTS AND INTERMEDIATES		250
8.1	Introduction.....	250
8.2	Methods.....	252
8.3	Results and Discussion	259
8.4	Pathway A	261
8.5	Pathway B	266
8.6	Pathway C	267
8.7	Conclusion.....	269

8.8	References	291
CHAPTER 9 CONCLUSIONS		301
Abstract.....		308
Autobiographical Statement		310

LIST OF TABLES

Table 2.1	Comparison of Bond Lengths (Å) and Angles (°) for Structures on the C ₃ H ₄ Ground State Neutral, Singlet Dication and Triplet Dication Surfaces Optimized at the QCISD 6-311G(d,p) Level of Theory.	25
Table 2.2	Calculated Adiabatic Double Ionization Energies (eV) for Allene, Propyne and Cyclopropene	27
Table 2.3	Relative Energies of Optimized C ₃ H ₄ ²⁺ Surface Stationary Points for Singlet and Triplet States (in kcal/mol).....	28
Table 2.4	Timing Data for Trajectories.....	36
Table 3.1	Basis Set Effects on the Excited State Energy and Length Oscillator Strength of Charge Transfer Bands in the Calculated Electronic Absorption Spectra of TiCl ₄ , Ni(CO) ₄ and Cr(CO) ₆ Using the B3LYP Density Functional.	53
Table 3.2	Theoretical Method Effects on the Excited State Energy and Length Oscillator Strength of Charge Transfer Bands in the Calculated Electronic Absorption Spectra of TiCl ₄ , Ni(CO) ₄ and Cr(CO) ₆ Using the 6-311++G(d,p) Basis Set	55
Table 3.3	Theoretical Cr(CO) ₆ Absorption Spectra Data from Other Studies Compared to B3LYP/6-311+G(d) Results.....	60
Table 4.1	Natural Chemical Shielding Analysis for Benzene, Pyrimidine, Cyclobutadiene, Rhodabenzene, and Niobapyrimidine	91
Table 4.2	Natural Chemical Shielding Analysis of π Orbital Contributions with Orbital Pictures	92
Table 4.3	Natural Chemical Shielding Analysis for Contributing Orbitals in ppm ...	100
Table 4.4	Metal-Pyrazolate and Metallapyrimidine Bond Lengths (Å) for the d ⁰ Series of Complexes	108
Table 4.5	Natural Chemical Shielding Analysis for the d ⁰ Series of [(pz) ₂ (M ⁿ⁺ -pyr)] ⁽ⁿ⁻⁵⁾⁺ Complexes.....	109
Table 4.6	Metal-Pyrazolate and Metallapyrimidine Bond Lengths (Å) for the M ^V series of Complexes.....	112

Table 4.7	Natural Chemical Shielding Analysis for the $[(pz)_2(M^V\text{-pyr})]^0$ Series of Complexes.....	113
Table 5.1	Optimized Metallapyrimidine Complex Geometries with 0, 1, and 2 Additional Protons or Methyl Groups.	135
Table 5.2	Relative Free-Energy Differences in kcal/mol for Oxidative Addition of a Metal to a Pyrazolato Ligand to Form a Metallacycle Complex from a Tris-pyrazolato Complex.....	137
Table 5.3	Chemical Shift Totals for Non, Singly, and Doubly Protonated and Methylated Pyrimidine and Metallacycles Species	138
Table 5.4	Comparison of the $NICS(1)_{zz}$ and $NICS(1)_{\pi zz}$ Chemical Shifts for Four Structural Isomers of $[pz_2\text{-Tc}^V\text{-pyr-H}^+]^+$	139
Table 5.5	Calculated $NICS(1)_{zz}$ and $NICS(1)_{\pi zz}$ Chemical Shifts for Metallapyrimidine Complexes Containing Nb^V , Tc^V , and Rh^V and Pyrimidine Showing the Charge versus Geometry Effects of Protonation	140
Table 5.6	Natural Chemical Shielding Analysis of the π Orbital Contributions to the $NICS(1)_{zz}$ Chemical Shift of Pyrimidine in Structural Combinations of Three Geometries with Three Protonation States.	143
Table 5.7	Natural Chemical Shielding Analysis of the π Orbital Contributions to the $NICS(1)_{zz}$ Chemical Shift of $[(pz)_2(Tc^{VII}\text{-pyr-nH})]^{(n+2)+}$ ($n = 0, 1, 2$) in Structural Combinations of Three Geometries with Three Protonation States.....	144
Table 5.8	Natural Chemical Shielding Analysis of the π Orbital Contributions to the $NICS(1)_{zz}$ Chemical Shift of $[(pz)_2(Mo^{VI}\text{-pyr-nH})]^{(n+1)+}$ ($n = 0, 1, 2$) in Structural Combinations of Three Geometries with Three Protonation States.....	145
Table 5.9	Natural Chemical Shielding Analysis of the π Orbital Contributions to the $NICS(1)_{zz}$ Chemical Shift of $[(pz)_2(Nb^V\text{-pyr-nH})]^{n+}$ ($n = 0, 1, 2$) in Structural Combinations of Three Geometries with Three Protonation States.....	146
Table 5.10	Natural Chemical Shielding Analysis of the π Orbital Contributions to the $NICS(1)_{zz}$ Chemical Shift of $[(pz)_2(Tc^V\text{-pyr-nH})]^{n+}$ ($n = 0, 1, 2$) in Structural Combinations of Three Geometries with Three Protonation States.....	147

Table 5.11	Natural Chemical Shielding Analysis of the π Orbital Contributions to the NICS(1) _{zz} Chemical Shift of [(pz) ₂ (Rh ^V -pyr-nH)] ⁿ⁺ (n = 0, 1, 2) in Structural Combinations of Three Geometries with Three Protonation States.....	149
Table 5.12	Natural Chemical Shielding Analysis of the π Orbital Contributions to the NICS(1) _{zz} Chemical Shift of [(pz) ₂ (M-pyr-Me)] Complexes and N-methylpyrimidine	151
Table 5.13	Natural Chemical Shielding Analysis of the π Orbital Contributions to the NICS(1) _{zz} Chemical Shift of [(pz) ₂ (M-pyr-2Me)] Complexes and N-methylpyrimidine	152
Table 6.1	Charge Values Obtained for the Nucleobase Subunit of Common Nucleosides Adenine, Guanine, Cytosine, and Uridine	170
Table 6.2	Charge Values Obtained for the Three Common Sugars in RNA, C3'-endo, C2'-endo, and 2'-O-methylribose Sugars.....	172
Table 6.3	Comparison of Adenosine Charges Computed in This Work with the Charges Available in PARM99 of AMBER	173
Table 6.4	Generic Names, Three-Letter Codes, Common Names, and PDB Source Information for All Parameterized DNA and RNA Nucleosides	175
Table 6.5	Multi-Orientation Fitting effects on the Calculated Pseudouridine Charges Using the R.E.D. Program	180
Table 6.6	Population Analysis effects on the Calculated Charges of the Thymine Nucleobase	181
Table 7.1	Experimental and Calculated Gas Phase Basicities and Proton Affinities for Nucleic Acid Bases in kcal/mol.....	220
Table 7.2	Experimental and Calculated Gas Phase Adiabatic (AIE) and Vertical Ionization Energies (VIE) for Nucleic Acid Bases in eV	221
Table 7.3	Experimental and Calculated pK _a Values	224
Table 7.4	Experimental and Calculated E°(XH+•/XH) Reduction Potentials in Acetonitrile Solution in eV	233
Table 7.5	Reference Compound Reduction Potentials in Aqueous and Acetonitrile Solution and Gas Phase Adiabatic Ionization Energies in eV.....	234

Table 7.6	Aqueous Solution Calculated $E^\circ(\text{XH}^+/\text{XH})$ Potential Relative to Adenine in eV	235
Table 7.7	Experimental and Calculated E_7 Reduction Potentials in Aqueous Solution in eV	236
Table 8.1	Calculated Reduction Potentials and $\text{p}K_a$'s for Reactant, Intermediate, and Product Species using B3LYP and CBS-QB3 Methodologies	275

LIST OF FIGURES

Figure 2.1	Geometries with relevant bond lengths (Å) and angles (°) for isomers on the ground neutral, singlet dication, and triplet dication state surfaces optimized at the QCISD/6-311G(d,p) level of theory.	24
Figure 2.2	Potential energy surfaces for singlet and triplet $C_3H_4^{2+}$. Relative energies with zero point energy in kcal/mol at the CBS-APNO (in bold), CCSD(T)/cc-pVTZ//B3LYP/6-311G(d,p) (<i>in italics</i>) and B3LYP/6-31G(d,p) levels of theory.	26
Figure 2.3	Fragment structures for the singlet and triplet dication optimized at the QCISD/6-311G(d,p) level of theory.	29
Figure 2.4	Fragmentation of vertically doubly ionized allene on the singlet surface. Left hand side shows the percentages and barriers for direct dissociation. Right hand side shows only the lowest barriers for indirect dissociation; percentages also include fragmentations occurring via higher barriers (199 trajectories calculated at the B3LYP/6-31G(d,p) level of theory with 240 kcal/mol initial kinetic energy).	30
Figure 2.5	Fragmentation of vertically doubly ionized allene on the triplet surface. Left hand side shows the percentages and barriers for direct dissociation. Right hand side shows only the lowest barriers for indirect dissociation; percentages also include fragmentations occurring via higher barriers (200 trajectories calculated at the B3LYP/6-31G(d,p) level of theory with 240 kcal/mol initial kinetic energy).	31
Figure 2.6	Fragmentation of vertically doubly ionized propyne on the singlet surface. Left hand side shows the percentages and barriers for direct dissociation. Right hand side shows only the lowest barriers for indirect dissociation; percentages also include fragmentations occurring via higher barriers (200 trajectories calculated at the B3LYP/6-31G(d,p) level of theory with 210 kcal/mol initial kinetic energy).	32
Figure 2.7	Fragmentation of vertically doubly ionized propyne on the triplet surface. Left hand side shows the percentages and barriers for direct dissociation. Right hand side shows only the lowest barriers for indirect dissociation; percentages also include fragmentations occurring via higher barriers (200 trajectories calculated at the B3LYP/6-31G(d,p) level of theory with 210 kcal/mol initial kinetic energy).	33

Figure 2.8	Fragmentation of vertically doubly ionized cyclopropene on the singlet surface. Left hand side shows the percentages and barriers for direct dissociation. Right hand side shows only the lowest barriers for indirect dissociation; percentages also include fragmentations occurring via higher barriers (200 trajectories calculated at the B3LYP/6-31G(d,p) level of theory with 200 kcal/mol initial kinetic energy).	34
Figure 2.9	Fragmentation of vertically doubly ionized cyclopropene on the triplet surface. Left hand side shows the percentages and barriers for direct dissociation. Right hand side shows only the lowest barriers for indirect dissociation; percentages also include fragmentations occurring via higher barriers (200 trajectories calculated at the B3LYP/6-31G(d,p) level of theory with 190 kcal/mol initial kinetic energy).	35
Figure 3.1	UV-vis absorption spectra of benzaldehyde at the B3LYP level of theory. (a) Comparison of spectra using different numbers of polarization functions. (b) Comparison of spectra using different numbers of diffuse functions.	51
Figure 3.2	Calculated electronic absorption spectra of TiCl_4 using the B3LYP level of theory with multiple different basis sets. Overall, transition state energies and intensities are shown to be relatively insensitive to the choice of a reasonably sized basis set.	52
Figure 3.3	Calculated electronic absorption spectrum of TiCl_4 at various levels of theory computed with the 6-311+G(d) basis set.	57
Figure 3.4	Calculated electronic absorption spectrum of $\text{Ni}(\text{CO})_4$ at various levels of theory computed with the 6-311+G(d) basis set.	58
Figure 3.5	Calculated electronic absorption spectrum of $\text{Cr}(\text{CO})_6$ at various levels of theory computed with the 6-311+G(d) basis set.	59
Figure 3.6	Calculated UV-vis absorption spectrum of TiF_6^{3-} at the B3LYP/6-311++G(d,p) level of theory using PCM solvation. Multiple curves primarily show unphysical Rydberg-like excited states being affected by using dielectric constants values from vacuum ($\epsilon=0$) to water ($\epsilon=78.3553$).	61
Figure 4.1	Potential energy surface and structures for the reaction of $[\text{Nb}(\text{pz})_3]^0$ to form $[(\text{pz})_2(\text{Nb-pyr})]^0$	90

Figure 4.2	Simplified orbital interaction diagram between kp^{3-} (left) and $(pz)_2M$ (right).	107
Figure 4.3	Molecular orbital isosurface plots (0.05 au) of the π orbitals for the $[(pz)_2(M^{n+}-pyr)]^{(n-5)+}$ complexes.....	110
Figure 4.4	C_2 symmetric structure for the $[(pz)_2(M^V-pyr)]^0$ complexes.....	111
Figure 4.5	Molecular orbital isosurface plots (0.05 au) of the π orbitals for $[(pz)_2(Tc^V-pyr)]^0$ and $[(pz)_2(Rh^V-pyr)]^0$	114
Figure 5.1	Structure and atom numbering of a bis-pyrazolato metallapyrimidine. Singly protonated or methylated species are substituted at N_5	133
Figure 5.2	Optimized geometries for bis-pyrazolato-metallapyrimidinium species for 2 nd row transition metals Tc^{VII} , Mo^{VI} , Nb^V , Tc^V , and Rh^V	134
Figure 5.3	Orbital diagrams of the localized valence π orbitals contributing to the NICS(1) _{zz} chemical shift showing the differences in the electronic structure between the unprotonated (left) and doubly protonated (right) Tc^V metallapyrimidine complex. Specific differences are seen in the occupation of the d orbitals, where the d- δ orbital is occupied in the unprotonated species and a non-interacting d orbital is occupied on the right leading to dramatic changes in the calculated aromaticity. (Diagrams have isovalue = 0.05).....	142
Figure 6.1	Flowchart of the protocol used in generating the parameters for the modified nucleotides.	168
Figure 6.2	Protocol for the determination of atom-centered partial charges. The starting structures were obtained either from a PDB file or created using GaussView. Hydrogen atoms were added using GaussView. Geometry optimization was done using Gaussian03. The electrostatic potential was computed using Merz-Kollman population analysis, and charges were produced by fitting the ESP using RESP as explained in the text.....	169
Figure 6.3	The charge fitting method used to generate the charges for the common nucleosides A, G, C, and U, using the modular nature of RNA to reduce the computational time. The charges for O1P, O2P, O3', O5', and P were obtained by using dimethyl phosphate (DMP) as a model system.....	171

Figure 6.4	Examples of modified nucleosides present in RNA. These modifications range from simple methylation, as in the case of 1MA, to more complex carbohydrate containing compounds such as QGG. Only the hydrogen atoms on the polar atoms are shown for clarity. In each case, the only lowest energy tautomer was considered for the protonation that exists at physiological pH.....	174
Figure 6.5	The effect of modifications in the stability and functioning of 16S rRNA of 30S ribosome (1J5E). (a) The dimethylated adenines (DMA) in the "dimethyl A loop" of 16S rRNA help in the stabilization of the loop through stacking interactions and forms a hydrophobic pocket with 2MG. (b) The methylated 966 and 967 positions of 16S rRNA increase the surface area for stacking and also form a van der Waals contact with the hydrophobic portion of Arg-128 of S9 protein (not shown).....	182
Figure 7.1	Effect of changing the solvent cavity parameter on the calculated pK_a for the B3LYP and CBS-QB3 methodologies. Each solid curve represents a third order polynomial fit of calculated pK_a data points collected at scaled solvent cavities. For all neutral species shown, the solvent cavity was left unscaled ($\alpha=1.0$), while the solvent cavity scaling values for ionic species were varied. Horizontal dotted lines represent experimentally measured pK_a 's. The intersection of a calculated pK_a curve with an experimental pK_a (depicted by a symbol specific to the nucleobase) indicate the optimal solvent cavity scaling value for a given nucleobase. The optimal solvent cavity scaling parameters for B3LYP are 0.9, 1.0 and 1.0 for anionic, cationic and neutral species, respectively. The optimal scaling factors for CBS-QB3 are 0.925, 0.975 and 1.0 for anionic, cationic and neutral species, respectively.....	223
Figure 7.2	Linear correlation plots of calculated pK_a 's versus experimental pK_a 's. Cation deprotonations are signified by a cross and neutral deprotonations are signified by a dot.	225
Figure 7.3	Calculated pK_a 's and oxidation potentials for 9-methylguanine. Experimentally measured values are shown in parenthesis. CBS-QB3 calculated values are shown in bold face text, while B3LYP calculated values are shown in regular text. Black numbers to the left of each isomer indicate the relative free energy in kcal/mol (regular font) and the population in percentage (<i>italics</i>). Red numbers shown in between isomers indicate calculated pK_a 's for the specific isomers, while red numbers on the top and bottom of the figure indicate the	

	ensemble averaged pK_a for each acid/base equilibrium. Blue numbers shown between the reduced (top) and oxidized species (bottom) indicate calculated one-electron oxidation potentials E° and E_7	226
Figure 7.4	Calculated pK_a 's and oxidation potentials for 9-methyladenine. See Figure 7.3 caption for details.	227
Figure 7.5	Calculated pK_a 's and oxidation potentials for 1-methylcytosine. See Figure 7.3 caption for details.	228
Figure 7.6	Calculated pK_a 's and oxidation potentials for 1-methylthymine. See Figure 7.3 caption for details.	229
Figure 7.7	Calculated pK_a 's and oxidation potentials for 1-methyluracil. See Figure 7.3 caption for details.	230
Figure 7.8	Calculated pK_a 's and oxidation potentials for 9-methylxanthine. See Figure 7.3 caption for details.	231
Figure 7.9	Calculated pK_a 's and oxidation potentials for 9-methyl-8-oxoguanine. See Figure 7.3 caption for details.....	232
Figure 8.1	Key intermediates and products along three significant reaction pathways following guanine oxidation. Pathway A starts with the 9-methyl-8-oxoguanine (8oxoG) intermediate structure and leads to the spiroiminodihydantoin (Sp) and guanidinohydantoin (Gh) products. Pathway B goes through the hemiaminal intermediate and produces the formamidopyrimidine (FAPyG) products. Pathway C starts at the 5-hydroxy-9-methylguanine (5OHG) and goes through the N-methyl-2-deoxo-spiroiminodihydantoin (Sp_{red}) intermediate and ends at the 5-carboxamido-5-formamido-(N-methyl)-2-iminohydantoin (2lh) product.	276
Figure 8.2	Calculated pK_a 's and reduction potentials for 9-methylguanine (G). Where applicable, relative free energy differences in kcal/mol (black) with the tautomer populations (black italics) are shown near individual tautomers. Tautomer specific pK_a 's (red) are shown between individual isomers. Ensemble averaged pK_a 's (red) are shown at the top and bottom of the figure. Ensemble oxidation potentials E° and E_7 (blue) are shown between the reduced and oxidized species on the right. Figure 8.3 through Figure 8.15 report oxidation potentials relative to guanine (E°_{rel} and E_{7rel}). Experimentally measured values are shown in parenthesis.	277

Figure 8.3	Calculated pK_a 's and relative reduction potentials for 9-methyl-8-oxoguanine (8oxoG). See Figure 8.2 caption for details. Blue values at the bottom of the figure are the relative E_7 reduction potentials for the oxidized 8oxoG and reduced 8oxoP one-electron redox pair.....	278
Figure 8.4	Calculated pK_a 's and relative reduction potentials for 2-amino-6,8-dioxo-9-methylpurine (8oxoP). See Figure 8.2 caption for details. Blue values at the top of the figure are the relative E_7 reduction potentials for the oxidized 8oxoG and reduced 8oxoP one-electron redox pair.....	279
Figure 8.5	Calculated pK_a 's and relative reduction potentials for 5-hydroxy-9-methyl-8-oxoguanine (5OH8OG). See Figure 8.2 caption for details.....	280
Figure 8.6	Calculated pK_a 's and relative reduction potentials for <i>gem</i> -diol. See Figure 8.2 caption for details.	281
Figure 8.7	Calculated pK_a 's and relative reduction potentials for 4-carboxy-1-methylguanidinohydantoin (4carboxyGh). See Figure 8.2 caption for details. Calculations show that if the carboxylic acid of oxidized 4carboxyGh is deprotonated, the molecule will dissociate into carbon dioxide and Gh.....	282
Figure 8.8	Calculated pK_a 's and relative reduction potentials for 1-methylguanidinohydantoin (Gh). See Figure 8.2 caption for details.	283
Figure 8.9	Calculated pK_a 's and relative reduction potentials for N-methylspiroiminodihydantoin (Sp). See Figure 8.2 caption for details.	284
Figure 8.10	Calculated pK_a 's and relative reduction potentials for 2-amino-8-hydroxy-9-methyl-1,7,8-trihydropurin-6-one (hemiaminal). See Figure 8.2 caption for details.....	285
Figure 8.11	Calculated pK_a 's and relative reduction potentials for 2,6-diamino-(N-methyl)-5-formamido-4-hydroxypyrimidine (FAPyG). See Figure 8.2 caption for details.	286
Figure 8.12	Calculated pK_a 's and relative reduction potentials for 2,5-diamino-(N-methyl)-6-formamido-4-hydroxypyrimidine (2,5FAPyG). See Figure 8.2 caption for details.	287

Figure 8.13	Calculated pK_a 's and relative reduction potentials for 5-hydroxy-9-methylguanine (5OHG). See Figure 8.2 caption for details.	288
Figure 8.14	Calculated pK_a 's and relative reduction potentials for N-methyl-2-deoxo-spiroiminodihydantoin (Sp_{red}). See Figure 8.2 caption for details.....	289
Figure 8.15	Calculated pK_a 's and relative reduction potentials for 5-carboxamido-5-formamido-(N-methyl)-2-iminohydantoin (2lh). See Figure 8.2 caption for details.	290

LIST OF SCHEMES

Scheme 2.1	Percentages of initial dissociation products from the fragmentation of $C_3H_4^{2+}$ on the singlet surface (top row) and triplet surface (bottom row), starting from allene, propyne, and cyclopropene, respectively.....	37
Scheme 4.1	$[(pz)_2(Nb-pyr)]^0$	88
Scheme 4.2	Oxidative Fragment Interaction in $[(pz)_2(Nb-pyr)]^0$	89
Scheme 7.1	Thermodynamic cycle used in the calculation of reduction potentials....	216
Scheme 7.2	Atomic numbering for purines and pyrimidine nucleobases. Charge, multiplicity and hydrogen atoms are not explicitly shown.	217
Scheme 7.3	Multiple tautomers contribute to the ensemble reduction potential.	218
Scheme 7.4	Thermodynamic cycle used in the calculation of pK_a 's	219
Scheme 7.5	Lowest energy gas phase tautomers of protonated uracil/thymine.	222
Scheme 8.1	Thermodynamic cycle used in the calculation of reduction potentials....	271
Scheme 8.2	Atomic numbering for purines and pyrimidine nucleobases. Charge, multiplicity and hydrogen atoms are not explicitly shown.	272
Scheme 8.3	Thermodynamic cycle used in the calculation of pK_a 's	273
Scheme 8.4	Multiple tautomers contribute to the ensemble reduction potential.	274

CHAPTER 1

INTRODUCTION

Computational chemistry is a scientific field that continues to grow exponentially in applicability and accuracy with the development of new methods and the expansion of its frontiers. The technological advancements in computing continue to have a dramatic impact on our ability to perform computations efficiently and tackle difficult problems. The expansion of calculational techniques coupled with the continual improvement of computing technology have combined to drive a scientific field that has impacted almost every sub-discipline in chemistry. In the quickly moving scientific world of today, specialists in the applications of computational chemistry are required to have expertise in multiple disciplines. In the chapters of this thesis, modern computational techniques are used to as a predictive tool generating new results as well as an analysis tool for providing a greater understanding of existing experimental data. The computational studies in this thesis span multiple areas of chemistry and impact fields such as chemical physics, organometallics, biomolecular simulations, solar energy conversion, and cancer research.

In Chapter 2, the fragmentation patterns of C_3H_4 dications are examined on the singlet and triplet state potential surfaces using ab initio classical trajectory calculations. Following an intense laser pulse (ca. 10^{14} W/cm²) and subsequent violent removal of electrons, a small organic system is energetically doomed to undergo Coulomb explosion and dissociation. If enough electrons remain in the system, dissociation will still occur, though it may not necessarily be spontaneous. The final fragmentation products may depend heavily on the reaction dynamics of a highly energetic, meta-

stable intermediate complex. Experimentalists have observed ultra-fast hydrogen dynamics in doubly ionized organic systems such as $\text{C}_3\text{H}_4^{2+}$.¹⁻³ It is very likely that the energized molecule does not experience vibrational energy redistribution before isomerization or even dissociation. Using classical dynamics simulations, we investigated the fragmentation products and dynamics prior to dissociation of highly energetic $\text{C}_3\text{H}_4^{2+}$ molecules following exposure to an intense laser pulse.

An investigation assessing some popular Time-Dependent Density Functional Theory (TD-DFT) methods for their performance in calculating excitation energies and intensities of charge transfer bands for inorganic complexes is detailed in Chapter 3. Numerous methods exist for computing the excited state spectra of molecules, but DFT functionals have the potential to calculate excited states as accurately as high level wavefunction methods at a fraction of the computational cost.⁴⁻⁶ Previous studies have established the performances of various popular functionals for calculating the excited state energies and intensities of small organic molecules.^{7,8} A few other studies have examined the performances of DFT functionals for calculating excited state energies,⁹⁻¹⁵ but there is very little information regarding the accuracy for predicting excited state transition intensities. A computationally efficient and accurate method for predicting energies and intensities of charge transfer bands in inorganic complexes would be an instrumental tool toward helping future theoretical investigations.

Continuing to stay within the field of inorganic complexes, Chapters 4 and 5 are investigations into the aromaticity and other properties of a novel set of metallacycle complexes. A recent experimental investigation by Winter and coworkers attempting to create new volatile precursors for thin film growth by atomic layer deposition produced

an unexpected and surprising result.¹⁶ A reaction between a Niobium(III) salt and a pyrazolate salt was expected to produce a Nb^{III}-tris-pyrazolato complex. Instead, the Nb metal center underwent two electron oxidative addition to one of the pyrazolato ligands by cleaving the N–N bond and forming a bis-pyrazolato niobapyrimidine. This was the first known example of a pyrazolate N–N bond cleavage at a single metal center. An initial theoretical investigation of the newly isolated niobapyrimidine and niobapyrimidinium complexes using Nucleus Independent Chemical Shift (NICS) calculations¹⁷ showed results indicating that the metallapyrimidine rings were weakly aromatic. A deeper investigation into the aromaticity of the niobapyrimidine complex in addition to several related metallapyrimidine complexes containing 2nd row transition metals is given in Chapter 4. Two series of 2nd row transition metal containing metallapyrimidine complexes were examined, one with no valence d electrons (Y^{III}, Zr^{IV}, Nb^V, Mo^{VI}, and Tc^{VII}) and one with a varying number of valence d electrons (Nb^V, Mo^V, Tc^V, Ru^V, and Rh^V). NICS calculations were separated into specific orbital components and compared against two classical examples of aromatic compounds, benzene and pyrimidine, and an anti-aromatic compound, cyclobutadiene.

The investigation and results detailed in Chapter 4 is expanded upon in Chapter 5, by studying the effects of metallacycle ring protonation on the aromaticity of 2nd row transition metal containing metallapyrimidine complexes. The experimental work that inspired metallapyrimidine investigation isolated two complexes, a niobapyrimidine complex and a niobapyrimidinium complex. In Chapter 5, attention is focused on the latter, where the effects on the aromaticity of the metallacycles are studied after proton and methyl substituents are coordinated to the ring nitrogen atoms. Specifically, we

investigated how aromaticity is affected by the geometry changes resulting from protonation/methylation and also the electronic effects protonation/methylation without changing the geometry. Two series of complexes were examined, a d^0 series of Nb^{V} , Mo^{VI} , and Tc^{VII} and a d^n series of Nb^{V} , Tc^{V} , and Rh^{V} .

For larger systems of biochemical interest, it is often necessary to use molecular mechanics or force field methods. Established techniques used to produce AMBER force field parameters for naturally occurring modified ribonucleic acids (RNA) and modified deoxyribonucleic acids (DNA) nucleosides are described in Chapter 6. The existing force field in AMBER can sufficiently characterize the van der Waals radii, bond stretching, angle bending, and dihedral twisting parameters necessary to calculate the classical bonding character of bioorganic nucleoside molecules.¹⁸

$$E = \sum_{\text{bonds}} K_r (r - r_0)^2 + \sum_{\text{angles}} K_\theta (\theta - \theta_0)^2 + \sum_{\text{dihedrals}} \frac{V_n}{2} [1 + \cos(n\phi)]$$

$$+ \sum_{\text{nonbonded}} 4\epsilon_{ij} \left(\left[\left(\frac{\sigma_{ij}}{r_{ij}} \right)^{12} - \left(\frac{\sigma_{ij}}{r_{ij}} \right)^6 \right] - \left[\frac{q_i q_j}{\epsilon R_{ij}} \right] \right) \quad (1)$$

However, atom-centered partial charges are required for the calculation of the non-bonded electrostatic forces in the traditional AMBER force field shown in eq (1). Charge parameters are available for the standard nucleic acid residues, but this is not the case for modified nucleosides. Parameterizing atom-centered partial charges requires the use of ab initio molecular orbital calculations. Running ab initio molecular orbital calculations on a nucleic acid sequence of more than a few base pairs is computationally prohibitive. Nucleic acid residues are modular and consist of three functional groups: a phosphate group, a ribose or deoxyribose sugar group, and a nucleic acid base. In the force field for nucleic acids developed by Cornell et al.,¹⁸ the

charge parameters for nucleic acid residues are fitted separately for each functional group using a restraining procedure.^{19,20} Utilizing the modular nature of nucleic acids, atom-centered partial charges were computed for 107 modified RNA and 42 modified DNA residues.

The DNA of biological systems is under constant oxidative stress. Unrepaired oxidative damage can result in mutations leading to carcinogenesis and cellular death.²¹⁻²⁷ It is generally well known that guanine is the easiest canonical nucleic acid base to oxidize.²⁸ Experimental measurements have established the order of reduction potentials among the canonical nucleobases.^{29,30} However, due to the delicate nature of experimental measurements in aqueous solution, there is not yet a consensus for the absolute or relative potentials of the canonical nucleic acid residues. Knowledge of the electrochemical properties of individual nucleoside subunits is a key first step in many areas of DNA research including a better understanding of the causes of DNA mutations and accurately determining the reduction potentials needed for DNA sequencing techniques by electrochemical detection methods. Gas phase thermochemical properties of reasonably sized molecules can be determined to within chemical accuracy. However, explicit solvation modeling can be computationally demanding and cost prohibitive. Modern solvation models are continually improving and can be used to accurately predict aqueous electrochemical potentials and acid dissociation constants for biomolecule subunits such as nucleic acid residues. In Chapter 7, we develop a computational methodology that can be used to calculate standard redox potentials and pK_a 's for the canonical nucleobases, guanine, adenine, cytosine, thymine, and uracil, and modified nucleobases, xanthine and 8-oxogaunine.

Many experimental groups have studied the nature and properties of intermediate species and products of guanine oxidation.^{23,27,28,31-38} Theoretical investigations have been carried out on the structure and energetics of short-lived intermediate species along the guanine oxidation pathway.³⁹⁻⁴² In Chapter 8, we used the computational methodology developed in Chapter 7 to calculate pK_a 's and aqueous oxidation potentials relative to guanine of some key intermediate and product species along the guanine oxidation reaction pathways.

The final chapter looks back at the topics studied and make some suggestions for future research.

1.1 References

1. Hoshina, K.; Furukawa, Y.; Okino, T.; Yamanouchi, K. Efficient ejection of H₃⁺ from hydrocarbon molecules induced by ultrashort intense laser fields. *J. Chem. Phys.* **2008**, *129*, 104302.
2. Xu, H.; Okino, T.; Yamanouchi, K. Ultrafast hydrogen migration in allene in intense laser fields: Evidence of two-body Coulomb explosion. *Chem. Phys. Lett.* **2009**, *469*, 255-260.
3. Xu, H. L.; Okino, T.; Yamanouchi, K. Tracing ultrafast hydrogen migration in allene in intense laser fields by triple-ion coincidence momentum imaging. *J. Chem. Phys.* **2009**, *131*, 151102.
4. Bauernschmitt, R.; Ahlrichs, R. Treatment of electronic excitations within the adiabatic approximation of time dependent density functional theory. *Chem. Phys. Lett.* **1996**, *256*, 454-464.
5. Chong, D. P. *Recent advances in density functional methods*. World Scientific: Singapore ; River Edge, N.J., 1995.
6. Gross, E. K. U.; Kohn, W. *Advances in Quantum Chemistry*. 1990; Vol. 21.
7. Caricato, M.; Trucks, G. W.; Frisch, M. J.; Wiberg, K. B. Electronic Transition Energies: A Study of the Performance of a Large Range of Single Reference Density Functional and Wave Function Methods on Valence and Rydberg States Compared to Experiment. *J. Chem. Theory Comput.* **2010**, *6*, 370-383.
8. Caricato, M.; Trucks, G. W.; Frisch, M. J.; Wiberg, K. B. Oscillator Strength: How Does TDDFT Compare to EOM-CCSD? *J. Chem. Theory Comput.* **2011**, *7*, 456-466.

9. Rosa, A.; Baerends, E. J.; van Gisbergen, S. J. A.; van Lenthe, E.; Groeneveld, J. A.; Snijders, J. G. Electronic spectra of $M(\text{CO})_6$ ($M = \text{Cr}, \text{Mo}, \text{W}$) revisited by a relativistic TDDFT approach. *J. Am. Chem. Soc.* **1999**, *121*, 10356-10365.
10. van Gisbergen, S. J. A.; Groeneveld, J. A.; Rosa, A.; Snijders, J. G.; Baerends, E. J. Excitation energies for transition metal compounds from time-dependent density functional theory. Applications to MnO_4^- , $\text{Ni}(\text{CO})_4$, and $\text{Mn}_2(\text{CO})_{10}$. *J. Phys. Chem. A* **1999**, *103*, 6835-6844.
11. Nooijen, M.; Lotrich, V. Extended similarity transformed equation-of-motion coupled cluster theory (extended-STEOM-CC): Applications to doubly excited states and transition metal compounds. *J. Chem. Phys.* **2000**, *113*, 494-507.
12. Neugebauer, J.; Baerends, E. J.; Nooijen, M. Vibronic structure of the permanganate absorption spectrum from time-dependent density functional calculations. *J. Phys. Chem. A* **2005**, *109*, 1168-1179.
13. Seth, M.; Ziegler, T. Calculation of excitation energies of open-shell molecules with spatially degenerate ground states. I. Transformed reference via an intermediate configuration Kohn-Sham density-functional theory and applications to d(1) and d(2) systems with octahedral and tetrahedral symmetries. *J. Chem. Phys.* **2005**, *123*, 144105.
14. Vlcek, A.; Zalis, S. Modeling of charge-transfer transitions and excited states in d(6) transition metal complexes by DFT techniques. *Coord. Chem. Rev.* **2007**, *251*, 258-287.

15. Jacquemin, D.; Wathelet, V.; Perpète, E. A.; Adamo, C. Extensive TD-DFT Benchmark: Singlet-Excited States of Organic Molecules. *J. Chem. Theory Comput.* **2009**, *5*, 2420-2435.
16. Perera, T. H.; Lord, R. L.; Heeg, M. J.; Schlegel, H. B.; Winter, C. H. Metallapyrimidines and Metallapyrimidiniums from Oxidative Addition of Pyrazolate N-N Bonds to Niobium(III), Niobium(IV), and Tantalum(IV) Metal Centers and Assessment of Their Aromatic Character. *Organometallics* **2012**, *31*, 5971-5974.
17. Chen, Z. F.; Wannere, C. S.; Corminboeuf, C.; Puchta, R.; Schleyer, P. V. Nucleus-independent chemical shifts (NICS) as an aromaticity criterion. *Chem. Rev.* **2005**, *105*, 3842-3888.
18. Cornell, W. D.; Cieplak, P.; Bayly, C. I.; Gould, I. R.; Merz, K. M.; Ferguson, D. M.; Spellmeyer, D. C.; Fox, T.; Caldwell, J. W.; Kollman, P. A. A 2nd Generation Force-Field for the Simulation of Proteins, Nucleic-Acids, and Organic-Molecules. *J. Am. Chem. Soc.* **1995**, *117*, 5179-5197.
19. Cieplak, P.; Cornell, W. D.; Bayly, C.; Kollman, P. A. Application of the Multimolecule and Multiconformational RESP Methodology to Biopolymers - Charge Derivation for DNA, RNA, and Proteins. *J. Comput. Chem.* **1995**, *16*, 1357-1377.
20. Bayly, C. I.; Cieplak, P.; Cornell, W. D.; Kollman, P. A. A Well-Behaved Electrostatic Potential Based Method Using Charge Restraints for Deriving Atomic Charges - the RESP Model. *J. Phys. Chem.* **1993**, *97*, 10269-10280.

21. Ames, B. N.; Shigenaga, M. K.; Hagen, T. M. Oxidants, antioxidants, and the degenerative diseases of aging. *Proc. Natl. Acad. Sci. U. S. A.* **1993**, *90*, 7915-7922.
22. Breen, A. P.; Murphy, J. A. Reactions of oxyl radicals with DNA. *Free Radic. Biol. Med.* **1995**, *18*, 1033-1077.
23. Burrows, C. J.; Muller, J. G. Oxidative nucleobase modifications leading to strand scission. *Chem. Rev.* **1998**, *98*, 1109-1151.
24. Cadet, J.; Berger, M.; Douki, T.; Morin, B.; Raoul, S.; Ravanat, J. L.; Spinelli, S. Effects of UV and visible radiation on DNA - Final base damage. *Biol. Chem.* **1997**, *378*, 1275-1286.
25. Cooke, M. S.; Olinski, R.; Evans, M. D. Does measurement of oxidative damage to DNA have clinical significance? *Clin. Chim. Acta* **2006**, *365*, 30-49.
26. Gimisis, T.; Cismas, C. Isolation, characterization, and independent synthesis of guanine oxidation products. *Eur. J. Org. Chem.* **2006**, 1351-1378.
27. Pratviel, G.; Meunier, B. Guanine oxidation: One- and two-electron reactions. *Chem.-Eur. J.* **2006**, *12*, 6018-6030.
28. Steenken, S. Purine-bases, nucleosides, and nucleotides - Aqueous-solution redox chemistry and transformation reactions of their radical cations and e- and OH adducts. *Chem. Rev.* **1989**, *89*, 503-520.
29. Oliveira-Brett, A. M.; Piedade, J. A. P.; Silva, L. A.; Diculescu, V. C. Voltammetric determination of all DNA nucleotides. *Anal. Biochem.* **2004**, *332*, 321-329.
30. Seidel, C. A. M.; Schulz, A.; Sauer, M. H. M. Nucleobase-specific quenching of fluorescent dyes. 1. Nucleobase one-electron redox potentials and their

- correlation with static and dynamic quenching efficiencies. *J. Phys. Chem.* **1996**, *100*, 5541-5553.
31. Candeias, L. P.; Steenken, S. Reaction of HO center dot with guanine derivatives in aqueous solution: Formation of two different redox-active OH-Adduct radicals and their unimolecular transformation reactions. Properties of G(-H)(center dot). *Chem.-Eur. J.* **2000**, *6*, 475-484.
 32. Luo, W. C.; Muller, J. G.; Rachlin, E. M.; Burrows, C. J. Characterization of spiroiminodihydantoin as a product of one-electron oxidation of 8-oxo-7,8-dihydroguanosine. *Org. Lett.* **2000**, *2*, 613-616.
 33. Llano, J.; Eriksson, L. A. Oxidation pathways of adenine and guanine in aqueous solution from first principles electrochemistry. *Phys. Chem. Chem. Phys.* **2004**, *6*, 4707-4713.
 34. Crean, C.; Geacintov, N. E.; Shafirovich, V. Oxidation of guanine and 8-oxo-7,8-dihydroguanine by carbonate radical anions: Insight from oxygen-18 labeling experiments. *Angew. Chem.-Int. Edit.* **2005**, *44*, 5057-5060.
 35. Fleming, A. M.; Muller, J. G.; Ji, I. S.; Burrows, C. J. Characterization of 2'-deoxyguanosine oxidation products observed in the Fenton-like system Cu(II)/H₂O₂/reductant in nucleoside and oligodeoxynucleotide contexts. *Org. Biomol. Chem.* **2011**, *9*, 3338-3348.
 36. Delaney, S.; Jarem, D. A.; Volle, C. B.; Yennie, C. J. Chemical and biological consequences of oxidatively damaged guanine in DNA. *Free Radic. Res.* **2012**, *46*, 420-441.

37. Fleming, A. M.; Muller, J. G.; Dlouhy, A. C.; Burrows, C. J. Structural Context Effects in the Oxidation of 8-Oxo-7,8-dihydro-2'-deoxyguanosine to Hydantoin Products: Electrostatics, Base Stacking, and Base Pairing. *J. Am. Chem. Soc.* **2012**, *134*, 15091-15102.
38. Jena, N. R.; Mishra, P. C. Formation of ring-opened and rearranged products of guanine: Mechanisms and biological significance. *Free Radic. Biol. Med.* **2012**, *53*, 81-94.
39. Wetmore, S. D.; Boyd, R. J.; Llano, J.; Lundqvist, M. J.; Eriksson, L. A. Hydroxyl radical reactions in biological media. In *Recent Advances in Density Functional Methods*, Barone, V.; Bencini, A.; Fantucci, P., Eds. World Scientific: Singapore, 2000; Vol. 3, pp 387-415.
40. Munk, B. H.; Burrows, C. J.; Schlegel, H. B. Exploration of mechanisms for the transformation of 8-hydroxy guanine radical to FAPyG by density functional theory. *Chem. Res. Toxicol.* **2007**, *20*, 432-444.
41. Munk, B. H.; Burrows, C. J.; Schlegel, H. B. An exploration of mechanisms for the transformation of 8-oxoguanine to guanidinohydantoin and spiroiminodihydantoin by density functional theory. *J. Am. Chem. Soc.* **2008**, *130*, 5245-5256.
42. Ye, Y.; Munk, B. H.; Muller, J. G.; Cogbill, A.; Burrows, C. J.; Schlegel, H. B. Mechanistic Aspects of the Formation of Guanidinohydantoin from Spiroiminodihydantoin under Acidic Conditions. *Chem. Res. Toxicol.* **2009**, *22*, 526-535.

CHAPTER 2

**AB INITIO CLASSICAL TRAJECTORY STUDY OF THE FRAGMENTATION OF C₃H₄
DICATION ON THE SINGLET AND TRIPLET SURFACES**

Reproduced with permission from *J. Phys. Chem. A* **2010**, 114, 7653-7660
Copyright 2010, American Chemical Society

2.1 Introduction

Coulomb explosion is one of the processes that can occur when molecules are subject to intense laser fields.¹⁻³ When a sufficient number of electrons are removed from a molecule, dissociation is spontaneous. For dications, however, dissociation is not necessarily spontaneous because enough electrons remain for significant bonding. Nevertheless, the barriers are diminished by the Coulombic repulsion. Thus, there may be an interesting interplay between energetics and dynamics in the fragmentation processes of dications.

Allene (H₂C=C=CH₂) was one of the first polyatomic molecules to be studied by laser induced Coulomb explosion.⁴ The dication of allene can be formed by interaction with short, intense laser pulses,⁴⁻⁷ by electron impact,⁸ or by double charge transfer.⁹⁻¹² Dissociation of the dication yields a variety of charged fragments: C₃H_n²⁺, C₃H_n⁺, C₂H_n⁺, CH_n⁺, and H_n⁺ ($n = 1-3$).^{4,6-8} The Coulomb explosion of propyne (H₃CC≡CH), an isomer of allene, yields a different pattern of intensities for the various fragments.⁸ Cyclopropene is another stable isomer of allene, but the dissociation of its dication has not been studied experimentally.

The potential energy surface for allene dication has been calculated by a number of investigators.¹³⁻¹⁶ The most recent study is a very thorough investigation of the

singlet and triplet potential surfaces of $\text{C}_3\text{H}_4^{2+}$ by Mebel and Bandrauk.¹⁶ Barriers for rearrangement and fragmentation were computed by density functional theory and coupled cluster methods. For cases suspected of having diradical character, structures and energies were also computed at the CASSCF and CASPT2 levels of theory. Branching ratios for various fragmentation pathways were estimated by RRKM theory.

In previous studies, we have used ab initio molecular dynamics to investigate the dissociation of small ions.^{17,18} These studies showed that the fragmentation trajectories could be grouped into two categories: (1) direct, involving only a few vibrations before dissociation; and (2) indirect, involving one or more rearrangement steps before dissociation. Although some of the indirect trajectories pass through recognizable transition states, others explore higher energy regions of the potential surface before dissociating (see the supporting information of the original text for movies). The latter is akin to the roaming mechanism for formaldehyde and acetaldehyde dissociation, which has been established both experimentally and theoretically.¹⁹⁻²¹

Ionization by short intense laser pulses can deposit considerable amounts of energy in the ions, but statistical methods such as RRKM may not be valid at higher energies. However, trajectory calculations may be able to shed some light on the dissociation processes at higher energies. We used ab initio molecular dynamics to examine the fragmentation of $\text{C}_3\text{H}_4^{2+}$ on both the singlet and triplet potential energy surfaces. Accurate energies and barrier heights were computed at the CBS-APNO²² level of theory and were compared to the extensive work by Mebel.¹⁶ Classical trajectories were calculated at the B3LYP/6-31G(d,p) level of theory since the energetics at this level of theory are in good agreement with more accurate methods.

Experimental studies have shown a strong isomer effect on the fragmentation pattern of $C_3H_4^{2+}$.⁸ To probe this computationally, trajectories were initiated at the neutral allene, propyne, and cyclopropene ground state geometries.

2.2 Methods

Electronic structure calculations were performed with the development version of the Gaussian software suite.²³ Geometries were optimized by density functional theory (DFT) using the B3LYP functional²⁴⁻²⁷ with the 6-31G(d,p) and 6-311G(d,p) basis sets²⁸⁻³¹ and by quadratic configuration interaction³² (QCISD) with the 6-311G(d,p) basis set. Vibrational frequencies were calculated at each level of theory to confirm that the structures were either minima or transition states. Reaction path following in mass-weighted Cartesian coordinates was used to connect transition states to their corresponding minima.^{33,34} Relative energies were calculated with the B3LYP/6-31G(d,p), B3LYP/6-311G(d,p), and CBS-APNO²² levels of theory.

Ab initio molecular dynamics calculations were carried out using classical trajectories computed with a Hessian-based predictor-corrector method^{35,36} at the B3LYP/6-31G(d,p) level of theory. A step size of $0.25 \text{ amu}^{1/2} \text{ bohr}$ was used, and the Hessians were updated for three molecular dynamics steps before being recalculated analytically; the angular forces were projected out for the corrector step. Sets of 200 trajectories were calculated for allene, propyne, and cyclopropene dications on the singlet and triplet potential energy surfaces starting from the geometry of the neutral ground state singlet. A fixed amount of kinetic energy (190 – 240 kcal/mol) was added to the initial structure. Initial momenta for the nuclei were chosen by using orthonormal

sampling³⁷ to allocate this kinetic energy. To simulate vertical ionizations, the initial positions of the nuclei were not displaced from their neutral ground state geometry. At each step in a trajectory, the SCF calculation was started with an unrestricted initial guess (using the GUESS=MIX keyword in Gaussian for singlet trajectories) to permit homolytic bond dissociation. For most trajectories, the energy was conserved to better than 10^{-5} hartree and the angular momentum was conserved to 10^{-8} \hbar . Only a few trajectories had to be discarded due to a significant fluctuation in the total energy before reaching a transition state for dissociation. Trajectories were integrated for a maximum of 600 steps (approximately 250 fs) and were terminated if the distance between the centers of mass of the fragments exceeded 12.0 bohr.

2.3 Structure and Energetics

Selected geometries on the C_3H_4 neutral and dication potential energy surfaces are shown in Figure 2.1. Tabulated bond and angle parameters are in Table 2.1. For allene, double ionization increases the CC bond length as expected. The singlet dication, **1s**, is planar to maximize the remaining π bonding, whereas in the triplet dication, **1t**, the two CH_2 groups are perpendicular similar to the neutral ground state. Formation of triplet propyne dication, **2t**, results in elongation of the triple bond and shortening of the single bond. The singlet propyne dication, **2s**, begins to look like $HCCCH^+ \cdots H_2$, with two of the CH bonds elongated to 1.27 Å and the associated H–H distance shortened to 0.95 Å. In cyclopropene singlet dication, **3s**, two electrons are removed from the π bond and the CH_2 group rotates into the plane in order to increase the π bonding. Excitation of singlet cyclopropene dication to the triplet promotes an

electron from a CC σ bonding orbital to a σ^* antibonding orbital, breaking a CC bond and opening the ring. Depending on which CC bond is broken, this results in triplet methylene dicarbene dication, **3t**, or triplet vinylmethylene dication, **4t**. Vinylmethylene, **4t**, is also an intermediate in the conversion of allene to propyne on the triplet dication surface. However, on the singlet dication surface vinylmethylene, **4s**, is only a very shallow minimum or a flat region of the potential energy surface on the pathway from allene to cyclopropene.

The relative energies calculated at the CBS-APNO level of theory are summarized in Figure 2.2 for the singlet and triplet C₃H₄ dications. Singlet allene, **1s**, is the most stable dication. A 1,2 hydrogen migration leads to the vinylmethylene structure, **4s**, which is 16 kcal/mol higher than **1s**. There is little or no barrier for this structure to return to **1s**, and only a small barrier exists for conversion to cyclopropene dication, **3s**. Singlet propyne dication, **2s**, is 51 kcal/mol higher than allene and is connected by a low barrier to the vinylmethylene dication, **4s**. Triplet allene dication, **1t**, is 41 kcal/mol higher in energy than the singlet and is the lowest energy structure on the triplet surface. A 1,2 hydrogen shift leads to the triplet vinylmethylene dication, **4t**, which is separated by small barriers from the allene and propyne isomers. Triplet methylene dicarbene dication, **3t**, has a very low barrier for conversion to vinylmethylene, **4t**. The adiabatic double ionization energies are listed in Table 2.2. The CBS-APNO values are 0.2 – 0.3 eV higher than Mebel's results at CCSD(T)/cc-pVTZ.¹⁶ Table 2.3 compares the relative energies for key structures and transition states calculated by B3LYP/6-31G(d,p) and B3LYP/6-311G(d,p) with our CBS-APNO values and Mebel's CCSD(T)/cc-pVTZ results.¹⁶ Snapshots of various

molecular fragments listed in Table 2.3 can be seen in Figure 2.3. With two exceptions, the CBS-APNO results agree very well with Mebel's data, with a mean absolute deviation of 1.7 kcal/mol. The mean absolute deviations for the B3LYP/6-31G(d,p) and B3LYP/6-311G(d,p) data compared to the CBS-APNO values are 5.8 and 5.4 kcal/mol, respectively. Since both sets of DFT calculations compare well with CBS-APNO calculations, the less expensive B3LYP/6-31G(d,p) level of theory was chosen for the ab initio molecular dynamics calculations.

2.4 Dynamics of the Dication Fragmentation

To simulate the fragmentation of the dications formed by vertical double ionization, the ab initio molecular dynamics calculations on the dication surfaces were initiated from the neutral ground state geometries. Since experimental studies found a significant isomer dependence of the fragmentation pattern,⁸ the trajectories were started from the three stable structures of C_3H_4 : allene, propyne, and cyclopropene. The fragmentation patterns also indicate that considerable rearrangement can occur before dissociation. Ionization by a short intense laser pulse can impart a considerable amount of energy to the resulting ions. Since no suitable estimate is available for the range of energies, somewhat arbitrary choices need to be made. As a matter of practicality for the computational simulation, the ions should have enough excess kinetic energy so that most dissociate in a relatively short time. With too much extra energy, the ions fragment before having a chance to rearrange; with too little energy, the dominant influence is the barrier height rather than the molecular dynamics. After some experimentation with singlet allene dication, we found that with 240 kcal/mol kinetic

energy ca. 95% of the trajectories dissociated within the 250 fs simulation time, and about half of the trajectories involved rearrangements. Since the vertically ionized singlet propyne and cyclopropene dications are 32 and 40 kcal/mol above the vertically ionized singlet allene dication, these trajectories were started with 210 and 200 kcal/mol of kinetic energy, respectively, so as to keep the total energy approximately constant. Relative to the vertically ionized singlet allene dication, energies of the vertically ionized triplet allene, propyne, and cyclopropene dications are -2, 26, and 45 kcal/mol, respectively; these were started with 240, 210, and 190 kcal/mol of kinetic energy, respectively. Since the triplet allene and propyne dication geometries are fairly close to the neutral geometries (see Figure 2.1), these vertically ionized triplet dications are only 6 and 18 kcal/mol higher than their equilibrium structures. By contrast, the methylene groups in singlet allene and cyclopropene dication are twisted by 90° compared to the neutral ground state geometries, and these vertically ionized singlet dications are 45 and 63 kcal/mol higher than the corresponding equilibrium structures. Vertically excited triplet cyclopropene dication is a saddle point and opens to vinylmethylene, **4t**, rather than methylene dicarbene, **3t**.

For singlet and triplet allene, propyne, and cyclopropene dication, 200 trajectories were calculated for a maximum simulation time of ca. 250 fs. The results of the ab initio molecular dynamics simulations are summarized in Figure 2.4 through Figure 2.9. The figures show the initial vertically excited dications and the adiabatic dication structures, the various intermediates, and the dissociation channels. The trajectories can be grouped into two categories: direct and indirect. Direct trajectories proceed to products without rearrangement. Several vibrations may occur before the

ion passes over the barrier, but the ion stays in the same valley that it started in. Indirect trajectories pass through one or more intermediates before dissociation. Direct processes and their barrier heights are shown on the left-hand side of Figure 2.4 through Figure 2.9. For about half of the trajectories, there is considerable rearrangement before dissociation. These indirect trajectories are shown on the right-hand side of Figure 2.4 through Figure 2.9. Because of the large amplitude motions, it is often difficult to assign a trajectory to a particular transition state. The dissociating trajectories are classified according to the lowest energy transition state leading to the observed product. The percentages for each indirect product also include fragmentations that occur via higher energy barriers leading to the same products.

For the selected initial energy, the average dissociation time is ca. 90 fs, with 90% of the trajectories completing in ca. 190 fs. Direct dissociation of H^+ is the fastest event, having an average time of 45 – 50 fs, with 90% completing within ca. 75 fs. Direct dissociations other than H^+ take approximately twice as long, in part because the fragments are heavier and require more time to separate. Indirect dissociation trajectories involve significant rearrangement and are 2 – 3 times longer than direct trajectories, averaging ca. 145 fs versus ca. 55 fs for direct dissociation. There is no significant difference for the average dissociation times for the singlets versus the triplets; likewise, the average times for allene, propyne, and cyclopropene are very similar. (For trajectory timings see Table 2.4).

Deprotonation is the dominant fragmentation process for all six sets of trajectories, ranging from 54 to 76% of the trajectories. Each set of trajectories displayed a ratio of ca. 2:1 between direct and indirect deprotonation. The ratios of the

other fragmentation products varied considerably with the starting structure and spin state of the dication.

For the direct dissociations, the largest percentages of products were formed via the lowest energy barriers. One exception is $\text{H}_3^+ + \text{CCCH}$ on the singlet propyne dication surface that is formed by dissociation of H_2 followed by abstraction of H^+ by H_2 as described by Mebel and Bandrauk.¹⁶ For the large excess kinetic energies used in the present study, H_2 dissociates with considerable energy and is less likely to return and abstract a proton. Other exceptions include the $\text{H}_2^+ + \text{cyclic-HCCCH}$ channel on the triplet propyne dication surface and the $\text{CH}^+ + \text{H}_2\text{CCH}^+$ channel on the triplet cyclopropene dication surface.

For the indirect dissociations, the channels with the lowest barriers also had the highest percentage of products. In cases where the final barriers are similar, higher percentages are found for processes going through the fewest intermediates or lowest intermediate barriers. Even though some of the indirect dissociation barriers are lower than the corresponding direct barriers, the percentage of indirect product was lower because of the need for rearrangement. The high yield for $\text{H}^+ + \text{H}_2\text{CCCH}^+$ on the triplet cyclopropene dication surface is the result of ring-opening to vinylmethylene which has a large driving force for rearrangement to propyne and allene dications, which both dissociate to $\text{H}^+ + \text{H}_2\text{CCCH}$.

A number of the trajectories dissociated into three fragments, for example, $\text{H} + \text{H}^+ + \text{C}_3\text{H}_2^+$. For these cases, the two C–H bonds broke in quick succession. Additional three-body fragmentations can occur in a stepwise process by subsequent dissociation of the initial two-body fragmentation products. Because the fragment ions

possess a large excess of kinetic energy, such fragmentation can happen readily. However, the stopping criteria for the trajectories were chosen to count only the first dissociation event.

2.5 Summary

The fragmentation patterns are summarized in Scheme 2.1. Although the specific percentages for various products will depend on the amount of the excess kinetic energy, some of the trends may be less sensitive to the initial conditions. Internal rearrangement can occur quite readily in the dications, and the ratio of direct to indirect dissociation is ca. 2:1 at this energy. In agreement with experiments on allene and propyne,^{4,8} deprotonation to give $\text{H}^+ + \text{C}_3\text{H}_3^+$ is calculated to be the dominant pathway, and that for $\text{H}_2^+ + \text{C}_2\text{H}_2^+$ is a factor of 5 – 10 lower. The yield of H_2/H_2^+ is highest on the singlet propyne and cyclopropene dication surface. For the allene dication, the calculated ratio of $\text{CH}_2^+ \gg \text{CH}^+ > \text{CH}_3^+$ is in good accord with ion coincidence measurements of laser induced Coulomb explosion (1:0.08:0.03).⁶ The highest yield of CH_3^+ is by direct dissociation on the triplet propyne surface. Production of CH_2^+ is more favorable on the singlet and triplet allene dication surfaces, whereas CH^+ is favored on the singlet propyne dication surface. In experiments on allene,⁶ a small amount of H_3^+ was produced and was taken as evidence that isomerization could occur before dissociation. The classical trajectory calculations confirm that extensive rearrangement occurs in conjunction with dissociation, although H_3^+ is not produced at the higher initial kinetic energies used in the present study.

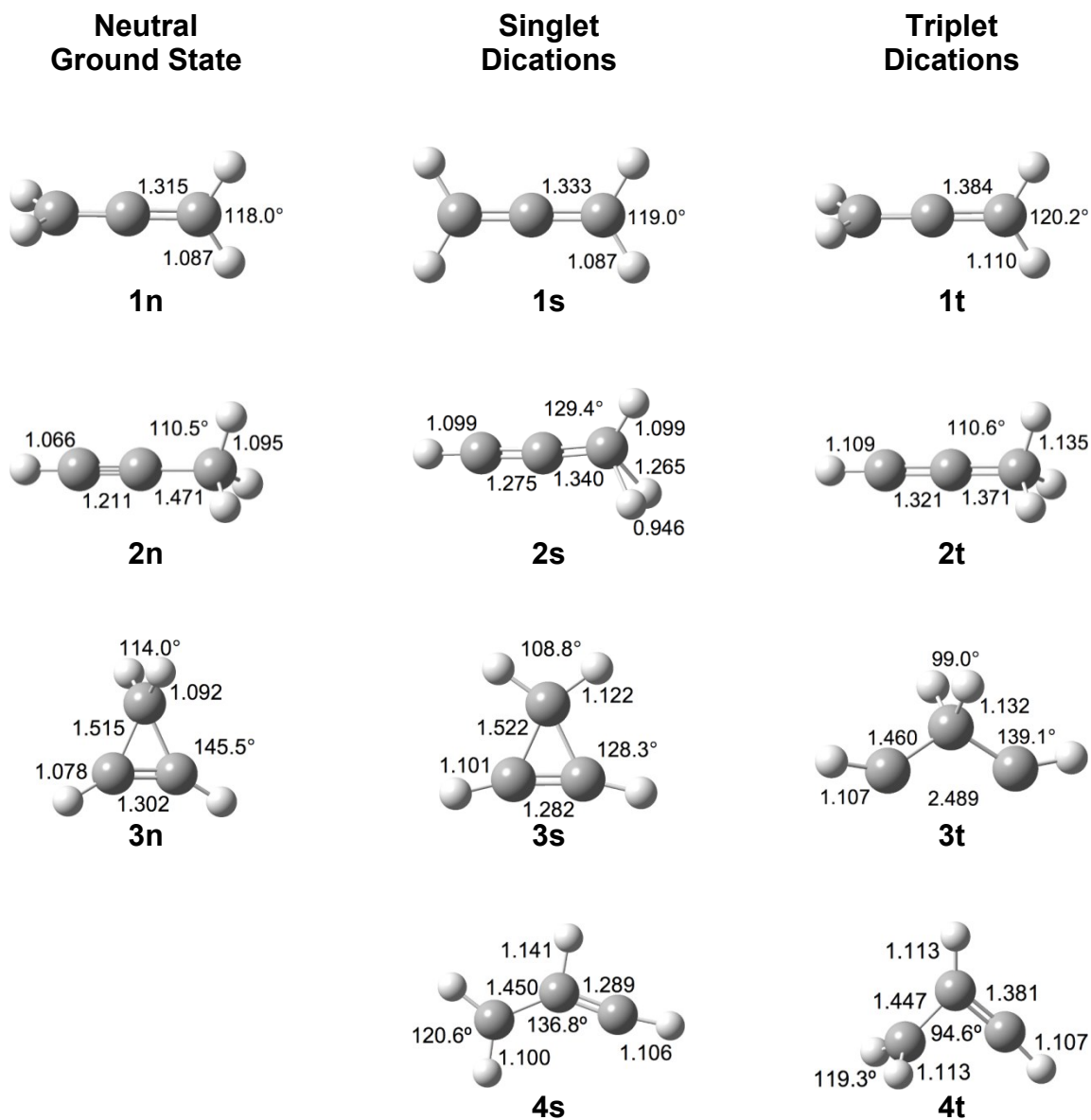


Figure 2.1 Geometries with relevant bond lengths (Å) and angles (°) for isomers on the ground neutral, singlet dication, and triplet dication state surfaces optimized at the QCISD/6-311G(d,p) level of theory.

Table 2.1 Comparison of Bond Lengths (Å) and Angles (°) for Structures on the C₃H₄ Ground State Neutral, Singlet Dication and Triplet Dication Surfaces Optimized at the QCISD 6-311G(d,p) Level of Theory

	¹ C ₃ H ₄ ⁰	¹ C ₃ H ₄ ²⁺	³ C ₃ H ₄ ²⁺
Allene	D _{2d} (¹ A ₁)	D _{2h} (¹ A _g)	D _{2d} (³ B ₂)
C–C	1.315	1.333	1.387
C–H	1.087	1.087	1.110
HCH	118.0°	119.0°	120.2°
Propyne	C _{3v} (¹ A ₁)	C _s (¹ A')	C _{3v} (³ A ₁)
C≡C	1.211	1.275	1.321
C–C	1.471	1.340	1.371
≡C–H	1.066	1.099	1.109
–C–H	1.095	1.099	1.135
Cyclopropene	C _{2v} (¹ A ₁)	C _{2v} (¹ A ₁)	C _{2v} (³ A ₁)
C=C	1.302	1.282	2.489
C–C	1.515	1.522	1.460
=C–H	1.078	1.101	1.107
–C–H	1.092	1.122	1.132
HCH	114.0°	108.8°	99.0°
C–C=C	145.5°	128.3°	139.1°
Vinylmethylene		C _s (¹ A')	C _s (³ A'')
H ₂ C–C		1.450	1.447
C–CH		1.289	1.381
–(C–H)–		1.100	1.113
–C–H		1.141	1.113
HC–H		1.106	1.107
HCH		120.6°	119.3°
CCC		136.8°	94.6°

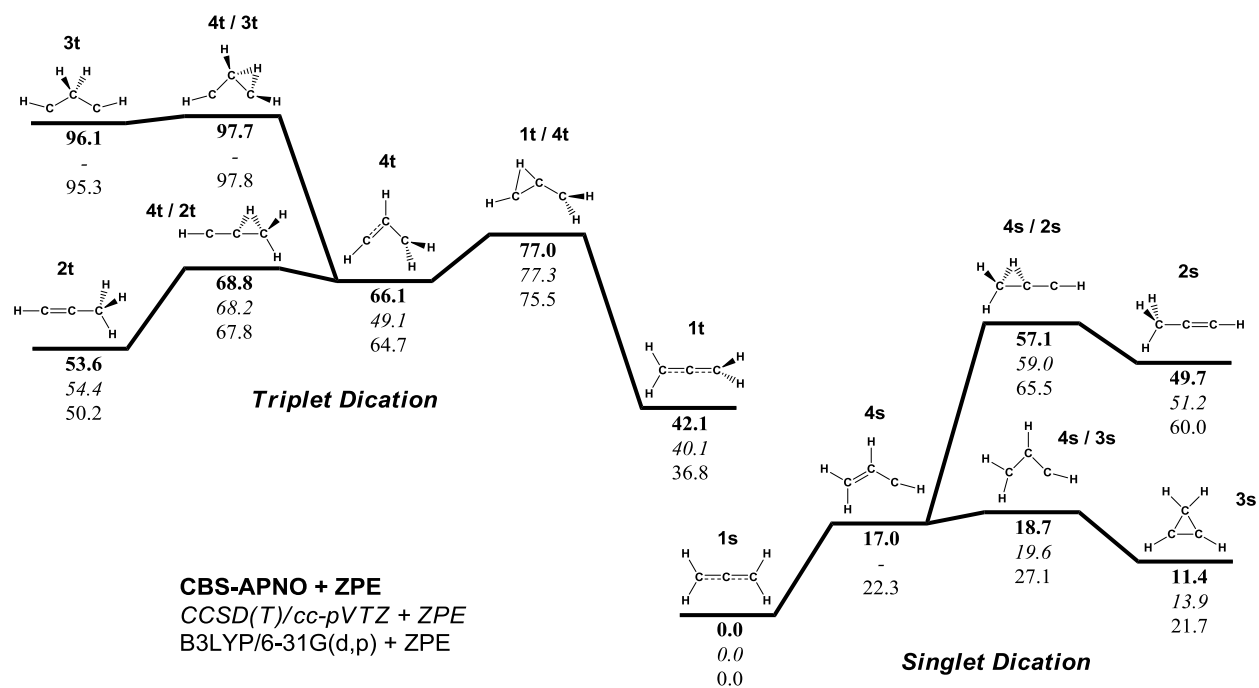


Figure 2.2 Potential energy surfaces for singlet and triplet $\text{C}_3\text{H}_4^{2+}$. Relative energies with zero point energy in kcal/mol at the CBS-APNO (in bold), CCSD(T)/cc-pVTZ//B3LYP/6-311G(d,p) (*in italics*) and B3LYP/6-31G(d,p) levels of theory.

Table 2.2 Calculated Adiabatic Double Ionization Energies (eV) for Allene, Propyne and Cyclopropene

	B3LYP/ 6-31G(d,p)	B3LYP/ 6-311G(d,p)	CBS-APNO	CCSD(T)/ cc-pVTZ ^a
1n → 1s	25.30	25.55	25.93	25.84
1n → 1t	26.89	27.17	27.75	27.58
2n → 2s	27.77	28.00	28.13	28.08
2n → 2t	27.34	27.64	28.30	28.22
3n → 3s	25.17	25.35	25.43	
3n → 4t	27.04	27.27	27.80	

^a Ref.¹⁶

Table 2.3 Relative Energies of Optimized $C_3H_4^{2+}$ Surface Stationary Points for Singlet and Triplet States (in kcal/mol)

	B3LYP/ 6-31G(d,p)	B3LYP/ 6-311G(d,p)	CBS-APNO	CBS-APNO +ZPE	CCSD(T)/ cc-pVTZ+ZPE ^a
1s	0.0	0.0	0.0	0.0	0.0
TS 1s/H⁺+H₂CCCH⁺	83.8	81.8	85.7	80.8	82.0
H⁺+H₂CCCH⁺	20.8	18.1	10.7	5.9	8.5
TS 1s/CH₂⁺+H₂CC⁺	127.5	127.7	128.6 ^b	124.0 ^b	114.7 ^c
CH₂⁺+H₂CC⁺	59.3	59.0	55.3	48.5	46.7
TS 1s/4s	22.1	21.4 ^d	15.4	14.6	
4s	22.0	21.6 ^d	16.3	17.0	
TS 4s/CH⁺+H₂CCH⁺	117.5	117.0	111.3	107.7	104.2
CH⁺+H₂CCH⁺	34.4	32.4	19.5	14.2	11.0
TS 4s/3s	26.5	26.2	18.6	18.7	19.6
3s	21.9	21.4	12.6	11.4	13.9
TS 3s/H⁺+c-C₃H₃⁺	75.4	74.6	72.4	67.2	69.6
H⁺+c-C₃H₃⁺	-6.2	-7.3	-17.7	-20.9	-18.4
TS 4s/2s	68.5	67.1	60.4	57.1	59.0
2s	61.8	60.0	51.3	49.7	51.2
TS 2s/CH₃⁺+C₂H⁺	117.2	117.7	114.7 ^b	112.8 ^b	124.1
CH₃⁺+C₂H⁺	66.8	66.6	57.8	54.1	80.9 ^e
1t	36.8	37.4	41.5	42.1	(40.1)
TS 1t/H⁺+H₂CCCH⁺	97.2	96.0	112.2 ^b	105.4 ^b	105.6
H⁺+H₂CCCH⁺	58.5	56.7	55.3	47.4	49.8
TS 1t/4t	80.0	79.1	81.8	77.0	77.3
4t	66.0	66.6	68.1	66.1	49.1 ^f
TS 4t/H⁺+c-C₃H₃⁺	117.4	116.2	121.2 ^b	113.8 ^b	114.5
H⁺+c-C₃H₃⁺	86.4	85.0	80.3	72.0	74.3
TS 4t/CH₂⁺+HCCH⁺	107.5	107.0	106.5	103.1	100.8
CH₂⁺+HCCH⁺	17.3	15.4	11.9	5.9	4.4
TS 4t/3t	102.2	101.7	101.7	97.7	
3t	97.9	98.9	98.3	96.1	
TS 4t/2t	70.7	70.4	71.4	68.8	68.2
2t	52.6	52.4	55.5	53.6	54.4
TS 2t/H⁺+H₂CCCH⁺	95.5	94.2	111.0 ^b	104.5 ^b	104.7
H⁺+H₂CCCH⁺	58.5	56.7	55.3	47.4	49.8
MAD	5.8^g	5.4^g			1.7^h

^a Reference 10. ^b CBS-APNO energy using the B3LYP/6-311G(d,p) geometry.

^c CASPT2(8,8)/cc-pVTZ//CASSCF(8,8)/6-311G(d,p). ^d Single point energy using the B3LYP/6-31G(d,p) geometry. ^e Not included in the MAD (lower electronic state found). ^f Not included in the MAD (unable to produce this state). ^g Mean Absolute Deviation to CBS-APNO. ^h Mean Absolute Deviation to CBS-APNO + ZPE.

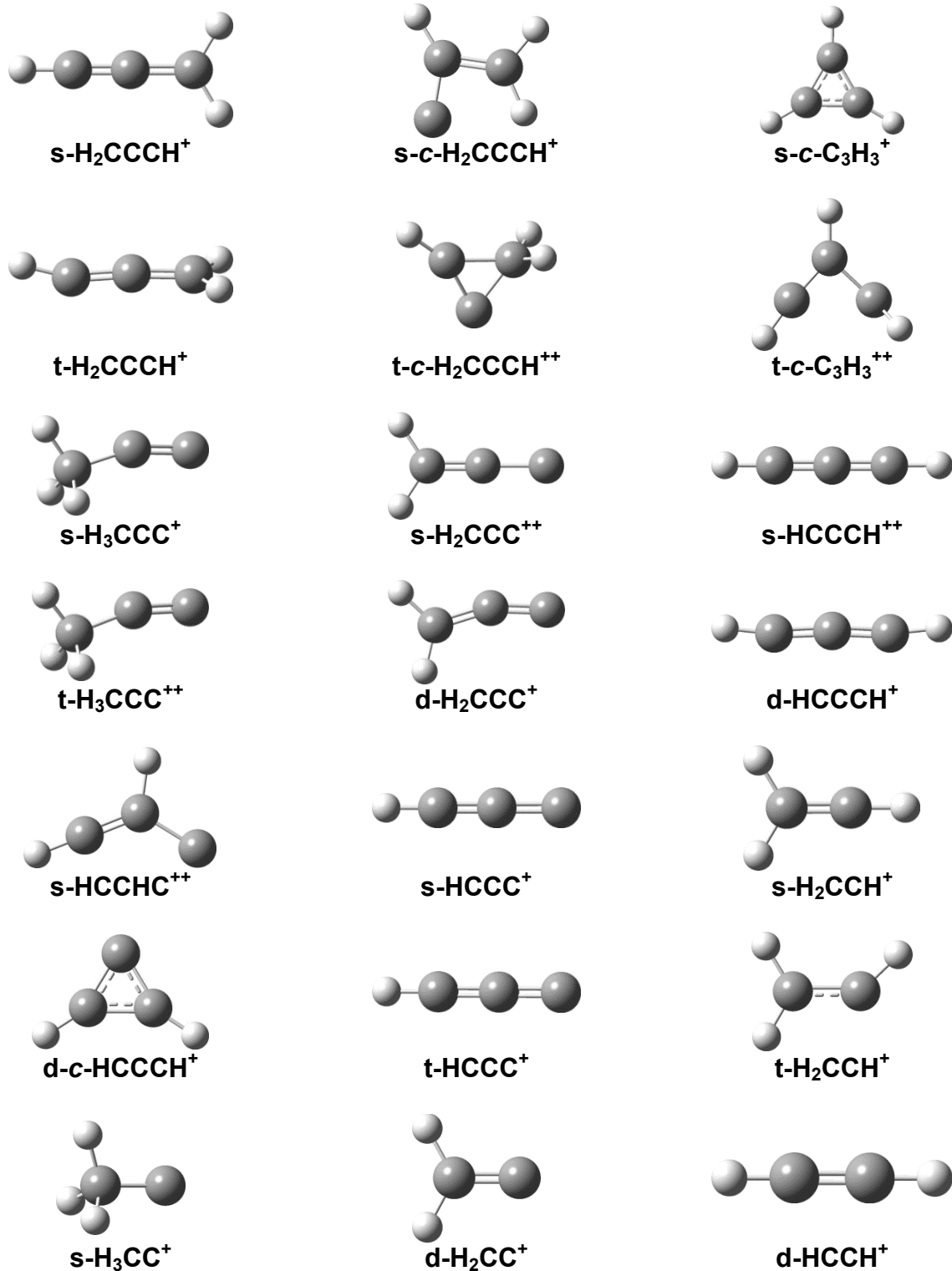


Figure 2.3 Fragment structures for the singlet and triplet dication optimized at the QCISD/6-311G(d,p) level of theory.

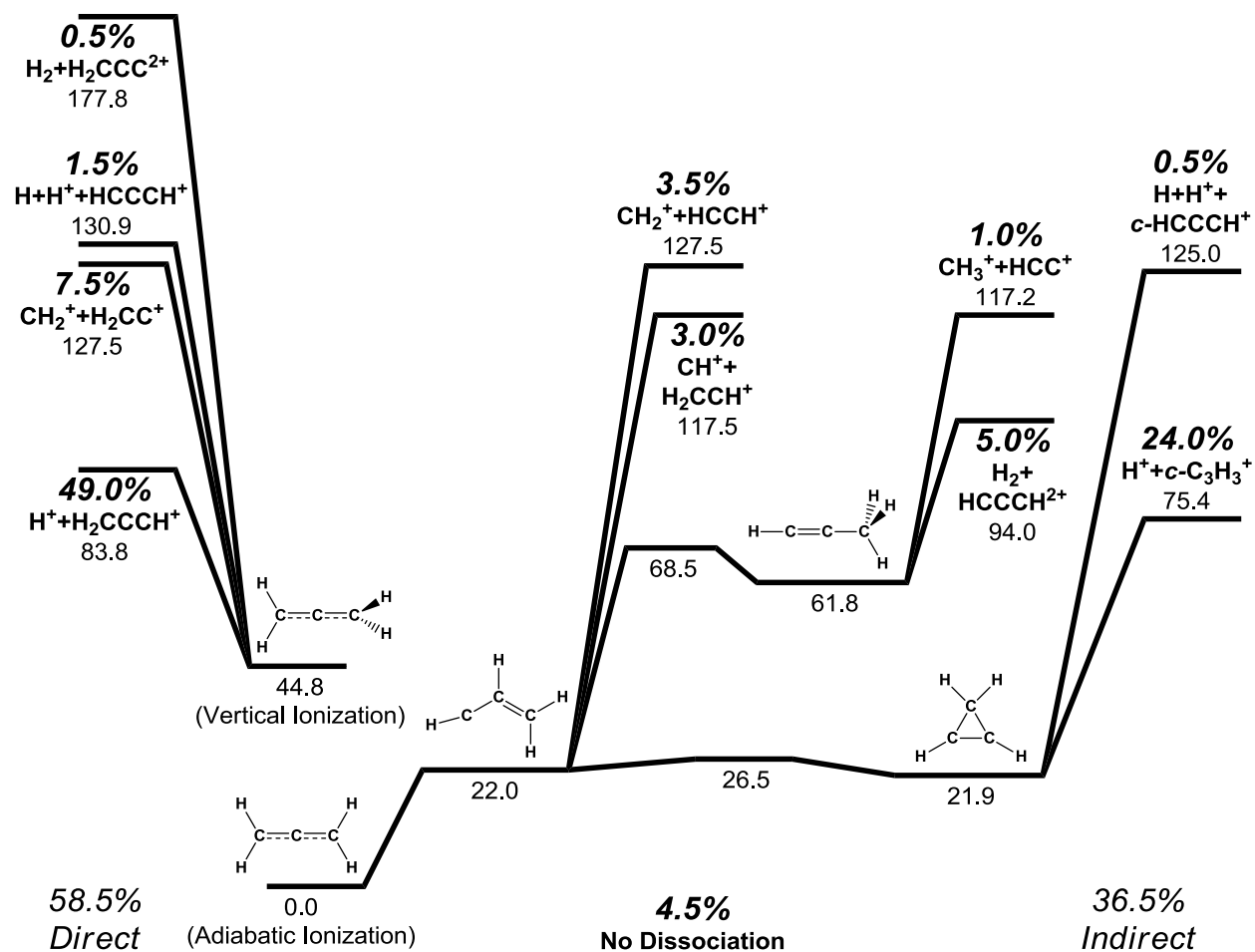


Figure 2.4 Fragmentation of vertically doubly ionized allene on the singlet surface. Left hand side shows the percentages and barriers for direct dissociation. Right hand side shows only the lowest barriers for indirect dissociation; percentages also include fragmentations occurring via higher barriers (199 trajectories calculated at the B3LYP/6-31G(d,p) level of theory with 240 kcal/mol initial kinetic energy).

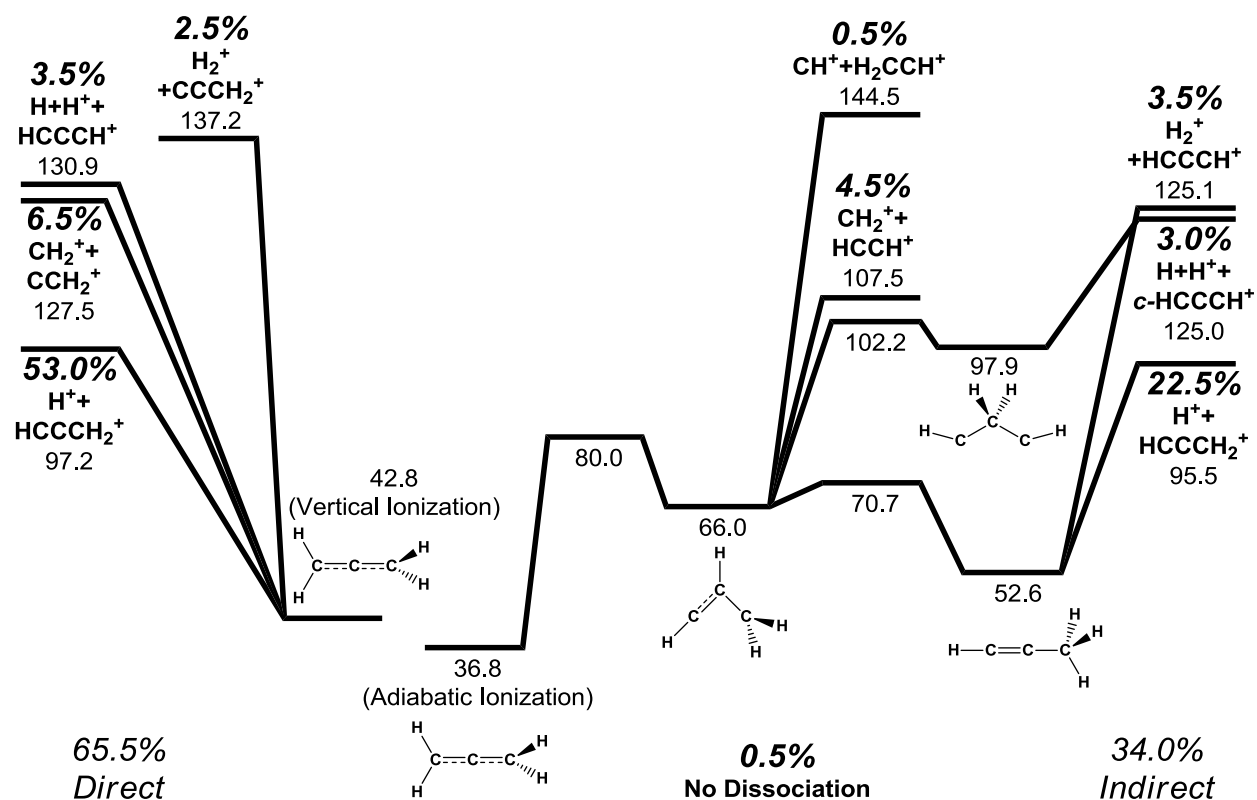


Figure 2.5 Fragmentation of vertically doubly ionized allene on the triplet surface. Left hand side shows the percentages and barriers for direct dissociation. Right hand side shows only the lowest barriers for indirect dissociation; percentages also include fragmentations occurring via higher barriers (200 trajectories calculated at the B3LYP/6-31G(d,p) level of theory with 240 kcal/mol initial kinetic energy).

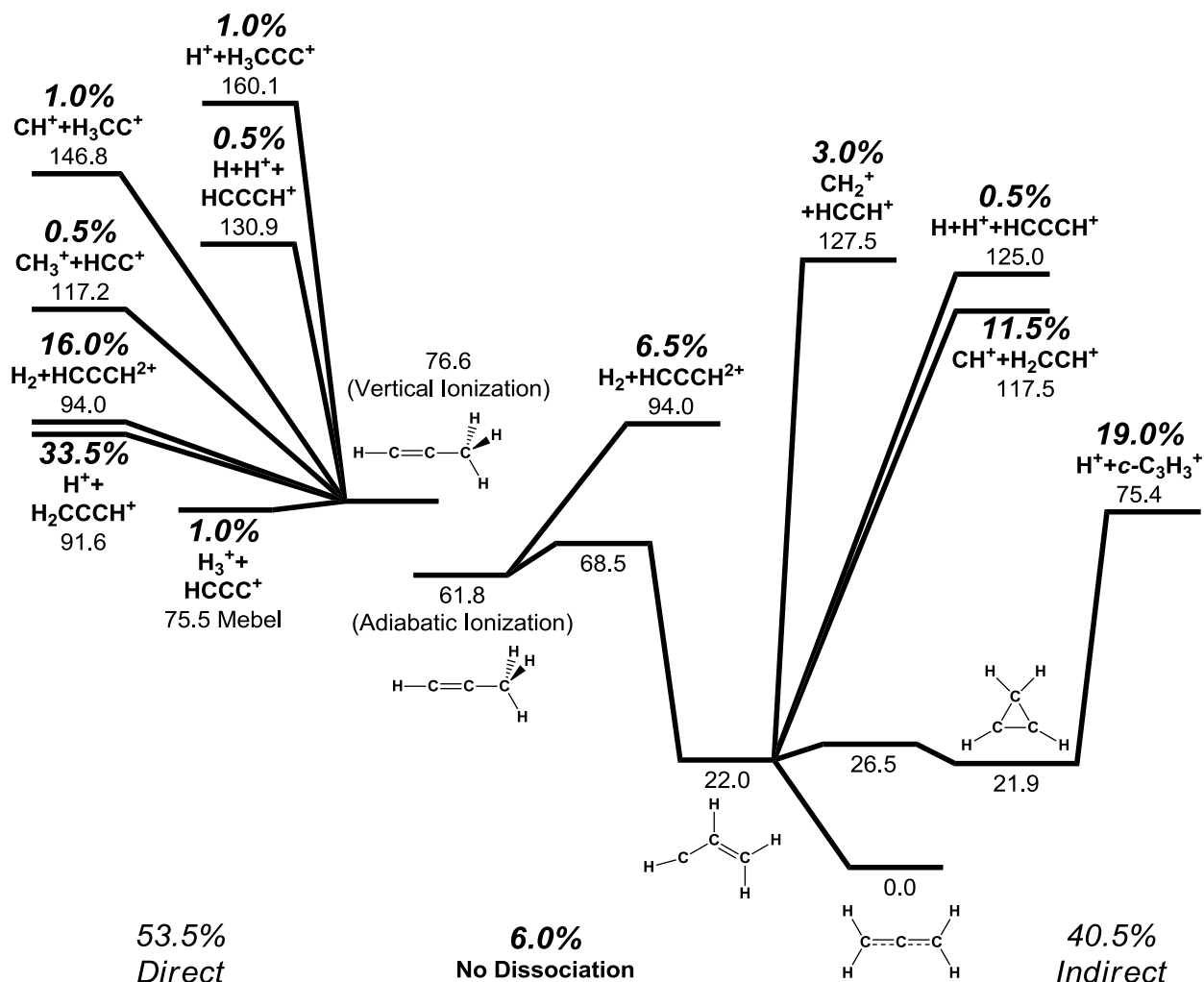


Figure 2.6 Fragmentation of vertically doubly ionized propyne on the singlet surface. Left hand side shows the percentages and barriers for direct dissociation. Right hand side shows only the lowest barriers for indirect dissociation; percentages also include fragmentations occurring via higher barriers (200 trajectories calculated at the B3LYP/6-31G(d,p) level of theory with 210 kcal/mol initial kinetic energy).

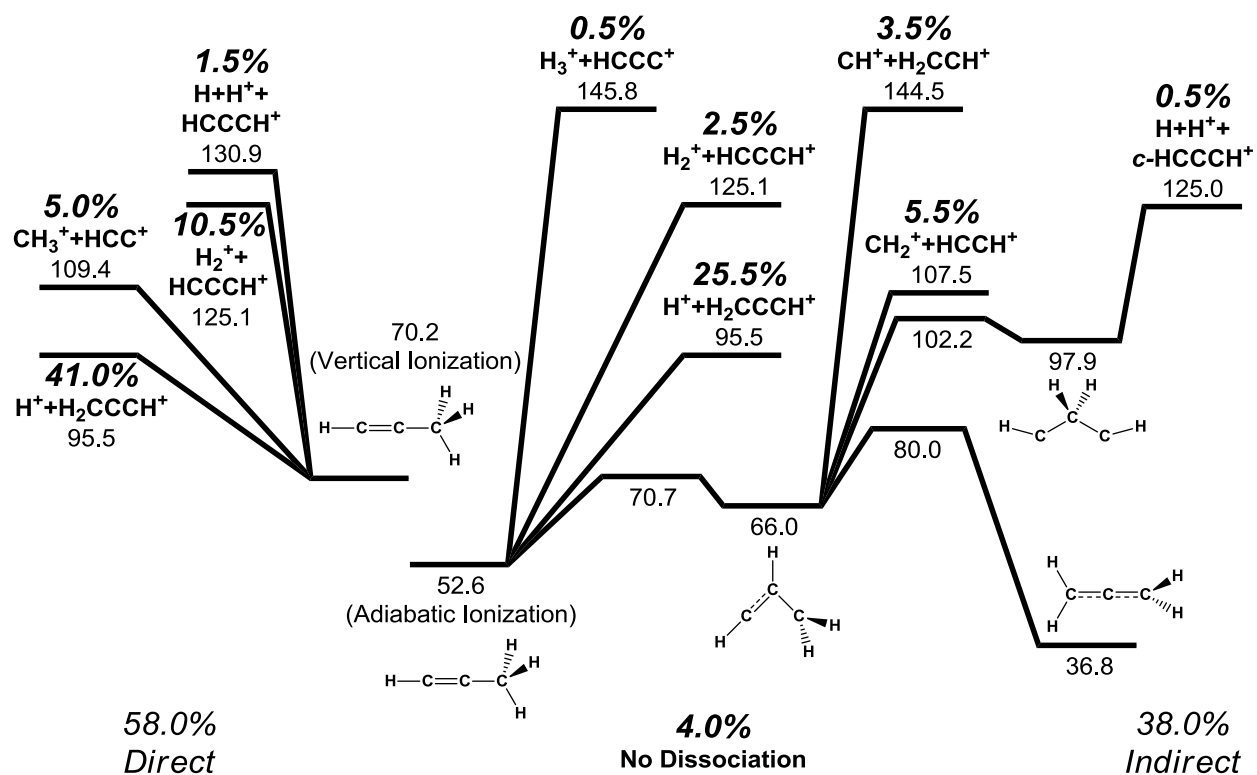


Figure 2.7 Fragmentation of vertically doubly ionized propyne on the triplet surface. Left hand side shows the percentages and barriers for direct dissociation. Right hand side shows only the lowest barriers for indirect dissociation; percentages also include fragmentations occurring via higher barriers (200 trajectories calculated at the B3LYP/6-31G(d,p) level of theory with 210 kcal/mol initial kinetic energy).

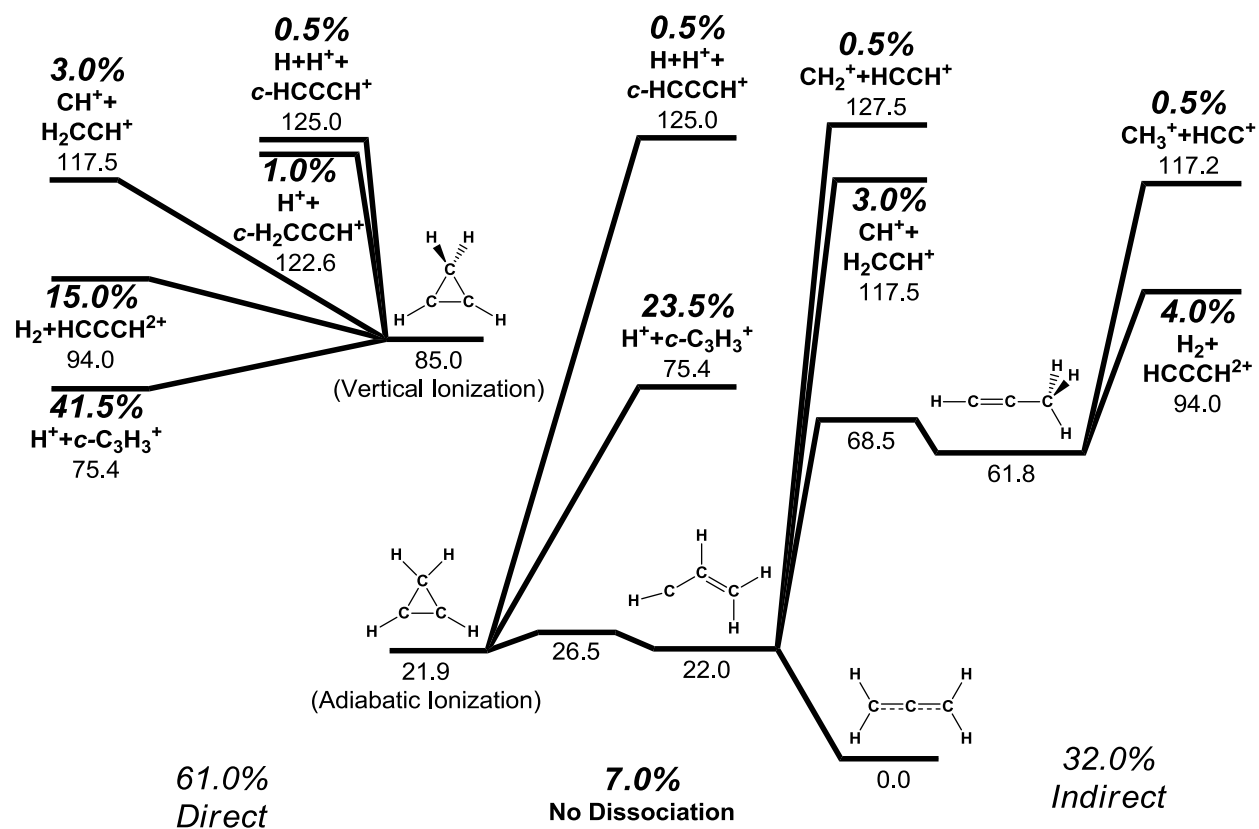


Figure 2.8 Fragmentation of vertically doubly ionized cyclopropene on the singlet surface. Left hand side shows the percentages and barriers for direct dissociation. Right hand side shows only the lowest barriers for indirect dissociation; percentages also include fragmentations occurring via higher barriers (200 trajectories calculated at the B3LYP/6-31G(d,p) level of theory with 200 kcal/mol initial kinetic energy).

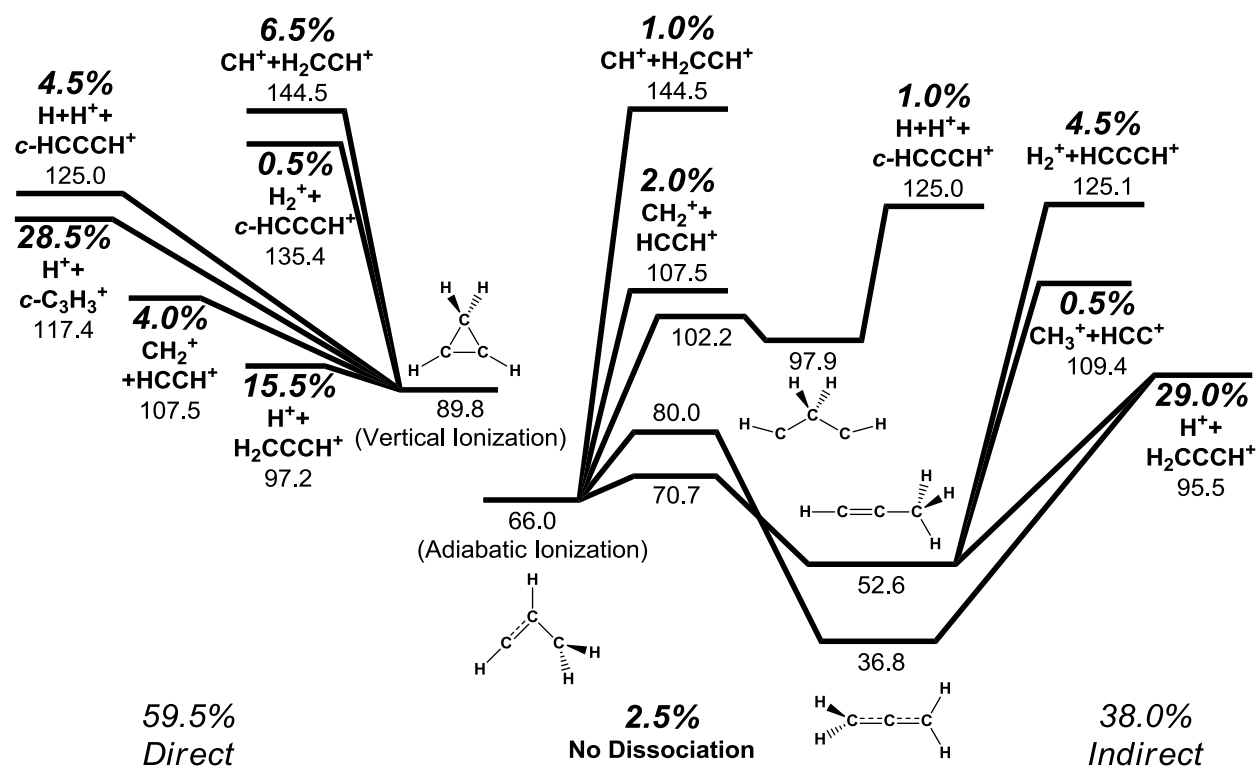
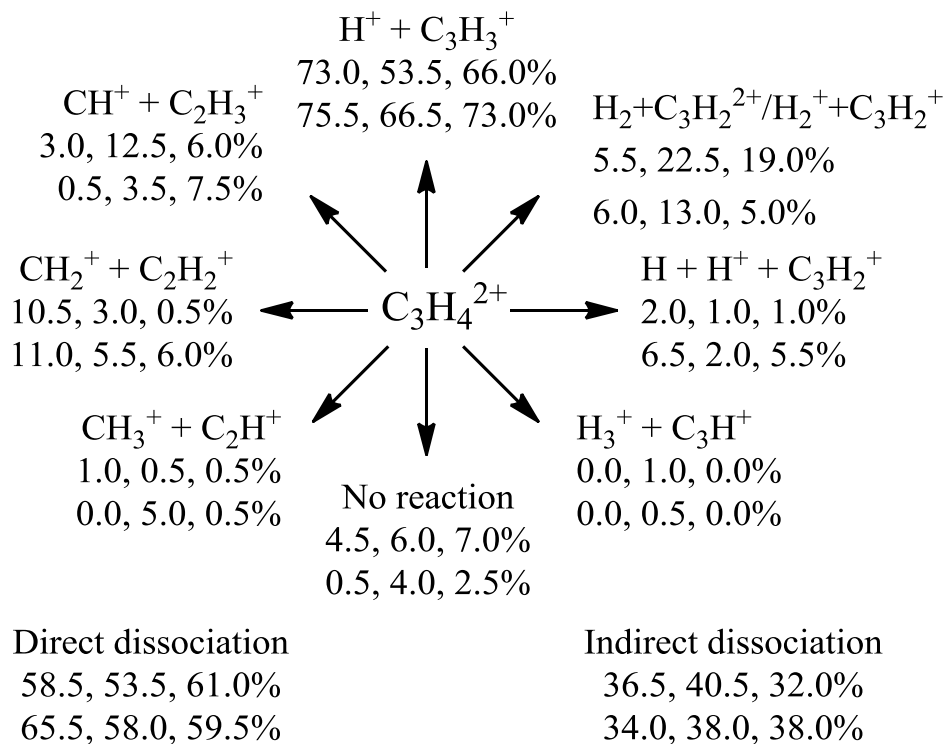


Figure 2.9 Fragmentation of vertically doubly ionized cyclopropene on the triplet surface. Left hand side shows the percentages and barriers for direct dissociation. Right hand side shows only the lowest barriers for indirect dissociation; percentages also include fragmentations occurring via higher barriers (200 trajectories calculated at the B3LYP/6-31G(d,p) level of theory with 190 kcal/mol initial kinetic energy).

Table 2.4 Timing Data for Trajectories

		Total	Direct	Indirect	H ⁺	Non H ⁺	Dir. H ⁺	Ind. H ⁺	Dir. Non H ⁺	Ind. Non H ⁺	No Dissoc.
Total											
	90%	189	107	243	156	241	78	215	143	260	283
	Average	91	57	146	77	124	48	131	82	176	262
Singlet											
	90%	198	89	243	157	244	78	210	120	258	265
	Average	91	53	152	77	122	47	134	68	181	254
Triplet											
	90%	183	120	244	151	215	77	218	153	267	292
	Average	90	61	140	78	126	50	128	97	170	280
Allene											
	90%	177	100	239	138	245	76	191	147	260	260
	Average	85	54	139	70	132	46	122	89	171	253
Propyne											
	90%	204	116	247	177	243	92	228	137	255	284
	Average	98	60	153	84	122	51	140	78	170	267
Cyclopropene											
	90%	182	103	241	155	232	77	225	126	262	284
	Average	90	58	145	80	117	49	131	82	187	260
Singlet Allene											
	90%	192	92	243	148	247	80	196	135	260	257
	Average	91	53	152	75	144	47	132	85	189	252
Singlet Propyne											
	90%	219	98	246	185	244	96	228	108	254	272
	Average	99	55	157	84	118	51	144	63	168	258
Singlet Cyclopropene											
	90%	181	82	239	152	234	64	208	93	259	258
	Average	83	50	148	73	108	43	129	65	202	252
Triplet Allene											
	90%	153	105	214	134	214	69	166	149	258	269
	Average	79	54	126	65	121	46	112	92	153	269
Triplet Propyne											
	90%	192	121	244	172	215	73	212	162	257	287
	Average	97	64	148	83	127	51	136	94	174	279
Triplet Cyclopropene											
	90%	180	120	246	163	206	87	228	146	271	293
	Average	96	67	142	86	128	54	133	103	173	283

^a Time in femtoseconds for 90% of the trajectories to complete and average time for trajectories to complete. A trajectory is considered complete if the inter-fragment center-of-mass distance exceeded 12.0 bohr or if the trajectory was sufficiently beyond the transition state before the number of steps was exceeded or before energy conservation problems occurred.



Scheme 2.1 Percentages of initial dissociation products from the fragmentation of $\text{C}_3\text{H}_4^{2+}$ on the singlet surface (top row) and triplet surface (bottom row), starting from allene, propyne, and cyclopropene, respectively.

2.6 References

1. Posthumus, J. H. The dynamics of small molecules in intense laser fields. *Rep. Prog. Phys.* **2004**, *67*, 623-665.
2. Corkum, P. B.; Ivanov, M. Y.; Wright, J. S. Subfemtosecond processes in strong laser fields. *Annu. Rev. Phys. Chem.* **1997**, *48*, 387-406.
3. Sheehy, B.; DiMauro, L. F. Atomic and molecular dynamics in intense optical fields. *Annu. Rev. Phys. Chem.* **1996**, *47*, 463-494.
4. Cornaggia, C. Carbon geometry of C₃H₃⁺ and C₃H₄⁺ molecular ions probed by laser induced coulomb explosion. *Phys. Rev. A* **1995**, *52*, R4328-R4331.
5. Hoshina, K.; Furukawa, Y.; Okino, T.; Yamanouchi, K. Efficient ejection of H₃⁺ from hydrocarbon molecules induced by ultrashort intense laser fields. *J. Chem. Phys.* **2008**, *129*, 104302.
6. Xu, H.; Okino, T.; Yamanouchi, K. Ultrafast hydrogen migration in allene in intense laser fields: Evidence of two-body Coulomb explosion. *Chem. Phys. Lett.* **2009**, *469*, 255-260.
7. Xu, H. L.; Okino, T.; Yamanouchi, K. Tracing ultrafast hydrogen migration in allene in intense laser fields by triple-ion coincidence momentum imaging. *J. Chem. Phys.* **2009**, *131*, 151102.
8. Scully, S. W. J.; Senthil, V.; Wyer, J. A.; Shah, M. B.; Montenegro, E. C.; Kimura, M.; Tawara, H. Direct evidence of a strong isomer effect in electron-impact double ionization of C₃H₄. *Phys. Rev. A* **2005**, *72*.

9. Andrews, S. R.; Parry, D. E.; Vairamani, M.; Harris, F. M. The allene dication - Calculated and measured triplet electronic state energies. *J. Chem. Soc.-Faraday Trans.* **1992**, *88*, 3403-3407.
10. Andrews, S. R.; Harris, F. M.; Parry, D. E. Double ionization of the propyne molecule to ground and electronically excited states of the doubly charged ion. *Chem. Phys.* **1995**, *194*, 215-222.
11. Andrews, S. R.; Parry, D. E.; Harris, F. M. The allene dication - Calculated and measured singlet electronic state energies. *J. Chem. Soc.-Faraday Trans.* **1995**, *91*, 1181-1183.
12. Jeffreys, N.; Parry, D. E.; Harris, F. M. Combined theoretical and experimental study of the triple ionization of allene (C_3H_4) to quadruplet electronic states of $C_3H_4^{3+}$. *J. Chem. Soc.-Faraday Trans.* **1998**, *94*, 1561-1564.
13. Frenking, G.; Schwarz, H. Ab initio molecular orbital calculations on the interconversion of allene and propyne cation radicals and the mechanism for hydrogen loss from $C_3H_4^+$. *Int. J. Mass Spectrom. Ion Process.* **1983**, *52*, 131-138.
14. Wong, M. W.; Radom, L. A theoretical study of the $C_3H_4(2^+)$ potential energy surface. *J. Mol. Struct.* **1989**, *198*, 391-402.
15. Lammertsma, K.; Schleyer, P. V. The nature of doubly charged $C_3H_4^{2+}$ ions - Structural and energetic relationships. *J. Am. Chem. Soc.* **1990**, *112*, 7935-7940.
16. Mebel, A. M.; Bandrauk, A. D. Theoretical study of unimolecular decomposition of allene cations. *J. Chem. Phys.* **2008**, *129*.

17. Li, X. S.; Schlegel, H. B. Ab initio classical trajectory calculations of acetylene dication dissociation. *J. Phys. Chem. A* **2004**, *108*, 468-472.
18. Zhou, J.; Schlegel, H. B. Ab Initio Classical Trajectory Study of the Dissociation of Neutral and Positively Charged Methanimine (CH_2NHn^+ $n=0-2$). *J. Phys. Chem. A* **2009**, *113*, 9958-9964.
19. Townsend, D.; Lahankar, S. A.; Lee, S. K.; Chambreau, S. D.; Suits, A. G.; Zhang, X.; Rheinecker, J.; Harding, L. B.; Bowman, J. M. The roaming atom: Straying from the reaction path in formaldehyde decomposition. *Science* **2004**, *306*, 1158-1161.
20. Lahankar, S. A.; Chambreau, S. D.; Townsend, D.; Suits, F.; Farnum, J.; Zhang, X. B.; Bowman, J. M.; Suits, A. G. The roaming atom pathway in formaldehyde decomposition. *J. Chem. Phys.* **2006**, *125*, 044303.
21. Suits, A. G. Roaming atoms and radicals: A new mechanism in molecular dissociation. *Accounts Chem. Res.* **2008**, *41*, 873-881.
22. Ochterski, J. W.; Petersson, G. A.; Montgomery, J. A. A complete basis set model chemistry .5. Extensions to six or more heavy atoms. *J. Chem. Phys.* **1996**, *104*, 2598-2619.
23. Frisch, M. J.; Trucks, G. W.; Schlegel, H. B.; Scuseria, G. E.; Robb, M. A.; Cheeseman, J. R.; Scalmani, G.; Barone, V.; Mennucci, B.; Petersson, G. A.; Nakatsuji, H.; Caricato, M.; Li, X.; Hratchian, H. P.; Izmaylov, A. F.; Bloino, J.; Zheng, G.; Sonnenberg, J. L.; Hada, M.; Ehara, M.; Toyota, K.; Fukuda, R.; Hasegawa, J.; Ishida, M.; Nakajima, T.; Honda, Y.; Kitao, O.; Nakai, H.; Vreven, T.; Montgomery, J., J. A.; Peralta, J. E.; Ogliaro, F.; Bearpark, M.; Heyd, J. J.;

- Brothers, E.; Kudin, K. N.; Staroverov, V. N.; Kobayashi, R.; Normand, J.;
 Raghavachari, K.; Rendell, A.; Burant, J. C.; Iyengar, S. S.; Tomasi, J.; Cossi,
 M.; Rega, N.; Millam, J. M.; Klene, M.; Knox, J. E.; Cross, J. B.; Bakken, V.;
 Adamo, C.; Jaramillo, J.; Gomperts, R.; Stratmann, R. E.; Yazyev, O.; Austin, A.
 J.; Cammi, R.; Pomelli, C.; Ochterski, J. W.; Salvador, P.; Dannenberg, J. J.;
 Dapprich, S.; Parandekar, P. V.; Mayhall, N. J.; Daniels, A. D.; Farkas, O.;
 Foresman, J. B.; Ortiz, J. V.; Cioslowski, J.; Fox, D. J. *Gaussian Development
 Version*, Revision H.X4; Gaussian, Inc.: Wallingford, CT, 2009.
24. Vosko, S. H.; Wilk, L.; Nusair, M. Accurate spin-dependent electron liquid
 correlation energies for local spin-density calculations - A critical analysis. *Can. J.
 Phys.* **1980**, *58*, 1200-1211.
 25. Lee, C. T.; Yang, W. T.; Parr, R. G. Development of the Colle-Salvetti correlation
 energy formula into a functional of the electron density. *Phys. Rev. B* **1988**, *37*,
 785-789.
 26. Becke, A. D. Density functional thermochemistry. III. The role of exact exchange.
J. Chem. Phys. **1993**, *98*, 5648-5652.
 27. Stephens, P. J.; Devlin, F. J.; Chabalowski, C. F.; Frisch, M. J. Ab-initio
 calculations of vibrational absorption and circular-dichroism spectra using
 density-functional force-fields. *J. Phys. Chem.* **1994**, *98*, 11623-11627.
 28. Ditchfield, R.; Hehre, W. J.; Pople, J. A. Self-consistent molecular orbital
 methods. IX. Extended Gaussian-type basis for molecular orbital studies of
 organic molecules. *J. Chem. Phys.* **1971**, *54*, 724.

29. Hehre, W. J.; Ditchfield, R.; Pople, J. A. Self-consistent molecular orbital methods. XII. Further extensions of Gaussian type basis sets for use in molecular orbital studies of organic molecules. *J. Chem. Phys.* **1972**, *56*, 2257.
30. Hariharan, P. C.; Pople, J. A. Influence of polarization functions on molecular orbital hydrogenation energies. *Theor. Chim. Acta* **1973**, *28*, 213-222.
31. Krishnan, R.; Binkley, J. S.; Seeger, R.; Pople, J. A. Self-consistent molecular orbital methods. XX. Basis set for correlated wave functions. *J. Chem. Phys.* **1980**, *72*, 650-654.
32. Pople, J. A.; Headgordon, M.; Raghavachari, K. Quadratic configuration interaction - A general technique for determining electron correlation energies. *J. Chem. Phys.* **1987**, *87*, 5968-5975.
33. Hratchian, H. P.; Schlegel, H. B. Accurate reaction paths using a Hessian based predictor-corrector integrator. *J. Chem. Phys.* **2004**, *120*, 9918-9924.
34. Hratchian, H. P.; Schlegel, H. B. Using Hessian updating to increase the efficiency of a Hessian based predictor-corrector reaction path following method. *J. Chem. Theory Comput.* **2005**, *1*, 61-69.
35. Millam, J. M.; Bakken, V.; Chen, W.; Hase, W. L.; Schlegel, H. B. Ab initio classical trajectories on the Born-Oppenheimer surface: Hessian-based integrators using fifth-order polynomial and rational function fits. *J. Chem. Phys.* **1999**, *111*, 3800-3805.
36. Bakken, V.; Millam, J. M.; Schlegel, H. B. Ab initio classical trajectories on the Born-Oppenheimer surface: Updating methods for Hessian-based integrators. *J. Chem. Phys.* **1999**, *111*, 8773-8777.

37. Bunker, D. L.; Hase, W. L. Non-RRKM unimolecular kinetics - Molecules in general, and CH₃NC in particular. *J. Chem. Phys.* **1973**, 59, 4621-4632.

CHAPTER 3

ASSESSING THE ACCURACY OF TD-DFT TRANSITION ENERGIES AND INTENSITIES FOR EXCITED STATE CHARGE TRANSFER BANDS IN INORGANIC COMPLEXES

3.1 Introduction

Solar radiation is the most abundant source of energy available on the planet. Harnessing this energy source and converting it to chemical energy with a similar efficiency seen in the photosynthetic cycle of plant life would provide a renewable supply of energy that would break our reliance on non-renewable fossil fuels. Most of the high energy photons emitted from the sun are absorbed in the upper atmosphere, but a significant amount of visible and near ultra-violet photons (ca. 3 – 12 eV) reach the Earth's surface. These fall into the ultra-violet and visible (UV-vis) regions of the light spectrum. Many transition metal complexes are known to absorb and emit light in this energy window, most clearly evident by the variety in color of these complexes. Accurately predicting the excited state spectrum of a chemical system using theoretical methods would allow candidate systems for solar energy conversion to be screened quickly and cheaply based on the energies (photon wavelength) and intensities (absorption efficiency) of the excited states.

Developments in computational method have greatly increased the ability for theory to produce accurate excited state calculation results.¹⁻³ Equations of motion coupled cluster^{4,5} (EOM-CC), complete active space self-consistent field^{6,7} (CAS-SCF), and multi-reference configuration interaction⁸ (MR-CI) are sophisticated wavefunction

techniques that have the ability to accurately compute excited state energies of systems, but they are prohibitively expensive for most inorganic complexes. Time-dependent density function theory⁹⁻¹¹ (TD-DFT) methods are a computationally efficient and popular method for excited state calculations. However, relatively few studies have performed benchmark calculations against high level wavefunction methods for transition metal complexes.^{12,13} A pair of recent studies by Caricato et al.^{14,15} compared excited state energies and intensities of small organic molecules generated by many different DFT functionals to the EOM-CCSD level of theory. This study aims to examine the adequacies of TD-DFT and wavefunction methods for accurately predicting excited state energies and intensities for simple first-row transition metal complexes.

3.2 Computation Details

Calculations were performed in development versions of the Gaussian software suite.¹⁶ Structures were optimized using the B3LYP density functional¹⁷⁻²⁰ with the 6-311G(d,p) basis set.^{21,22} Wave functions were tested for their stability^{22,23} and harmonic vibrational frequency calculations were used to confirm minimum energy structures.²³⁻²⁵ Oscillator strengths in the length formalism²⁶ (fL) were calculated from the transition energies (ΔE) and transition dipoles (μ) of the computed excited states, shown in eq (1).

$$fL = \frac{2}{3} \Delta E \times \mu^2 \quad \text{where } \mu = \langle \psi_i | r_{ij} | \psi_j \rangle \quad (1)$$

Calculation results on an initial test set of ten organic molecules agreed with the results subsequently published by Caricato et al.¹⁵ The initial test set consisted of carbon

monoxide, acetylene, ethylene, formaldehyde, formamide, butadiene, acetone, benzene, pyridine, phenol and benzaldehyde.

Initially, we needed to determine basis set choice affected the modeling of excited states. Figure 3.1 shows calculated excited state spectra for benzaldehyde at the B3LYP level of theory computed with basis sets having different amounts of polarization functions (Figure 3.1a) and different amounts of diffuse functions (Figure 3.1b). Significant improvement of the calculated excited state spectra is not observed after the addition of one set polarization functions (Figure 3.1a). For excited state energies near the ionization threshold (ca. 7 eV) and below, additional diffuse functions after one set do not show significant improvement (Figure 3.1b). Therefore, the most reasonable choice of basis set for small organic molecules is 6-311++G(d,p).

In calculating the excited state spectra of the small organic systems, we used a small variety of wave function (CIS,²⁷ RPA,²⁸ and EOM-CCSD^{4,5}) and density function theory levels (B3LYP, PBE0,²⁹⁻³¹ LC- ω PBE,³² and CAM-B3LYP³³). The results obtained for the small organic systems are in agreement with the result reported by Caricato. Compared to experimental data, long range corrected functionals slightly overestimate energies but generate accurate oscillator strengths. Hybrid functionals yield accurate energies but slightly overestimate oscillator strengths. Wavefunction methods severely overestimate both energies and oscillator strengths, while pure functionals underestimate both energies and oscillator strengths.

3.3 Inorganic Complex Results and Discussions

Similar to the protocol for the small organic compounds, a reasonable basis set needed to be agreed upon for calculating the electronic spectra for inorganic complexes. In an effort to reduce possible complications, a small initial test set of transition metal complexes, TiCl_4 , $\text{Ni}(\text{CO})_4$, and $\text{Cr}(\text{CO})_6$ was chosen with the intent of having simple electronic structure characteristics such as closed shell systems, high geometric symmetry, and either an empty or full d-shell. For the initial set of inorganic complexes, a larger number of basis sets were examined than for the small organic molecules including Pople basis sets: 6-311G, 6-311G(d), 6-311+G(d), 6-311G(2df), and 6-311G(3df);^{21,22,34,35} Dunning basis sets: cc-pVDZ, cc-pVTZ, aug-cc-pVDZ, and aug-cc-pVTZ;^{36,37} Ahlrichs basis sets: SVP and TZVP;^{38,39} and basis sets with core potentials: SDD, SDDall, and LANL2DZ.⁴⁰⁻⁴³ Using TiCl_4 as a representative of the initial set of inorganic complexes, Figure 3.2 shows the excited state spectra calculated at the B3LYP level of theory with several different basis sets. There appears to be a slight overestimation of the $e \rightarrow t_1$ transition in $\text{Ni}(\text{CO})_4$ using the 6-311G and 6-311G(d) basis sets (Table 3.1). Also, there is a severe underestimation of the $t_2 \rightarrow e$ transition intensity in TiCl_4 using the LANL2DZ basis set (black curve in Figure 3.2) that is thought to be a result of a misrepresentation of the chlorine atoms by the basis set. Otherwise, the basis sets show very little differences for the test set of TiCl_4 , $\text{Ni}(\text{CO})_4$, and $\text{Cr}(\text{CO})_6$ (Table 3.1).

After establishing the effects of basis sets on the initial set of inorganic complexes, multiple levels of theory were examined for their effects on the calculated electronic absorption spectra. Methods included hybrid functionals: B3LYP, PBE0, and

M06;⁴⁴ long range corrected functionals: LC- ω PBE, CAM-B3LYP, and ω B97X;^{45,46} pure functionals: BP86,^{18,47} OPBE,⁴⁸ and M06L,⁴⁴ and wavefunction methods: CIS and RPA. We intended for the EOM-CCSD level of theory to be included as a sort of benchmark for the inorganic complexes, however, poor orbital descriptions in the Hartree-Fock reference wave function prevented meaningful results from being produced in the calculations that were able to be completed. The 6-311+G(d) basis set was chosen to accompany each level of theory due to its relatively good performance for the small organic test set and the homogeneity in the results for the inorganic complexes. Experimentally, TiCl_4 has two ligand to metal charge transfer (LMCT) bands, a $t_1 \rightarrow e$ band at 4.43 eV and a $t_2 \rightarrow e$ band at 5.38 eV.⁴⁹ Comparison of the theoretical methods used to generate the TiCl_4 spectrum in Figure 3.3 shows that pure functionals tend to underestimate excited state energies by ca. 0.5 eV, hybrid functionals are in good agreement to within 0.2 eV, long range corrected functionals tend to overestimate excited state energies by ca. 0.4 eV, simple wavefunction methods poorly overestimate energies by a large amount, ca. 2.5 eV (Table 3.2). Therefore, all DFT methods are in relatively good agreement with one another, while CIS and RPA show large overestimations, specifically in the $t_1 \rightarrow e$ band. Relationships between transition intensities for the methods used to calculate the electronic spectra for TiCl_4 are similar to the results shown for inorganic complexes $\text{Ni}(\text{CO})_4$ (Figure 3.4) and $\text{Cr}(\text{CO})_6$ (Figure 3.5). The calculated $t_2 \rightarrow e$ transition in $\text{Cr}(\text{CO})_6$ is energetically overestimated (Table 3.3). All levels of theory seem to uniformly overestimate the excited state energies of $\text{Ni}(\text{CO})_4$.⁵⁰

The results from the first set of inorganic complexes provided satisfactory evidence that differences in the calculated electronic absorption spectra resulting from basis set choice were small. By contrast, comparing the calculated electronic spectra from one theory method versus another showed the possibility for dramatically different results. Another set of transition metal complexes was selected to further investigate possible differences arising from changing the number of occupied valence d-orbitals. This set consisted of trianionic hexahalide first row transition metals complexes TiF_6^{3-} , VF_6^{3-} , CrF_6^{3-} , MnF_6^{3-} , FeF_6^{3-} , and CoF_6^{3-} . Gas phase calculations on TiF_6^{3-} shown in Figure 3.6 (brown curve) illustrate the problems that we encountered. Due to the highly anionic nature of the complex, the highest occupied molecular orbital is unphysical and Rydberg-like instead of localized on the metal or ligand. Since the experimental spectra are not measured in the gas phase, we used a self-consistent reaction field (SCRF) with a range of dielectric constants to assess the effects on the electronic structure. Even a small dielectric constant corrected the ground state electronic structure, but it did not completely resolve the problems for a number of the lowest energy excited states since they involved transitions to low-lying unphysical orbitals. A negative side effect of the solvation was that the energy of the ligand to metal charge transfer (LMCT) state, seen experimentally for TiF_6^{3-} around 5.8 eV, was increased by increasing the dielectric constant. Additionally, depending on the dielectric constant of the model, the LMCT states were overlapping with some of the unphysical states making the observed band intensities higher than expected.

3.4 Summary

In this chapter, we have compared various density functional classes and wave function approaches for calculating the electronic spectra for some small organic molecules and a few first row transition metal complexes. For excited states below the ionization threshold in the inorganic complexes, it is sufficient to have a double-zeta quality basis set with one set of polarization functions and one set of diffuse functions. However, some care should be taken with basis sets employing ECPs. For some systems like $\text{Cr}(\text{CO})_6$, the Hartree-Fock wavefunction is a very poor starting point and wavefunction methods such as CIS and RPA give unrealistic results. We intended to use EOM-CC as a benchmark calculation for oscillator strengths and unknown excitation energies of other inorganic complexes, but poor orbital descriptions in the Hartree-Fock reference wavefunction prevented us from using EOM-CC altogether. For anionic species like MF_6^{3-} , DFT yields the wrong ground state wavefunction. However, for neutral and cationic systems, TD-DFT is a valuable tool for modeling the electronic spectra of transition metal complexes. Nevertheless, many aspects still need to be explored. For example, we would like to find suitable functionals and basis sets to calculate metal to ligand charge transfer, ligand to metal charge transfer and metal centered excited states with comparable accuracy.

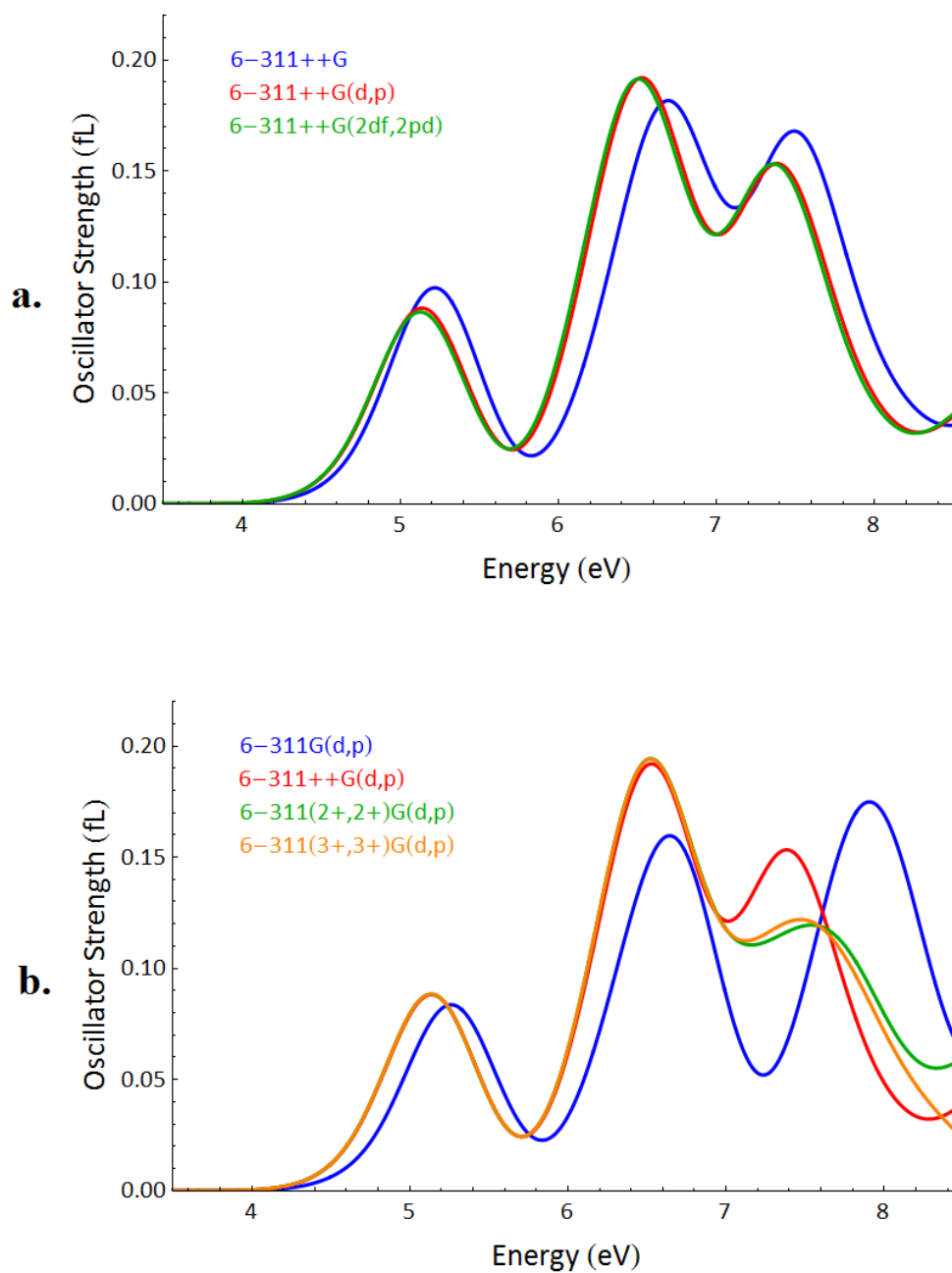


Figure 3.1 UV-vis absorption spectra of benzaldehyde at the B3LYP level of theory. (a) Comparison of spectra using different numbers of polarization functions. (b) Comparison of spectra using different numbers of diffuse functions.

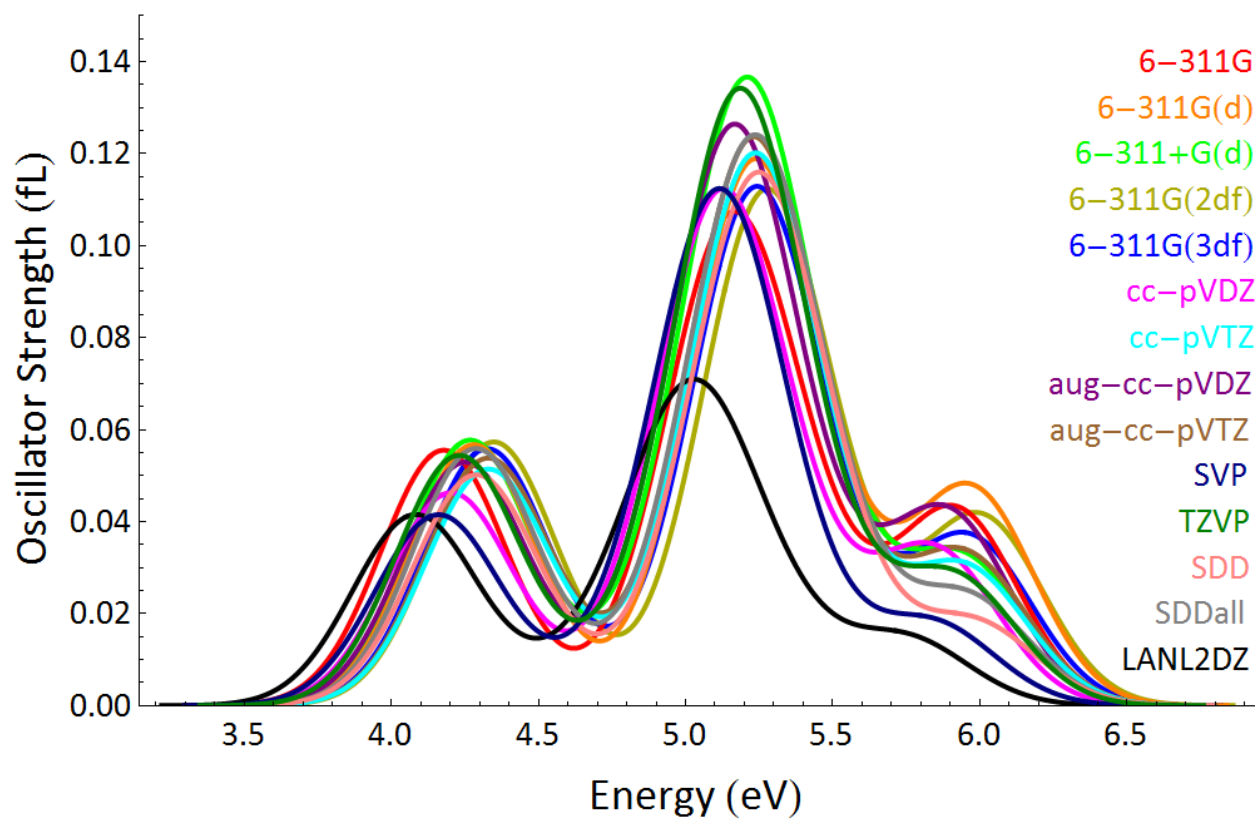


Figure 3.2 Calculated electronic absorption spectra of TiCl_4 using the B3LYP level of theory with multiple different basis sets. Overall, transition state energies and intensities are shown to be relatively insensitive to the choice of a reasonably sized basis set.

Table 3.1 Basis Set Effects on the Excited State Energy and Length Oscillator Strength of Charge Transfer Bands in the Calculated Electronic Absorption Spectra of TiCl_4 , $\text{Ni}(\text{CO})_4$ and $\text{Cr}(\text{CO})_6$ Using the B3LYP Density Functional

<i>TiCl₄</i>						
	t1→e		t2→e		e→t2 + t2→t2	
	eV	fL	eV	fL	eV	fL
6-311G(2df,2pd)	4.35	0.0573	5.28	0.1185	5.98	0.0408
6-311G(3df,3pd)	4.33	0.0558	5.24	0.1206	5.94	0.0363
6-311G	4.18	0.0555	5.17	0.1191	5.90	0.0423
6-311G++(d,p)	4.27	0.0576	5.21	0.1536	5.87	0.0315
6-311G(d,p)	4.28	0.0567	5.24	0.1287	5.95	0.0465
aug-cc-pVDZ	4.25	0.0528	5.17	0.1383	5.86	0.0414
aug-cc-pVTZ	4.33	0.0537	5.23	0.1335	5.91	0.0327
cc-pVDZ	4.20	0.0462	5.13	0.1236	5.81	0.0333
cc-pVTZ	4.33	0.0513	5.24	0.1305	5.90	0.0297
lanl2DZ	4.08	0.0414	5.03	0.0840	5.74	0.0144
SDDall	4.29	0.0558	5.24	0.1386	5.95	0.0234
SDD	4.29	0.0501	5.25	0.1293	5.97	0.0180
SVP	4.16	0.0414	5.12	0.1242	5.81	0.0177
TZVP	4.23	0.0543	5.13	0.1497	5.89	0.0276
<i>MAD</i>	<i>0.06</i>	<i>0.0043</i>	<i>0.05</i>	<i>0.0112</i>	<i>0.05</i>	<i>0.0080</i>

<i>Ni(CO)₄</i>						
	t2→t2 + t2→e		e→t2 + t2→t1		e→t1 + t2→t2	
	eV	fL	eV	fL	eV	fL
6-311G(2df,2pd)	5.01	0.2331	6.29	0.4146	7.41	1.1511
6-311G(3df,3pd)	5.07	0.2322	6.33	0.4398	7.41	1.0632
6-311G	4.73	0.2259	5.99	0.3615	7.17	1.3977
6-311G++(d,p)	5.05	0.2682	6.31	0.5598	7.35	1.0017
6-311G(d,p)	4.94	0.2409	6.24	0.4143	7.38	1.2570
aug-cc-pVDZ	5.01	0.2544	6.28	0.5469	7.32	1.0235
aug-cc-pVTZ	5.03	0.2553	6.29	0.5466	7.32	0.9723
cc-pVDZ	5.07	0.2517	6.35	0.4026	7.42	1.0446
cc-pVTZ	5.07	0.2589	6.33	0.4410	7.40	1.0416
lanl2DZ	4.94	0.2901	6.18	0.4506	7.32	1.1022
SDDall	4.84	0.2652	6.10	0.4908	7.15	1.0566
SDD	4.76	0.2583	6.04	0.4557	7.10	0.9966
SVP	5.06	0.2370	6.31	0.3789	7.40	1.1529
TZVP	5.05	0.2700	6.30	0.4692	7.37	1.1562
<i>MAD</i>	<i>0.09</i>	<i>0.0138</i>	<i>0.09</i>	<i>0.0483</i>	<i>0.08</i>	<i>0.0871</i>

<i>Cr(CO)₆</i>				
	t2g→t1u		t2g→t2u	
	eV	fL	eV	fL
6-311G(2df,2pd)	4.50	0.0510	6.07	1.7515
6-311G(3df,3pd)	4.50	0.0498	6.05	1.7202
6-311G	4.33	0.0462	5.99	1.9554
6-311G++(d,p)	4.48	0.0588	6.01	1.8625
6-311G(d,p)	4.50	0.0540	6.11	1.8663
aug-cc-pVDZ	4.47	0.0537	5.98	1.7672
aug-cc-pVTZ	4.48	0.0522	5.98	1.7466
cc-pVDZ	4.49	0.0534	6.09	1.7482
cc-pVTZ	4.49	0.0561	6.04	1.7532
lanl2DZ	4.44	0.0531	6.00	1.7748
SDDall	4.41	0.0600	6.00	1.9332
SDD	4.32	0.0543	5.95	1.8699
SVP	4.57	0.0525	6.15	1.7277
TZVP	4.54	0.0621	6.09	1.8444
<i>MAD</i>	<i>0.05</i>	<i>0.0030</i>	<i>0.05</i>	<i>0.0685</i>

Table 3.2 Theoretical Method Effects on the Excited State Energy and Length Oscillator Strength of Charge Transfer Bands in the Calculated Electronic Absorption Spectra of TiCl_4 , $\text{Ni}(\text{CO})_4$ and $\text{Cr}(\text{CO})_6$ Using the 6-311++G(d,p) Basis Set

<i>TiCl₄</i>						
	t1→e		t2→e		e→t2 + t2→t2	
	eV	fL	eV	fL	eV	fL
B3LYP	4.27	0.0576	5.21	0.1536	5.92	0.0315
BP86	3.84	0.0522	4.93	0.1685	5.60	0.0606
CAM-B3LYP	4.58	0.0681	5.45	0.1557	6.27	0.0138
CIS	6.86	0.1695	7.91	0.0807		
HF	6.76	0.1380	7.86	0.0564		
LC-ωPBE	4.83	0.0789	5.65	0.1602	6.61	0.0045
M06	4.32	0.0633	5.30	0.1779	6.16	0.0483
M06I	4.18	0.0594	5.25	0.2001	6.08	0.0552
OPBE	3.86	0.0522	4.97	0.1830	5.84	0.0489
PBE0	4.45	0.0612	5.38	0.1647	6.09	0.0249
ωB97X	4.74	0.0759	5.58	0.1593	6.49	0.0093
<i>MAD</i>	<i>0.27</i>	<i>0.0074</i>	<i>0.19</i>	<i>0.0119</i>	<i>0.24</i>	<i>0.0180</i>

<i>Ni(CO)₄</i>						
	t2→t2 + t2→e		e→t2 + t2→t1		e→t1 + t2→t2	
	eV	fL	eV	fL	eV	fL
B3LYP	5.08	0.2682	6.28	0.5598	7.34	1.0017
BP86	4.79	0.1164	5.51	0.2784	6.87	1.3270
CAM-B3LYP	5.43	0.3570	6.70	0.7254	7.78	0.8706
CIS	5.28	0.3090	6.25	0.8299	8.69	0.4733
HF	4.89	0.3879	6.40	0.6981	8.56	0.4137
LC-ωPBE	5.86	0.3906	7.05	0.8349	8.06	0.8682
M06	5.11	0.2358	6.37	0.6546	7.41	1.0146
M06I	5.09	0.1560	6.15	0.3333	7.08	1.2867
OPBE	4.97	0.1137	5.54	0.3018	6.93	1.3002
PBE0	5.18	0.3066	6.46	0.6387	7.56	0.9204
ωB97X	5.62	0.3960	6.90	0.8043	7.97	0.8220
<i>MAD</i>	<i>0.23</i>	<i>0.0891</i>	<i>0.34</i>	<i>0.1724</i>	<i>0.50</i>	<i>0.2271</i>

<i>Cr(CO)₆</i>				
	t2g→t1u		t2g→t2u	
	eV	fL	eV	fL
B3LYP	4.48	0.0588	6.01	1.8625
BP86	4.09	0.0302	5.66	1.5892
CAM-B3LYP	4.77	0.0975	6.28	2.0820
CIS	6.32	0.4860	7.91	3.1503
HF	6.24	0.5136	7.74	2.4915
LC- ω PBE	4.98	0.1449	6.47	2.2596
M06	4.48	0.0624	6.04	2.0106
M06I	4.32	0.0419	5.91	1.7476
OPBE	4.18	0.0317	5.73	1.5571
PBE0	4.65	0.0717	6.17	1.9410
ω B97X	4.88	0.1284	6.38	2.1863
<i>MAD</i>	<i>0.55</i>	<i>0.1266</i>	<i>0.54</i>	<i>0.3220</i>

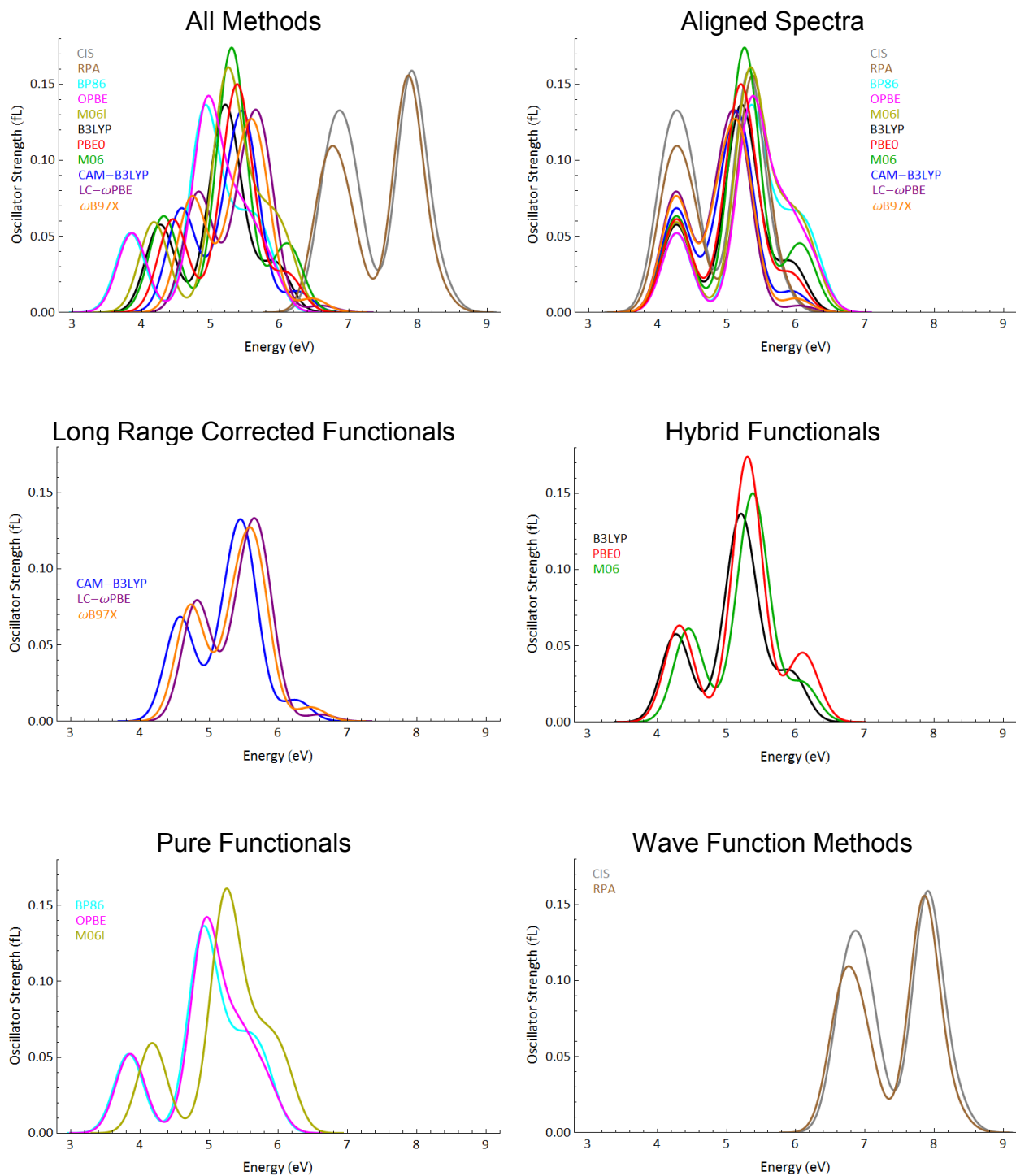


Figure 3.3 Calculated electronic absorption spectrum of TiCl_4 at various levels of theory computed with the 6-311+G(d) basis set.

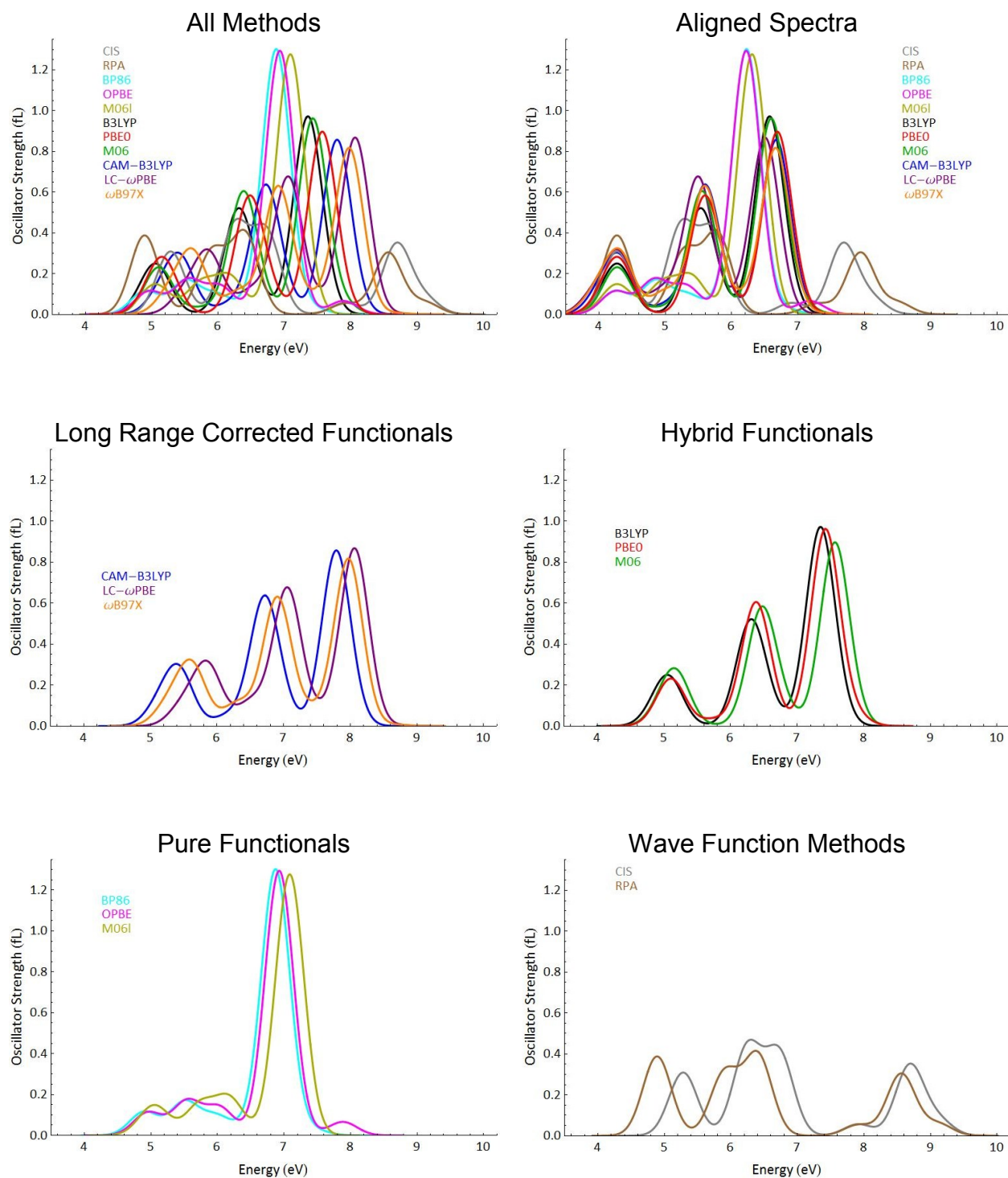


Figure 3.4 Calculated electronic absorption spectrum of Ni(CO)_4 at various levels of theory computed with the 6-311+G(d) basis set.

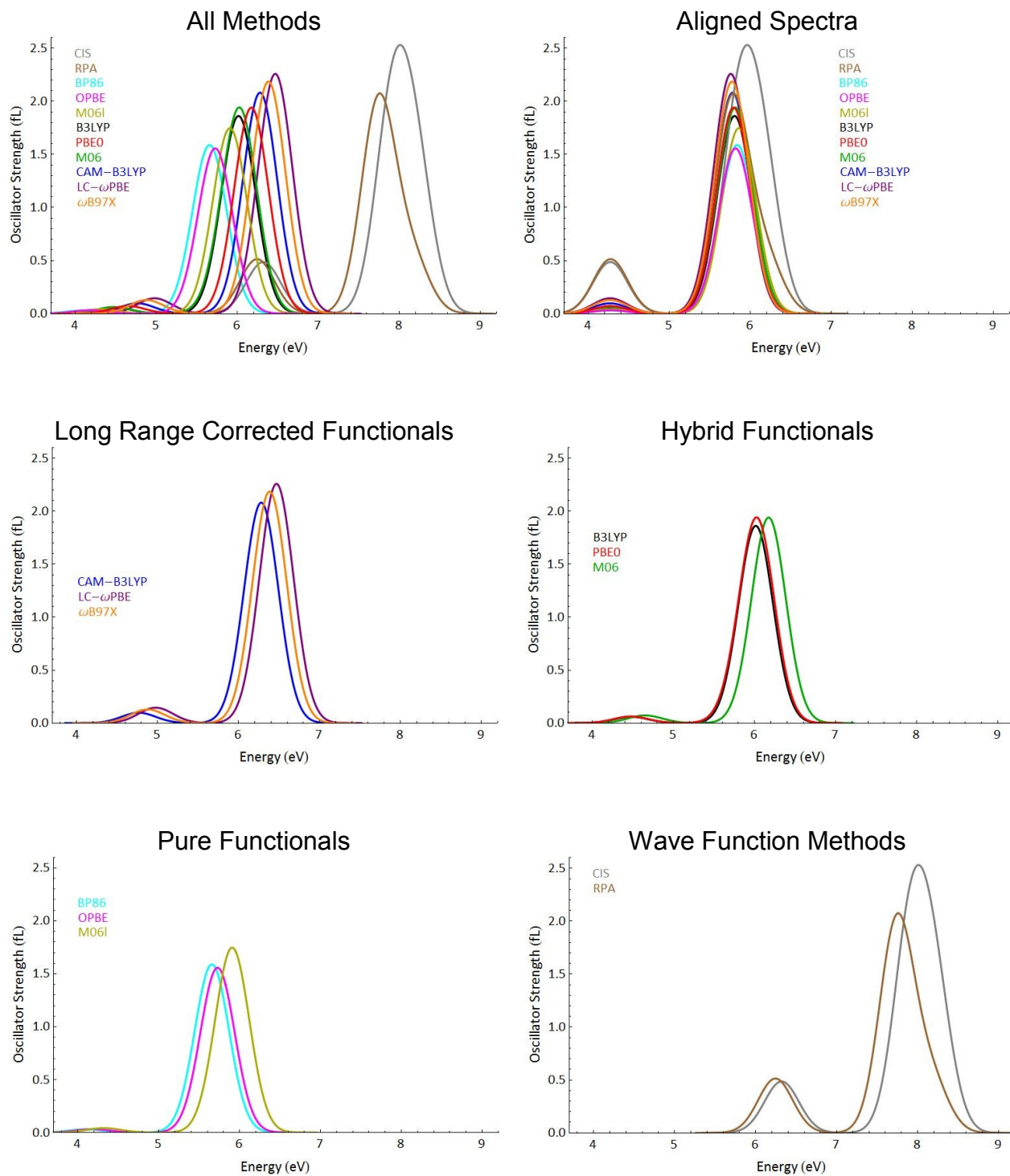


Figure 3.5 Calculated electronic absorption spectrum of Cr(CO)_6 at various levels of theory computed with the 6-311+G(d) basis set.

Table 3.3 Theoretical $\text{Cr}(\text{CO})_6$ Absorption Spectra Data from Other Studies Compared to B3LYP/6-311+G(d) Results

E / eV	$3d(t_2g) \rightarrow \pi^*(t_1u)$		$3d(t_2g) \rightarrow \pi^*(t_2u)$	
	$\lambda(\text{max})$	f	$\lambda(\text{max})$	f
Experiment ⁵¹	4.43	0.25	5.41	2.30
CASPT2/ANO ¹²	4.11-4.54	0.20-1.33	5.07-5.20	1.63-2.58
EOM-CCSD/Wachters+ccpVDZ ^a	4.95-5.06	0.13-0.14	6.10-6.22	2.10-2.16
EOM-KS-CCSD/Wachters+ccpVDZ ^a	5.07	0.12	6.24	2.13
STEOM-CCSD/Wachters+ccpVDZ ^a	4.37	0.22	5.20	1.48
B3LYP	4.48	0.06	6.01	1.86
BP86	4.09	0.03	5.66	1.59
CAM-B3LYP	4.77	0.10	6.28	2.08
LC- ω PBE	4.98	0.14	6.47	2.26
M06	4.48	0.06	6.04	1.84
M06L	4.32	0.04	5.91	1.75
OPBE	4.18	0.03	5.73	1.56
PBE0	4.65	0.07	6.17	1.94
ω B97X	4.88	0.13	6.38	2.19
CIS ^b	6.32	0.48	7.92	1.86
RPA ^b	6.25	0.51	7.74	2.00

^a Ref.¹³ Oscillator strengths for second $d \rightarrow \pi$ transition have been tripled to account for degeneracy. ^b Denotes results obtained with an unstable wavefunction.

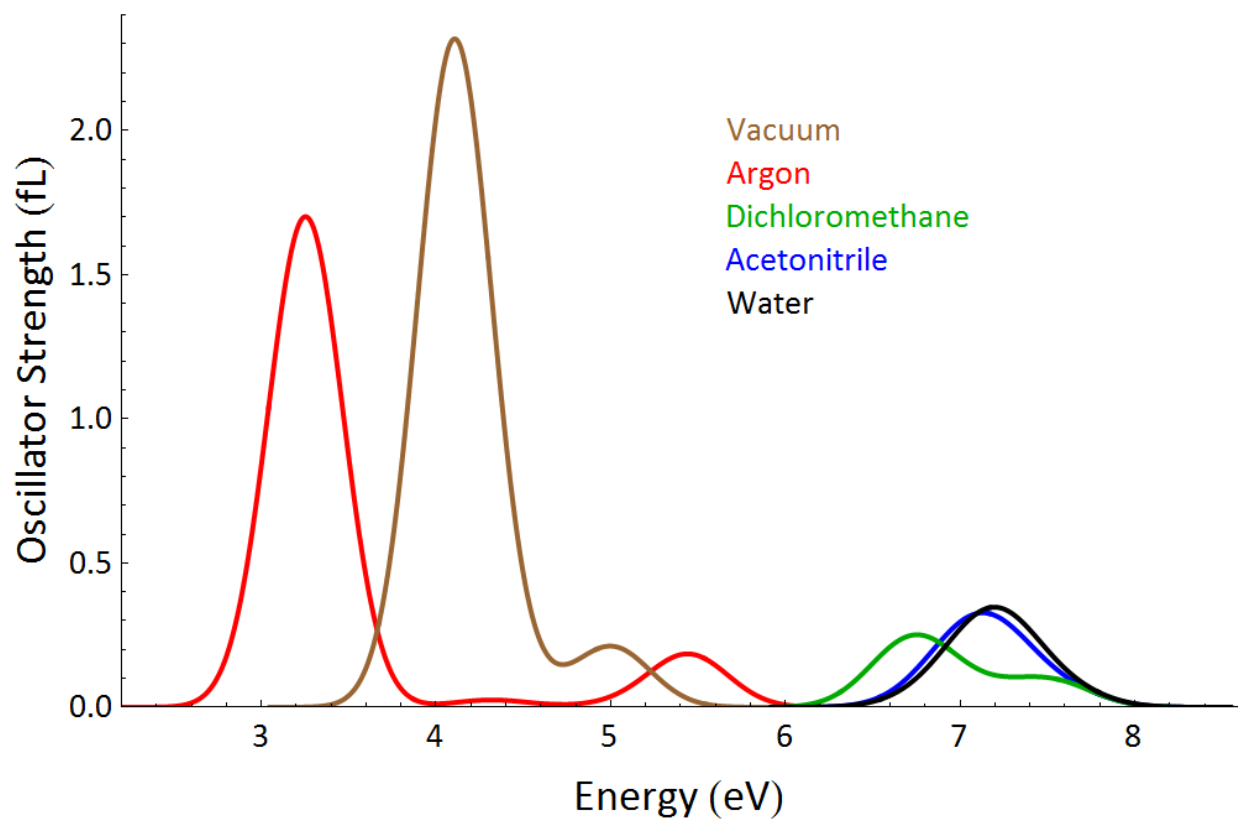


Figure 3.6 Calculated UV-vis absorption spectrum of TiF_6^{3-} at the B3LYP/6-311++G(d,p) level of theory using PCM solvation. Multiple curves primarily show unphysical Rydberg-like excited states being affected by using dielectric constants values from vacuum ($\epsilon=0$) to water ($\epsilon=78.3553$).

3.5 References

1. Marques, M. A. L.; Gross, E. K. U. Time-dependent density functional theory. *Annu. Rev. Phys. Chem.* **2004**, *55*, 427-455.
2. Onida, G.; Reining, L.; Rubio, A. Electronic excitations: density-functional versus many-body Green's-function approaches. *Rev. Mod. Phys.* **2002**, *74*, 601-659.
3. Dreuw, A.; Head-Gordon, M. Single-reference ab initio methods for the calculation of excited states of large molecules. *Chem. Rev.* **2005**, *105*, 4009-4037.
4. Koch, H.; Jorgensen, P. Coupled-cluster response functions. *J. Chem. Phys.* **1990**, *93*, 3333-3344.
5. Stanton, J. F.; Bartlett, R. J. The equation of motion coupled-cluster method - A systematic biorthogonal approach to molecular excitation energies, transition probabilities, and excited state properties. *J. Chem. Phys.* **1993**, *98*, 7029-7039.
6. Hegarty, D.; Robb, M. A. Application of unitary group methods to configuration-interaction calculations. *Mol. Phys.* **1979**, *38*, 1795-1812.
7. Yamamoto, N.; Vreven, T.; Robb, M. A.; Frisch, M. J.; Schlegel, H. B. A direct derivative MC-SCF procedure. *Chem. Phys. Lett.* **1996**, *250*, 373-378.
8. Lischka, H.; Shepard, R.; Pitzer, R. M.; Shavitt, I.; Dallos, M.; Muller, T.; Szalay, P. G.; Seth, M.; Kedziora, G. S.; Yabushita, S.; Zhang, Z. Y. High-level multireference methods in the quantum-chemistry program system COLUMBUS: Analytic MR-CISD and MR-AQCC gradients and MR-AQCC-LRT for excited states, GUGA spin-orbit CI and parallel CI density. *Phys. Chem. Chem. Phys.* **2001**, *3*, 664-673.

9. Gross, E. K. U.; Kohn, W. *Advances in Quantum Chemistry*. 1990; Vol. 21.
10. Chong, D. P. *Recent advances in density functional methods*. World Scientific: Singapore ; River Edge, N.J., 1995.
11. Bauernschmitt, R.; Ahlrichs, R. Treatment of electronic excitations within the adiabatic approximation of time dependent density functional theory. *Chem. Phys. Lett.* **1996**, 256, 454-464.
12. Pierloot, K.; Tsokos, E.; Vanquickenborne, L. G. Optical spectra of Ni(CO)(4) and Cr(CO)(6) revisited. *J. Phys. Chem.* **1996**, 100, 16545-16550.
13. Villaume, S.; Strich, A.; Daniel, C.; Perera, S. A.; Bartlett, R. J. A coupled cluster study of the electronic spectroscopy and photochemistry of Cr(CO)(6). *Phys. Chem. Chem. Phys.* **2007**, 9, 6115-6122.
14. Caricato, M.; Trucks, G. W.; Frisch, M. J.; Wiberg, K. B. Electronic Transition Energies: A Study of the Performance of a Large Range of Single Reference Density Functional and Wave Function Methods on Valence and Rydberg States Compared to Experiment. *J. Chem. Theory Comput.* **2010**, 6, 370-383.
15. Caricato, M.; Trucks, G. W.; Frisch, M. J.; Wiberg, K. B. Oscillator Strength: How Does TDDFT Compare to EOM-CCSD? *J. Chem. Theory Comput.* **2011**, 7, 456-466.
16. Frisch, M. J.; Trucks, G. W.; Schlegel, H. B.; Scuseria, G. E.; Robb, M. A.; Cheeseman, J. R.; Scalmani, G.; Barone, V.; Mennucci, B.; Petersson, G. A.; Nakatsuji, H.; Hada, M.; Caricato, M.; Li, X.; Hratchian, H. P.; Izmaylov, A. F.; Bloino, J.; Zheng, G.; Sonnenberg, J. L.; Hada, M.; Ehara, M.; Toyota, K.; Fukuda, R.; Hasegawa, J.; Ishida, M.; Nakajima, T.; Honda, Y.; Kitao, O.; Nakai,

- H.; Vreven, T.; Montgomery, J., J. A.; Peralta, J. E.; Ogliaro, F.; Bearpark, M.; Heyd, J. J.; Brothers, E.; Kudin, K. N.; Staroverov, V. N.; Keith, T.; Kobayashi, R.; Normand, J.; Raghavachari, K.; Rendell, A.; Burant, J. C.; Iyengar, S. S.; Tomasi, J.; Cossi, M.; Rega, N.; Millam, J. M.; Klene, M.; Knox, J. E.; Cross, J. B.; Bakken, V.; Adamo, C.; Jaramillo, J.; Gomperts, R.; Stratmann, R. E.; Yazyev, O.; Austin, A. J.; Cammi, R.; Pomelli, C.; Ochterski, J. W.; Martin, R. L.; Morokuma, K.; Zakrzewski, V. G.; Voth, G. A.; Salvador, P.; Dannenberg, J. J.; Dapprich, S.; Parandekar, P. V.; Mayhall, N. J.; Daniels, A. D.; Farkas, O.; Foresman, J. B.; Ortiz, J. V.; Cioslowski, J.; Fox, D. J. *Gaussian Development Version*, Gaussian, Inc.: Wallingford, CT, 2010.
17. Vosko, S. H.; Wilk, L.; Nusair, M. Accurate spin dependent electron liquid correlation energies for local spin density calculations - A critical analysis. *Can. J. Phys.* **1980**, *58*, 1200-1211.
 18. Lee, C. T.; Yang, W. T.; Parr, R. G. Development of the Colle-Salvetti correlation energy formulation into a functional of the electron density. *Phys. Rev. B* **1988**, *37*, 785-789.
 19. Becke, A. D. Density functional thermochemistry. III. The role of exact exchange. *J. Chem. Phys.* **1993**, *98*, 5648-5652.
 20. Stephens, P. J.; Devlin, F. J.; Chabalowski, C. F.; Frisch, M. J. Ab initio calculations of vibrational absorption and circular dichroism spectra using density functional force fields. *J. Phys. Chem.* **1994**, *98*, 11623-11627.

21. Krishnan, R.; Binkley, J. S.; Seeger, R.; Pople, J. A. Self-consistent molecular orbital methods. XX. Basis set for correlated wave functions. *J. Chem. Phys.* **1980**, 72, 650-654.
22. McLean, A. D.; Chandler, G. S. Contracted Gaussian basis sets for molecular calculations. I. 2nd row atoms, Z=11-18. *J. Chem. Phys.* **1980**, 72, 5639-5648.
23. Schlegel, H. B. Optimization of equilibrium geometries and transition structures. *J. Comput. Chem.* **1982**, 3, 214-218.
24. Schlegel, H. B.; McDouall, J. J. In *Computational advances in organic chemistry: molecular structure and reactivity*, Kluwer Academic Publishers: Dordrecht ; Boston, 1991.
25. Bauernschmitt, R.; Ahlrichs, R. Stability analysis for solutions of the closed shell Kohn-Sham equation. *J. Chem. Phys.* **1996**, 104, 9047-9052.
26. Mukamel, S. *Principles of nonlinear optical spectroscopy*. Oxford University Press: New York, 1995.
27. Foresman, J. B.; Headgordon, M.; Pople, J. A.; Frisch, M. J. Toward a systematic molecular orbital theory for excited states. *J. Phys. Chem.* **1992**, 96, 135-149.
28. Dunning, T. H.; McKoy, V. Nonempirical calculations on excited states - ethylene molecule. *J. Chem. Phys.* **1967**, 47, 1735-1747.
29. Perdew, J. P.; Burke, K.; Ernzerhof, M. Generalized gradient approximation made simple. *Phys. Rev. Lett.* **1996**, 77, 3865-3868.
30. Perdew, J. P.; Burke, K.; Ernzerhof, M. Generalized gradient approximation made simple (vol 77, pg 3865, 1996). *Phys. Rev. Lett.* **1997**, 78, 1396-1396.

31. Adamo, C.; Barone, V. Toward reliable density functional methods without adjustable parameters: The PBE0 model. *J. Chem. Phys.* **1999**, *110*, 6158-6170.
32. Tawada, Y.; Tsuneda, T.; Yanagisawa, S.; Yanai, T.; Hirao, K. A long-range-corrected time-dependent density functional theory. *J. Chem. Phys.* **2004**, *120*, 8425-8433.
33. Yanai, T.; Tew, D. P.; Handy, N. C. A new hybrid exchange-correlation functional using the Coulomb-attenuating method (CAM-B3LYP). *Chem. Phys. Lett.* **2004**, *393*, 51-57.
34. Clark, T.; Chandrasekhar, J.; Spitznagel, G. W.; Schleyer, P. V. Efficient diffuse function augmented basis sets for anion calculations. III. The 3-21+G basis set for 1st row elements, Li - F. *J. Comput. Chem.* **1983**, *4*, 294-301.
35. Frisch, M. J.; Pople, J. A.; Binkley, J. S. Self-consistent molecular orbital methods. XXV. Supplementary functions for Gaussian basis sets. *J. Chem. Phys.* **1984**, *80*, 3265-3269.
36. Kendall, R. A.; Dunning, T. H.; Harrison, R. J. Electron affinities of the 1st row atoms revisited - Systematic basis sets and wave functions. *J. Chem. Phys.* **1992**, *96*, 6796-6806.
37. Woon, D. E.; Dunning, T. H. Gaussian basis sets for use in correlated molecular calculations. III. The atoms aluminum through argon. *J. Chem. Phys.* **1993**, *98*, 1358-1371.
38. Schafer, A.; Horn, H.; Ahlrichs, R. Fully optimized contracted Gaussian basis sets for atoms Li to Kr. *J. Chem. Phys.* **1992**, *97*, 2571-2577.

39. Schafer, A.; Huber, C.; Ahlrichs, R. Fully optimized contracted Gaussian basis sets of triple zeta valence quality for atoms Li to Kr. *J. Chem. Phys.* **1994**, *100*, 5829-5835.
40. Dunning Jr., T. H.; Hay, P. J. *Modern Theoretical Chemistry*. Plenum: New York, 1976; Vol. 3.
41. Hay, P. J.; Wadt, W. R. Ab initio effective core potentials for molecular calculations - Potentials for the transition metal atoms Sc to Hg. *J. Chem. Phys.* **1985**, *82*, 270-283.
42. Dolg, M.; Wedig, U.; Stoll, H.; Preuss, H. Energy adjusted ab initio pseudopotentials for the 1st row transition elements. *J. Chem. Phys.* **1987**, *86*, 866-872.
43. Bergner, A.; Dolg, M.; Kuchle, W.; Stoll, H.; Preuss, H. Ab initio energy adjusted pseudopotentials for elements of groups 13-17. *Mol. Phys.* **1993**, *80*, 1431-1441.
44. Zhao, Y.; Truhlar, D. G. The M06 suite of density functionals for main group thermochemistry, thermochemical kinetics, noncovalent interactions, excited states, and transition elements: two new functionals and systematic testing of four M06-class functionals and 12 other functionals. *Theor. Chem. Acc.* **2008**, *120*, 215-241.
45. Chai, J. D.; Head-Gordon, M. Systematic optimization of long-range corrected hybrid density functionals. *J. Chem. Phys.* **2008**, *128*, 6615-6620.
46. Chai, J. D.; Head-Gordon, M. Long-range corrected hybrid density functionals with damped atom-atom dispersion corrections. *Phys. Chem. Chem. Phys.* **2008**, *10*, 6615-6620.

47. Becke, A. D. Density functional exchange energy approximation with correct asymptotic behavior. *Phys. Rev. A* **1988**, 38, 3098-3100.
48. Handy, N. C.; Cohen, A. J. Left-right correlation energy. *Mol. Phys.* **2001**, 99, 403-412.
49. Bancroft, G. M.; Pellach, E.; Tse, J. S. High resolution He-I and He-II photoelectron spectra of TiCl_4 , SnCl_4 , and $(\text{CH}_3)_4\text{Sn}$. *Inorg. Chem.* **1982**, 21, 2950-2955.
50. Kotzian, M.; Rosch, N.; Schroder, H.; Zerner, M. C. Optical spectra of transition metal carbonyls - $\text{Cr}(\text{CO})_6$, $\text{Fe}(\text{CO})_6$, $\text{Fe}(\text{CO})_5$, and $\text{Ni}(\text{CO})_4$. *J. Am. Chem. Soc.* **1989**, 111, 7687-7696.
51. Beach, N. A.; Gray, H. B. Electronic structures of metal hexacarbonyls. *J. Am. Chem. Soc.* **1968**, 90, 5713-5721.

CHAPTER 4

CAN METALLAPYRIMIDINES BE AROMATIC? A COMPUTATIONAL STUDY INTO A NEW CLASS OF METALLACYCLES

Reproduced with permission from J. Chem. Theory Comput., **2012**, 8, 4950
Copyright 2012, American Chemical Society

4.1 Introduction

Despite being introduced in the middle 1800s,¹ aromaticity is still a topical concept that fascinates experimental and theoretical chemists alike.² The bonding theories developed to explain benzene are a cornerstone of electronic structure theory. Aromaticity is so fundamental that introductory chemistry books present benzene and other $4n+2$ π systems as aromatic, while in reality there is no single, universally accepted measure of aromaticity. Some definitions of aromaticity are based on structural equivalences in the ring,³ while others are based on the energetic stabilization of the cyclical form.⁴ A comprehensive collection of definitions would span numerous volumes.⁵ A commonly invoked set of consequences predicted by simple quantum mechanical models is summarized in Pople's ring-current model that was introduced to explain downfield proton shifts.⁶ In this model, an applied magnetic field perpendicular to the ring of interest induces current in the conjugated π system, which in turn creates a magnetic field that opposes (aligns with) the applied field outside (inside) the ring. While this model was originally developed to explain proton resonances and has received criticism in its general application,⁷⁻⁹ ring current is well-established and non-experimentally observable quantities are readily computed.¹⁰⁻¹³

Aromatic systems where one of the CH groups is replaced by ML_n have attracted considerable attention in this field.^{14,15} First investigated theoretically by Hoffmann,¹⁶ these molecules have been intensely studied by a variety of computational methods over the past decade, with particular attention paid to their aromatic character.¹⁷⁻²⁰ Metal chelates are not typically aromatic,²¹ but it is generally agreed upon that metallabenzenes are weakly aromatic. Questions still remain, such as how many of the d orbital electrons are involved in aromaticity^{14,16,18,20} and what are the structural and electronic requirements for aromaticity in metallacycles. Our goal in the present chapter is to explore the structure, bonding, and some magnetic criteria in a newly identified class of metallacycles, namely metallapyrimidines, that may shed some light on the larger question of aromaticity in metallacycles.

In this chapter, we investigate a simplified example of our previously reported niobapyrimidine²² and a series of hypothetical metallapyrimidine complexes containing second-row transition metals to provide a better understanding of the structure and bonding in this new class of metallacycle. First, we explore a putative mechanism for the formation of the previously isolated niobapyrimidine. Next, we use nucleus independent chemical shift (NICS)¹¹ values to evaluate the aromaticity of niobapyrimidine and compare them to established aromatic and antiaromatic systems. NICS calculations can be misleading due to non- π orbital contributions, especially for inorganic systems;^{23,24} so, we decompose the total chemical shift into orbital-specific components using the natural chemical shielding (NCS) analysis in NBO.²⁵ To understand how metal-ligand covalency affects aromaticity, we study a series of isoelectronic d^0 metallapyrimidines featuring second-row transition metals in a variety of

oxidation states (Y^{III} through Tc^{VII}). Finally, we vary the d electron count of the metal by studying formally pentavalent metals in neutral metallapyrimidine complexes. The NCS analysis of each series provides insight into how aromaticity might be encouraged in this new class of metallacycle.

4.2 Computational Details

All calculations were performed using a development version of Gaussian.²⁶ Geometry optimizations were carried out at the B3LYP/6-31+G(d) level of theory,²⁷⁻³⁰ with metal atoms represented by the Stuttgart-Dresden-Bonn (SDD) effective core potential and its accompanying basis set.³¹⁻³³ Wave functions were tested for wave function stability,^{34,35} and all optimized structures were confirmed as minima or transition states by analyzing the harmonic vibrational frequencies.³⁶ Transition states were obtained through full transition state searches and confirmed to connect reactant and product using an intrinsic reaction coordinate calculation.³⁷ For thermodynamic discussions, we analyzed both the electronic energy (E_{el}) and the gas-phase Gibbs free energy (G_g°). The gas-phase Gibbs free energy was obtained by adding to E_{el} the zero-point vibrational energy (ZPE) and the thermal free energy corrections ($\Delta G_{0 \rightarrow 298K}^\circ$) derived from standard approximations, as shown in eq (1).³⁸

$$G_g^\circ = E_{el} + ZPE + \Delta G_{0 \rightarrow 298K}^\circ \quad (1)$$

We used the nucleus independent chemical shift (NICS) method^{11,39} to evaluate aromaticity due to its conceptual simplicity and accessibility in standard quantum chemistry packages. NICS(0) is evaluated by placing a ghost atom (Bq) at the geometric mean of the ring atoms and computing the isotropic chemical shift (σ_{iso}) at

this ghost atom. Due to sign convention, $\text{NICS}(0) = -\sigma(\text{Bq})_{\text{iso}}$, we report $-\sigma$ values throughout the chapter for consistency. Large negative values indicate aromaticity, while large positive values indicate antiaromaticity. Since the introduction of this aromaticity criterion, a number of improved NICS metrics have been proposed that overcome failures in $\text{NICS}(0)$ such as for inorganic systems such as the ones we are studying.^{23,24} For our work, we study the $\text{NICS}(1)_{\text{zz}}$ value that measures the chemical shift tensor component orthogonal to the ring at a point located 1 Å above the $\text{NICS}(0)$ point. We evaluated $\text{NICS}(1)_{\text{zz}}$ both above and below the ring because there was not always a mirror plane containing the metallacycle. This was accomplished by constructing the normalized cross product between the $\text{NICS}(0)\text{--M}$ and $\text{NICS}(0)\text{--N}$ vectors. Chemical shift tensor components were evaluated using the Gauge-Including Atomic Orbital (GIAO) formalism.⁴⁰ Molecules were realigned so the three Bq atoms defined the z-axis, which allowed us to analyze the chemical shift tensor component orthogonal to the ring of interest (σ_{zz}). Finally, an orbital decomposition of $\text{NICS}(1)_{\text{zz}}$ was performed using the Natural Chemical Shielding (NCS) program in NBO.²⁵ NCS decomposes the total chemical shift into diamagnetic (field-free) and paramagnetic (field-induced) contributions from natural localized molecular orbitals and enabled us to analyze contributions to $\text{NICS}(1)_{\text{zz}}$ due only to π orbitals. All NBO calculations were performed using version 3.1 that is built in to Gaussian.⁴¹

4.3 Niobapyrimidine Formation

Winter and coworkers recently reported the unexpected formation and isolation of the first niobapyrimidine.²² They were investigating metal complexes with multiple

pyrazolate ligands as volatile precursors for atomic layer deposition film growth.⁴² Use of Nb^{III} , Nb^{IV} , and Ta^{IV} salts led to isolation of the first niobapyrimidine, niobapyrimidinium, and tantalapyrimidinium complexes, respectively. We focus here on the simpler metallapyrimidine class that does not involve a protonated nitrogen. In the synthesis of the niobapyrimidine complex, a niobium(III) salt was reacted with a pyrazolate (pz) salt, and the expected product was $[\text{Nb}^{\text{III}}(\text{pz})_3]^0$. Instead, they isolated the bis-pyrazolate niobapyrimidine complex shown in Scheme 4.1. Because we will refer to this compound and similar species throughout this manuscript, we introduce the shorthand $[(\text{L})_2(\text{M-pyr})]^{n+}$ to denote a bis-ligated metallapyrimidine. The structure in Scheme 4.1 is abbreviated $[(\text{pz})_2(\text{Nb-pyr})]^0$ in this notation.

The ring-opening activation of pyrazolates by metal complexes is rare, but not unprecedented.⁴³ The compounds of interest here are unique because they involve the activation of a pyrazolate N–N bond at a single metal center. In the case of $[(\text{pz})_2(\text{Nb-pyr})]^0$, the ring-opening oxidative addition of the N–N bond presumably occurs after formation of an intermediate tris-pyrazolate complex. To understand this transformation better, we investigated the electronic structure of the hypothetical $[\text{Nb}(\text{pz})_3]^0$ species and the reaction path leading to $[(\text{pz})_2(\text{Nb-pyr})]^0$. This was done for a simplified system where the ^tBu groups on C_2 and C_4 employed experimentally for steric protection and solubility were replaced with hydrogens.

Despite not being isolated and characterized experimentally, we were able to find a well-defined minimum for the $[\text{Nb}(\text{pz})_3]^0$ complex. The optimized structure of $[\text{Nb}(\text{pz})_3]^0$ is best described as a low-spin $d^2\text{-Nb}^{\text{III}}$ species; the HOMO is a doubly occupied Nb d orbital that is more than 3.13 eV higher in energy than the HOMO–1

(pyrazolate- π), and only 2.32 eV lower in energy than the LUMO (another Nb d orbital). The complex is C_s symmetric (Figure 4.1, $[\text{Nb}(\text{pz})_3]^0$), and all three of the pyrazolates are η^2 bound and have similar structures, as exemplified by the N–N bond lengths of 1.36 to 1.38 Å. This suggests the pyrazolates in this reactant are not activated, or at least that no one of the three is more predisposed to N–N cleavage than the others. We identified a C_1 symmetric transition state that involves rotation of the two non-activated pyrazolates in opposite directions, and a significant amount of activation of the third pyrazolate (Figure 4.1, TS). This is evidenced by the N–N distance of 1.84 Å and Nb–N bond lengths of 1.93 and 2.06 Å. The pyrazolate is ~40% activated in the transition state when compared to the final N–N separation of 2.61 Å in the product. The product (Figure 4.1, $[(\text{pz})_2(\text{Nb-pyr})]^0$ isomer 2) is C_s symmetric with the niobapyrimidine ring lying perpendicular to the mirror plane. The ring is slightly nonplanar with a ca. 10° deformation toward a chair-like structure. The Nb–N bond lengths are symmetric in the product with only a single value of 1.89 Å calculated. The ring C–C and C–N bonds are also symmetric and the pyrazolates are η^2 bound. The reaction barrier is consistent with facile activation at +22.3 kcal/mol, with a large driving force to product formation of –29.5 kcal/mol. We found an additional, isoenergetic isomer (+0.3 kcal/mol) of $[(\text{pz})_2(\text{Nb-pyr})]^0$ that is also C_s symmetric (isomer 1), but with a planar niobapyrimidine ring lying in the mirror plane. We expect the potential energy surface connecting isomer 1 and isomer 2 to be very flat based on low-frequency modes in both structures, and did not attempt to locate a transition state that connects isomer 1 to isomer 2 or to reactants. Isomer 1 showed asymmetry in the pyrimidine ring, as evidenced by Nb–N bond lengths of 1.83 and 1.98 Å, and was more similar in structure to the

crystallographically determined structure with ^tBu groups that also showed a nearly planar niobapyrimidine ring with bond asymmetry. It is possible that the bulky ^tBu groups prevent isomer 2 from being accessible experimentally. While we present both species in Figure 4.1, we restrict our NICS analysis in the subsequent section to isomer 1, since it is more similar to existing experimental data and has a planar niobapyrimidine ring.

The major driving force for niobapyrimidine formation is the high energy Nb-based HOMO in the tris-pyrazolate complex. Oxidative addition of pyrazolate results in a d⁰-Nb^V species that has a trianionic 3-ketimidoprop-1-en-1-imide (kp³⁻, Scheme 4.2) ligand that forms the niobapyrimidine ring. The planarity of this ring raises a question about whether aromaticity may be another driving force for niobapyrimidine formation. In the previously reported NICS(1)_{zz} calculations, it was suggested that the niobapyrimidine ring was slightly aromatic, but there has been considerable concern in the literature about non-π contributions to the zz chemical shift tensor component used in NICS calculations, especially when metals are involved.²⁴ Therefore, we investigated these results in further depth for [(pz)₂(Nb-pyr)]⁰ and compared them to species for which the degree of aromaticity/antiaromaticity is well established: benzene, pyrimidine, cyclobutadiene, and the metallacycle rhodabenzene ([(H₃P)₂(Cl)₂Rh(κ²-C₅H₅)]⁰).

4.4 Natural Chemical Shielding for [(pz)₂(Nb-pyr)]⁰

Previously, NICS(1)_{zz} values were computed for the crystallographically determined structures of niobapyrimidine and niobapyrimidinium²² (no optimization, full ^tBu groups unlike the results presented here). On the basis of these results

(NICS(1)_{zz} = −9.9 and −5.5, respectively), it was concluded that metallapyrimidines are weakly aromatic. The simplified model for niobapyrimidine studied here (^tBu replaced by H) agrees well with a value of −8.8. Moreover, these values compare well to the NICS(1)_{zz} value of −6.5 that we computed at the same level of theory for a related rhodabenzene species that has been established to be weakly aromatic.^{18,19} To put this in perspective, benzene and pyrimidine are computed to have NICS(1)_{zz} values of −28.7 and −26.9, respectively, while cyclobutadiene has a value of +60.2. The NICS(1)_{zz} metric was introduced to analyze the component of the chemical shift tensor perpendicular to the ring of interest. This should eliminate or greatly diminish contributions from orbitals not involved with the π system, but we address this issue here explicitly by decomposing the $-\sigma_{zz}$ chemical shift tensor component into field-free (diamagnetic) and field-induced (paramagnetic) contributions from individual, localized molecular orbitals obtained through the Natural Chemical Shielding (NCS) analysis in NBO.²⁵ NCS results for the ring π orbitals are presented in Table 4.1 for benzene, pyrimidine, cyclobutadiene, rhodabenzene, and niobapyrimidine. Complete NCS tables with contributions from all orbital types (i.e., σ orbitals, π orbitals, etc.) may be found in Table 4.2 and Table 4.3 for all species, as well as isosurface plots for all π orbitals.

The sum of total contributions from π orbitals is formally equivalent to the NICS(1) _{π_{zz}} metric.¹¹ To calibrate our expectations, we analyzed benzene, the classic example of an aromatic ring. The total contribution of the three π orbitals or NICS(1) _{π_{zz}} is −29.4 ppm, in good agreement with the NICS(1)_{zz} value of −28.7 for benzene. While individual contributions from non- π orbitals are not zero, their sum is small, as evidenced by the small difference of 0.4 ppm. Each of the localized C–C π orbitals

contributes -9.8 ppm to the overall sum with a paramagnetic contribution of -5.6 ppm and a diamagnetic contribution of -4.2 ppm. Similar results are found for pyrimidine, where the $\text{NICS}(1)_{\pi\text{zz}}$ of -27.2 ppm agrees well with the $\text{NICS}(1)_{\text{zz}}$ value of -26.9 , with each of the three π orbitals contributing ca. -9 ppm. The C–N π orbitals of pyrimidine are slightly different from one another because one involves the carbon atom between the nitrogen atoms in the localized Lewis description of this π manifold. The C–C π orbital has a slightly larger paramagnetic and slightly smaller diamagnetic contribution than the C–N π orbitals, but all three make negative contributions similar to benzene. Cyclobutadiene provides a clear counterexample of antiaromaticity with a $\text{NICS}(1)_{\text{zz}}$ value of $+60.2$ that agrees with the $\text{NICS}(1)_{\pi\text{zz}}$ of 54.6 ppm, though there is a disagreement of ~ 5 ppm that indicates other orbitals contribute to the NICS value. Each π orbital induces a large positive paramagnetic contribution of 30.7 ppm compared to the small negative diamagnetic contribution of -3.4 ppm. Thus, an indicator of highly aromatic (antiaromatic) systems is that the π orbitals make large negative (positive) paramagnetic contributions to the perpendicular chemical shift tensor used for the $\text{NICS}(1)_{\text{zz}}$ metric, consistent with the expectation of field-induced (paramagnetic) behavior.

Previous reports have established that rhodabenzene is weakly aromatic through energy decomposition analysis of the π bonding¹⁸ and induced current analysis.¹⁹ Therefore, we analyze that metallacycle species first. The $\text{NICS}(1)_{\pi\text{zz}}$ of -5.4 ppm agrees well with the $\text{NICS}(1)_{\text{zz}}$ value of -6.5 , though this arises predominantly from diamagnetic (-10.0 ppm) and not paramagnetic (4.6 ppm) contributions. The total contribution of the Rh d orbitals is negligible (0.2 ppm), with the orbital pointing into the

ring ($d-\pi$) making a small negative contribution (-1.8 ppm) and the orbital perpendicular to the ring ($d-\delta$) making a small positive contribution (2.0 ppm). This is due to the paramagnetic contributions of -2.0 and 3.0 ppm, respectively. The two ring-based π orbitals contribute -2.8 ppm each. The value of -2.8 ppm is due to diamagnetic contributions (-4.6 ppm) with a small positive paramagnetic contribution (1.8 ppm). Niobapyrimidine, with a $d^0\text{-Nb}^V$ center, has 6 π electrons. The $\text{NICS}(1)_{\pi zz}$ of -6.8 ppm agrees with the $\text{NICS}(1)_{zz}$ value of -8.8 . Thus, one important point is that neither of the metallacycle $\text{NICS}(1)_{zz}$ values is qualitatively incorrect due to non- π contributions. The NBO analysis identified Nb–N, C–N, and C–C π bonds, consistent with the localization of bonds in the ring. The Nb–N bond contributes little (-0.8 ppm) compared to the C–N (-4.6 ppm) and C–C (-1.4 ppm) π bonds. This is similar to rhodabenzene, though in this case the orbital involving Nb makes a small negative rather than positive contribution. In both cases the slight aromatic character indicated by the $\text{NICS}(1)_{zz}$ value is due to negative diamagnetic contributions from the π bonds located on the organic fragment of the metallacycle. The finding of positive field-induced (paramagnetic) contributions and an overall negative chemical shift due to field-free (diamagnetic) contributions suggests that aromaticity may not be a strong driving force in these systems. This is consistent with our locating a second, isoenergetic structure (isomer 2) that has a nonplanar metallacycle, which would not be expected for an aromatic system.

4.5 d^0 $[(pz)_2(M^{n+}-pyr)]^{(n-5)+}$ Complexes ($M = Y^{III}, Zr^{IV}, Nb^V, Mo^VI, Tc^{VII}$)

We hypothesize that the ability of the formally trianionic kp^{3-} ligand to bond covalently with the d^0 metal is a critical feature in these metallacycles and thus for the potential aromaticity of the ring. Considering the metallacycle as an interaction of a bis-pyrazolate metal fragment and the trianionic kp^{3-} ligand fragment (see Scheme 4.2), the d^0 $(pz)_2M$ fragment has two unoccupied d orbitals that can potentially accept electron density, and the kp^{3-} ligand has three occupied π orbitals (Figure 4.2). Of the two metal orbitals, the one pointing into the ring ($d-\pi$) is expected to be a stronger acceptor than the orbital perpendicular to the ring ($d-\delta$).

To explore the effect of metal oxidation state while maintaining a formal d electron count of zero, we optimized a series of second-row transition metal complexes: $[(pz)_2(Y^{III}-pyr)]^{2-}$, $[(pz)_2(Zr^{IV}-pyr)]^{1-}$, $[(pz)_2(Nb^V-pyr)]^0$, $[(pz)_2(Mo^VI-pyr)]^{1+}$, and $[(pz)_2(Tc^{VII}-pyr)]^{2+}$. We identified two structures for each of these species. One structure was similar to isomer 1 with bond length asymmetry in a planar metallapyrimidine ring, and the other structure was similar to isomer 2 with nearly symmetric bonds but a nonplanar metallapyrimidine ring. The Tc^{VII} complexes were the only exception, where we located a low symmetry structure that was intermediate between isomer 1 and isomer 2. This species was more stable than isomer 1 by 4.5 kcal/mol. This is in contrast to the other four complexes where isomer 1 and isomer 2 are isoenergetic. We label the lower energy structure for Tc^{VII} isomer 2 for convenience because the technetiapyrimidine ring is nonplanar. Bond lengths are presented in Table 4.4 for isomer 1 for each metal as well as isomer 2 for Tc^{VII} . We again choose to focus

on isomer 1 because of its relevance to the established crystal structure and the planarity of the metallacycle.

The Y^{III} complex stands out in this series with η^1 pyrazolate ligands, while all of the other complexes have η^2 bound pyrazolates. Within the metallapyrimidine ring, the Y–N bonds are long (>2.1 Å) and similar to one another ($\Delta = 0.02$ Å). The C–N and C–C bond lengths are very uniform at 1.308 ± 0.004 and 1.432 ± 0.004 Å, respectively. In contrast, the Nb–N bond lengths differ by 0.15 at 1.833 and 1.979 Å and are indicative of a localized bonding pattern consistent with the metallacycle shown in Scheme 4.1. The Zr^{IV} results are intermediate with some localization as evidenced by the difference in Zr–N bond lengths of 0.09 Å. Asymmetry in the M–N bonds is a maximum for Mo^{VI} with a difference of 0.16 Å, though this is very similar to the value for both Nb^V and Tc^{VII} . The Tc–N bonds for isomer 1 are both very short (<1.9 Å) but show an asymmetry of $\Delta = 0.15$ Å. Isomer 2 for Tc^{VII} shows similar bonding, though the metal-pyrazolate bonding is slightly less asymmetric and less localized bonding in the ring is observed. There is a clear trend between the M–N bond lengths and metal oxidation state, but localization does not strictly increase with increasing oxidation state. Collectively, these trends suggest that our hypothesis of weaker metal-ligand communication with low metal oxidation states is correct. However, the Y^{III} species is the closest to having symmetric bonding within the metallacycle, which is usually argued as a criterion for aromaticity. Could less covalent bonding with the metal actually enhance aromaticity? We turned to the NCS analysis of the $NICS(1)_{zz}$ values to investigate this point further.

NICS(1)_{zz} values range from +5.1 for Y^{III} to −19.7 for Tc^{VII} (isomer 1 only) where values follow an approximately linear trend with the metal oxidation state (Table 4.5). In each of these species, the NCS analysis of π orbital contributions is close to the NICS(1)_{zz} value, suggesting the trend is not an artifact, but the contribution of non- π orbitals increases with metal oxidation state. For the Y^{III} complex none of the π orbitals have metal character (Figure 4.3). Combined with the NICS(1)_{zz} value of +5.1 due to a large paramagnetic π contribution of 12.6 ppm, these results suggest that the Y complex is slightly antiaromatic and that the delocalized bond length pattern is not indicative of aromaticity. The Zr^{IV} C–N π orbitals show a slight amount of metal character, but the qualitative pattern is more similar to those of Y than those of the other complexes. For both Y and Zr the C–C–C π bond makes a large, positive paramagnetic contribution to the NICS(1)_{zz}. The Nb, Mo, and Tc complexes were observed to have localized bonds consistent with the bond lengths in Table 4.4, and this is reflected in the orbital plots in Figure 4.3. Here, we observe a qualitatively different orbital pattern with localized M–N, C–N, and C–C π bonds. All three of these π bonds make an overall negative contribution of −1 to −6 ppm, but this is due to diamagnetic and not paramagnetic contributions. Although the Tc–N bond makes a negative paramagnetic contribution of −1.1 ppm, the paramagnetic π sum for the Tc^{VII} species is still 0.5 ppm. Overall paramagnetic contributions tend toward zero from 12.6 for Y^{III} to 0.5 for Tc^{VII} changing almost linearly with the oxidation state of the metal.

NICS(1)_{zz} values suggest these d⁰ complexes are weakly aromatic, while the field-induced (paramagnetic) contributions of the π orbitals and the isoenergetic, nonplanar isomers suggest instead that these compounds are non- or antiaromatic.

Regardless of which metric we base our final conclusion on, the isoelectronic d^0 metallapyrimidines show no convincing patterns of aromaticity. The trend toward nonaromatic behavior with increasing oxidation state coincides with an increased amount of metal d orbital character in the π orbitals. In an extreme limit, this would involve formal electron transfer from kp^{3-} to the metal. Therefore, this suggested to us that looking at isostructural metal complexes with different d electron counts, especially in the d- π or d- δ orbital (Figure 4.2), could produce an aromatic metallapyrimidine.

4.6 $M^V [(pz)_2(M-pyr)]^0$ Complexes ($M = Nb^V, Mo^V, Tc^V, Ru^V, Rh^V$)

We turned our attention to a series of metallapyrimidines with formally pentavalent metals to evaluate the impact of d orbital occupation on the aromaticity of the metallacycle. Geometry optimization afforded a C_2 symmetric structure (C_2 axis along M-C3) for all of the complexes except Nb^V (Figure 4.4). There is a noticeable deviation from a tetrahedral disposition as evidenced by Npz-M-Npz angles of 120 – 145 degrees. A structure similar to isomer 1 was also located on the potential energy surface for each of these pentavalent metal complexes, but isomer 1 is higher in energy than the C_2 symmetric structure by 8 – 12 kcal/mol. We also attempted to find a C_2 symmetric structure for Nb^V , but each attempted optimization reverted to isomer 2. The structural parameters for the C_2 symmetry structures of Mo^V thru Rh^V are included in Table 4.6. The most notable feature is that the M-N, C-N, and C-C bonds are equivalent in these metallacycles and, unlike the d^0 isomer 2 series that also featured equivalent bonds, each metallapyrimidine ring is planar. Short M-N bond lengths of 1.78 – 1.88 Å are observed in the metallapyrimidine ring, and the C-N and C-C bond

lengths varied between 1.31 and 1.33 and 1.40 – 1.41 Å, respectively. At the same level of theory, the C–N and C–C bond lengths for pyrimidine are 1.34 and 1.39 Å, respectively. The symmetric, planar geometry and the bond length data, combined with the fact that the localized isomer 1 structure is much higher in energy, suggest that these complexes demonstrate aromaticity.

To quantify the aromaticity in these complexes, we turned to the NICS/NCS analyses. NICS(1)_{zz} values of –15.4, –36.0, –31.6, and –22.4 for the Mo^V, Tc^V, Ru^V, and Rh^V complexes further suggest that they are aromatic. In fact, these values compare well to the values of –28.7 and –26.9 for benzene and pyrimidine. However, the Tc^{VII} species in the d⁰ complexes also had a reasonable NICS(1)_{zz} value of –19.7 that, upon further investigation, was found to be due to diamagnetic and not paramagnetic contributions. The NCS breakdown is detailed for [(pz)₂(Tc^V-pyr)]⁰ and [(pz)₂(Rh^V-pyr)]⁰ in Table 4.7.

The NICS(1)_{πzz} for the Tc^V species of –30.3 ppm agrees reasonably well with the NICS(1)_{zz} value of –36.0. This value is due to a large negative paramagnetic contribution of –19.6 ppm and a diamagnetic contribution of –10.7 ppm, similar to the values of –16.6 and –12.7 ppm observed for benzene. Each of the ring π orbitals contributes between –8 and –9 ppm. The two C–N π orbitals have equal paramagnetic (–4.3 ppm) and diamagnetic (–4.8 ppm) contributions, while the deloc π orbital (see Figure 4.5) value is due entirely to paramagnetic contributions (–7.8 ppm). The Tc d-δ orbital also makes a negative contribution of –4.1 ppm that is predominantly due to paramagnetic contributions (–3.1 ppm). It is important to note that two of the Tc orbitals have the proper symmetry to conjugate with the ring: (i) the d-π orbital acts as an

acceptor as evidenced in the orbital plot for the deloc π orbital (Figure 4.5), and (ii) the $d-\delta$ orbital acts as a weak donor. Thus, whether we consider it to be a 6-electron (excluding $d-\delta$) or an 8-electron system that defies traditional electron counting for aromatic systems, the Tc^{V} complex provides a convincing example of aromaticity in a metallapyrimidine.

Despite seeming to be a 10-electron π system, the Rh^{V} complex shows similar behavior to that of technetium. This is misleading, however, as the coordination environment at the Rh center has the Rh $d-\delta$ orbital doubly occupied and another d orbital (nonbonding, in the plane of the metallacycle) that is orthogonal to the rhodapyrimidine π orbitals. Occupation of $d-\pi$ is unfavorable because the orbital lobes partially overlap with the ancillary pyrazolate lone pairs, imparting antibonding character. Thus, the ring π electron count is still 8-electrons, and only four contributing orbitals are included in Table 4.7. The $\text{NICS}(1)_{\pi\text{zz}}$ of -20.0 ppm agrees well with the $\text{NICS}(1)_{\text{zz}}$ value of -22.4 , which is smaller than that of the Tc^{V} complex but still indicative of strong aromaticity. Importantly, the paramagnetic contribution is greater than the diamagnetic contribution at -10.4 versus -9.6 ppm. The $d-\delta$ orbital has a small contribution of -1.3 here compared to -4.1 for Tc. All three of the π orbitals in the ring make negative contributions of -5 to -7 ppm. The deloc π orbital is dominated by the paramagnetic contribution of -5.5 ppm, with a positive diamagnetic contribution of 0.9 ppm. The C–N π orbitals make contributions of -7.1 ppm but this is mostly due to diamagnetic (-4.9 ppm) instead of paramagnetic (-2.2 ppm) contributions. We suspect this has to do with enlargement of the ring, most noticeable in the longer M–N bond

lengths of 1.9 versus 1.8 Å for Rh^{V} versus Tc^{V} , due to occupation of the d orbital that lies in the plane of the rhodapyrimidine.

Finally, we wanted to investigate whether metallapyrimidine formation is thermodynamically feasible for these species that demonstrate properties that are consistent with aromatic systems. While it does not prove that such compounds can be isolated in the lab, we evaluated the thermodynamics for $\text{M}^{\text{III}}(\text{pz})_3 \rightarrow (\text{pz})_2(\text{M}^{\text{V}}\text{-pyr})$ for each these species to see if ring opening of the pyrazolate is feasible. Formation of the metallapyrimidine is exergonic by -29, -44, -48, and -24 kcal/mol for Nb, Mo, Tc, and Ru, but endergonic by 5 kcal/mol for Rh. This trend is sensible because both Ru^{III} and Rh^{III} are stable redox states for those metals and because the aromaticity is predicted to be largest for the Tc species providing a larger driving force for metallacycle formation. Such low coordination number complexes of Mo and Tc are unlikely to be isolated without the use of extremely bulky steric groups on the pyrazolates, but we are working to find feasible redox couples that will result in d^2 complexes with occupied $d\text{-}\delta$ and unoccupied $d\text{-}\pi$ orbitals that could afford metallapyrimidines with strong aromaticity.

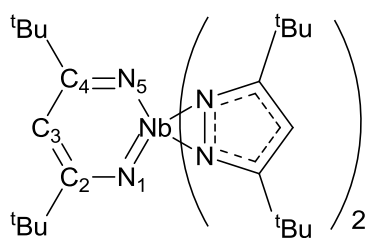
4.7 Conclusions

In this chapter, we have utilized the natural chemical shielding analysis to decompose $\text{NICS}(1)_{\text{zz}}$ contributions of metallapyrimidines into diamagnetic (field-free) and paramagnetic (field-induced) contributions from localized π orbitals for a new class of metallacycle, metallapyrimidines. $\text{NICS}(1)_{\text{zz}}$ for niobapyrimidine suggested that the ring is aromatic, but our NCS analysis showed this is not due to field-induced contributions. Instead, positive paramagnetic contributions suggest this species is

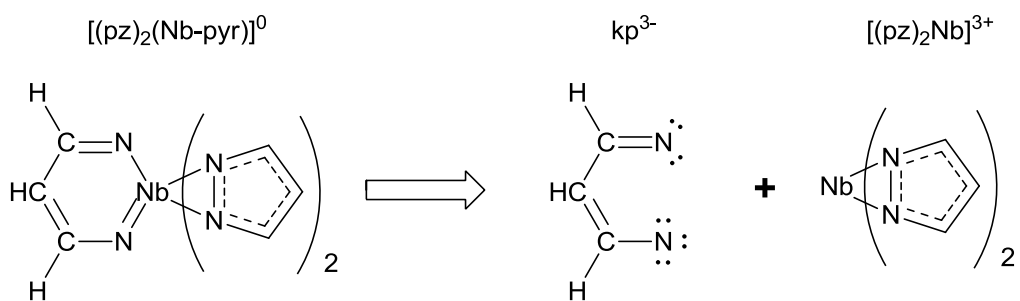
better described as slightly antiaromatic instead of slightly aromatic, consistent with our finding of an isoenergetic isomer for this species that has a nonplanar niobapyrimidine ring. In a series of d^0 metallapyrimidines, all complexes demonstrated similar behavior, though the Tc^{VII} species was found to be nonaromatic, which prompted us to vary the d electron count of the metal. Variation of the metal d electron count was accomplished by studying a series of M^V metallapyrimidine complexes where $M = Nb, Mo, Tc, Ru,$ and Rh , which span d^0 to d^4 . These complexes were subjected to the NCS analysis, which showed strong evidence for aromaticity, with the negative $NICS(1)_{zz}$ values arising from large negative paramagnetic contributions in the $NICS(1)_{\pi zz}$.

One must always exercise caution when interpreting aromatic indicators of a single type as we have done here. However, the NCS data for the M^V complexes suggested to us a conceptual picture for how metallaaromaticity can be encouraged; both of the d orbitals capable of conjugating with the π system of kp^{3-} must be utilized. We discovered in the d^0 series that having both the $d-\pi$ and $d-\delta$ orbitals unoccupied, which can theoretically both act as acceptors, does not lead to aromaticity across a wide range of metal orbital energies that we accessed by varying the metal valency. Bond localization or nonplanarity was observed instead. Our M^V series of complexes showed that having one of these orbitals occupied and one unoccupied leads to clear examples of aromatic systems according to the NCS decomposition of the $NICS(1)_{zz}$ value. We suspect that the $d-\pi$ orbital must be unoccupied due to its ability to conjugate strongly with the ring π orbitals as an acceptor and provide a conduit for continuous electronic communication across the metallacycle, as evidenced by the large field-induced contribution from the deloc π orbital in the Tc^V and Rh^V species. The

covalent character of this bonding is so persistent that the localization algorithm maintains delocalization of this orbital across the ring. The role of the $d-\delta$ orbital is less clear. We have interpreted it as conjugating with the ring here due to the nitrogen character in the deloc orbital plot for the Tc^V species, but its role may actually be to prevent certain structural distortions, as we observed for the d^0 complexes. If the latter is the case, then metallapyrimidines are classic 6π electron systems, though the distribution of electrons between the metal and ligand is different from that proposed for metallabenzene. (We analyzed the $Tc(V)$ and $Rh(V)$ metallapyrimidine complexes including the contributions of the $d-\delta$ orbital, but all conclusions are qualitatively the same if we only consider the 6π electrons.) Unfortunately, we encountered no examples of a doubly occupied $d-\pi$ and unoccupied $d-\delta$ orbital in our studies to verify this hypothesis explicitly. Alternative coordination environments are a promising avenue for exploration of this point in the future and may enable a unified theory for aromaticity in metallapyrimidines, and possibly metallacycles in general, as a function of not only the d electron count but the d orbital ordering. Future work will also include the evaluation of aromaticity in metallapyrimidines and related metallacycles using alternative aromaticity indicators, such as induced ring current measurements and computing barriers for cycloaddition chemistry at the metallapyrimidine.



Scheme 4.1 $[(pz)_2(Nb-pyr)]^0$



Scheme 4.2 Oxidative Fragment Interaction in $[(pz)_2(Nb-pyr)]^0$.

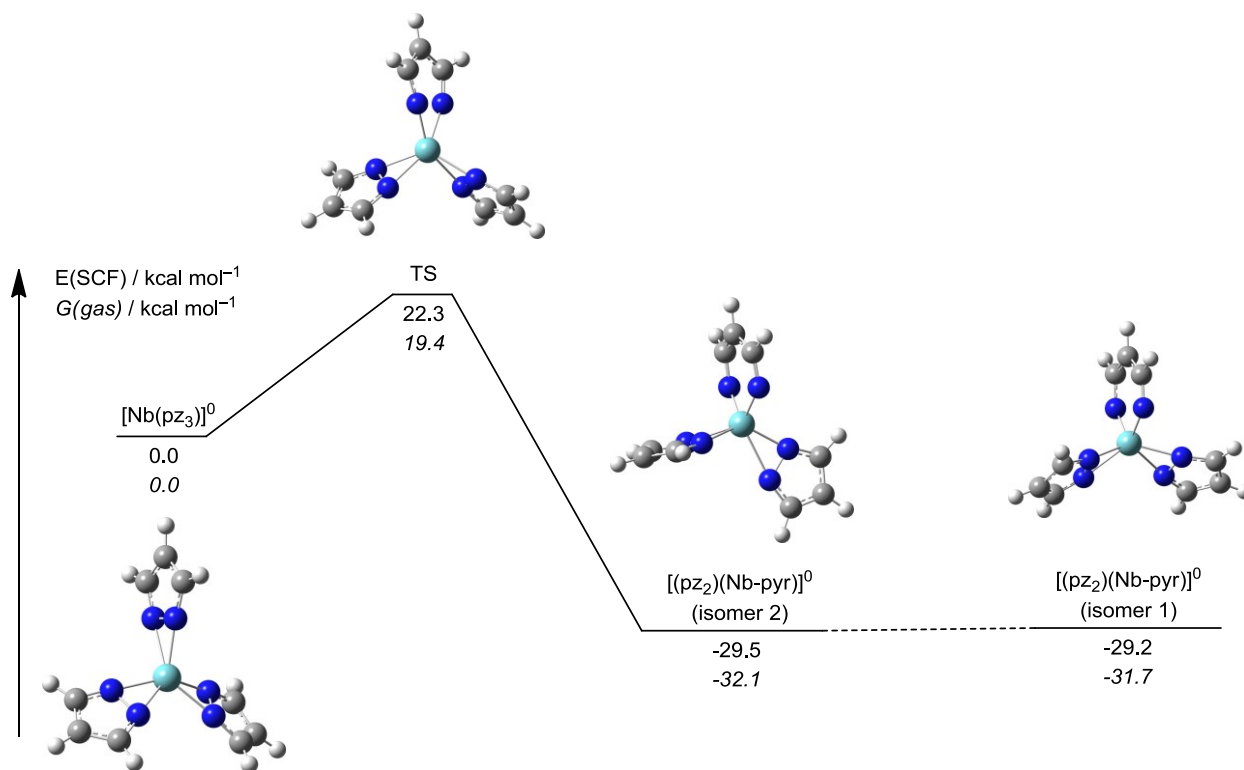


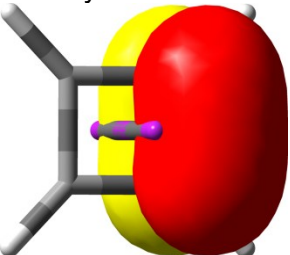
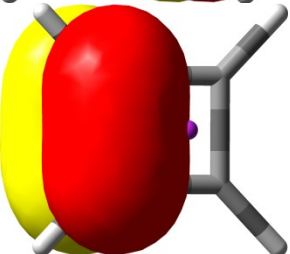
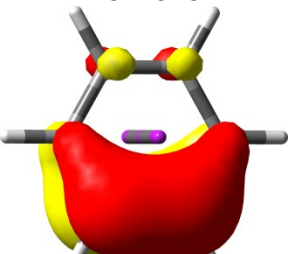
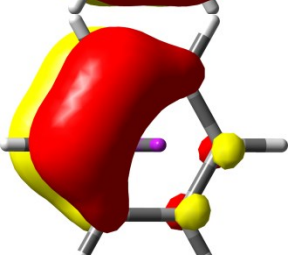
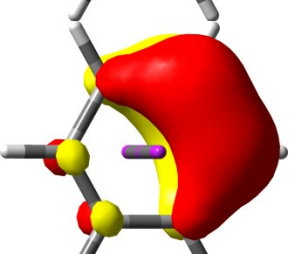
Figure 4.1 Potential energy surface and structures for the reaction of [Nb(pz)₃]⁰ to form [(pz)₂(Nb-pyr)]⁰.

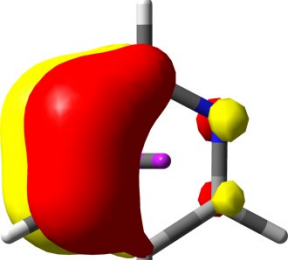
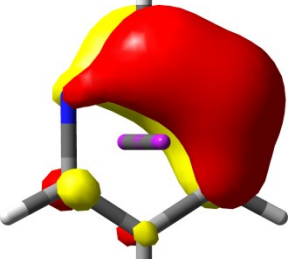
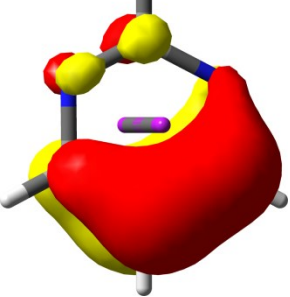
Table 4.1 Natural Chemical Shielding Analysis for Benzene, Pyrimidine, Cyclobutadiene, Rhodabenzene, and Niobapyrimidine^a

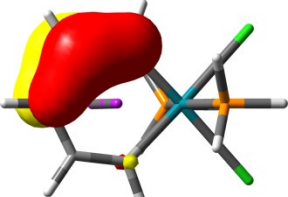
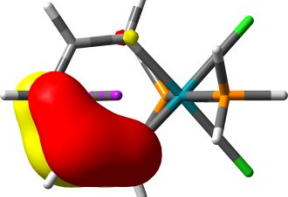
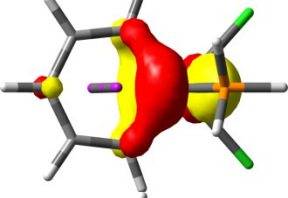
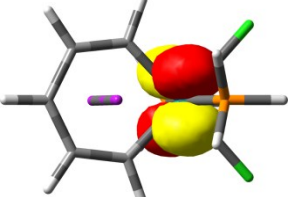
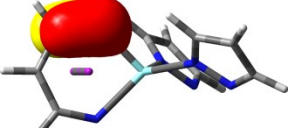
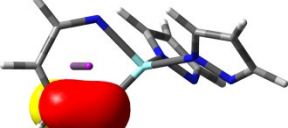
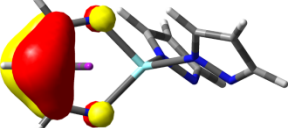
Species	NLMO Description	Total Contribution	Paramagnetic	Diamagnetic
Benzene NICS(1) _{zz} = -28.7	C-C π	-9.8	-5.6	-4.2
	C-C π	-9.8	-5.6	-4.2
	C-C π	-9.8	-5.6	-4.2
	NICS(1) _{πzz}	-29.4	-16.8	-12.6
Pyrimidine NICS(1) _{zz} = -26.9	C-C π	-9.2	-4.9	-4.3
	C-N π	-9.1	-4.3	-4.8
	C-N π	-8.8	-4.4	-4.4
	NICS(1) _{πzz}	-27.1	-13.6	-13.5
Cyclobutadiene NICS(1) _{zz} = +60.2	C-C π	27.3	30.7	-3.4
	C-C π	27.3	30.7	-3.4
	NICS(1) _{πzz}	54.6	61.4	-6.8
Rhodabenzene [(H ₃ P) ₂ (Cl) ₂ Rh (κ^2 -C ₅ H ₅)] ⁰ NICS(1) _{zz} = -6.5	C-C-C π	-2.8	1.8	-4.6
	C-C-C π	-2.8	1.8	-4.6
	Rh d- π	-1.8	-2.0	0.2
	Rh d- δ	2.0	3.0	-1.0
	NICS(1) _{πzz}	-5.4	4.6	-10.0
Niobapyrimidine [(pz) ₂ (Nb-pyr)] ⁰ NICS(1) _{zz} = -8.8	Nb-N π	-0.8	2.5	-3.3
	C-N π	-4.6	1.2	-5.8
	C-C π	-1.4	1.5	-2.9
	NICS(1) _{πzz}	-6.8	5.2	-12.0

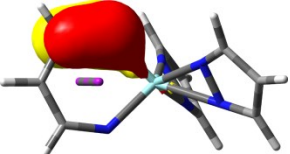
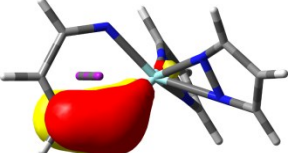
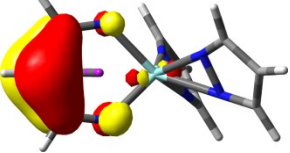
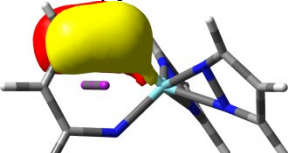
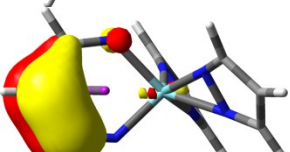
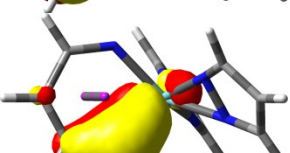
^a π orbital contributions (ppm) to the negative zz component of the chemical shielding tensor in the atomic origin for the ring of interest are listed.

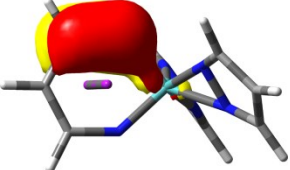
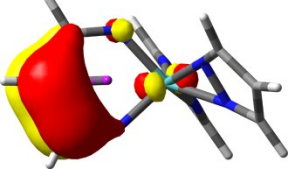
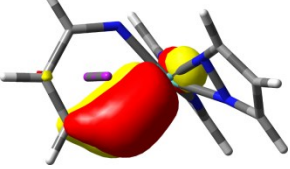
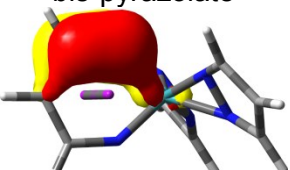
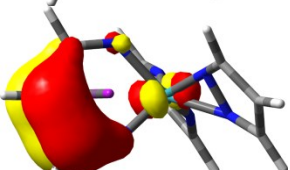
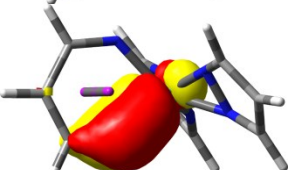
Table 4.2 Natural Chemical Shielding Analysis of π Orbital Contributions with Orbital Pictures^a

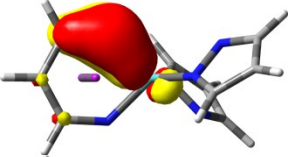
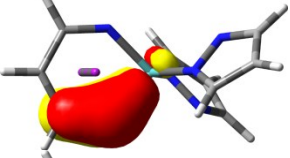
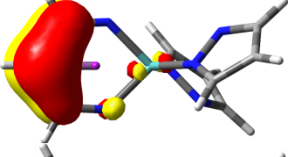
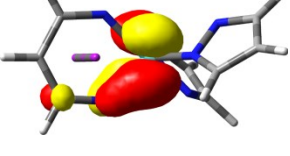
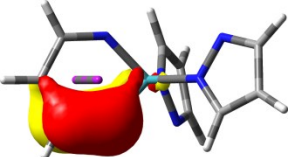
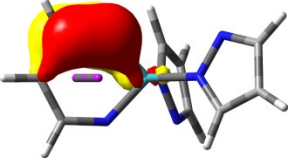
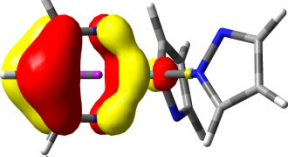
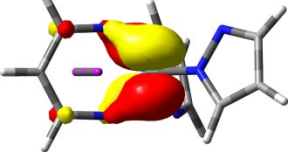
Species/Orbital	GVMO ^b	NLMO ^c	Total Contribution ^d	Paramagnetic	Diamagnetic
Cyclobutene					
	14	1	27.3	30.7	-3.4
	13	7	27.3	30.7	-3.4
		NICS(1) _{π_{ZZ}}	54.6	61.4	-6.8
Benzene					
	21	3	-9.8	-5.6	-4.2
	19	6	-9.8	-5.6	-4.2
	20	11	-9.8	-5.6	-4.2
		NICS(1) _{π_{ZZ}}	-29.4	-16.8	-12.6

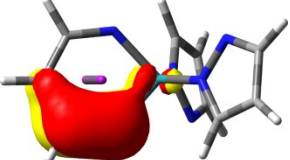
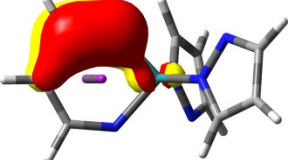
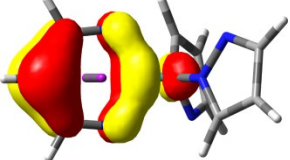
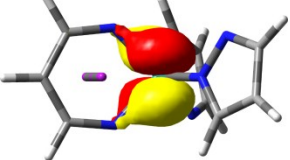
Species/Orbital	GVMO ^b	NLMO ^c	Total Contribution ^d	Paramagnetic	Diamagnetic
Pyrimidine					
	19	12	-9.1	-4.3	-4.8
	20	2	-8.8	-4.4	-4.4
	21	7	-9.2	-4.9	-4.3
		NICS(1) _{πzz}	-27.1	-13.6	-13.5

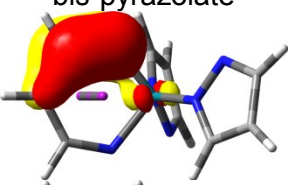
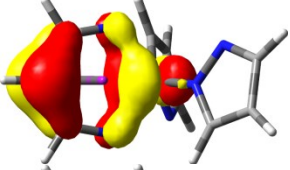
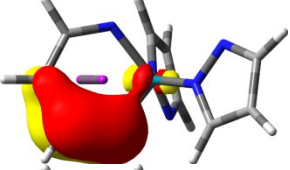
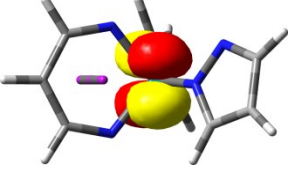
Species/Orbital	GVMO ^b	NLMO ^c	Total Contribution ^d	Paramagnetic	Diamagnetic
Rhodabenzene					
	58	13	-2.8	1.8	-4.6
	59	17	-2.8	1.8	-4.6
	54	61	-1.8	-2.0	0.2
	53	60	2.0	3.0	-1.0
NICS(1) _{πZZ}			-5.4	4.6	-10.0
Yttrium ^{III} bis-pyrazolate					
	54	4	-2.2	2.0	-4.3
	53	9	-1.5	2.9	-4.4
	59	51	8.6	7.7	1.0
NICS(1) _{πZZ}			5.0	12.6	-7.7

Species/Orbital	GVMO ^b	NLMO ^c	Total Contribution ^d	Paramagnetic	Diamagnetic
Zirconium ^{IV} bis-pyrazolate					
	53	4	-2.6	2.7	-5.4
	54	10	-5.9	-0.8	-5.1
	59	55	5.7	5.1	0.6
		NICS(1) _{πzz}	-2.8	7.0	-9.8
Niobium ^V bis-pyrazolate					
	54	4	-4.6	1.2	-5.8
	57	6	-1.4	1.5	-2.9
	56	34	-0.8	2.5	-3.3
		NICS(1) _{πzz}	-6.8	5.2	-12.0

Species/Orbital	GVMO ^b	NLMO ^c	Total Contribution ^d	Paramagnetic	Diamagnetic
Molybdenum^{VI} bis-pyrazolate					
	54	4	-4.9	1.7	-6.6
	56	7	-1.9	1.7	-3.6
	55	37	-3.6	0.3	-3.9
		NICS(1) _{πzz}	-10.3	3.7	-14.0
Technetium^{VII} bis-pyrazolate					
	51	4	-5.7	1.1	-6.8
	56	6	-3.4	0.6	-3.9
	55	36	-4.9	-1.1	-3.8
		NICS(1) _{πzz}	-14.0	0.5	-14.5

Species/Orbital	GVMO ^b	NLMO ^c	Total Contribution ^d	Paramagnetic	Diamagnetic
Molybdenum ^V bis-pyrazolate					
	54α/381β	2α/2β	−4.3	0.1	−4.3
	53α/377β	9α/9β	−4.3	0.1	−4.3
	56α/380β	34α/34β	−1.8	1.2	−2.9
	58α	60α	−3.7	−1.4	−2.4
		NICS(1) _{πzz}	−14.1	−0.1	−14.0
Technetium ^V bis-pyrazolate					
	49	4	−9.2	−4.3	−4.8
	50	9	−9.2	−4.3	−4.8
	60	55	−7.8	−7.8	−0.1
	57	60	−4.1	−3.1	−1.0
		NICS(1) _{πzz}	−30.3	−19.6	−10.7

Species/Orbital	GVMO ^b	NLMO ^c	Total Contribution ^d	Paramagnetic	Diamagnetic
Ruthenium ^V bis-pyrazolate					
	53α/375β	9α/10β	−8.6	−4.3	−4.2
	56α/376β	2α/4β	−8.6	−4.3	−4.2
	59α/386β	34α/16β	−2.6	−2.1	−0.5
	55α/378β	61α/60β	−3.3	−2.6	−0.7
		NICS(1) _{πZZ}	−23.0	−13.3	−9.7

Species/Orbital	GVMO ^b	NLMO ^c	Total Contribution ^d	Paramagnetic	Diamagnetic
Rhodium ^V bis-pyrazolate					
	52	4	−7.1	−2.2	−4.9
	62	7	−4.6	−5.5	0.9
	51	10	−7.1	−2.2	−4.9
	53	61	−1.3	−0.6	−0.7
NICS(1) _{πzz}			−19.3	−11.4	−7.9

^a π orbital contributions (ppm) to the negative zz component of the chemical shielding tensor in the atomic origin for the ring of interest are listed. ^b Molecular orbital number in GaussView. ^c Natural localized molecular orbital number. ^d The C–N π -orbital chemical shift values have been averaged to reflect the symmetry in the molecule.

Table 4.3 Natural Chemical Shielding Analysis for Contributing Orbitals in ppm^a

Species	GVMO ^b	NLMO ^c	NLMO Description ^d	Total Contribution ^e	Paramag.	Diamag.
Cyclobutadiene NICS(1) _{zz} = 60.2	14	1	C–C π	27.3	30.7	–3.4
	6	2	C–C σ	–0.5	4.0	–4.5
	11	3	C–C σ	2.5	7.1	–4.6
	7	4	C–H σ	–0.1	1.1	–1.2
	12	5	C–C σ	2.5	7.1	–4.6
	8	6	C–H σ	–0.1	1.1	–1.2
	13	7	C–C π	27.3	30.7	–3.4
	5	8	C–C σ	–0.5	4.0	–4.5
	10	9	C–H σ	–0.1	1.1	–1.2
	9	10	C–H σ	–0.1	1.1	–1.2
			Sum	58.4	88.0	–29.6
			NICS(1) _{zz}	54.6	61.4	–6.7
Benzene NICS(1) _{zz} = –28.7	11	1	C–C σ	–0.6	3.0	–3.6
	9	2	C–C σ	–0.6	3.0	–3.6
	21	3	C–C π	–9.8	–5.6	–4.2
	7	8	C–C σ	–0.6	3.0	–3.6
	19	6	C–C π	–9.8	–5.6	–4.2
	12	8	C–C σ	–0.6	3.0	–3.6
	8	10	C–C σ	–0.6	3.0	–3.6
	20	11	C–C π	–9.8	–5.6	–4.2
	10	13	C–C σ	–0.6	3.0	–3.6
			Sum	–33.3	1.8	–35.1
			NICS(1) _{zz}	–29.3	–16.7	–12.6
Pyrimidine NICS(1) _{zz} = –26.9	7	1	C–C σ	–1.6	1.0	–2.7
	20	2	C–N π	–8.9	–4.4	–4.4
	8	3	C–C σ	–1.6	1.0	–2.7
	16	4	C–H σ	0.8	–0.2	1.0
	9	5	C–C σ	–1.1	1.9	–2.9
	11	6	C–C σ	–1.6	2.1	–3.6
	21	7	C–C π	–9.2	–4.9	–4.3
	12	9	C–C σ	–1.6	2.1	–3.6
	10	11	C–C σ	–1.1	1.9	–2.9
	19	12	C–N π	–9.1	–4.3	–4.8
	17	20	C–H σ	1.8	–0.1	1.9
	18	21	C–H σ	1.8	–0.1	1.9
			Sum	–31.4	–4.1	–27.2
			NICS(1) _{zz}	–27.2	–13.7	–13.5

Species	GVMO ^b	NLMO ^c	NLMO Description ^d	Total Contribution ^e	Paramag.	Diamag.
Rhodabenzene NICS(1) _{zz} = -6.8	48	1	C-H σ	2.0	1.1	0.9
	43	2	C-H σ	-2.5	-3.0	0.4
	36	3	C-H σ	2.8	2.9	-0.1
	44	4	C-H σ	-2.5	-3.0	0.4
	47	5	C-H σ	2.0	1.1	0.9
	40	8	P-H σ	-0.3	0.9	-1.2
	37	9	P-H σ	-0.3	0.9	-1.2
	32	12	C-C σ	-1.2	-0.1	-1.1
	58	13	C-C-C π	-2.8	1.8	-4.6
	52	14	Rh-C σ	-0.3	2.1	-2.4
	34	15	C-C σ	-0.0	2.7	-2.8
	33	16	C-C σ	-1.2	-0.1	-1.1
	59	17	C-C-C π	-2.8	1.8	-4.6
	35	18	C-C σ	-0.0	2.7	-2.8
	51	19	Rh-C σ	-0.3	2.1	-2.4
	45	21	Rh-P σ	-1.0	-0.5	-0.6
	26	48	Rh s-orbital	0.9	-0.4	1.3
	28	50	Rh p-orbital	0.9	-0.3	1.2
	55	59	Rh d orbital	-0.4	-1.5	1.1
	53	60	Rh d orbital	1.9	3.0	-1.0
	54	61	C-Rh-C π	-1.8	-2.0	0.2
			Sum	-7.3	12.0	-19.3
			NICS(1) _{zz}	-5.6	4.5	-10.1
Yttrium^{III} bis-pyrazolate NICS(1) _{zz} = 5.1	32	1	C-C σ	-3.7	-0.4	-3.3
	41	2	C-H σ	1.4	-0.1	1.5
	21	3	C-N σ	-2.9	1.0	-3.9
	54	4	C-N π	-2.2	2.0	-4.3
	33	5	C-C σ	-3.6	-0.2	-3.4
	40	6	C-H σ	2.6	2.6	-0.0
	42	7	C-H σ	1.4	-0.1	1.6
	20	8	C-N σ	-3.0	1.0	-4.0
	53	9	C-N π	-1.5	2.9	-4.4
	38	21	pz C-H σ	-0.1	0.9	-1.0
	56	30	Y-N σ	2.6	-4.4	6.9
	55	31	Y-N σ	2.4	-4.6	7.0
	16	47	Y s-orbital	-0.4	-2.4	2.0
	19	49	Y p-orbital	-0.0	-1.3	1.3
	59	51	C-C-C π	8.6	7.7	1.0
	43	52	Y-N(pz) σ	0.7	-0.5	1.2
	46	58	N lone pair	-0.5	1.6	-2.1
	45	59	N lone pair	-0.4	1.9	-2.3
			Sum	1.5	7.8	-6.3
			NICS(1) _{zz}	5.0	12.6	-7.7

Species	GVMO ^b	NLMO ^c	NLMO Description ^d	Total Contribution ^e	Paramag.	Diamag.
Zirconium^{IV} bis-pyrazolate NICS(1) _{zz} = -3.0	41	1	C-C σ	-3.4	0.4	-3.8
	52	2	C-H σ	2.1	-0.0	2.1
	24	3	C-N σ	-1.8	2.6	-4.4
	53	4	C-N π	-2.6	2.7	-5.4
	56	5	Zr-N σ	0.6	-1.5	2.1
	32	6	C-C σ	-2.6	1.3	-4.0
	44	7	C-H σ	2.0	2.0	0.1
	45	8	C-H σ	0.6	-0.5	1.2
	27	9	C-N σ	-1.0	3.5	-4.5
	54	10	C-N π	-5.9	-0.8	-5.1
	25	11	pz N-N σ	-2.0	0.6	-2.5
	42	14	Zr-N(pz) σ	1.0	-2.6	3.6
	26	17	pz N-N σ	-0.8	0.4	-1.2
	43	22	Zr-N(pz) σ	0.3	-1.1	1.4
	33	33	N lone pair	-1.8	-0.6	-1.1
	55	34	Zr-N σ	2.1	-0.0	2.1
	34	35	N lone pair	-0.9	-1.9	1.0
	16	51	Zr s-orbital	-0.6	-3.0	2.4
	19	52	Zr p-orbital	0.8	-1.0	1.8
	18	53	Zr p-orbital	-0.9	-1.2	0.3
	17	54	Zr p-orbital	1.2	0.8	0.4
	59	55	C-C-C π	5.7	5.1	0.6
	46	56	pz N lone pair	0.9	-0.9	1.8
	58	58	pz N-N π	0.4	1.6	-1.1
			Sum	-6.5	5.9	-12.3
			NICS(1) _{π_{zz}}	-2.8	7.0	-9.8
Niobium^V bis-pyrazolate NICS(1) _{zz} = -8.8	34	1	C-C σ	-2.9	0.8	-3.7
	20	3	C-N σ	-1.4	2.0	-3.4
	54	4	C-N π	-4.6	1.2	-5.8
	28	5	C-C σ	-2.1	1.6	-3.8
	57	6	C-C π	-1.4	1.5	-2.9
	44	7	C-H σ	1.4	1.5	-0.1
	25	9	C-N σ	-1.2	3.0	-4.2
	26	10	pz N-N σ	-0.7	0.3	-1.0
	41	13	Nb-N(pz) σ	0.3	-1.0	1.2
	27	16	pz N-N σ	-1.9	0.4	-2.3
	42	21	Nb-N(pz) σ	0.8	-2.9	3.7
	33	32	N lone pair	-3.2	-1.6	-1.7
	55	33	Nb-N σ	1.8	0.9	0.9
	56	34	Nb-N π	-0.8	2.5	-3.3
	46	35	N lone pair	0.8	-3.5	4.3
	16	51	Nb s-orbital	-0.5	-2.6	2.1
	19	53	Nb p-orbital	0.2	-1.0	1.3
	17	54	Nb p-orbital	1.4	1.0	0.4
	47	56	Nb-N(pz) σ	0.7	-0.9	1.6
	59	58	pz N-N π	0.8	1.8	-1.0
	49	59	Nb-N σ	-1.5	0.2	-1.7
			Sum	-14.2	5.3	-19.5
			NICS(1) _{π_{zz}}	-6.8	5.2	-12.0

Species	GVMO ^b	NLMO ^c	NLMO Description ^d	Total Contribution ^e	Paramag.	Diamag.
Molybdenum^{VI} bis-pyrazolate NICS(1) _{zz} = -14.1	47	1	C-C σ	-1.8	1.5	-3.4
	20	3	C-N σ	-2.3	1.9	-4.2
	54	4	C-N π	-4.9	1.7	-6.6
	57	5	Mo-N σ	0.0	-1.4	1.4
	28	6	C-C σ	-1.9	1.6	-3.5
	56	7	C-C π	-1.9	1.7	-3.6
	21	10	C-N σ	-2.4	2.3	-4.7
	27	11	pz N-N σ	-1.2	0.9	-2.1
	35	14	Mo-N(pz) σ	0.8	-1.9	2.7
	42	17	Mo-N(pz) σ	0.2	-1.2	1.4
	43	21	Mo-N(pz) σ	-0.6	-1.7	1.1
	29	35	N lone pair	-2.9	-1.5	-1.4
	51	36	Mo-N σ	1.5	2.5	-1.1
	55	37	Mo-N π	-3.6	0.3	-3.9
	34	38	N lone pair	-1.7	-2.5	0.8
	16	54	Mo s-orbital	-0.3	-2.3	2.0
	19	55	Mo p-orbital	0.7	-0.8	1.5
	17	57	Mo p-orbital	1.5	1.1	0.4
	59	58	pz N-N π	1.1	2.3	-1.2
			Sum	-19.6	4.5	-24.1
			NICS(1) _{πzz}	-10.3	3.7	-14.0
Technetium^{VII} bis-pyrazolate NICS(1) _{zz} = -19.7	30	1	C-C σ	-2.9	1.1	-4.0
	21	3	C-N σ	-1.8	0.8	-2.5
	51	4	C-N π	-5.7	1.1	-6.8
	29	5	C-C σ	-1.9	1.3	-3.2
	56	6	C-C π	-3.4	0.6	-3.9
	35	8	C-H σ	0.4	1.1	-0.7
	20	9	C-N σ	-3.7	1.0	-4.7
	26	10	pz N-N σ	-1.1	1.4	-2.4
	52	12	pz C-N π	-0.7	0.6	-1.3
	37	13	Tc-N(pz) σ	0.7	-0.6	1.3
	53	15	pz C-N π	1.2	0.8	0.4
	27	17	pz N-N σ	-0.2	1.0	-1.2
	44	20	Tc-N(pz) σ	-0.4	-1.3	0.9
	28	34	N lone pair	-2.5	-2.3	-0.2
	50	35	Tc-N σ	-0.2	1.7	-1.9
	55	36	Tc-N π	-4.9	-1.1	-3.8
	48	37	N lone pair	1.8	-0.4	2.2
	16	53	Tc s-orbital	-0.1	-1.8	1.7
	19	54	Tc p-orbital	0.9	-0.5	1.4
	17	55	Tc p-orbital	1.3	1.3	0.0
	18	56	Tc p-orbital	1.5	1.2	0.3
	60	58	σ^*	1.3	2.9	-1.5
	49	59	Tc-N σ	-3.5	-0.9	-2.6
			Sum	-23.9	8.9	-32.8
			NICS(1) _{πzz}	-14.0	0.5	-14.5

Species	GVMO ^b	NLMO ^c	NLMO Description ^d	Total Contribution ^e	Paramag.	Diamag.
Molybdenum^v bis-pyrazolate NICS(1) _{zz} = -15.4	29α/352β	1α/1β	C–C σ	-2.2	1.2	-3.4
	54α/381β	2α/2β	C–N π	-2.2	1.4	-3.6
	20α/344β	4α/4β	C–N σ	-2.5	1.5	-4.0
	28α/353β	5α/5β	C–C σ	-2.1	1.3	-3.4
	21α/245β	8α/8β	C–N σ	-2.1	1.8	-4.0
	53α/377β	9α/9β	C–N π	-6.4	-1.3	-5.1
	26α/350β	10α/10β	pz N–N σ	-0.6	0.6	-1.2
	34α/358β	14α/15β	Mo–N(pz) σ	1.0	-1.4	2.3
	35α/359β	19α/20β	Mo–N(pz) σ	-0.3	-1.4	1.1
	46α/370β	32α/32β	Mo–N σ	1.0	-2.1	3.1
	45α/369β	33α/33β	Mo–N σ	1.1	-2.3	3.4
	56α/380β	34α/34β	deloc π	-1.8	1.2	-2.9
	16α/340β	50α/50β	Mo s-orbital	-0.5	-2.4	1.9
	19α/341β	51α/51β	Mo p-orbital	0.6	-1.0	1.6
	59α/342β	56α/53β	Mo p-orbital	2.2	1.4	0.8
	47α/371β	58α/58β	N lone pair	-2.0	0.5	-2.6
	48α/372β	59α/59β	N lone pair	-2.2	0.7	-3.0
	58α	60α	Mo δ-orbital	-3.7	-1.4	-2.4
			Sum	-21.0	-1.0	-20.0
			NICS(1) _{πzz}	-14.1	-0.1	-14.0
Technetium^v bis-pyrazolate NICS(1) _{zz} = -36.0	29	1	C–C σ	-2.3	1.6	-4.0
	20	3	C–N σ	-2.8	0.7	-3.6
	49	4	C–N π	-8.9	-4.1	-4.8
	28	5	C–C σ	-2.4	1.6	-4.0
	21	8	C–N σ	-2.7	1.1	-3.7
	50	9	C–N π	-9.4	-4.6	-4.8
	24	10	pz N–N σ	-0.9	1.0	-1.9
	26	13	pz C–N σ	-1.0	0.3	-1.3
	34	20	pz C–C σ	-0.6	0.9	-1.5
	38	24	pz C–H σ	0.0	1.3	-1.3
	32	32	N lone pair	-2.3	-1.9	-0.5
	51	33	Tc–N σ	1.1	0.5	0.6
	33	34	N lone pair	-2.2	-1.7	-0.5
	52	35	Tc–N σ	1.1	0.8	0.3
	16	51	Tc s-orbital	-0.4	-2.1	1.8
	17	52	Tc p-orbital	-0.2	-1.5	1.3
	60	55	deloc π	-7.8	-7.8	-0.1
	47	56	pz N lone pair	1.9	0.3	1.6
	58	57	pz N–N π	-0.1	1.1	-1.2
	57	60	Tc δ-orbital	-4.1	-3.1	-1.0
			Sum	-44.1	-15.7	-28.4
			NICS(1) _{πzz}	-30.3	-19.6	-10.7

Species	GVMO ^b	NLMO ^c	NLMO Description ^d	Total Contribution ^e	Paramag.	Diamag.
Ruthenium^V bis-pyrazolate NICS(1) _{zz} = -31.6	29α/352β	1α/1β	C-C σ	-2.5	1.3	-3.9
	20α/345β	4α/3β	C-N σ	-2.4	0.9	-3.2
	56α/376β	2α/4β	C-N π	-8.5	-4.6	-3.9
	28α/353β	5α/5β	C-C σ	-2.6	1.3	-3.9
	38α/?β	6α/?β	C-H σ	0.6	0.6	-0.1
	60α/384β	56α/7β	pz C-N π	-2.0	-2.6	0.6
	21α/344β	8α/9β	C-N σ	-2.3	1.0	-3.3
	53α/375β	9α/10β	C-N π	-8.6	-4.1	-4.5
	22α/346β	10α/11β	pz N-N π	-0.8	0.9	-1.7
	27α/351β	13α/14β	pz C-N σ	-1.4	0.2	-1.6
	59α/386β	34α/16β	deloc π	-2.6	-2.1	-0.5
	33α/356β	20α/19β	pz C-C σ	-0.6	0.9	-1.5
	36α/358β	24α/23β	pz C-H σ	0.1	1.4	-1.3
	51α/382β	11α/27β	pz C-C π	-1.0	0.2	-1.2
	45α/369β	32α/31β	Ru-N σ	0.3	-1.0	1.2
	46α/370β	33α/32β	Ru-N σ	0.7	-0.6	1.3
	16α/340β	50α/48β	Ru s-orbital	0.1	-1.5	1.7
	17α/342β	51α/49β	Ru p-orbital	-0.4	-1.6	1.2
	50α/374β	54α/52β	pz N lone pair	2.2	0.6	1.6
	61α/379β	57α/54β	pz C-N π	0.6	0.9	-0.3
	18α/?β	52α/?β	Ru p-orbital	-0.6	-0.7	0.1
	?α/368β	?α/58β	N lone pair	-1.5	-0.5	-1.0
	?α/367β	?α/59β	N lone pair	-1.7	-0.7	-1.0
	55α/378β	61α/60β	Ru δ-orbital	-3.3	-2.6	-0.7
	54α	60α	Ru d orbital	1.7	0.2	1.5
			Sum	-37.4	-12.2	-25.2
			NICS(1) _{πzz}	-23.0	-13.3	-9.7

Species	GVMO ^b	NLMO ^c	NLMO Description ^d	Total Contribution ^e	Paramag.	Diamag.
Rhodium^v bis-pyrazolate NICS(1) _{zz} = -22.4	29	1	C-C σ	-2.5	1.3	-3.7
	21	3	C-N σ	-2.3	0.8	-3.0
	52	4	C-N π	-7.0	-2.2	-4.8
	28	5	C-C σ	-2.8	1.0	-3.7
	34	6	C-H σ	0.9	1.2	-0.3
	62	7	deloc π	-4.6	-5.5	0.9
	20	9	C-N σ	-2.3	0.8	-3.0
	51	10	C-N π	-7.1	-2.1	-5.0
	22	11	pz N-N σ	-0.8	0.6	-1.4
	25	14	pz C-N σ	-1.5	0.1	-1.6
	32	21	pz C-C σ	-0.6	0.9	-1.5
	35	25	pz C-H σ	0.1	1.4	-1.3
	16	50	Rh s-orbital	0.7	-0.9	1.6
	17	51	Rh p-orbital	-0.3	-1.4	1.1
	19	52	Rh p-orbital	-1.8	-1.9	0.1
	49	54	pz N lone pair	2.3	0.7	1.6
	59	55	pz N-N π	1.0	1.5	-0.5
	54	60	Rh d orbital	0.6	-1.0	1.7
	53	61	Rh δ -orbital	-1.3	-0.6	-0.7
			Sum	-29.1	-5.4	-23.7
			NICS(1) _{πzz}	-20.0	-10.4	-9.6

^a Orbital contributions (ppm) to the negative zz component of the chemical shielding tensor in the atomic origin for the ring of interest are listed. ^b Molecular orbital number in GaussView. ^c Natural localized molecular orbital number. ^d Sums include only the contribution of the orbitals listed; NICS(1)_{zz} includes the contribution of all orbitals. ^e Chemical shifts for open-shell dⁿ species are averages of alpha and beta contributions. C-N π -orbital chemical shift values have not been averaged to reflect the symmetry.

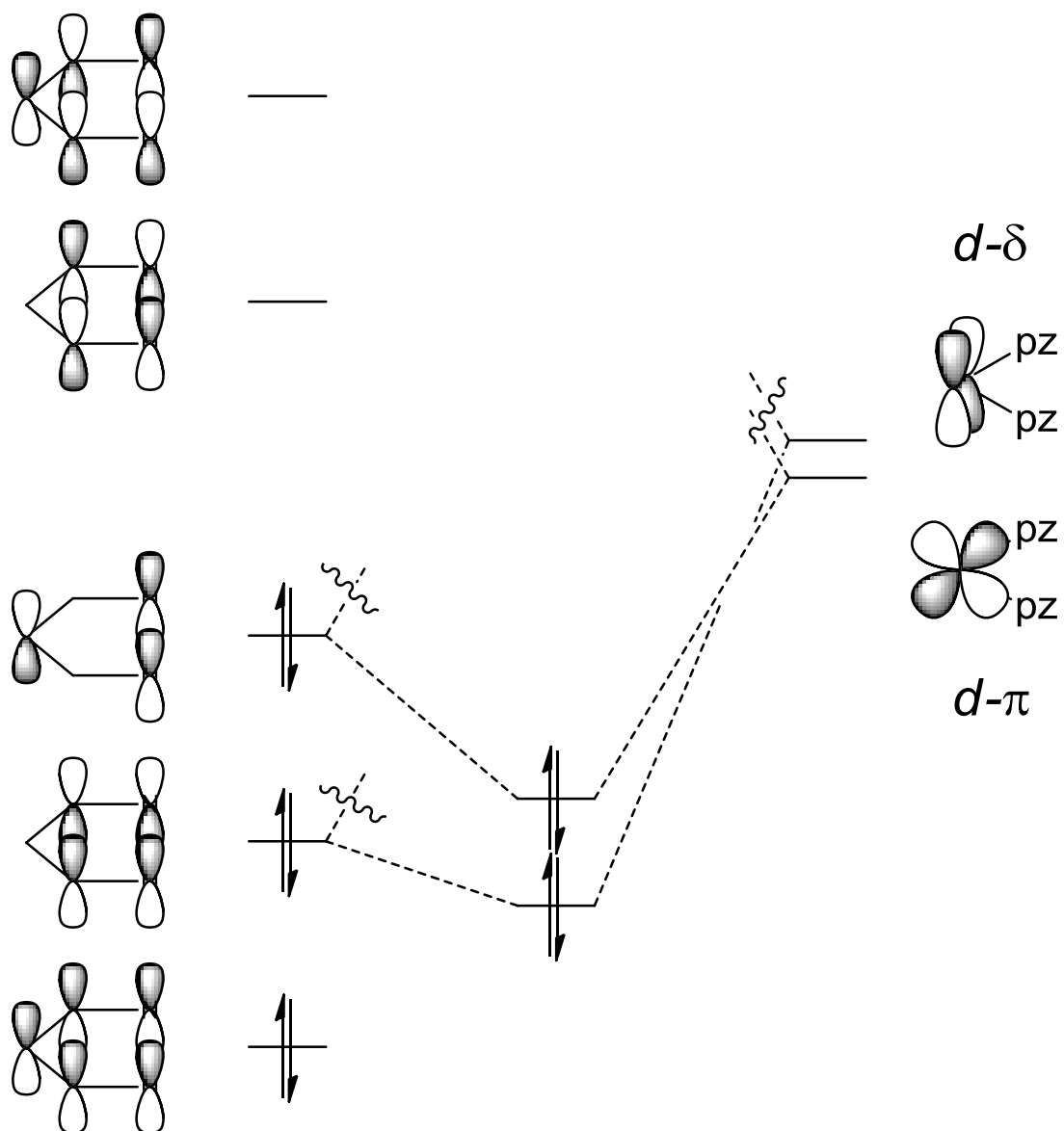


Figure 4.2 Simplified orbital interaction diagram between kp^{3-} (left) and $(pz)_2M$ (right).

Table 4.4 Metal-Pyrazolate and Metallapyrimidine Bond Lengths (Å) for the d^0 Series of Complexes

Complex	M–pz	M=N ₁	N ₁ –C ₂	C ₂ =C ₃	C ₃ –C ₄	C ₄ =N ₅	N ₅ –M
$[(\eta^1\text{-pz})_2(\text{Y}^{\text{III}}\text{-pyr})]^{2-}$	2.446 3.325	2.151	1.311	1.428	1.436	1.304	2.169
$[(\eta^2\text{-pz})_2(\text{Zr}^{\text{IV}}\text{-pyr})]^{1-}$	2.265 2.389	1.967	1.329	1.401	1.434	1.304	2.056
$[(\eta^2\text{-pz})_2(\text{Nb}^{\text{V}}\text{-pyr})]^0$	2.135 2.223	1.833	1.351	1.379	1.441	1.299	1.979
$[(\eta^2\text{-pz})_2(\text{Mo}^{\text{VI}}\text{-pyr})]^{1+}$	2.049 2.122	1.764	1.359	1.372	1.446	1.298	1.925
$[(\eta^2\text{-pz})_2(\text{Tc}^{\text{VII}}\text{-pyr})]^{2+}$ isomer 1	2.002 2.068	1.745	1.344	1.382	1.444	1.300	1.899
$[(\eta^2\text{-pz})_2(\text{Tc}^{\text{VII}}\text{-pyr})]^{2+}$ isomer 2	1.938/2.019 2.292/2.089	1.757	1.334	1.395	1.431	1.312	1.851

Table 4.5 Natural Chemical Shielding Analysis for the d^0 Series of $[(pz)_2(M^{n+}-pyr)]^{(n-5)+}$ Complexes^a

Species	NLMO Description	Total Contribution	Paramagnetic	Diamagnetic
Y^{III} NICS(1) _{zz} = +5.1	C–N π	–2.2	2.0	–4.3
	C–N π	–1.5	2.9	–4.4
	C–C–C π	8.6	7.7	1.0
	NICS(1) _{πzz}	5.0	12.6	–7.7
Zr^{IV} NICS(1) _{zz} = –3.0	C–N π	–2.6	2.7	–5.4
	C–N π	–5.9	–0.8	–5.1
	C–C–C π	5.7	5.1	0.6
	NICS(1) _{πzz}	–2.8	7.0	–9.8
Nb^V NICS(1) _{zz} = –8.8	Nb–N π	–0.8	2.5	–3.3
	C–N π	–4.6	1.2	–5.8
	C–C π	–1.4	1.5	–2.9
	NICS(1) _{πzz}	–6.8	5.2	–12.0
Mo^{VI} NICS(1) _{zz} = –14.1	Mo–N π	–3.6	0.3	–3.9
	C–N π	–4.9	1.7	–6.6
	C–C π	–1.9	1.7	–3.6
	NICS(1) _{πzz}	–10.3	3.7	–14.0
Tc^{VII} NICS(1) _{zz} = –19.7	Tc–N π	–4.9	–1.1	–3.8
	C–N π	–5.7	1.1	–6.8
	C–C π	–3.4	0.6	–3.9
	NICS(1) _{πzz}	–14.0	0.5	–14.5

^a π orbital contributions (ppm) to the negative zz component of the chemical shielding tensor in the atomic origin for the ring of interest are listed.

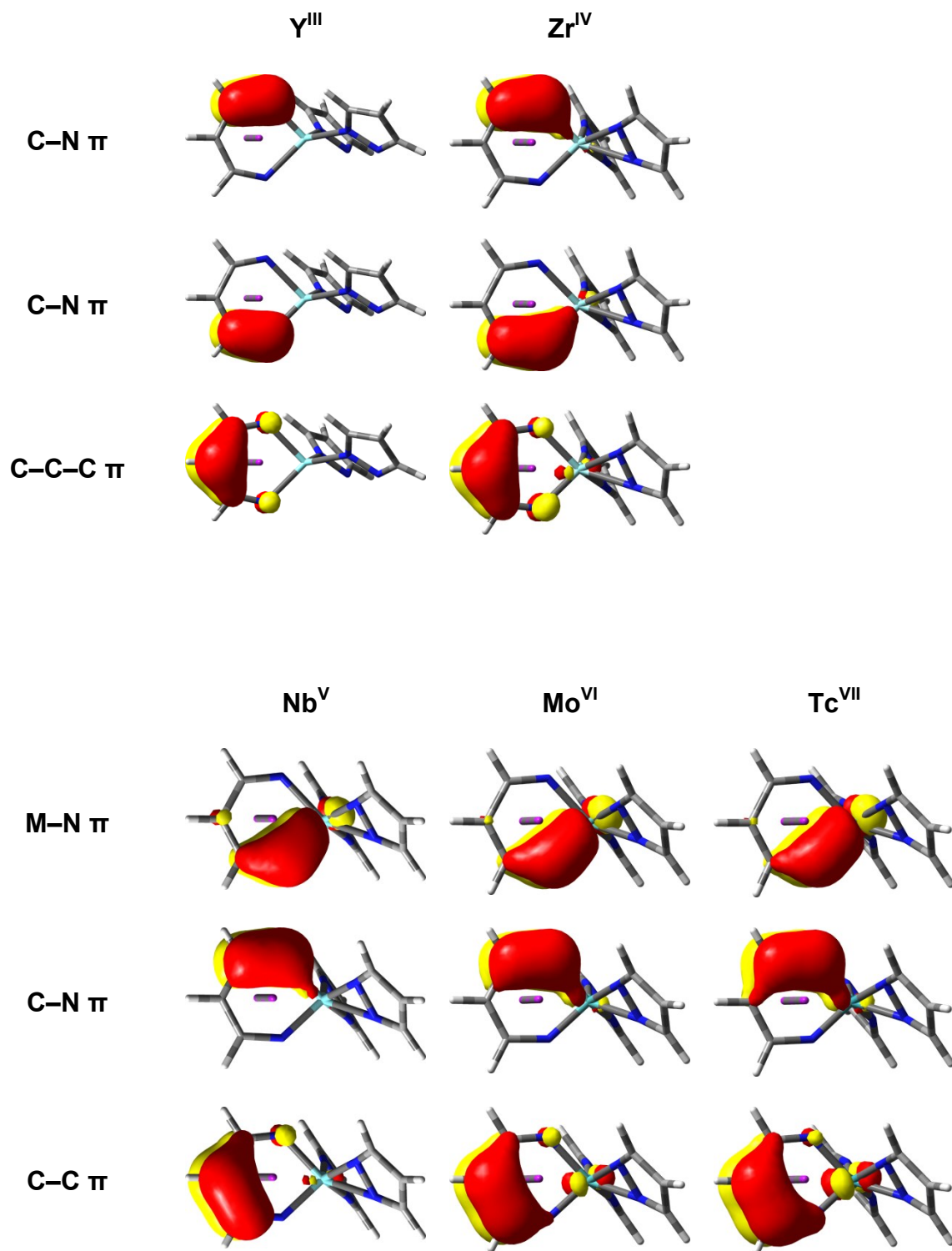


Figure 4.3 Molecular orbital isosurface plots (0.05 au) of the π orbitals for the $[(\text{pz})_2(\text{M}^{n+}\text{-pyr})]^{(n-5)+}$ complexes.

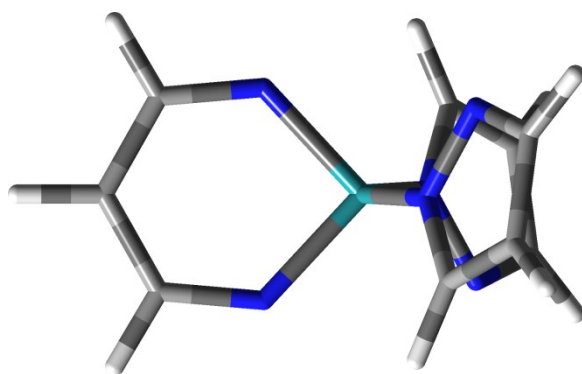


Figure 4.4 C₂ symmetric structure for the [(pz)₂(M^V-pyr)]⁰ complexes.

Table 4.6 Metal-Pyrazolate and Metallapyrimidine Bond Lengths (Å) for the M^V series of Complexes

Complex	d electron count	S	M–pz	M–N	N–C	C–C
$[(\eta^1\text{-pz})_2(\text{Mo}^V\text{-pyr})]^0$	d^1	1/2	2.043 2.499	1.820	1.336	1.404
$[(\eta^1\text{-pz})_2(\text{Tc}^V\text{-pyr})]^0$	d^2	0	1.980 2.856	1.784	1.330	1.403
$[(\eta^1\text{-pz})_2(\text{Ru}^V\text{-pyr})]^0$	d^3	1/2	1.960 2.843	1.824	1.321	1.404
$[(\eta^1\text{-pz})_2(\text{Rh}^V\text{-pyr})]^0$	d^4	0	1.965 2.830	1.880	1.312	1.411

Table 4.7 Natural Chemical Shielding Analysis for the $[(pz)_2(M^V\text{-pyr})]^0$ Series of Complexes^a

Species	NLMO Description	Total Contribution	Paramagnetic	Diamagnetic
Mo^V NICS(1) _{zz} = -15.4	C–N π	-4.3	0.1	-4.3
	C–N π	-4.3	0.1	-4.3
	deloc π	-1.8	1.2	-2.9
	Mo d- δ	-3.7	-1.4	-2.4
	NICS(1) _{πzz}	-14.1	-0.1	-14.0
Tc^V NICS(1) _{zz} = -36.0	C–N π	-9.2	-4.3	-4.8
	C–N π	-9.2	-4.3	-4.8
	deloc π	-7.8	-7.8	-0.1
	Tc d- δ	-4.1	-3.1	-1.0
	NICS(1) _{πzz}	-30.3	-19.6	-10.7
Ru^V NICS(1) _{zz} = -31.6	C–N π	-8.6	-4.3	-4.2
	C–N π	-8.6	-4.3	-4.2
	deloc π	-2.6	-2.1	-0.5
	Ru d- δ	-3.3	-2.6	-0.7
	NICS(1) _{πzz}	-23.0	-13.3	-9.7
Rh^V NICS(1) _{zz} = -22.4	C–N π	-7.1	-2.2	-4.9
	C–N π	-7.1	-2.2	-4.9
	deloc π	-4.6	-5.5	0.9
	Rh d- δ	-1.3	-0.6	-0.7
	NICS(1) _{πzz}	-20.0	-10.4	-9.6

^a π orbital contributions (ppm) to the negative zz component of the chemical shielding tensor in the atomic origin for the ring of interest are listed. The C–N π orbital chemical shift values have been averaged to reflect the symmetry in the molecule.

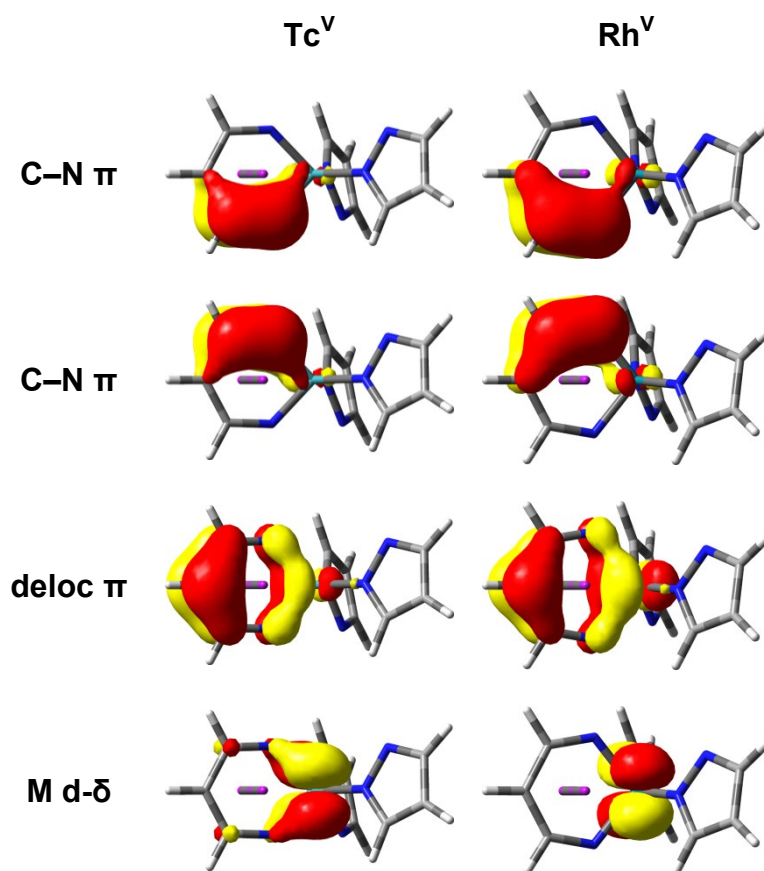


Figure 4.5 Molecular orbital isosurface plots (0.05 au) of the π orbitals for $[(\text{pz})_2(\text{Tc}^{\text{V}}\text{-pyr})]^0$ and $[(\text{pz})_2(\text{Rh}^{\text{V}}\text{-pyr})]^0$.

4.8 References

1. Hofmann, A. W. On insolinic acid. *Proc. R. Soc. London* **1856**, 8, 1-3.
2. Schleyer, P. V. Introduction: Aromaticity. *Chem. Rev.* **2001**, 101, 1115-1117.
3. Krygowski, T. M.; Cyranski, M. K. Structural aspects of aromaticity. *Chem. Rev.* **2001**, 101, 1385-1419.
4. Cyranski, M. K. Energetic aspects of cyclic pi-electron delocalization: Evaluation of the methods of estimating aromatic stabilization energies. *Chem. Rev.* **2005**, 105, 3773-3811.
5. Schleyer, P. V. Introduction: Delocalization - pi and sigma. *Chem. Rev.* **2005**, 105, 3433-3435.
6. Pople, J. A. Proton magnetic resonance of hydrocarbons. *J. Chem. Phys.* **1956**, 24, 1111.
7. Viglione, R. G.; Zanasi, R.; Lazzeretti, P. Are ring currents still useful to rationalize the benzene proton magnetic shielding? *Org. Lett.* **2004**, 6, 2265-2267.
8. Faglioni, F.; Ligabue, A.; Pelloni, S.; Soncini, A.; Viglione, R. G.; Ferraro, M. B.; Zanasi, R.; Lazzeretti, P. Why downfield proton chemical shifts are not reliable aromaticity indicators. *Org. Lett.* **2005**, 7, 3457-3460.
9. Wannere, C. S.; Corminboeuf, C.; Allen, W. D.; Schaefer, H. F.; Schleyer, P. V. Downfield proton chemical shifts are not reliable aromaticity indicators. *Org. Lett.* **2005**, 7, 1457-1460.
10. Gomes, J.; Mallion, R. B. Aromaticity and ring currents. *Chem. Rev.* **2001**, 101, 1349-1383.

11. Chen, Z. F.; Wannere, C. S.; Corminboeuf, C.; Puchta, R.; Schleyer, P. V. Nucleus-independent chemical shifts (NICS) as an aromaticity criterion. *Chem. Rev.* **2005**, *105*, 3842-3888.
12. Geuenich, D.; Hess, K.; Kohler, F.; Herges, R. Anisotropy of the induced current density (ACID), a general method to quantify and visualize electronic delocalization. *Chem. Rev.* **2005**, *105*, 3758-3772.
13. Islas, R.; Heine, T.; Merino, G. The Induced Magnetic Field. *Accounts Chem. Res.* **2012**, *45*, 215-228.
14. Bleeke, J. R. Metallabenzenes. *Chem. Rev.* **2001**, *101*, 1205-1227.
15. Wright, L. J. Metallabenzenes and metallabenzenoids. *Dalton Trans.* **2006**, 1821-1827.
16. Thorn, D. L.; Hoffmann, R. Delocalization in metallocycles. **1979**, *3*, 39-45.
17. Iron, M. A.; Lucassen, A. C. B.; Cohen, H.; van der Boom, M. E.; Martin, J. M. L. A computational foray into the formation and reactivity of metallabenzenes. *J. Am. Chem. Soc.* **2004**, *126*, 11699-11710.
18. Fernandez, I.; Frenking, G. Aromaticity in metallabenzenes. *Chem.-Eur. J.* **2007**, *13*, 5873-5884.
19. Periyasamy, G.; Burton, N. A.; Hillier, I. H.; Thomas, J. M. H. Electron delocalization in the metallabenzenes: A computational analysis of ring currents. *J. Phys. Chem. A* **2008**, *112*, 5960-5972.
20. Havenith, R. W. A.; De Proft, F.; Jenneskens, L. W.; Fowler, P. W. Relativistic ring currents in metallabenzenes: an analysis in terms of contributions of localised orbitals. *Phys. Chem. Chem. Phys.* **2012**, *14*, 9897-9905.

21. Milcic, M. K.; Ostojic, B. D.; Zaric, S. D. Are chelate rings aromatic? Calculations of magnetic properties of acetylacetonato and o-benzoquinonediimine chelate rings. *Inorg. Chem.* **2007**, *46*, 7109-7114.
22. Perera, T. H.; Lord, R. L.; Heeg, M. J.; Schlegel, H. B.; Winter, C. H. Metallapyrimidines and Metallapyrimidiniums from Oxidative Addition of Pyrazolate N-N Bonds to Niobium(III), Niobium(IV), and Tantalum(IV) Metal Centers and Assessment of Their Aromatic Character. *Organometallics* **2012**, *31*, 5971-5974.
23. Schleyer, P. V.; Jiao, H. J.; Hommes, N.; Malkin, V. G.; Malkina, O. L. An evaluation of the aromaticity of inorganic rings: Refined evidence from magnetic properties. *J. Am. Chem. Soc.* **1997**, *119*, 12669-12670.
24. Fallah-Bagher-Shaidaei, H.; Wannere, C. S.; Corminboeuf, C.; Puchta, R.; Schleyer, P. V. Which NICS aromaticity index for planar pi rings is best? *Org. Lett.* **2006**, *8*, 863-866.
25. Bohmann, J. A.; Weinhold, F.; Farrar, T. C. Natural chemical shielding analysis of nuclear magnetic resonance shielding tensors from gauge-including atomic orbital calculations. *J. Chem. Phys.* **1997**, *107*, 1173-1184.
26. Frisch, M. J.; Trucks, G. W.; Schlegel, H. B.; Scuseria, G. E.; Robb, M. A.; Cheeseman, J. R.; Scalmani, G.; Barone, V.; Mennucci, B.; Petersson, G. A.; Nakatsuji, H.; Caricato, M.; Li, X.; Hratchian, H. P.; Izmaylov, A. F.; Bloino, J.; Zheng, G.; Sonnenberg, J. L.; Liang, W.; Hada, M.; Ehara, M.; Toyota, K.; Fukuda, R.; Hasegawa, J.; Ishida, M.; Nakajima, T.; Honda, Y.; Kitao, O.; Nakai, H.; Vreven, T.; Montgomery, J., J. A.; Peralta, J. E.; Ogliaro, F.; Bearpark, M.;

- Heyd, J. J.; Brothers, E.; Kudin, K. N.; Staroverov, V. N.; Keith, T.; Kobayashi, R.; Normand, J.; Raghavachari, K.; Rendell, A.; Burant, J. C.; Iyengar, S. S.; Tomasi, J.; Cossi, M.; Rega, N.; Millam, J. M.; Klene, M.; Knox, J. E.; Cross, J. B.; Bakken, V.; Adamo, C.; Jaramillo, J.; Gomperts, R.; Stratmann, R. E.; Yazyev, O.; Austin, A. J.; Cammi, R.; Pomelli, C.; Ochterski, J. W.; Martin, J. M. L.; Morokuma, K.; Zakrzewski, V. G.; Voth, G. A.; Salvador, P.; Dannenberg, J. J.; Dapprich, S.; Parandekar, P. V.; Mayhall, N. J.; Daniels, A. D.; Farkas, O.; Foresman, J. B.; Ortiz, J. V.; Cioslowski, J.; Fox, D. J. *Gaussian Development Version, Revision H.20+*. Wallingford CT, 2010.
27. Vosko, S. H.; Wilk, L.; Nusair, M. Accurate spin-dependent electronic liquid correlation energies for local spin-density calculations - A critical analysis. *Can. J. Phys.* **1980**, *58*, 1200-1211.
 28. Lee, C. T.; Yang, W. T.; Parr, R. G. Development of the Colle-Salvetti correlation energy formulation into a functional of the electron density. *Phys. Rev. B* **1988**, *37*, 785-789.
 29. Becke, A. D. Density functional thermochemistry. III. The role of exact exchange. *J. Chem. Phys.* **1993**, *98*, 5648-5652.
 30. Stephens, P. J.; Devlin, F. J.; Chabalowski, C. F.; Frisch, M. J. Ab initio calculations of vibrational absorptions and circular dichroism spectra using density functional force fields. *J. Phys. Chem.* **1994**, *98*, 11623-11627.
 31. Kaupp, M.; Schleyer, P. V.; Stoll, H.; Preuss, H. Pseudopotential approaches to Ca, Sr, and Ba hydrides - Why are some alkaline earth MX₂ compounds bent. *J. Chem. Phys.* **1991**, *94*, 1360-1366.

32. Bergner, A.; Dolg, M.; Kuchle, W.; Stoll, H.; Preuss, H. Ab initio energy adjusted pseudopotentials for elements of groups 13-17. *Mol. Phys.* **1993**, *80*, 1431-1441.
33. Dolg, M.; Stoll, H.; Preuss, H.; Pitzer, R. M. Relativistic and correlation effects for element 105 (Hahnium, Ha) - A comparative study of M and MO (M = Nb, Ta, Ha) using energy adjusted ab initio pseudopotentials. *J. Phys. Chem.* **1993**, *97*, 5852-5859.
34. Schlegel, H. B.; McDouall, J. J. In *Computational advances in organic chemistry: molecular structure and reactivity*, Kluwer Academic Publishers: Dordrecht ; Boston, 1991.
35. Bauernschmitt, R.; Ahlrichs, R. Stability analysis for solutions of the closed shell Kohn-Sham equation. *J. Chem. Phys.* **1996**, *104*, 9047-9052.
36. Schlegel, H. B. Optimization of equilibrium geometries and transition structures. *J. Comput. Chem.* **1982**, *3*, 214-218.
37. Fukui, K. The path of chemical reactions - The IRC approach. *Accounts Chem. Res.* **1981**, *14*, 363-368.
38. Foresman, J. B.; Frisch, A.; Gaussian Inc. *Exploring chemistry with electronic structure methods*. 2nd ed.; Gaussian, Inc.: Pittsburgh, PA, 1996.
39. Schleyer, P. V.; Maerker, C.; Dransfeld, A.; Jiao, H. J.; Hommes, N. Nucleus-independent chemical shifts: A simple and efficient aromaticity probe. *J. Am. Chem. Soc.* **1996**, *118*, 6317-6318.
40. Cheeseman, J. R.; Trucks, G. W.; Keith, T. A.; Frisch, M. J. A comparison of models for calculating nuclear magnetic resonance shielding tensors. *J. Chem. Phys.* **1996**, *104*, 5497-5509.

41. Glendening, E. D.; Reed, A. E.; Carpenter, J. E.; Weinhold, F. *NBO Version 3.1*, Theoretical Chemistry Institute and Department of Chemistry, The University of Wisconsin-Madison: Madison, WI 53706, 2009.
42. Dezelah, C. L.; Wiedmann, M. K.; Mizohata, K.; Baird, R. J.; Niinisto, L.; Winter, C. H. A pyrazolate-based metalorganic tantalum precursor that exhibits high thermal stability and its use in the atomic layer deposition of Ta₂O₅. *J. Am. Chem. Soc.* **2007**, *129*, 12370-12371.
43. Rinehart, J. D.; Kozimor, S. A.; Long, J. R. Tetranuclear Uranium Clusters by Reductive Cleavage of 3,5-Dimethylpyrazolate. *Angew. Chem.-Int. Edit.* **2010**, *49*, 2560-2564.

CHAPTER 5

PROTONATION AND GEOMETRY EFFECTS ON THE AROMATICITY OF METALLAPYRIMIDINE COMPLEXES CONTAINING 2ND ROW TRANSITION METALS

5.1 Introduction

In the previous chapter, we set out to examine the aromatic properties of a novel class of metallacycles based on a surprise experimental product produced by Perera et al.¹ In attempting to create precursor compounds for thin film growth by atomic layer deposition, a Nb^{III} salt was reacted with a pyrazolate salt with the expectations of creating a volatile Nb^{III}-tris-pyrazolato complex. However, they were unsuccessful in isolating the Nb^{III}-tris-pyrazolato complex and instead obtained a bis-pyrazolato niobapyrimidine complex and additionally a bis-pyrazolato niobapyrimidinium complex. Theoretical studies using Nucleus Independent Chemical Shift (NICS) calculations² were performed to gauge the overall aromaticity of these novel metallacycle compounds. Results from these preliminary calculations showed chemical shifts of –9.9 ppm for the niobapyrimidine ring and –5.5 ppm for the niobapyrimidinium ring indicating a weakly aromatic system compared to pyrimidine (–26.6 ppm).

The theoretical investigation³ in Chapter 4 further examined the aromaticity of these novel metallapyrimidine complexes by studying two series of 2nd row transition metal metallacycles. Based on the NICS calculations, the metallapyrimidines with empty valence d orbitals (d⁰ systems) were found to be weakly to non-aromatic due to the absence of strong paramagnetic contributions of the ring π orbitals to the total

chemical shift that are otherwise seen in known aromatic compounds such as benzene. However, metallapyrimidines containing Tc^{V} (a d^2 system) and Rh^{V} (a d^4 system) showed very strong paramagnetic contributions from the π orbitals to the total chemical shift.

In this chapter, we aim to examine the series of 2nd row transition metal metallapyrimidine complexes further by evaluating the effects of ring protonation and methylation on the specific aromaticity measured by NICS and NCS analysis. The experimental work by Perera et al. also isolated a metallapyrimidinium complex where a ring nitrogen atom was protonated in the final structure. Using the NICS and NCS metrics for evaluating aromaticity, we have investigated the effect of protonation and methylation on the structure and aromaticity of 2nd row transition metal metallapyrimidine complexes.

5.2 Computational Details

All calculations were performed using a development version of the Gaussian software.⁴ Geometries of the complexes were optimized at the B3LYP level of theory.⁵⁻⁸ Carbon, hydrogen, and nitrogen atoms were modeled by the 6-31+G(d) basis set,⁹⁻¹⁴ while metal atoms were modeled by the Stuttgart-Dresden-Bonn (SDD) effective core potential and accompanying basis set.¹⁵⁻¹⁷ Wave functions for optimized structures were tested for stability.^{18,19} Harmonic vibrational frequency calculations were used to confirm that optimized structures were minimum structures or transition states.²⁰ Intrinsic reaction coordinate calculations were used to further validate that computed transition states connected the proposed minima along the reaction path.²¹ Gas phase

Gibbs free energies were obtained by summing the calculated electronic energies with a zero point energies correction and a thermal free energy corrections.²²

Aromaticity was assessed using the Nucleus Independent Chemical Shift (NICS) computations.^{2,23} NICS calculations have traditionally been carried out by computing the isotropic chemical shift (σ_{iso}) at a point represented by a ghost atom. The ghost atom has no basis functions and is placed at the geometric mean of the positions of the nuclei making up the ring system. In this study, chemical shifts are reported as $-\sigma$ since the sign convention is $\text{NICS} = -\sigma_{\text{iso}}$. Calculating the σ_{iso} at the geometric center of a ring system is referred to as a NICS(0) calculation. NICS(0) calculations have been known to be problematic for studying inorganic systems similar to the ones studied here.^{24,25} An alternative NICS implementation has been used in this study to circumvent the issues related to NICS(0) calculations and involves the evaluation of NICS(1) at points that are located 1 Å above and below the NICS(0) point and orthogonal to the plane of the ring. The NICS(1) points were determined by taking the normalized cross product between two vectors created from the NICS(0) point to the metal atomic center and the NICS(0) point to the either of the ring nitrogen atomic centers. To simplify the analysis of the calculated results, molecular coordinates were aligned such that the NICS(0) point was defined at the Cartesian origin and the two NICS(1) points were aligned along the z-axis. We considered only the tensor component orthogonal to the plane of the metallacycle ring (σ_{zz}) of the calculated chemical shift at the NICS(1) points. In some cases, molecular symmetry was not present in the plane of the metallacycle, therefore the average was taken between the two NICS(1)_{zz} values. Chemical shift tensors were computed according to the Gauge Including Atomic Orbital (GIAO)

formalism.²⁶ Further analysis of the NICS(1)_{zz} values was achieved by using the Natural Chemical Shielding (NCS) module of the NBO program. Based on the natural localized molecular orbitals computed by NBO, NCS performs an orbital decomposition of a calculated chemical shift tensor into diamagnetic (field-free) and paramagnetic (field-induced) components. NCS orbital decomposition allowed us to focus solely on the π orbital contributions to the chemical shift at the NICS(1)_{zz} points. NBO calculations were carried out in Gaussian using the built-in version of NBO 3.1.

5.3 Results and Discussions

The structure and atom numbering of a protonated metallapyrimidine is shown in Figure 5.1. Five different singly and doubly protonated and methylated metallapyrimidine complexes were examined, Tc^{VII} , Mo^{VI} , Nb^{V} , Tc^{V} , and Rh^{V} (Figure 5.2), comprising a small d^0 series (Nb^{V} , Mo^{VI} , and Tc^{VII}) and a small d^n series (Nb^{V} , Tc^{V} , and Rh^{V}). Except for $[(\text{pz})_2(\text{Tc}^{\text{VII}}\text{-pyr-H})]^{3+}$ and the doubly protonated d^0 metallacycle species, optimized geometries for the metallacycle species are at least C_s symmetric containing one plane of symmetry coincidental with the plane of the metallacycle. Bond lengths for the protonated and methylated metallapyrimidine species are collected in Table 3.2. The M-NH^+ bond distances are between 0.15 Å and 0.20 Å longer than the corresponding unprotonated metallapyrimidine, while the other bond lengths between ring atoms show little variation (< 0.03 Å) between the protonated and unprotonated species. The differences between the bond lengths for N-methylation versus protonation are small, with the M-NCH_3^+ bonds elongated by less than 0.1 Å while the other ring bonds change by less than 0.03 Å. In the cases of the singly

protonated/methylated d^n metallacycles, the additional coordination on the nitrogen atoms caused the coordination of one of the pyrazolato ligand to change from η^2 to η^1 . Optimized geometries for the doubly protonated/methylated d^0 species (Nb^V , Mo^VI , Tc^{VII}) show severe puckering of the metallacycle by 30° to 50° for the $M-N_5-N_1-C_3$ dihedral angle, making the interpretation of the NICS values problematic. However, the d^n species, Tc^V and Rh^V , still show bond delocalization with planar metallacycle rings. The Tc^V species has C_{2v} molecular symmetry while the Rh^V species has C_2 molecular symmetry. Overall, double protonation elongates the $M-N$ bonds over single protonation. Interestingly, doubly protonated/methylated Tc^V and Rh^V show η^2 pyrazolato ligand bonding in contrast to the η^1 pyrazolato ligand bonding seen in the unprotonated and singly protonated d^n metallacycles.

Table 5.2 shows the gas phase free energies for oxidative addition of the metal to an unsubstituted, protonated, and methylated pyrazolato ligand in tris-pyrazolato complexes $[M-(pz)_3]$ containing Tc^{VII} , Mo^VI , Nb^V , Tc^V , and Rh^V . For the unsubstituted metallapyrimidine species, the kinetic barriers are all in the ca. 20 – 25 kcal/mol range, except for the Rh^V complex which has a barrier height twice as large as the others at 51.2 kcal/mol. The formation of an unsubstituted metallapyrimidine species is thermodynamically favorable in the gas phase for the Mo^VI , Nb^V , and Tc^V complexes, but not for Rh^V and Tc^{VII} . Comparing the oxidative addition for the metallapyrimidine species to the metallapyrimidinium species, we see similar energies for barrier heights to insertion for the d^0 complexes. However, the reaction free energies of metallacycle formation for protonated complexes become more favorable for the d^0 species by ca. 19 – 25 kcal/mol, and the formation of a substituted Tc^{VII} metallapyrimidine

complexes becomes thermodynamically favorable. Tc^{V} and Rh^{V} protonated complexes form thermodynamically less favorable metallacycles by 19.5 and 14.8 kcal/mol, respectively. Differences between the gas phase reaction free energies and barriers of protonated and methylated complexes are small and systematic. The reaction free energies are less favorable by 0.6 – 4.8 kcal/mol for a methylated pyrazolato versus a protonated pyrazolato ligand. Free energy barriers are higher by 0.8 – 3.5 kcal/mol for a methylated pyrazolato versus a protonated pyrazolato ligand.

The $\text{NICS}(1)_{\text{zz}}$, $\text{NICS}(1)_{\pi\text{zz}}$, π orbital paramagnetic contributions, and π orbital diamagnetic contributions for pyrimidine and metallapyrimidine species that are unsubstituted, protonated, methylated, doubly protonated, and doubly methylated are shown in Table 5.3. Full details of the NICS and NCS analysis are available in Table 5.6 through Table 5.13. There is little variance between the diamagnetic shifts among the sets for each metal. For pyrimidine, chemical shifts are relatively unaffected by nitrogen substituents. Protonation/methylation minimally reduced the measured aromaticity in the $\text{NICS}(1)_{\text{zz}}$, $\text{NICS}(1)_{\pi\text{zz}}$, and paramagnetic shifts by ca. 2 ppm. Double protonation/methylation of pyrimidine has the same effect of reducing the chemical shifts by ca. 2 ppm compared to the single substitution.

In Chapter 4, we concluded that the d^0 metallapyrimidine species (Tc^{VII} , Mo^{VI} , and Nb^{V}) were non-aromatic based on a lack of paramagnetic contribution toward the $\text{NICS}(1)_{\pi\text{zz}}$ chemical shift despite somewhat large negative $\text{NICS}(1)_{\text{zz}}$ values. Substitution at the ring nitrogen atoms does not affect the calculated chemical shifts enough to change our original non-aromatic classification. Protonation/methylation seems to moderately reduce the $\text{NICS}(1)_{\text{zz}}$ values of the Tc^{VII} and Mo^{VI} species, but otherwise does not

appear to have any significant or systematic effect on the d^0 species. It should be noted that the protonated/methylated Tc^{VII} species showed signatures of a +5 metal oxidation state identified by a populated d orbital in the calculated molecular orbitals. A sign of increased aromaticity is observed in the doubly protonated/methylated d^0 complexes due to more negative NICS(1)_{zz} and paramagnetic values, however, the chemical shift values of these systems should be taken with caution due to the severe ring puckering resulting from the double substitution.

Among the set of metal centers studied, substitution has the most dramatic effect on the Tc^V complexes. Protonation reduces the aromaticity by 3.5 – 4.5 ppm, and methylation reduces the aromaticity further by another 2 ppm. Double substitution severely reduces the aromaticity by 15.1 – 22.9 ppm in the NICS(1)_{zz}, NICS(1)_{πzz}, and paramagnetic chemical shifts, and because of the absence of a significant paramagnetic contribution, the doubly substituted Tc^V complexes are judged to be non-aromatic. The significant reduction in aromaticity of the doubly substituted Tc^V complexes is highlighted by the fact that the $d-\delta$ orbital is not occupied, though the system is still has a d^2 metal center. Our previous study implicated the $d-\delta$ orbital as playing an important role in the π orbital conjugation and high degree of aromaticity that was calculated for the d^n species. Finding that aromaticity is destroyed by switching the d orbital occupation and leaving the $d-\delta$ unoccupied reinforces the notion that the $d-\delta$ orbital plays a critical role in metallacycle aromaticity. Additionally, a higher energy isomer (ca. 15 kcal/mol) of doubly protonated Tc^V with one of the pyrazolato ligands turned 90° perpendicular to the other ligand has an occupied $d-\delta$ orbital and a NICS(1)_{πzz} of –19.1 ppm with a paramagnetic shift of –8.0 ppm.

Only small changes are observed in the calculated chemical shift results for the Rh^{V} complexes. Aromaticity is shown to be systematically reduced by substitution, but the largest differences between substituted and unsubstituted values for the $\text{NICS}(1)_{\text{zz}}$, $\text{NICS}(1)_{\text{zz}}$, and paramagnetic values are 7.0, 1.5, and 3.4 ppm, respectively.

The change in NICS values on protonation and methylation seen in Table 5.3 could be the result of changes in geometry as well as changes in the electronic structure. In the process of optimizing the geometries of the substituted metallapyrimidine species, as many as four low energy structures were found, differing primarily in the bonding and orientation of the pyrazolato ligands. Using $[(\text{pz})_2(\text{Tc}^{\text{V}}\text{-pyr-H})]^+$ as an example, the chemical shifts for four structural isomers are compared in Table 5.4. Energetically, the isomers span a range of roughly 18 kcal/mol, but relatively small differences are observed between total chemical shift values. The largest differences between values are $\text{NICS}(1)_{\text{zz}} = 6.5$ ppm, $\text{NICS}(1)_{\text{zz}} = 2.6$ ppm, paramagnetic = 3.6 ppm, and diamagnetic = 0.9 ppm. This indicates that the binding mode of the pyrazolato ligands is not the source of the changes seen in Table 5.3.

As noted in Table 3.2, protonation and methylation change the bond lengths in the pyrimidine rings significantly. These differences in geometry along with perturbations of the electronic structure resulting from protonation and methylation are the primary cause of the changes in the NICS values seen in Table 5.3. To help separate these two effects, Table 5.5 lists the $\text{NICS}(1)_{\text{zz}}$ and $\text{NICS}(1)_{\text{zz}}$ chemical shifts as a function of the geometry and protonation state. Table 5.6 through Table 5.13 give the full NCS analysis and orbital contributions to the $\text{NICS}(1)_{\text{zz}}$ chemical shifts for each species. $\text{NICS}(1)_{\text{zz}}$ chemical shifts are in very good agreement with the $\text{NICS}(1)_{\text{zz}}$ chemical

shifts showing that the valence π orbitals are the major contributors to the NICS(1)_{zz} chemical shift.

By examining protonation at a fixed geometry, one can see the effect of the electronic perturbations on the NICS values. For pyrimidine, protonation reduces the aromaticity slightly at each geometry based on the NICS(1)_{zz} values (< 5 ppm). For the metallacycles, protonation without changing the geometry also produces small but systematic reductions in NICS(1)_{zz} values (< 5 ppm). The exceptions are double protonation of Tc^V and Tc^{VII} at the unprotonated geometry (12 ppm and 7 ppm, respectively), and double protonation of Nb^V at the doubly protonated geometry (8 ppm).

By calculating the NICS(1)_{zz} values of a given protonation state at different geometries, the effect of geometry on the aromaticity can be separated from electronic effects due to changes in protonation. For the pyrimidine series, the geometric perturbations due to protonation are small and the chemical shifts are nearly unaffected. For the metallacycles, the changes are larger and less systematic. In many cases, going from the unprotonated geometry to the singly protonated geometry produces small changes in the NICS(1)_{zz} values (unprotonated Tc^{VII} is an exception). Going to the geometry of the doubly protonated species causes larger changes in the NICS(1)_{zz} values. While the changes are small for Tc^{VII}, the NICS chemical shifts indicate a large increase in the aromaticity of Mo^{VI} and Nb^V. However, as mentioned previously, the geometries of the doubly protonated d⁰ complexes contain severely puckered metallacycle rings and NICS(1) chemical shift interpretations are problematic. Although the geometry changes resulting from protonation appear to increase in the aromaticity for Nb^V, the data in

Table 5.9 show that total paramagnetic contributions are still small or positive at the optimized geometry and the Nb^{V} complexes cannot be classified as aromatic under this analysis.

For the Tc^{V} species, a very significant drop in aromaticity is observed for the geometry change due to double protonation. The M–N bonds elongate by ca. 0.2 Å but the metallacycle ring remains planar. These differences are the result of changes in the electronic structure, as shown in Figure 5.3. In the unprotonated species, the d- δ orbital is occupied and participates in the π bonding of the metallacycle ring. The d- δ orbital along with the delocalized π orbitals contribute –11 ppm to the total paramagnetic term (see Table 5.10). In the doubly protonated species, the d- δ orbital is unoccupied and the occupied d orbital does not interact with the π orbitals of metallacycle ring. This change in d orbital occupation causes the paramagnetic contributions of the remaining π orbitals to be diminished, while slightly enhancing the diamagnetic contributions from the π orbitals. The change in the occupation of the d- δ orbital is due to the geometry since the d- δ orbital is also unoccupied in the unprotonated and singly protonated Tc^{V} species at this geometry. The empty d- δ orbital is available to participate in binding with the pyrazolato ligands, resulting in a change from η^1 to η^2 binding. The net effect of the electronic structure changes that occur upon double protonation of the Tc^{V} complex is a +18 ppm reduction of the paramagnetic contribution to the $\text{NICS}(1)_{\text{zz}}$ value, making the system non-aromatic.

5.4 Summary

The effect of protonation and N-methylation on the aromaticity of a set of 2nd row transition metal bis-pyrazolato-metallapyrimidine complexes was probed using NICS calculations. Two series of substituted metallapyrimidine complexes were examined: a d⁰ series consisting of Tc^{VII}, Mo^{VI}, and Nb^V and a dⁿ series of Nb^V, Tc^V, and Rh^V. Formation of the complexes starts with a tris-pyrazolato organometallic complex and proceeds by way of a two electron oxidative addition where the metal center cleaves the N–N bond of a pyrazolato ligand creating a 6-membered metallapyrimidine ring. The barrier heights for metallapyrimidine formation in both the protonated and methylated species were very similar to the unsubstituted metallacycles. In the d⁰ metal complexes, protonation caused the oxidative addition to be thermodynamically more favorable by ca. 19 – 25 kcal/mol, while in the dⁿ metal complexes the reaction became less favorable by ca. 20 kcal/mol. Methylation was energetically similar to protonation, but was systematically less favorable by up to 5 kcal/mol.

The geometries of the substituted metallapyrimidines showed increased M–N bond lengths for the nitrogen atoms coordinated to the substituent proton or methyl group, while other bond lengths between ring atoms remained relatively unchanged. Double protonation or methylation of the d⁰ species caused the metallacycle ring to pucker by 30° to 50°. In some cases, the substituent groups caused changes in the positioning and binding of the pyrazolato ligands. Geometry differences between protonation and methylation for either single or double substitution were generally small.

Differences in the aromaticity as gauged by the NICS values are the result of changes in geometry and electronic structure upon protonation/methylation.

Protonation without change in geometry caused small systematic reductions in the aromaticity according to the NICS(1)_{zz} chemical shifts. Geometry changes without changing the protonation state had a much more dramatic effect on the chemical shift values. Chemical shift differences between the singly and unsubstituted geometries were small, but tended toward reducing the aromaticity. In the d⁰ complexes, the geometry changes due to double substitution caused the appearance of increased aromaticity over the geometries of single substitution, but the results may be problematic due to a puckered metallacycle ring. In Tc^V, the geometry changes from double substitution lead to a change in the d orbital occupations.

Overall, single protonation reduced the aromaticity of the metallacycles by only a small amount compared to the unsubstituted complexes. The effect of methylation was similar to protonation, slightly reducing the NICS(1)_{zz} chemical shifts by increasing the total paramagnetic contributions compared to protonated species. Double protonation/methylation of the d⁰ complexes appeared to increase the aromaticity as gauged by the NICS(1)_{zz} chemical shifts; however, the severely puckered ring geometries of these species cause the NICS(1) analysis to be problematic. The Tc^V species was strongly affected by double substitution leading to a change in the electronic structure of the system which switched the occupancy of a d-δ orbital for a non-interacting d orbital. This change destroyed the aromaticity by diminishing the paramagnetic contribution to nearly zero, but allowed the pyrazolato ligands to interact with the empty d-δ orbital in an η² manner.

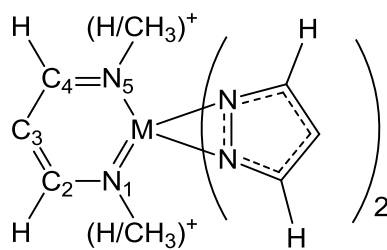


Figure 5.1 Structure and atom numbering of a bis-pyrazolato metallapyrimidine. Singly protonated or methylated species are substituted at N_5 .

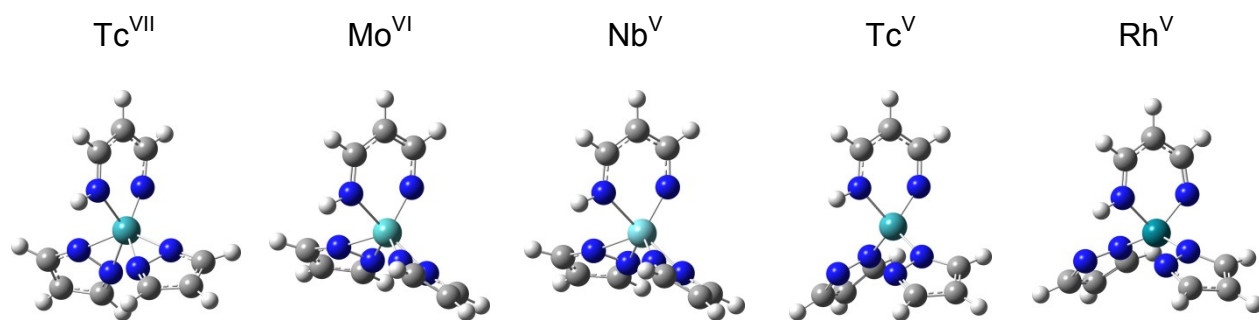


Figure 5.2 Optimized geometries for bis-pyrazolato-metallapyrimidinium species for 2nd row transition metals Tc^{VII} , Mo^{VI} , Nb^{V} , Tc^{V} , and Rh^{V} .

Table 5.1 Optimized Metallapyrimidine Complex Geometries with 0, 1, and 2 Additional Protons or Methyl Groups^a

Complex	M-pz	M-N ₁	N ₁ -C ₂	C ₂ -C ₃	C ₃ -C ₄	C ₄ -N ₅	N ₅ -M
pyrimidine (pyr)		1.338	1.340	1.395	1.395	1.340	1.338
pyrimidinium (pyr-H) ⁺		1.314	1.344	1.403	1.382	1.355	1.357
N-methylpyrimidinium (pyr-Me) ⁺		1.316	1.340	1.401	1.382	1.357	1.359
doubly protonated pyrimidine (pyr-2H) ²⁺		1.337	1.363	1.392	1.392	1.363	1.337
N,N'-dimethylpyrimidine (pyr-2Me) ²⁺		1.341	1.361	1.389	1.389	1.361	1.341
$[(\eta^2\text{-pz})_2(\text{Tc}^{\text{VII}}\text{-pyr})]^{2+}$	1.938/2.019 2.292/2.089	1.757	1.334	1.395	1.431	1.312	1.851
$[(\eta^2\text{-pz})_2(\text{Tc}^{\text{VII}}\text{-pyr-H})]^{3+}$	1.968/2.009 2.101/2.033	1.737	1.332	1.388	1.436	1.319	2.073
$[(\eta^2\text{-pz})_2(\text{Tc}^{\text{VII}}\text{-pyr-Me})]^{3+}$	1.969/2.022 2.113/2.029	1.730	1.330	1.387	1.438	1.319	2.099
$[(\eta^2\text{-pz})_2(\text{Tc}^{\text{VII}}\text{-pyr-2H})]^{4+ \text{ b}}$	1.965/2.017 2.049/2.032	1.998	1.333	1.423	1.441	1.316	2.043
$[(\eta^2\text{-pz})_2(\text{Tc}^{\text{VII}}\text{-pyr-2Me})]^{4+ \text{ c}}$	1.963/1.991 2.056/2.031	2.018	1.339	1.416	1.434	1.320	2.064
$[(\eta^2\text{-pz})_2(\text{Mo}^{\text{VI}}\text{-pyr})]^+$	2.049 2.122	1.764	1.359	1.372	1.446	1.298	1.925
$[(\eta^2\text{-pz})_2(\text{Mo}^{\text{VI}}\text{-pyr-H})]^{2+}$	2.029 2.041	1.754	1.344	1.379	1.426	1.321	2.109
$[(\eta^2\text{-pz})_2(\text{Mo}^{\text{VI}}\text{-pyr-Me})]^{2+}$	2.035 2.043	1.742	1.348	1.373	1.433	1.317	2.139
$[(\eta^2\text{-pz})_2(\text{Mo}^{\text{VI}}\text{-pyr-2H})]^{3+ \text{ d}}$	1.975/1.993 2.047/2.024	1.980	1.344	1.407	1.420	1.330	2.046
$[(\eta^2\text{-pz})_2(\text{Mo}^{\text{VI}}\text{-pyr-2Me})]^{3+ \text{ e}}$	1.967/1.997 2.053/2.040	1.972	1.351	1.401	1.424	1.326	2.062
$[(\eta^2\text{-pz})_2(\text{Nb}^{\text{V}}\text{-pyr})]^0$	2.135 2.223	1.833	1.351	1.379	1.441	1.299	1.979
$[(\eta^2\text{-pz})_2(\text{Nb}^{\text{V}}\text{-pyr-H})]^{1+}$	2.106 2.117	1.821	1.332	1.389	1.412	1.328	2.156
$[(\eta^2\text{-pz})_2(\text{Nb}^{\text{V}}\text{-pyr-Me})]^{1+}$	2.112 2.120	1.809	1.337	1.382	1.419	1.323	2.186
$[(\eta^2\text{-pz})_2(\text{Nb}^{\text{V}}\text{-pyr-2H})]^{2+ \text{ f}}$	2.044/2.081 2.088/2.035	2.027	1.352	1.395	1.413	1.330	2.098
$[(\eta^2\text{-pz})_2(\text{Nb}^{\text{V}}\text{-pyr-2Me})]^{2+ \text{ g}}$	2.033/2.056 2.094/2.097	2.104	1.325	1.420	1.395	1.354	2.016

$[(\eta^1\text{-pz})_2(\text{Tc}^{\text{V}}\text{-pyr})]^0$	1.980 2.856	1.784	1.330	1.403	1.403	1.330	1.784
$[(\eta^1\text{-pz})_2(\text{Tc}^{\text{V}}\text{-pyr-H})]^{1+}$	1.926 2.664	1.761	1.310	1.411	1.387	1.350	1.962
$[(\eta^1/\eta^2\text{-pz})_2(\text{Tc}^{\text{V}}\text{-pyr-Me})]^{1+}$	1.940/2.001 2.888/2.139	1.753	1.326	1.388	1.412	1.328	2.045
$[(\eta^2\text{-pz})_2(\text{Tc}^{\text{V}}\text{-pyr-2H})]^{2+}$	2.010 2.010	1.990	1.336	1.395	1.395	1.336	1.990
$[(\eta^2\text{-pz})_2(\text{Tc}^{\text{V}}\text{-pyr-2Me})]^{2+}$	1.993 2.045	1.980	1.344	1.387	1.398	1.330	2.016
$[(\eta^1\text{-pz})_2(\text{Rh}^{\text{V}}\text{-pyr})]^0$	1.965 2.830	1.880	1.312	1.411	1.411	1.312	1.880
$[(\eta^1\text{-pz})_2(\text{Rh}^{\text{V}}\text{-pyr-H})]^{1+}$	1.934 2.765	1.864	1.310	1.413	1.401	1.318	1.930
$[(\eta^1/\eta^2\text{-pz})_2(\text{Rh}^{\text{V}}\text{-pyr-Me})]^{1+}$	1.940/1.969 2.882/2.256	1.873	1.318	1.399	1.410	1.313	1.981
$[(\eta^2\text{-pz})_2(\text{Rh}^{\text{V}}\text{-pyr-2H})]^{2+}$	1.991 2.127	1.960	1.320	1.407	1.407	1.320	1.960
$[(\eta^2\text{-pz})_2(\text{Rh}^{\text{V}}\text{-pyr-2Me})]^{2+}$	2.010 2.128	1.985	1.321	1.403	1.403	1.321	1.985

^a The first proton/methyl adds at the N₅ position. Metallacycle ring is severely puckered with a M–N₅–N₁–C₃ dihedral of: ^b 152.0°, ^c 142.6°, ^d 141.8°, ^e 134.0°, ^f 140.8°, and ^g 129.9°.

Table 5.2 Relative Free-Energy Differences in kcal/mol for Oxidative Addition of a Metal to a Pyrazolato Ligand to Form a Metallacycle Complex from a Tris-pyrazolato Complex^a

	TS	$[(pz)_2(M-pyr)]$
Tc ^{VII} (d ⁰)	+26.6	+18.3
Mo ^{VI} (d ⁰)	+24.7	−8.3
Nb ^V (d ⁰)	+19.4	−31.8
Tc ^V (d ²)	+24.6	−35.7
Rh ^V (d ⁴)	+51.2	+6.9
	TS	$[(pz)_2(M-pyr-H)]$
Tc ^{VII} (d ⁰)	+28.3	−5.0
Mo ^{VI} (d ⁰)	+24.9	−27.5
Nb ^V (d ⁰)	+16.0	−56.8
Tc ^V (d ²)		−16.2
Rh ^V (d ⁴)	+58.6	+21.7
	TS	$[(pz)_2(M-pyr-Me)]$
Tc ^{VII} (d ⁰)	+29.6	−0.9
Mo ^{VI} (d ⁰)	+26.0	−22.7
Nb ^V (d ⁰)	+19.5	−52.0
Tc ^V (d ²)		−12.9
Rh ^V (d ⁴)	+59.4	+22.3

^a All energies are relative to the M-pz₃ complex for each species.

Table 5.3 Chemical Shift Totals for Non, Singly, and Doubly Protonated and Methylated Pyrimidine and Metallacycles Species

	NICS(1) _{zz}	NICS(1) _{ttzz}	Paramagnetic	Diamagnetic
pyr	-26.9	-27.2	-13.7	-13.5
(pyr-H) ⁺	-24.9	-25.1	-11.4	-13.7
(pyr-Me) ⁺	-25.0	-25.5	-11.7	-13.8
(pyr-2H) ²⁺	-23.5	-23.4	-9.6	-13.8
(pyr-2Me) ²⁺	-23.7	-24.8	-10.8	-14.0
[(pz) ₂ (Tc ^{VII} -pyr)] ²⁺	-19.7	-14.0	+0.5	-14.5
[(pz) ₂ (Tc ^{VII} -pyr-H)] ^{3+ a}	-12.5	-10.5	+3.5	-14.0
[(pz) ₂ (Tc ^{VII} -pyr-Me)] ^{3+ a}	-10.5	-4.3	+5.3	-9.6
[(pz) ₂ (Tc ^{VII} -pyr-2H)] ⁴⁺	-14.0			
[(pz) ₂ (Tc ^{VII} -pyr-2Me)] ⁴⁺	-14.5			
[(pz) ₂ (Mo ^{VI} -pyr)] ⁺	-14.1	-10.3	+3.7	-14.0
[(pz) ₂ (Mo ^{VI} -pyr-H)] ²⁺	-12.9	-11.8	+1.3	-13.1
[(pz) ₂ (Mo ^{VI} -pyr-Me)] ²⁺	-9.8	-10.0	+3.1	-13.1
[(pz) ₂ (Mo ^{VI} -pyr-2H)] ³⁺	-20.2			
[(pz) ₂ (Mo ^{VI} -pyr-2Me)] ³⁺	-20.9	-17.0	-4.8	-12.2
[(pz) ₂ (Nb ^V -pyr)]	-8.8	-6.8	+5.2	-12.0
[(pz) ₂ (Nb ^V -pyr-H)] ⁺	-10.0	-9.8	+1.8	-11.6
[(pz) ₂ (Nb ^V -pyr-Me)] ⁺	-7.6	-8.4	+3.4	-11.8
[(pz) ₂ (Nb ^V -pyr-2H)] ²⁺	-10.0	-13.9	-4.0	-9.9
[(pz) ₂ (Nb ^V -pyr-2Me)] ²⁺	-20.3	-15.8	-4.7	-11.1
[(pz) ₂ (Tc ^V -pyr)]	-36.0	-30.2	-19.5	-10.7
[(pz) ₂ (Tc ^V -pyr-H)] ⁺	-30.5	-26.7	-15.4	-11.3
[(pz) ₂ (Tc ^V -pyr-Me)] ⁺	-24.4	-24.3	-12.8	-11.5
[(pz) ₂ (Tc ^V -pyr-2H)] ²⁺	-13.1	-15.1	-1.3	-13.8
[(pz) ₂ (Tc ^V -pyr-2Me)] ²⁺	-12.4	-14.2	-1.7	-12.5
[(pz) ₂ (Rh ^V -pyr)]	-22.4	-20.1	-10.5	-9.6
[(pz) ₂ (Rh ^V -pyr-H)] ⁺	-20.1	-19.5	-9.2	-10.3
[(pz) ₂ (Rh ^V -pyr-Me)] ⁺	-17.1	-18.6	-7.6	-11.0
[(pz) ₂ (Rh ^V -pyr-2H)] ²⁺	-15.4	-19.1	-8.0	-11.1
[(pz) ₂ (Rh ^V -pyr-2Me)] ²⁺	-15.7	-18.6	-7.1	-11.5

^a Molecular orbital analysis indicates a +5 metal oxidation state.

Table 5.4 Comparison of the NICS(1)_{zz} and NICS(1)_{πzz} Chemical Shifts for Four Structural Isomers of [pz₂-Tc^V-pyr-H⁺]⁺

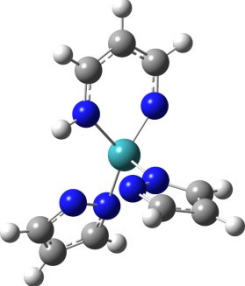
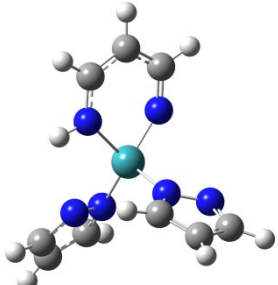
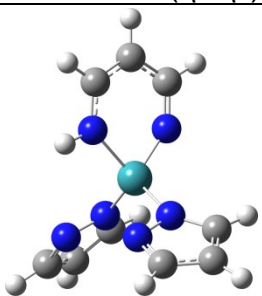
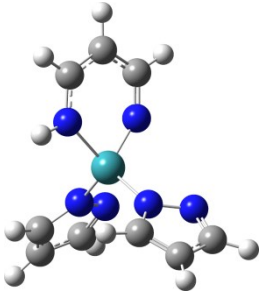
Structure 1 (η^1/η^2)	NICS(1) _{zz} = -24.6		relative energy = 0.00 kcal/mol	
	Orbital	Total	Para.	Dia.
	C-NH π	-6.5	-2.8	-3.8
	Tc-N π	-6.2	-2.7	-3.5
	C-C π	-6.8	-3.0	-3.8
	Tc-δ	-4.6	-4.0	-0.6
	Sum π	-24.1	-12.4	-11.6
Structure 2 (η^1/η^2)	NICS(1) _{zz} = -27.8		relative energy = 0.43 kcal/mol	
	Orbital	Total	Para.	Dia.
	C-NH π	-7.2	-3.6	-3.7
	Tc-N π	-7.0	-3.7	-3.2
	C-C π	-7.7	-4.0	-3.8
	Tc-δ	-4.6	-4.0	-0.6
	Sum π	-26.6	-15.3	-11.3
Structure 3 (η^1/η^1)	NICS(1) _{zz} = -30.5		relative energy = 5.48 kcal/mol	
	Orbital	Total	Para.	Dia.
	C-N π	-6.8	-2.4	-4.3
	C-C π	-18.4	-14.7	-3.7
	Tc-NH π	+1.6	+3.9	-2.3
	Tc-δ	-3.1	-2.2	-0.9
	Sum π	-26.7	-15.4	-11.3
Structure 4 (η^1/η^1)	NICS(1) _{zz} = -30.3		relative energy = 18.25 kcal/mol	
	Orbital	Total	Para.	Dia.
	C-N π	-7.4	-3.6	-3.8
	Tc-NH π	-6.5	-4.1	-2.4
	C-C π	-8.1	-4.3	-3.8
	Tc-δ	-4.7	-4.0	-0.7
	Sum π	-26.7	-16.0	-10.7

Table 5.5 Calculated NICS(1)_{zz} and NICS(1)_{πzz} Chemical Shifts for Metallapyrimidine Complexes Containing Nb^V, Tc^V, and Rh^V and Pyrimidine Showing the Charge versus Geometry Effects of Protonation

	NICS(1) _{zz}			NICS(1) _{πzz}		
	0 H ⁺	1 H ⁺	2 H ⁺	0 H ⁺	1 H ⁺	2 H ⁺
Pyrimidine						
Geom. of 0 H ⁺	−26.9	−24.9	−22.9	−27.2	−24.8	−22.4
Geom. of 1 H ⁺	−27.2	−24.9	−23.3	−27.6	−25.1	−23.0
Geom. of 2 H ⁺	−27.3	−25.5	−23.5	−27.9	−25.6	−23.4
Tc ^{VII} d ⁰						
Geom. of 0 H ⁺	−19.7	−15.4	−8.8 ^b	−14.0	−13.3	
Geom. of 1 H ⁺	−12.8	−12.5 ^b	−9.9 ^b	−9.2	−10.5	−7.8
Geom. of 2 H ⁺ ^a	−12.3	−13.6 ^b	−14.0 ^b	−7.5		
Mo ^{VI} d ⁰						
Geom. of 0 H ⁺	−14.1	−11.2	−10.5	−10.3	−9.7	
Geom. of 1 H ⁺	−16.4	−12.9	−12.9	−12.7	−11.9	
Geom. of 2 H ⁺ ^a	−22.5	−20.6	−20.2			
Nb ^V d ⁰						
Geom. of 0 H ⁺	−8.8	−7.3	−6.3	−6.8	−6.3	−6.2
Geom. of 1 H ⁺	−12.5	−10.0	−9.0	−10.8	−9.8	−8.7
Geom. of 2 H ⁺ ^a	−20.5	−17.8	−10.0	−17.9	−13.1	−13.9

Tc^V d²						
Geom. of 0 H ⁺	−36.0	−32.6	−20.4	−30.2	−28.5	−17.8
Geom. of 1 H ⁺	−34.7	−30.5	−29.8	−28.7	−26.7	−26.4
Geom. of 2 H ⁺	−16.1 ^c	−14.6 ^c	−13.1 ^c	−17.9 ^c	−15.9 ^c	−15.1 ^c
Rh^V d⁴						
Geom. of 0 H ⁺	−22.4	−20.9	−16.4	−20.1	−19.3	−15.2
Geom. of 1 H ⁺	−22.0	−20.1	−15.8	−21.2	−19.5	−15.6
Geom. of 2 H ⁺	−17.2	−17.4	−15.4	−15.3	−17.5	−19.1

^a Optimized geometry contains a severely puckered metallapyrimidine ring. ^b Orbital analysis indicates a +5 metal oxidation state. ^c Orbital analysis shows a d² species, however, the d-δ orbital is unoccupied while an in-plane, non-bonding d-orbital is occupied. Only three pi orbital contributions are included in the analysis.

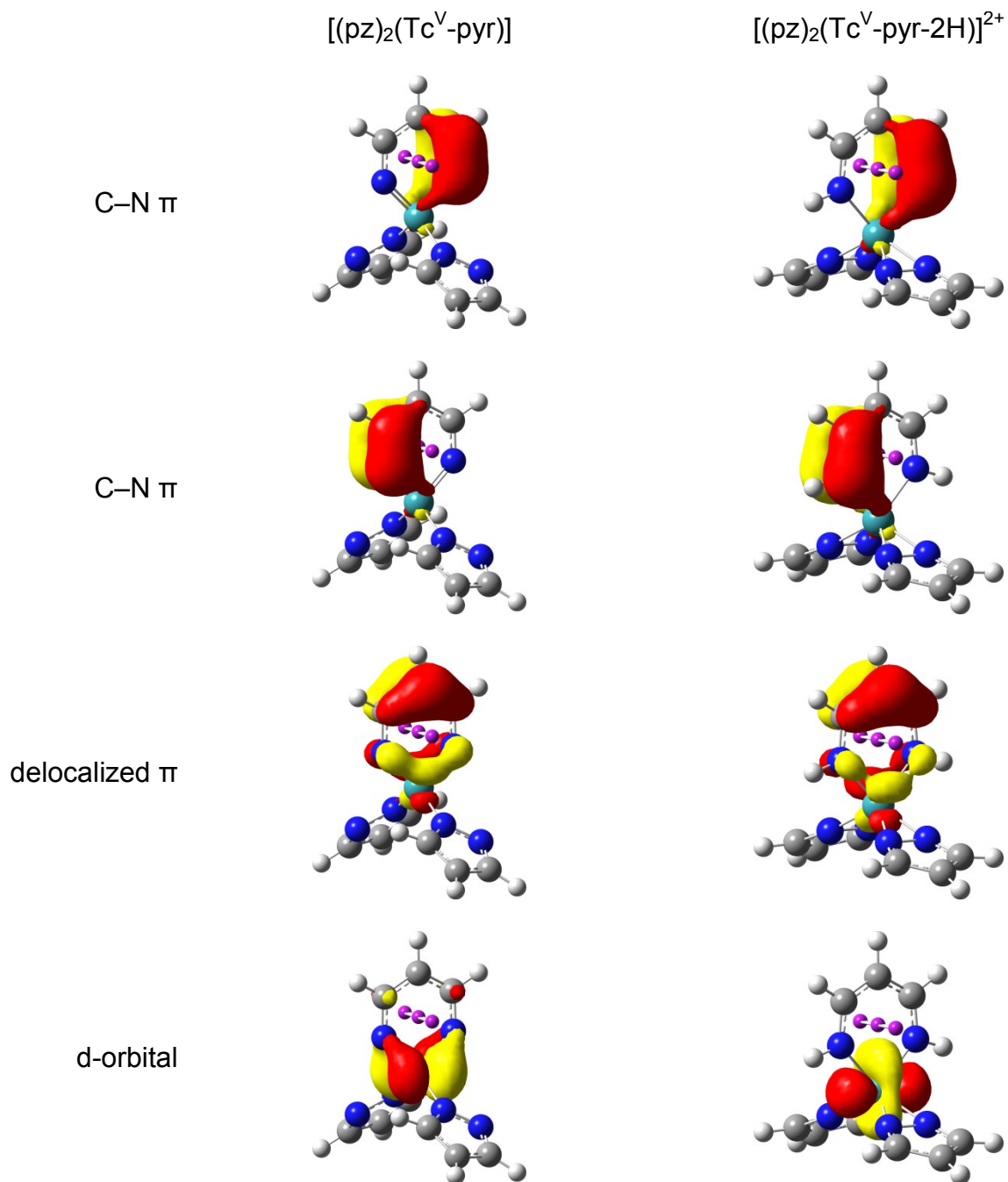


Figure 5.3 Orbital diagrams of the localized valence π orbitals contributing to the NICS(1)_{zz} chemical shift showing the differences in the electronic structure between the unprotonated (left) and doubly protonated (right) Tc^V metallapyrimidine complex. Specific differences are seen in the occupation of the d orbitals, where the d- δ orbital is occupied in the unprotonated species and a non-interacting d orbital is occupied on the right leading to dramatic changes in the calculated aromaticity. (Diagrams have isovalue = 0.05)

Table 5.6 Natural Chemical Shielding Analysis of the π Orbital Contributions to the NICS(1)_{zz} Chemical Shift of Pyrimidine in Structural Combinations of Three Geometries with Three Protonation States

Species	NLMO Description	Total Contribution	Paramagnetic	Diamagnetic
pyr NICS(1) _{zz} = -26.9	C-C π	-9.2	-4.9	-4.3
	C-N π	-9.1	-4.3	-4.8
	C-N π	-8.9	-4.5	-4.4
	NICS(1) _{πzz}	-27.2	-13.7	-13.5
pyr <i>geom of</i> (pyr-H) ⁺ NICS(1) _{zz} = -27.2	C-C π	-9.5	-5.2	-4.3
	C-N π	-9.2	-4.6	-4.6
	C-N π	-8.9	-4.2	-4.7
	NICS(1) _{πzz}	-27.6	-14.0	-13.6
pyr <i>geom of</i> (pyr-2H) ²⁺ NICS(1) _{zz} = -27.3	C-C π	-9.7	-5.3	-4.4
	C-N π	-9.2	-4.6	-4.6
	C-N π	-9.0	-4.5	-4.5
	NICS(1) _{πzz}	-27.9	-14.4	-13.5
(pyr-H) ⁺ <i>geom of</i> pyr NICS(1) _{zz} = -24.9	C-C π	-8.8	-4.3	-4.5
	C-N π	-8.5	-3.4	-5.1
	C-NH π	-7.5	-3.4	-4.1
	NICS(1) _{πzz}	-24.8	-11.4	-13.7
(pyr-H) ⁺ NICS(1) _{zz} = -24.9	C-C π	-8.9	-4.2	-4.7
	C-N π	-8.7	-3.7	-5.0
	C-NH π	-7.5	-3.5	-4.0
	NICS(1) _{πzz}	-25.1	-11.4	-13.7
(pyr-H) ⁺ <i>geom of</i> (pyr-2H) ²⁺ NICS(1) _{zz} = -25.5	C-C π	-9.3	-4.6	-4.7
	C-N π	-8.6	-3.8	-4.8
	C-NH π	-7.7	-3.6	-4.1
	NICS(1) _{πzz}	-25.6	-12.0	-13.6
(pyr-2H) ²⁺ <i>geom of</i> pyr NICS(1) _{zz} = -22.9	C-C π	-8.4	-3.7	-4.7
	C-NH π	-7.1	-2.5	-4.6
	C-NH π	-6.9	-2.5	-4.4
	NICS(1) _{πzz}	-22.4	-8.7	-13.7
(pyr-2H) ²⁺ <i>geom of</i> (pyr-H) ⁺ NICS(1) _{zz} = -23.3	C-C π	-8.7	-4.0	-4.7
	C-NH π	-7.3	-2.7	-4.6
	C-NH π	-7.0	-2.5	-4.5
	NICS(1) _{πzz}	-23.0	-9.2	-13.8
(pyr-2H) ²⁺ NICS(1) _{zz} = -23.5	C-C π	-8.9	-4.0	-4.9
	C-NH π	-7.3	-2.8	-4.5
	C-NH π	-7.2	-2.8	-4.4
	NICS(1) _{πzz}	-23.4	-9.6	-13.8

Table 5.7 Natural Chemical Shielding Analysis of the π Orbital Contributions to the NICS(1)_{zz} Chemical Shift of $[(pz)_2(Tc^{VII}-pyr-nH)]^{(n+2)+}$ ($n = 0, 1, 2$) in Structural Combinations of Three Geometries with Three Protonation States

Species	NLMO Description	Total Contribution	Paramagnetic	Diamagnetic
$[(pz)_2(Tc^{VII}-pyr)]^{2+}$ NICS(1) _{zz} = -19.7	Tc-N π	-4.9	-1.1	-3.8
	C-N π	-5.7	+1.1	-6.8
	C-C π	-3.4	+0.6	-3.9
	NICS(1) _{πzz}	-14.0	+0.5	-14.5
$[(pz)_2(Tc^{VII}-pyr)]^{2+}$ <i>geom of</i> $[(pz)_2(Tc^{VII}-pyr-H)]^{3+}$ NICS(1) _{zz} = -12.8	Tc-N π	-4.4	-0.3	-4.1
	C-N π	-3.6	+1.7	-5.3
	C-C π	-1.3	+2.6	-3.9
	NICS(1) _{πzz}	-9.2	+4.1	-13.3
$[(pz)_2(Tc^{VII}-pyr)]^{2+}$ <i>geom of</i> $[(pz)_2(Tc^{VII}-pyr-2H)]^{4+}$ NICS(1) _{zz} = -12.3	C-N π	-1.8	+3.7	-5.5
	C-N π	-5.7	+1.6	-7.3
	deloc π	+0.0	+0.0	+0.0
	NICS(1) _{πzz}	-7.5	+5.3	-12.8
$[(pz)_2(Tc^{VII}-pyr-H)]^{3+}$ <i>geom of</i> $[(pz)_2(Tc^{VII}-pyr)]^{2+}$ NICS(1) _{zz} = -15.4	Tc-N π	-4.5	-0.8	-3.7
	C-NH π	-5.2	+0.4	-5.6
	C-C π	-3.6	+0.7	-4.3
	NICS(1) _{πzz}	-13.3	+0.3	-13.6
$[(pz)_2(Tc^{VII}-pyr-H)]^{3+}$ ^a NICS(1) _{zz} = -12.5	Tc-N π	-3.9	+0.1	-4.0
	C-NH π	-4.3	+0.8	-5.1
	C-C π	-1.4	+0.7	-2.1
	Tc d - δ	-1.0	+1.9	-2.9
	NICS(1) _{πzz}	-10.5	+3.5	-14.0
$[(pz)_2(Tc^{VII}-pyr-2H)]^{4+}$ ^a <i>geom of</i> $[(pz)_2(Tc^{VII}-pyr-H)]^{3+}$ NICS(1) _{zz} = -9.9	Tc-NH π	-3.3	+1.0	-4.3
	C-NH π	-4.3	+0.8	-5.1
	C-C π	+0.4	+3.5	-1.5
	Tc d - δ	-0.7	+0.8	-1.5
	NICS(1) _{πzz}	-7.8	+6.2	-14.0

^a Molecular orbital analysis indicates a +5 metal oxidation state.

Table 5.8 Natural Chemical Shielding Analysis of the π Orbital Contributions to the NICS(1)_{zz} Chemical Shift of $[(pz)_2(Mo^{VI}\text{-pyr-nH})]^{(n+1)+}$ ($n = 0, 1, 2$) in Structural Combinations of Three Geometries with Three Protonation States

Species	NLMO Description	Total Contribution	Paramagnetic	Diamagnetic
$[(pz)_2(Mo^{VI}\text{-pyr})]^+$ NICS(1) _{zz} = -14.1	Mo-N π	-3.6	+0.3	-3.9
	C-N π	-4.9	+1.7	-6.6
	C-C π	-1.9	+1.7	-3.6
	NICS(1) _{zz}	-10.3	+3.7	-14.0
$[(pz)_2(Mo^{VI}\text{-pyr})]^+$ <i>geom of</i> $[(pz)_2(Mo^{VI}\text{-pyr-H})]^{2+}$ NICS(1) _{zz} = -16.4	Mo-N π	+0.9	+4.5	-3.6
	C-N π	-3.6	+2.6	-6.2
	C-C π	-10.0	-6.5	-3.5
	NICS(1) _{zz}	-12.7	+0.6	-13.3
$[(pz)_2(Mo^{VI}\text{-pyr-H})]^{2+}$ <i>geom of</i> $[(pz)_2(Mo^{VI}\text{-pyr})]^+$ NICS(1) _{zz} = -11.2	Mo-N π	-2.7	+1.1	-3.8
	C-NH π	-4.5	+0.8	-5.3
	C-C π	-2.5	+1.7	-4.2
	NICS(1) _{zz}	-9.7	+3.6	-13.3
$[(pz)_2(Mo^{VI}\text{-pyr-H})]^{2+}$ NICS(1) _{zz} = -12.9	Mo-N π	+2.2	+6.0	-3.8
	C-NH π	-4.4	+0.7	-5.7
	C-C π	-9.7	-5.4	-4.2
	NICS(1) _{zz}	-11.9	+1.3	-13.1

Table 5.9 Natural Chemical Shielding Analysis of the π Orbital Contributions to the NICS(1)_{zz} Chemical Shift of [(pz)₂(Nb^V-pyr-nH)]ⁿ⁺ (n = 0, 1, 2) in Structural Combinations of Three Geometries with Three Protonation States

Species	NLMO Description	Total Contribution	Paramagnetic	Diamagnetic
[(pz) ₂ (Nb ^V -pyr)] NICS(1) _{zz} = -8.8	Nb-N π	-0.8	+2.5	-3.3
	C-N π	-4.6	+1.2	-5.8
	C-C π	-1.4	+1.5	-2.9
	NICS(1) _{zz}	-6.8	+5.2	-12.0
[(pz) ₂ (Nb ^V -pyr)] <i>geom of</i> [(pz) ₂ (Nb ^V -pyr-H)] ⁺ NICS(1) _{zz} = -12.5	Nb-N π	+2.6	+5.8	-3.2
	C-N π	-3.4	+2.1	-5.5
	C-C π	-10.0	-7.1	-2.9
	NICS(1) _{zz}	-10.8	+0.8	-11.6
[(pz) ₂ (Nb ^V -pyr)] <i>geom of</i> [(pz) ₂ (Nb ^V -pyr-2H)] ²⁺ NICS(1) _{zz} = -20.5	C-N π	-8.1	-3.0	-5.1
	C-N π	-6.9	-1.9	-5.0
	deloc π	-2.9	-2.6	-0.3
	NICS(1) _{zz}	-17.9	-7.5	-10.4
[(pz) ₂ (Nb ^V -pyr-H)] ⁺ <i>geom of</i> [(pz) ₂ (Nb ^V -pyr)] NICS(1) _{zz} = -7.3	Nb-N π	-5.8	-0.2	-5.6
	C-NH π	-3.9	+0.7	-4.6
	C-C π	+3.4	+4.9	-1.5
	NICS(1) _{zz}	-6.3	+5.4	-11.7
[(pz) ₂ (Nb ^V -pyr-H)] ⁺ NICS(1) _{zz} = -10.0	Nb-N π	-5.1	+0.4	-5.5
	C-NH π	-3.5	+1.1	-4.6
	C-C π	-1.2	+0.3	-1.5
	NICS(1) _{zz}	-9.8	+1.8	-11.6
[(pz) ₂ (Nb ^V -pyr-H)] ⁺ <i>geom of</i> [(pz) ₂ (Nb ^V -pyr-2H)] ²⁺ NICS(1) _{zz} = -17.8	C-NH π	-5.2	-0.5	-4.7
	C-N π	-5.3	-1.5	-3.8
	deloc π	-2.6	-0.7	-1.9
	NICS(1) _{zz}	-13.1	-2.7	-10.4
[(pz) ₂ (Nb ^V -pyr-2H)] ²⁺ <i>geom of</i> [(pz) ₂ (Nb ^V -pyr)] NICS(1) _{zz} = -6.3	Nb-NH π	-1.1	+2.0	-3.1
	C-NH π	-3.6	+1.3	-4.9
	C-C π	-1.5	+2.4	-3.9
	NICS(1) _{zz}	-6.2	+5.7	-11.9
[(pz) ₂ (Nb ^V -pyr-2H)] ²⁺ <i>geom of</i> [(pz) ₂ (Nb ^V -pyr-H)] ⁺ NICS(1) _{zz} = -9.0	Nb-NH π	-5.0	-0.1	-4.9
	C-NH π	-2.9	+2.0	-4.9
	C-C π	-0.8	+1.4	-2.2
	NICS(1) _{zz}	-8.7	+3.3	-12.0
[(pz) ₂ (Nb ^V -pyr-2H)] ²⁺ NICS(1) _{zz} = -10.0	C-NH π	-5.3	-1.2	-4.1
	C-NH π	-5.9	-1.8	-4.1
	deloc π	-2.7	-1.0	-1.7
	NICS(1) _{zz}	-13.9	-4.0	-9.9

Table 5.10 Natural Chemical Shielding Analysis of the π Orbital Contributions to the NICS(1)_{zz} Chemical Shift of $[(pz)_2(Tc^V\text{-pyr-nH})]^{n+}$ ($n = 0, 1, 2$) in Structural Combinations of Three Geometries with Three Protonation States

Species	NLMO Description	Total Contribution	Paramagnetic	Diamagnetic
$[(pz)_2(Tc^V\text{-pyr})]$ NICS(1) _{zz} = -36.0	C-N π	-9.1	-4.3	-4.8
	C-N π	-9.1	-4.3	-4.8
	deloc π	-7.9	-7.8	-0.1
	Tc $d\text{-}\delta$	-4.1	-3.1	-1.0
	NICS(1) _{πzz}	-30.2	-19.5	-10.7
$[(pz)_2(Tc^V\text{-pyr})]$ <i>geom of</i> $[(pz)_2(Tc^V\text{-pyr-H})]^+$ NICS(1) _{zz} = -34.7	C-N π	-9.1	-4.7	-4.4
	Tc-N π	+2.5	+5.1	-2.6
	C-C π	-19.7	-16.8	-2.9
	Tc $d\text{-}\delta$	-2.4	-1.0	-1.4
	NICS(1) _{πzz}	-28.7	-17.4	-11.3
$(pz)_2(Tc^V\text{-pyr})$ <i>geom of</i> $(pz)_2(Tc^V\text{-pyr-2H})^{2+}$ NICS(1) _{zz} = -16.1 ^a	C-N π	-8.4	-2.0	-6.4
	C-N π	-8.4	-2.0	-6.4
	deloc π	-1.0	-1.1	+0.1
	NICS(1) _{πzz}	-17.9	-5.1	-12.8
$[(pz)_2(Tc^V\text{-pyr-H})]^+$ <i>geom of</i> $[(pz)_2(Tc^V\text{-pyr})]$ NICS(1) _{zz} = -32.6	C-N π	-8.8	-4.3	-4.5
	Tc-NH π	-7.6	-4.8	-2.8
	C-C π	-8.2	-4.9	-3.3
	Tc $d\text{-}\delta$	-3.9	-3.0	-0.9
	NICS(1) _{πzz}	-28.5	-17.0	-11.5
$[(pz)_2(Tc^V\text{-pyr-H})]^+$ NICS(1) _{zz} = -30.5	C-NH π	+1.6	+3.9	-2.3
	Tc-N π	-6.8	-2.4	-4.3
	C-C π	-18.4	-14.7	-3.7
	Tc $d\text{-}\delta$	-3.1	-2.2	-0.9
	NICS(1) _{πzz}	-26.7	-15.4	-11.3
$[(pz)_2(Tc^V\text{-pyr-H})]^+$ <i>geom of</i> $[(pz)_2(Tc^V\text{-pyr-2H})]^{2+}$ NICS(1) _{zz} = -14.6 ^a	C-NH π	-8.0	-2.2	-5.8
	C-N π	-8.0	-1.2	-6.8
	deloc π	-0.0	-0.0	-0.0
	NICS(1) _{πzz}	-15.9	-3.3	-12.6

$[(pz)_2(Tc^V\text{-pyr-2H})]^{2+}$ <i>geom of</i> $[(pz)_2(Tc^V\text{-pyr})]$ $NICS(1)_{zz} = -20.4$	C–NH π	–6.9	–2.8	–4.1
	Tc–NH π	–4.9	–1.4	–3.5
	C–C π	–3.0	+0.8	–3.8
	Tc d - δ	–3.0	–3.2	+0.2
	$NICS(1)_{\pi zz}$	–17.8	–6.6	–11.2
$[(pz)_2(Tc^V\text{-pyr-2H})]^{2+}$ <i>geom of</i> $[(pz)_2(Tc^V\text{-pyr-H})]^+$ $NICS(1)_{zz} = -29.8$	C–NH π	–7.4	–3.4	–4.1
	Tc–NH π	–6.0	–3.6	–2.5
	C–C π	–8.1	–4.2	–3.9
	Tc d - δ	–4.9	–3.9	–1.0
	$NICS(1)_{\pi zz}$	–26.4	–15.0	–11.4
$[(pz)_2(Tc^V\text{-pyr-2H})]^{2+}$ $NICS(1)_{zz} = -13.1^a$	C–NH π	–7.3	–1.2	–6.1
	C–NH π	–7.3	–1.2	–6.1
	deloc π	–0.5	+1.0	–1.5
	$NICS(1)_{\pi zz}$	–15.1	–1.3	–13.8

^a The Tc d - δ orbital is unoccupied, but an in-plane d - xy orbital is occupied and non-contributing.

Table 5.11 Natural Chemical Shielding Analysis of the π Orbital Contributions to the NICS(1)_{zz} Chemical Shift of [(pz)₂(Rh^V-pyr-nH)]ⁿ⁺ (n = 0, 1, 2) in Structural Combinations of Three Geometries with Three Protonation States

Species	NLMO Description	Total Contribution	Paramagnetic	Diamagnetic
[(pz) ₂ (Rh ^V -pyr)] NICS(1) _{zz} = -22.4	C-N π	-7.1	-2.2	-4.9
	C-N π	-7.1	-2.2	-4.9
	deloc π	-4.6	-5.5	+0.9
	Rh d - δ	-1.3	-0.6	-0.7
	NICS(1) _{πzz}	-20.1	-10.5	-9.6
[(pz) ₂ (Rh ^V -pyr)] <i>geom of</i> [(pz) ₂ (Rh ^V -pyr-H)] ⁺ NICS(1) _{zz} = -22.0	C-N π	-9.1	-4.3	-4.8
	C-N π	-7.4	-1.5	-5.9
	deloc π	-3.5	-4.1	+0.6
	Rh d - δ	-1.2	-0.5	-0.7
	NICS(1) _{πzz}	-21.2	-10.4	-10.8
[(pz) ₂ (Rh ^V -pyr)] <i>geom of</i> [(pz) ₂ (Rh ^V -pyr-2H)] ²⁺ NICS(1) _{zz} = -17.2	C-N π	-6.2	-0.0	-6.2
	C-N π	-5.3	-0.4	-4.9
	deloc π	-3.8	-4.6	+0.8
	Rh d - δ ^a	-0.0	-0.0	-0.0
	NICS(1) _{πzz}	-15.3	-5.0	-10.3
[(pz) ₂ (Rh ^V -pyr-H)] ⁺ <i>geom of</i> [(pz) ₂ (Rh ^V -pyr)] NICS(1) _{zz} = -20.9	C-NH π	-5.8	-2.9	-2.9
	C-N π	-6.6	-1.8	-4.8
	deloc π	-4.1	-2.9	-1.2
	Rh d - δ	-2.8	-2.1	-0.7
	NICS(1) _{πzz}	-19.3	-9.7	-9.6
[(pz) ₂ (Rh ^V -pyr-H)] ⁺ NICS(1) _{zz} = -20.1	C-NH π	-5.2	-1.5	-3.7
	C-N π	-8.6	-3.3	-5.3
	deloc π	-3.6	-2.9	-0.7
	Rh d - δ	-2.2	-1.6	-0.6
	NICS(1) _{πzz}	-19.5	-9.2	-10.3
[(pz) ₂ (Rh ^V -pyr-H)] ⁺ <i>geom of</i> [(pz) ₂ (Rh ^V -pyr-2H)] ²⁺ NICS(1) _{zz} = -17.4	C-NH π	-5.9	-1.6	-4.3
	C-N π	-6.0	-0.9	-5.1
	deloc π	-4.3	-3.8	-0.5
	Rh d - δ	-1.3	-0.6	-0.7
	NICS(1) _{πzz}	-17.5	-6.9	-10.6

$[(pz)_2(Rh^V-pyr-2H)]^{2+}$ <i>geom of</i> $[(pz)_2(Rh^V-pyr)]$ $NICS(1)_{zz} = -16.4$	C–NH π	–4.7	–1.6	–3.1
	C–NH π	–4.5	–1.3	–3.2
	deloc π	–3.3	–1.5	–1.8
	Rh d - δ	–2.7	–2.2	–0.5
	$NICS(1)_{\pi zz}$	–15.2	–6.6	–8.6
$[(pz)_2(Rh^V-pyr-2H)]^{2+}$ <i>geom of</i> $[(pz)_2(Rh^V-pyr-H)]^+$ $NICS(1)_{zz} = -15.8$	C–NH π	–6.4	–2.8	–3.6
	C–NH π	–4.1	–0.6	–3.5
	deloc π	–3.0	–1.2	–1.8
	Rh d - δ	–2.1	–1.6	–0.5
	$NICS(1)_{\pi zz}$	–15.6	–6.2	–9.4
$[(pz)_2(Rh^V-pyr-2H)]^{2+}$ $NICS(1)_{zz} = -15.4$	C–NH π	–7.3	–1.4	–5.9
	C–NH π	–6.5	–2.4	–4.1
	deloc π	–3.4	–3.1	–0.3
	Rh d - δ	–1.9	–1.1	–0.8
	$NICS(1)_{\pi zz}$	–19.1	–8.0	–11.1

^a The Rh d - δ orbital was occupied, but was not a contributing orbital in the NCS analysis.

Table 5.12 Natural Chemical Shielding Analysis of the π Orbital Contributions to the NICS(1)_{zz} Chemical Shift of [(pz)₂(M-pyr-Me)] Complexes and N-methylpyrimidine

Species	NLMO Description	Total Contribution	Paramagnetic	Diamagnetic
(pyr-Me) ⁺ NICS(1) _{zz} = -25.0	C-N π	-8.5	-3.5	-5.0
	C-N(CH ₃) π	-8.1	-3.9	-4.1
	C-C π	-8.9	-4.3	-4.6
	NICS(1) _{πzz}	-25.5	-11.7	-13.8
[(pz) ₂ (Tc ^{VII} -pyr-Me)] ³⁺ NICS(1) _{zz} = -10.5	Tc-N π	+1.1	+0.8	-1.8
	C-N(CH ₃) π	-3.8	+1.4	-5.2
	deloc π	-1.0	+0.8	-1.8
	Tc d- δ	-0.6	+2.2	-2.8
	NICS(1) _{πzz}	-4.3	+5.3	-9.6
[(pz) ₂ (Mo ^{VI} -pyr-Me)] ²⁺ NICS(1) _{zz} = -9.8	Mo-N π	-3.4	+0.3	-3.7
	C-N(CH ₃) π	-4.2	+1.2	-5.3
	C-C π	-2.5	+1.6	-4.1
	NICS(1) _{πzz}	-10.0	+3.1	-13.1
[(pz) ₂ (Nb ^V -pyr-Me)] ⁺ NICS(1) _{zz} = -7.6	Nb-N π	-1.5	+1.8	-3.3
	C-N(CH ₃) π	-4.3	+0.6	-4.8
	C-C π	-2.6	+1.0	-3.6
	NICS(1) _{πzz}	-8.4	+3.4	-11.8
[(pz) ₂ (Tc ^V -pyr-Me)] ⁺ NICS(1) _{zz} = -24.4	Tc-N π	-6.1	-2.9	-3.2
	C-N(CH ₃) π	-6.6	-2.6	-4.0
	C-C π	-6.6	-2.9	-3.7
	Tc d- δ	-4.8	-4.3	-0.6
	NICS(1) _{πzz}	-24.2	-12.8	-11.5
[(pz) ₂ (Rh ^V -pyr-Me)] ⁺ NICS(1) _{zz} = -17.1	Rh-N π	-5.2	-2.7	-2.5
	C-N(CH ₃) π	-5.1	-1.0	-4.1
	C-C π	-6.0	-2.2	-3.8
	Rh d- δ	-2.3	-1.8	-0.5
	NICS(1) _{πzz}	-18.6	-7.6	-11.0

Table 5.13 Natural Chemical Shielding Analysis of the π Orbital Contributions to the NICS(1)_{zz} Chemical Shift of [(pz)₂(M-pyr-2Me)] Complexes and N-methylpyrimidine

Species	NLMO Description	Total Contribution	Paramagnetic	Diamagnetic
(pyr-2Me) ²⁺ NICS(1) _{zz} = -23.7	C-N(CH ₃) π	-8.0	-3.4	-4.6
	C-N(CH ₃) π	-8.0	-3.4	-4.6
	C-C π	-8.8	-4.0	-4.8
	NICS(1) _{zz}	-24.8	-11.7	-13.8
[(pz) ₂ (Mo ^{VI} -pyr-2Me)] ³⁺ NICS(1) _{zz} = -20.9	C-N(CH ₃) π	-5.0	+0.1	-5.1
	C-N(CH ₃) π	-6.4	-1.3	-5.1
	deloc π	-5.7	-3.6	-2.0
	NICS(1) _{zz}	-17.0	-4.8	-12.2
[(pz) ₂ (Nb ^V -pyr-2Me)] ²⁺ NICS(1) _{zz} = -20.3	C-N(CH ₃) π	-5.1	-0.9	-4.2
	C-N(CH ₃) π	-6.4	-2.2	-4.2
	deloc π	-4.2	-1.5	-2.7
	NICS(1) _{zz}	-15.8	-4.7	-11.1
[(pz) ₂ (Tc ^V -pyr-2Me)] ²⁺ NICS(1) _{zz} = -12.4	C-N(CH ₃) π	-6.7	-1.1	-5.6
	C-N(CH ₃) π	-7.2	-1.5	-5.7
	deloc π	-0.2	+0.9	-1.1
	NICS(1) _{zz}	-14.2	-1.7	-12.5
[(pz) ₂ (Rh ^V -pyr-2Me)] ²⁺ NICS(1) _{zz} = -15.7	C-N(CH ₃) π	-6.5	-1.7	-4.8
	C-N(CH ₃) π	-7.2	-1.5	-5.7
	deloc π	-3.1	-3.0	-0.1
	Rh d - δ	-1.7	-0.8	-0.9
	NICS(1) _{zz}	-18.5	-7.1	-11.5

5.5 References

1. Perera, T. H.; Lord, R. L.; Heeg, M. J.; Schlegel, H. B.; Winter, C. H.
Metallapyrimidines and Metallapyrimidiniums from Oxidative Addition of
Pyrazolate N-N Bonds to Niobium(III), Niobium(IV), and Tantalum(IV) Metal
Centers and Assessment of Their Aromatic Character. *Organometallics* **2012**, *31*,
5971-5974.
2. Chen, Z. F.; Wannere, C. S.; Corminboeuf, C.; Puchta, R.; Schleyer, P. V.
Nucleus-independent chemical shifts (NICS) as an aromaticity criterion. *Chem.
Rev.* **2005**, *105*, 3842-3888.
3. Psciuk, B. T.; Lord, R. L.; Winter, C. H.; Schlegel, H. B. Can Metallapyrimidines
Be Aromatic? A Computational Study into a New Class of Metallacycles. *J.
Chem. Theory Comput.* **2012**, *8*, 4950-4959.
4. Frisch, M. J.; Trucks, G. W.; Schlegel, H. B.; Scuseria, G. E.; Robb, M. A.;
Cheeseman, J. R.; Scalmani, G.; Barone, V.; Mennucci, B.; Petersson, G. A.;
Nakatsuji, H.; Caricato, M.; Li, X.; Hratchian, H. P.; Izmaylov, A. F.; Bloino, J.;
Zheng, G.; Sonnenberg, J. L.; Liang, W.; Hada, M.; Ehara, M.; Toyota, K.;
Fukuda, R.; Hasegawa, J.; Ishida, M.; Nakajima, T.; Honda, Y.; Kitao, O.; Nakai,
H.; Vreven, T.; Montgomery, J., J. A.; Peralta, J. E.; Ogliaro, F.; Bearpark, M.;
Heyd, J. J.; Brothers, E.; Kudin, K. N.; Staroverov, V. N.; Keith, T.; Kobayashi, R.;
Normand, J.; Raghavachari, K.; Rendell, A.; Burant, J. C.; Iyengar, S. S.; Tomasi,
J.; Cossi, M.; Rega, N.; Millam, J. M.; Klene, M.; Knox, J. E.; Cross, J. B.;
Bakken, V.; Adamo, C.; Jaramillo, J.; Gomperts, R.; Stratmann, R. E.; Yazyev,
O.; Austin, A. J.; Cammi, R.; Pomelli, C.; Ochterski, J. W.; Martin, J. M. L.;

- Morokuma, K.; Zakrzewski, V. G.; Voth, G. A.; Salvador, P.; Dannenberg, J. J.; Dapprich, S.; Parandekar, P. V.; Mayhall, N. J.; Daniels, A. D.; Farkas, O.; Foresman, J. B.; Ortiz, J. V.; Cioslowski, J.; Fox, D. J. *Gaussian Development Version, Revision H.20+*. Wallingford CT, 2010.
5. Vosko, S. H.; Wilk, L.; Nusair, M. Accurate spin-dependent electronic liquid correlation energies for local spin-density calculations - A critical analysis. *Can. J. Phys.* **1980**, *58*, 1200-1211.
 6. Lee, C. T.; Yang, W. T.; Parr, R. G. Development of the Colle-Salvetti correlation energy formulation into a functional of the electron density. *Phys. Rev. B* **1988**, *37*, 785-789.
 7. Becke, A. D. Density functional thermochemistry. III. The role of exact exchange. *J. Chem. Phys.* **1993**, *98*, 5648-5652.
 8. Stephens, P. J.; Devlin, F. J.; Chabalowski, C. F.; Frisch, M. J. Ab initio calculations of vibrational absorptions and circular dichroism spectra using density functional force fields. *J. Phys. Chem.* **1994**, *98*, 11623-11627.
 9. Ditchfield, R.; Hehre, W. J.; Pople, J. A. Self-consistent molecular-orbital methods .9. Extended gaussian-type basis for molecular-orbital studies of organic molecules. *J. Chem. Phys.* **1971**, *54*, 724-728.
 10. Hehre, W. J.; Ditchfield, R.; Pople, J. A. Self-consistent molecular-orbital methods .12. Further extensions of gaussian-type basis sets for use in molecular-orbital studies of organic-molecules. *J. Chem. Phys.* **1972**, *56*, 2257.
 11. Hariharan, P. C.; Pople, J. A. Influence of polarization functions on molecular-orbital hydrogenation energies. *Theor. Chim. Acta* **1973**, *28*, 213-222.

12. Hariharan, P. C.; Pople, J. A. Accuracy of AH equilibrium geometries by single determinant molecular-orbital theory. *Mol. Phys.* **1974**, *27*, 209-214.
13. Gordon, M. S. The isomers of silacyclopropane. *Chem. Phys. Lett.* **1980**, *76*, 163-168.
14. Francl, M. M.; Pietro, W. J.; Hehre, W. J.; Binkley, J. S.; Gordon, M. S.; Defrees, D. J.; Pople, J. A. Self-consistent molecular-orbital methods. 23. A polarization-type basis set for 2nd-row elements. *J. Chem. Phys.* **1982**, *77*, 3654-3665.
15. Kaupp, M.; Schleyer, P. V.; Stoll, H.; Preuss, H. Pseudopotential approaches to Ca, Sr, and Ba hydrides - Why are some alkaline earth MX₂ compounds bent. *J. Chem. Phys.* **1991**, *94*, 1360-1366.
16. Bergner, A.; Dolg, M.; Kuchle, W.; Stoll, H.; Preuss, H. Ab initio energy adjusted pseudopotentials for elements of groups 13-17. *Mol. Phys.* **1993**, *80*, 1431-1441.
17. Dolg, M.; Stoll, H.; Preuss, H.; Pitzer, R. M. Relativistic and correlation effects for element 105 (Hahnium, Ha) - A comparative study of M and MO (M = Nb, Ta, Ha) using energy adjusted ab initio pseudopotentials. *J. Phys. Chem.* **1993**, *97*, 5852-5859.
18. Schlegel, H. B.; McDouall, J. J. In *Computational advances in organic chemistry: molecular structure and reactivity*, Kluwer Academic Publishers: Dordrecht ; Boston, 1991.
19. Bauernschmitt, R.; Ahlrichs, R. Stability analysis for solutions of the closed shell Kohn-Sham equation. *J. Chem. Phys.* **1996**, *104*, 9047-9052.
20. Schlegel, H. B. Optimization of equilibrium geometries and transition structures. *J. Comput. Chem.* **1982**, *3*, 214-218.

21. Fukui, K. The path of chemical reactions - The IRC approach. *Accounts Chem. Res.* **1981**, *14*, 363-368.
22. Foresman, J. B.; Frisch, A.; Gaussian Inc. *Exploring chemistry with electronic structure methods*. 2nd ed.; Gaussian, Inc.: Pittsburgh, PA, 1996.
23. Schleyer, P. V.; Maerker, C.; Dransfeld, A.; Jiao, H. J.; Hommes, N. Nucleus-independent chemical shifts: A simple and efficient aromaticity probe. *J. Am. Chem. Soc.* **1996**, *118*, 6317-6318.
24. Schleyer, P. V.; Jiao, H. J.; Hommes, N.; Malkin, V. G.; Malkina, O. L. An evaluation of the aromaticity of inorganic rings: Refined evidence from magnetic properties. *J. Am. Chem. Soc.* **1997**, *119*, 12669-12670.
25. Fallah-Bagher-Shaidaei, H.; Wannere, C. S.; Corminboeuf, C.; Puchta, R.; Schleyer, P. V. Which NICS aromaticity index for planar pi rings is best? *Org. Lett.* **2006**, *8*, 863-866.
26. Cheeseman, J. R.; Trucks, G. W.; Keith, T. A.; Frisch, M. J. A comparison of models for calculating nuclear magnetic resonance shielding tensors. *J. Chem. Phys.* **1996**, *104*, 5497-5509.

CHAPTER 6

AMBER FORCE FIELD PARAMETERS FOR MODIFIED DNA NUCLEOSIDES AND NATURALLY OCCURRING MODIFIED RNA NUCLEOSIDES

Reproduced with permission from J. Chem. Theory Comput., **2007**, 3, 1464
Copyright 2007, American Chemical Society

Excerpts of this chapter, including equations, figures and tables, also appear in the Ph.D. thesis of
Raviprasad Aduri reproduced with permission

6.1 Introduction

Ribonucleic acids (RNA) play important roles in diverse biological functions including protein synthesis, gene silencing, and in the regulation of gene expression.¹⁻³ RNA is initially synthesized as a phosphodiester polymer of four nucleosides, namely adenosine, guanosine, cytidine, and uridine, which are called the “common” nucleosides. In addition to the four common nucleosides, there are many modified nucleosides found in RNA.⁴ These nucleoside modifications are formed post-transcriptionally. Presently there are at least 107 modifications that have been discovered in natural RNA.⁵⁻⁸ Modified nucleosides are found in almost all tRNAs, ribosomal RNAs of both the small and large subunits of the ribosome, mRNAs, snoRNA, and other functionally important RNA molecules.⁵ Currently, the biological functions of many modifications are unknown, though some roles are beginning to be elucidated.⁹⁻¹¹ The most commonly occurring modification is pseudouridine, in which the C5 of uracil is covalently attached to the sugar C1', resulting in a C–C glycosidic bond instead of the usual C–N glycosidic bond.¹² The next most common modification found in RNA is the methylation of the 2'-O position of the ribose sugar. The lifetimes of base pairs involving certain modified nucleosides are reported to be longer than the

typical Watson-Crick base pairs, making these modifications essential for the viability of extremophiles.⁵

Altered DNA bases that are damaged from high energy photons or reactive oxygen species can lead to reaction pathways resulting in the formation of modified adducts and other mutations.^{13,14} Adducts and mutations to DNA bases are known to lead to cellular death and carcinogenesis.¹⁵ Aromatic fused ring structures such as benzo[a]pyrene or chrysene are oxidized in the liver by cytochrome P450 where an aromatic fused ring diol-epoxide can form.¹⁶ The diol-epoxide group can then react with an exocyclic amino group in a water elimination reaction and intercalate into a DNA helix.¹⁷ These intercalated adducts can lead to carcinogenesis.¹⁸

Owing to the ubiquitous presence of the modified nucleosides in RNA and the dangerous implications of DNA base modifications, it is essential to develop accurate and reliable force field parameters for these modifications that enable the simulation of molecular dynamics of RNA with or without modifications.¹⁹ Stable MD simulations require uniformity in the force field parameter sets for modified nucleosides to be consistent with the present force field for the common nucleosides.

Molecular mechanics (MM) and molecular dynamics (MD) are useful for revealing dynamics and structure of bio-macromolecules thereby elucidating biological function. There are several MM force fields available for performing simulations of biomolecules including CHARMM,²⁰ AMBER,²¹ XPLOR,²² and GROMOS.²³ Armed with an increasing amount of computational resources, researchers have successfully incorporated more accuracy and elegance to force fields including polarizable functions,²⁴ lone pairs, coupled stretching and bending modes, and sophisticated

models of solvation and electrostatics.²⁵ AMBER is one of the most widely used force fields in the simulation of biological molecules possessing the necessary parameters for the common nucleosides and amino acids. AMBER force field parameters have been developed for phosphorothioate nucleic acids²⁶ as well as for various polyphosphates.²⁷ Presently, force field parameters are available²⁸ for modifications found in tRNA^{Phe} and some of the 2' sugar modifications.²⁹ Some groups have reported parameters for a few modifications present in the anticodon stem loop of the tRNA.³⁰⁻³²

An expanding knowledge surrounding the role of RNA in various biological processes and the presence of a large variety of modified nucleosides provide an important demand for the development of force field parameters for modified nucleosides suitable for use with the well-established AMBER force field. The goal of this study was to obtain parameters for 50 modified DNA nucleosides and 107 modified nucleosides found in natural RNA.⁴ The modified force field parameters were developed to be consistent with the Cornell et al. force field³³ of AMBER.

6.2 Parameterization Strategy

The strategic approach used for developing AMBER force field parameters for the modifications in RNA and DNA is summarized in Figure 6.1. The parameterization protocol developed by Cornell et al.³³ was followed to be consistent with the AMBER force field. Despite improvements in computing resources that would have enabled us to perform calculations at higher levels of theory, electronic structure calculations were carried out at the Hartree-Fock level of theory using the 6-31G(d) basis set in

accordance with the Cornell et al. force field. All electronic structure calculations were performed using the GAUSSIAN03 program suite.³⁴

When available, the starting geometries for ab initio calculations were obtained from the PDB database and were otherwise constructed using GaussView. The physiological pH of 7.0 was used in deciding the protonation states of all functional groups, while other protonation states observed at different pH were not considered.³⁵ For a given protonation state, only the lowest energy tautomeric state was considered in this study. Each nucleoside was manually inspected to ensure the proper valence of each heavy atom. All structures were geometry optimized at the HF/6-31G(d) level of theory, and vibrational frequency calculations were used to confirm minimum energy structures. After geometry optimization, the electrostatic potential (ESP) was fit using the electrostatic charge computing method developed by Besler, Merz and Kollman.³⁶ The Merz-Kollman population analysis uses the Connolly algorithm to construct a spherical surface of points around each atomic center and then remove points within a specific proximity to other atom centers thereby creating a molecular surface of points. The points are positioned along spherical shells with radii of 1.4, 1.6, 1.8, and 2.0 times the van der Waals radius of the constituent atoms at a density of one per square Angström.³⁷ Atom-centered partial charges were calculated using the Restrained Electrostatic Potential (RESP) charge fitting methodology developed by Kollman and colleagues.³⁸ RESP uses a Levenberg-Marquardt nonlinear optimization procedure to compute a set of atom-centered point charges that best reproduce the surface charges that were derived quantum mechanically.³⁷ Figure 6.2 shows a schematic diagram summarizing the protocol for generating atom-centered partial charges.

RESP charge fitting was performed in two steps with the ANTECHAMBER module³⁹ of AMBER. During the first stage of the RESP fit, all geometrically equivalent polar atoms were set to have equal charges, as in the case of hydrogen atoms in an amino group or the oxygen atoms in a carboxylate group. Nonpolar atoms that are geometrically equivalent were equivalenced in the second stage of the fit, such as the hydrogen atoms in a methyl group, and the terminal carbon atoms in an isopropyl group. The "equivalencing" feature of the RESP methodology also allows for the ESP of separate quantum calculations to be simultaneously restrained to atom-centered partial charges as if they were a single structure. A modular approach to fitting charges can be established by forcing atom-centered partial charges of different atoms or atomic groups to be equivalent. Cieplak et al.⁴⁰ previously outlined a modular approach for the RESP fitting of nucleic acids achieved by recombining the phosphate, sugar and base moieties using the RESP "equivalencing" of methyl and hydroxyl groups. This strategy greatly reduces the computational burden from electronic structure calculations for each nucleic acid residue. An example of the calculated charges obtained for the nucleobase subunit of common nucleosides adenosine, guanosine, cytosine and uracil are listed in Table 6.1.

Figure 6.3 depicts the RESP modular approach using adenosine as an example. Dimethyl phosphate (DMP) was used as the model system to account for the phosphate charge. Nucleosides with modifications to the base moiety were modeled by replacing the sugar with a methyl group. Conversely, nucleosides with modifications on the sugar moiety were modeled by replacing the base with a methyl group.

The five member ring in the sugar moiety is known to naturally exist in several pucker conformations. Initially, sugar charges were calculated for the C2'-endo and C3'-endo ribose sugar conformations to establish possible differences. Sugar charges were calculated by multi-equivalencing the four natural RNA bases A, G, C, and U with each sugar conformation. The resulting standard deviation of charges comparing C3'-endo versus C2'-endo ribose sugars was 0.0269e, which is less than the systematic error in the RESP methodology. Modified bases could play a role in altering the sugar pucker, but the sugar pucker preferences for the modified nucleosides are not well understood.^{41,42} Separate parameterization of sugar conformers was not performed after the ribose sugar charges were shown to be relatively insensitive changes in conformation. Since only the dominant sugar conformations were used in the initial development of AMBER parameters, we decided to use sugar charges derived from the C3'-endo ribose for RNA residues and C2'-endo ribose for DNA residues. The charges obtained for different types of sugars and conformations are given in Table 6.2.

As mentioned above, the modular nature of nucleotides allowed for restraining the charge of a methyl group to replace either sugar or base moiety during the ab initio calculation. For each modified base, the corresponding total sugar charge was restrained to the charge of the methyl group substituting the sugar moiety. The total charge of the ribose and deoxyribose sugars were calculated to be 0.118186e and 0.090746e, respectively. When fitting the atom centered partial charges of 2'-O-methylribose sugar, the methyl group replacing the base was restrained to the equivalent and opposite charge value obtained for the unmodified ribose sugar of -0.118186e. Another advantage to the modular fitting approach is that it allows for the

portability of parameters to appropriately construct different combinations of bases and sugars. Anticipating the future discovery of new modified bases, this strategy will allow for easier parameterization of other modified nucleic acids.

To confirm that our modular fit reproduces the charges generated on whole nucleosides, we compared the results of a QM calculation on a whole adenosine nucleoside versus an adenine with a methyl replacing the ribose shown in Table 6.3. Charges from the two methods are in good agreement with a standard deviation of 0.0506e for adenosine, suggesting that our modular approach is a faithful way of obtaining the charges for nucleic acids. The largest deviations are observed on internal carbon atoms C8, C6, and C4, which are well known to be difficult to determine accurately.²⁶ Comparing our charges generated for adenosine with the charges reported in PARM99 also shows good agreement with a standard deviation of 0.0362e. Similar agreement was observed for cytidine, guanosine, and uridine. It was not possible to reproduce the charges exactly because the optimized geometry and orientation of the structures used to generate PARM99 were not available.

Figure 3.6 depicts examples of some base modifications.

6.3 Naming Convention

We were unable to find a literature consensus in the naming convention used for the modified nucleosides found in RNA. Consequently, we were compelled to develop a consistent three-letter code indicating the nature of the modification as clearly as possible without conflicting with amino acid or other names. For example, 1MA stands for 1-methyladenosine, 5FC is the code for 5-formylcytidine, and MRX was used to

indicate the presence of a 2'-O-methyl group on the ribose sugar (e.g. MRA, MRP). We verified that the three-letter codes used for modified nucleotides did not interfere with any of the letter codes that were already used in AMBER. Generic names, three-letter codes, and PDB reference codes are given in Table 6.4. A detailed explanation of the naming convention used for the modified nucleosides are given in the original paper.⁴³

6.4 Generating the Parameters

The functional form of the AMBER force field is given in eq (1).

$$E = \sum_{\text{bonds}} K_r (r - r_0)^2 + \sum_{\text{angles}} K_\theta (\theta - \theta_0)^2 + \sum_{\text{dihedrals}} \frac{V_n}{2} [1 + \cos(n\phi)] \\ + \sum_{\text{nonbonded}} 4\epsilon_{ij} \left(\left[\left(\frac{\sigma_{ij}}{r_{ij}} \right)^{12} - \left(\frac{\sigma_{ij}}{r_{ij}} \right)^6 \right] - \left[\frac{q_i q_j}{\epsilon R_{ij}} \right] \right) \quad (1)$$

The total internal energy of a molecule is decomposed into energy components representing bond stretching, angle bending, torsional angle twisting, Lennard-Jones potential, and nonbonded Coulomb electrostatic terms. The present study is focused on developing the atom-centered partial charges necessary to compute the electrostatic term in eq (1). Aside from the atom-centered partial charges, the other force field parameters were referenced to the PARM99 force field.⁴⁴ When a molecular parameter could not be recognized or was incorrectly classified by PARM99, the Generalized Amber Force Field (GAFF)⁴⁵ was referenced to assign correct parameters for the modified nucleosides. GAFF contains atom types for all atoms present in the modified nucleosides studied except selenium.

The modified RNA base 5-methylaminomethyl-2-selenouridine (SEU) contains a selenium atom modification replacing the O2 oxygen. Since there were no existing

parameters in AMBER for selenium, we decided to parameterize the bond force constant, two bond angle force constants, and the polarizability for selenium. The selenium atom was given a mass of 79.92 amu and a polarizability of 3.800 \AA^3 . The Lennard-Jones parameters were set to 2.10 and 0.29 for the 12 and 6 term coefficients, respectively. The calculated harmonic force constant for the carbon-selenium bond was $303.20 \text{ kcal/mol/\AA}^2$ with an equilibrium bond length of 1.812 \AA . The harmonic force constant for each of the selenium-carbon-nitrogen bond angles was $65.7 \text{ kcal/mol/radian}^2$ with an equilibrium angle of 123.88° for each.

6.5 Electrostatic Potential Calculations

The optimized geometry of a given molecule may differ slightly based on the QM program used due to differences in convergence criteria and thus alter charge values. It is well known that the atomic charges derived from a grid of electrostatic potentials computed by quantum mechanical calculations depend slightly on the rotational orientation of the molecule.⁴⁶ This effect is a result of using a finite grid of point charges to model the electrostatic potential.

The multi-orientation charge fitting technique can be used to overcome charge differences due to the geometrical orientation of the molecule. Multi-orientation charge fitting reduces the round-off errors in calculated atomic charges by sampling multiple different orientations of the molecule. Using the RNA nucleoside pseudouridine (PSU) as a model system and the R.E.D. II code,⁴⁷ we did not observe significant changes between the optimized charges using 4, 8, 12, and 20 different orientations (Table 6.5). Due to the relatively insignificant standard deviation in charge values resulting from

orientation effects (ca. 0.016e), we decided not to perform multi-orientation charge fitting on the modified nucleosides.

In an effort to overcome possible multi-orientation effects on the charges, we decided to study the effects of increasing the population grid size and density for calculating the electrostatic potential. Different grid sizes were tested with the Merz-Kollman³⁶ as well as the Chelp-G⁴⁸ population analysis methods (Table 6.6). Using thymine as a model system, no significant changes in charge values were observed as the number of shells or the density of ESP points were increased using either Merz-Kollman or Chelp-G charge fitting methodology. Additionally, the more accurate Chelp-G population analysis also showed no significant deviations from the Merz-Kollman fitted charges. After observing insignificant deviations in charge values resulting from different population analysis schemes, we concluded that the standard Merz-Kollman population analysis was sufficient to produce the atom-centered partial charges for the modified nucleosides.

6.6 Testing the Parameters

Parameters were only developed for internal nucleic acid residues and not for residues occurring at the 5' or 3' termini. Once the parameters for the modified nucleosides were computed, they were incorporated into AMBER to test the stability of MD trajectories of RNA with modified nucleotides. A molecular dynamics simulation of yeast tRNA^{Phe} containing 14 different modifications⁴⁹ was carried out using the crystal structure 1EHZ.pdb for the starting coordinates. The LEAP interface of AMBER was used to successfully implement the parameters of the modified nucleosides. SANDER²¹

was used to do the energy minimization and molecular dynamics with two different methods: (a) use of implicit solvent with generalized-Born electrostatics⁵⁰ and (b) use of explicit solvent with particle-mesh Ewald electrostatics.^{51,52} We also conducted an MD study of the tRNA^{Phe} without modifications to test for any significant role the modifications may have in the stability and functioning of tRNA^{Phe}. To build the unmodified version of tRNA^{Phe}, the modified nucleosides were replaced with their respective common nucleosides (e.g., DHU with uridine). We performed 1 ns generalized-Born simulations on both the modified as well as the unmodified tRNA^{Phe}. The modified tRNA^{Phe} structure remains stable throughout a 1 ns simulation using generalized-Born implicit solvent dynamics (data not shown), validating that the parameters developed can be reliably used in AMBER for simulations.

With the availability of the geometries for these modified nucleosides, we were able to model all 12 known modifications in *E. coli* 16S rRNA into *T. thermophilus* 30S ribosome crystal structure (1J5E). Interestingly, all of the modifications were accommodated in the published PDB structure without any steric conflicts. The location of the modifications suggests they may play a functional role in stabilizing the RNA enabling the binding of a protein as seen in Figure 6.5.

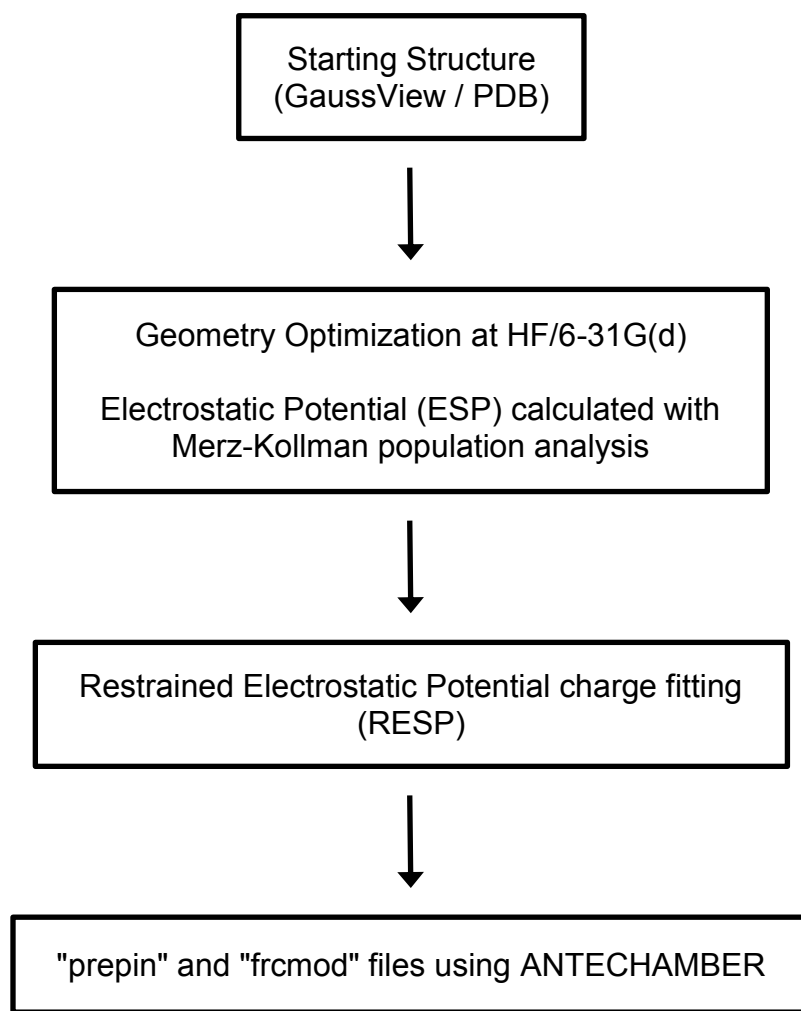


Figure 6.1 Flowchart of the protocol used in generating the parameters for the modified nucleotides.

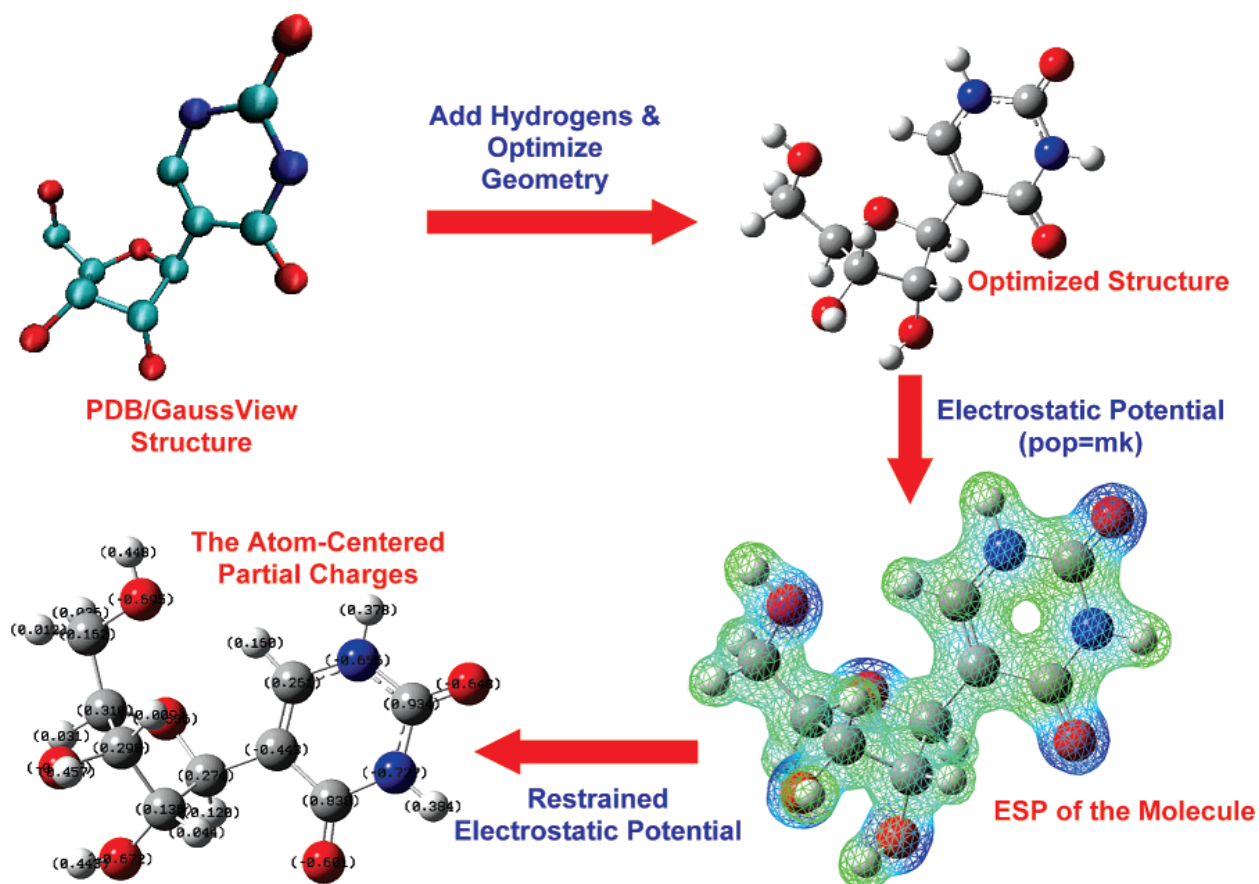


Figure 6.2 Protocol for the determination of atom-centered partial charges. The starting structures were obtained either from a PDB file or created using GaussView. Hydrogen atoms were added using GaussView. Geometry optimization was done using Gaussian03. The electrostatic potential was computed using Merz-Kollman population analysis, and charges were produced by fitting the ESP using RESP as explained in the text.

Table 6.1 Charge Values Obtained for the Nucleobase Subunit of Common Nucleosides Adenine, Guanine, Cytosine, and Uridine

Adenosine		Guanosine		Cytidine		Uridine	
N9	0.0172	N9	0.0268	N1	-0.2152	N1	0.1110
C8	0.1299	C8	0.1066	C2	0.8867	C2	0.4539
N7	-0.5850	N7	-0.5575	O2	-0.6560	O2	-0.5407
C6	0.7111	C6	0.5316	N3	-0.8128	N3	-0.3681
N6	-0.9386	O6	-0.5483	C4	0.9020	C4	0.6022
C5	0.0586	C5	0.1513	N4	-0.9919	O4	-0.5652
C4	0.3050	C4	0.1563	C5	-0.5972	C5	-0.3135
N3	-0.6835	N3	-0.5959	C6	0.1262	C6	-0.2320
C2	0.5741	C2	0.7191	H5	0.2023	H5	0.1697
N1	-0.7536	N2	-0.9044	H6	0.1875	H6	0.2557
H8	0.1749	N1	-0.5287	NH1	0.4251	H3	0.3087
H2	0.0467	H8	0.1767	NH2	0.4251		
HN1	0.4125	HN1	0.3968				
HN2	0.4125	HN2	0.3968				
		H1	0.3546				

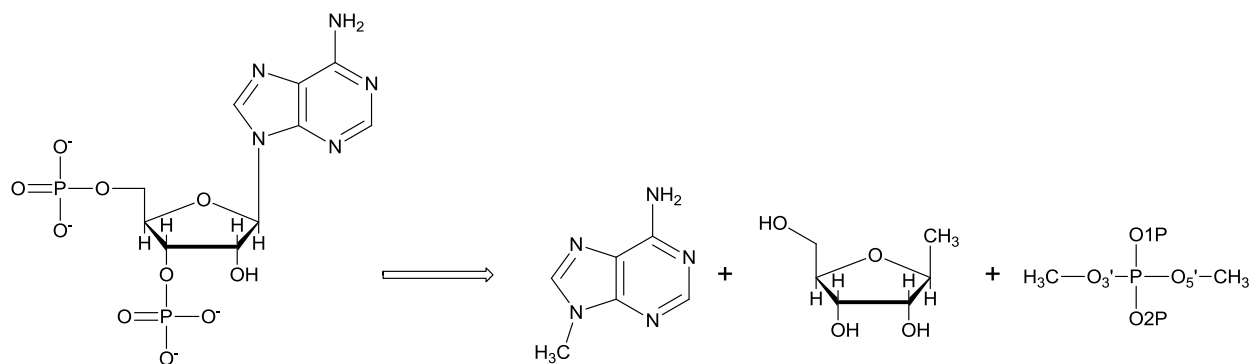


Figure 6.3 The charge fitting method used to generate the charges for the common nucleosides A, G, C, and U, using the modular nature of RNA to reduce the computational time. The charges for O1P, O2P, O3', O5', and P were obtained by using dimethyl phosphate (DMP) as a model system.

Table 6.2 Charge Values Obtained for the Three Common Sugars in RNA, C3'-endo, C2'-endo, and 2'-O-methylribose Sugars

Atom name	C3'-endo ribose	C2'-endo ribose	C2'-endo 2'-O-methylribose	C2'-endo deoxyribose
P	1.0878	1.0825	1.0878	1.0915
O1P	-0.7667	-0.7655	-0.7667	-0.7674
O2P	-0.7667	-0.7655	-0.7667	-0.7674
O5'	-0.4713	-0.5036	-0.4725	-0.4555
C5'	0.0635	0.0292	0.1289	0.0488
C4'	0.0386	0.0625	0.1522	0.0814
O4'	-0.3272	-0.3851	-0.4652	-0.3836
C3'	0.2125	0.2165	0.0675	0.2128
O3'	-0.4890	-0.4649	-0.4878	-0.4978
C2'	0.0775	0.1064	0.0405	-0.0907
O2'	-0.5913	-0.6198	-0.3277	N/A
C1'	0.0460	0.1096	0.3686	0.0765
H5'	0.0689	0.0823	0.0426	0.0711
H5''	0.0689	0.0823	0.0426	0.0711
H4'	0.1168	0.1215	0.0394	0.0766
H3'	0.0825	0.0858	0.1460	0.0536
H2'1	0.0929	0.0659	0.0904	0.0615
H2'2	N/A	N/A	N/A	0.0615
H1'	0.0904	0.1462	0.0417	0.1487
HO2'	0.4101	0.4210	N/A	N/A
CM2	N/A	N/A	-0.0385	N/A
HM'1	N/A	N/A	0.0651	N/A
HM'2	N/A	N/A	0.0651	N/A
HM'3	N/A	N/A	0.0651	N/A

Table 6.3 Comparison of Adenosine Charges Computed in This Work with the Charges Available in PARM99 of AMBER

Atom name	Adenosine Nucleoside	Adenosine PARM99	Adenosine Modular Fit
N9	0.0172	−0.0251	−0.0503
C8	0.1299	0.2006	0.1060
C7	−0.5850	−0.6073	−0.5725
C6	0.7111	0.7009	0.6394
N6	−0.9386	−0.9019	−0.8963
C5	0.0586	0.0515	0.0553
C4	0.3050	0.3053	0.4499
N3	−0.6835	−0.7615	−0.7282
C2	0.5741	0.5875	0.5587
N1	−0.7536	−0.6997	−0.7354
H8	0.1749	0.1553	0.1734
H2	0.0467	0.0473	0.0579
HN1	0.4125	0.4115	0.4122
HN2	0.4125	0.4115	0.4122
SD (PARM99)	0.0362	N/A	0.0529
SD (Nucleoside)	N/A	0.0362	0.0506

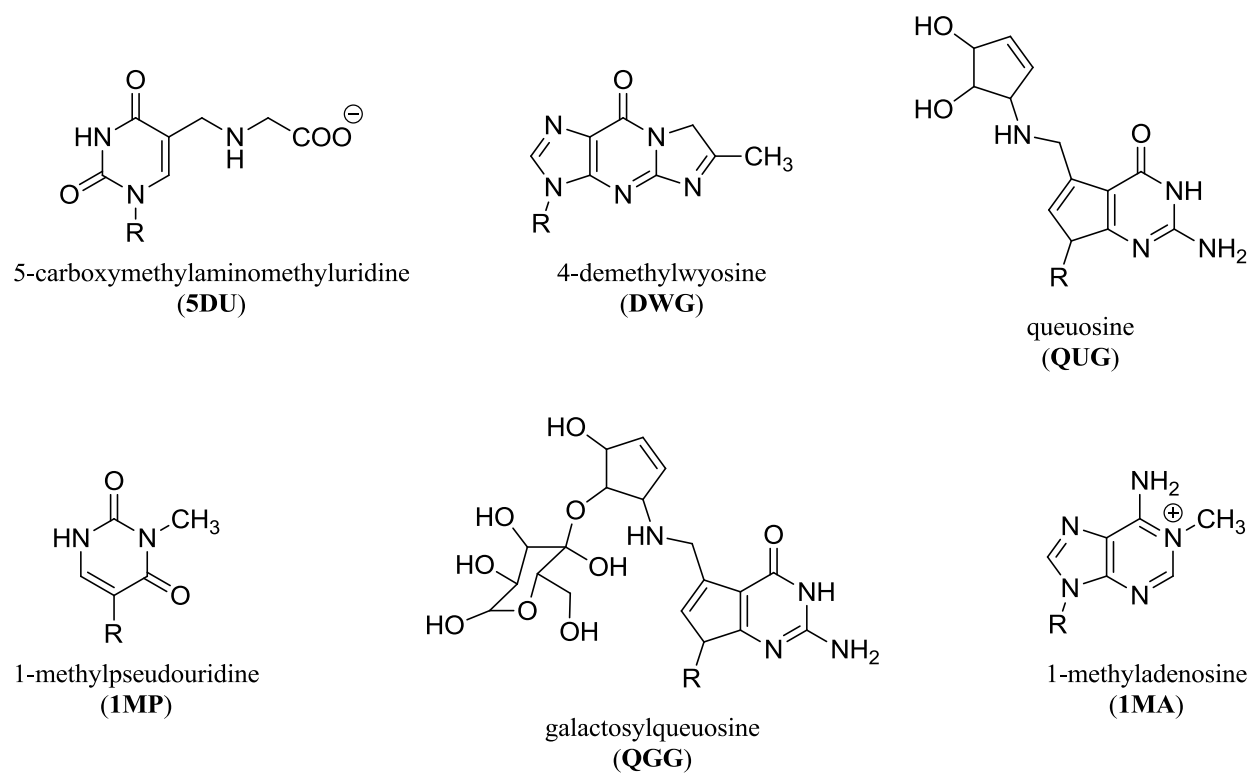


Figure 6.4 Examples of modified nucleosides present in RNA. These modifications range from simple methylation, as in the case of 1MA, to more complex carbohydrate containing compounds such as QGG. Only the hydrogen atoms on the polar atoms are shown for clarity. In each case, the only lowest energy tautomer was considered for the protonation that exists at physiological pH.

Table 6.4 Generic Names, Three-Letter Codes, Common Names, and PDB Source Information for All Parameterized DNA and RNA Nucleosides

<i>RNA Modifications</i>			
3-letter code	Name	Common Name/ Alternate Codes	Source ^a
1MA	1-methyladenosine		1EHZ
26A	2-methylthio-N ⁶ -hydroxynorvalyl carbamoyl-adenosine		
2MA	2-methyladenosine		1EFW
2RA	2'-O-ribosylphosphate adenosine		1YFZ
66A	N ⁶ -methyl-N ⁶ -threonylcarbamoyl-adenosine		
6AA	N ⁶ -acetyl-adenosine		
6GA	N ⁶ -glycylcarbamoyl-adenosine		
6IA	N ⁶ -isopentenyl-adenosine		
6MA	N ⁶ -methyl-adenosine		
6TA	N ⁶ -threonylcarbamoyl-adenosine		
DMA	N ⁶ ,N ⁶ -dimethyl-adenosine	M2A	
HIA	N ⁶ -(cis-hydroxyisopentenyl)-adenosine		
HNA	N ⁶ -hydroxynorvalylcarbamoyl-adenosine		
M2A	1,2'-O-dimethyl-adenosine		
MMA	N ⁶ ,2'-O-dimethyl-adenosine		
MRA	2'-O-methyl-adenosine	A2M	
MTA	N ⁶ ,N ⁶ ,2'-O-trimethyl-adenosine		
SIA	2-methylthio-N ⁶ -(cis-hydroxyisopentenyl)-adenosine		
SMA	2-methylthio-N ⁶ -methyl-adenosine		
SPA	2-methylthio-N ⁶ -isopentenyl-adenosine	MIA	1B23
STA	2-methylthio-N ⁶ -threonylcarbamoyl-adenosine	12A	1FIR
2SC	2-thiocytidine		
3MC	3-methylcytidine		3MCT
4AC	N ⁴ -acetylcytidine		
4MC	N ⁴ -methylcytidine		
5FC	5-formylcytidine		

5MC	5-methylcytidine		1EHZ
HMC	5-hydroxymethylcytidine		
K2C	lysidine		
MAC	N ⁴ -acetyl-2'-O-methylcytidine		
MFC	5-formyl-2'-O-methylcytidine		
MMC	5,2'-O-dimethylcytidine		
MRC	2'-O-methylcytidine	OMC	1EHZ
M4C	N ⁴ ,2'-O-dimethylcytidine		
MTC	N ⁴ ,N ⁴ ,2'-O-trimethylcytidine		
1MG	1-methylguanosine		2ASY
27G	N ² ,7-dimethylguanosine		
2MG	N ² -methylguanosine		1EHZ
2RG	2'-O-ribosylphosphate guanosine		
7MG	7-methylguanosine	G7M	1EHZ
BUG	under modified hydroxywybutosine	UBG	
DAG	7-aminomethyl-7-deazaguanosine		1EFZ
DCG	7-cyano-7-deazaguanosine		
DMG	N ² ,N ² -dimethylguanosine	M2G	1EHZ
DWG	4-demethylwyosine		
EQG	epoxyqueuosine		
HWG	hydroxywybutosine		
IWG	isowyosine		
M7G	N ² ,7,2'-O-trimethylguanosine		
MMG	N ² ,2'-O-dimethylguanosine		
M1G	1,2'-O-dimethylguanosine		
MRG	2'-O-methylguanosine	OMG	1EHZ
MTG	N ² ,N ² ,2'-O-trimethylguanosine		
N2G	N ² ,N ² ,7-trimethylguanosine		
PBG	peroxywybutosine		
QGG	galactosyl-queuosine		
QMG	mannosyl-queuosine		
QUG	queuosine	QUO	
RCG	archaeosine		
WBG	wybutosine	YG	1EHZ
WMG	methylwyosine		
WYG	wyosine		
2SU	2-thiouridine	SUR	
3AU	3-(3-amino-3-carboxypropyl)uridine		
3MU	3-methyluridine		

4SU	4-thiouridine	S4U	1B23
52U	5-methyl-2-thiouridine		
5AU	5-methylaminomethyluridine		
5CU	5-carboxymethyluridine		
5DU	5-carboxymethylaminomethyluridine		
5HU	5-hydroxyuridine		
5MU	5-methyluridine		1EHZ
5TU	5-taurinomethyluridine		
BCU	5-carbamoylmethyluridine		
CMU	5-(carboxyhydroxymethyl)uridine methyl ester		
DHU	dihydrouridine	H2U	1EHZ
DMU	5-methyldihydrouridine		
ESU	5-methylaminomethyl-2-thiouridine		
HCU	5-(carboxyhydroxymethyl)uridine		
IAU	5-(isopentenylaminomethyl)uridine		
ISU	5-(isopentenylaminomethyl)-2-thiouridine		
M3U	3,2'-O-dimethyluridine		
MAU	5-carboxymethylaminomethyl-2'-O-methyluridine		
MCU	5-carbamoylmethyl-2'-O-methyluridine		
MEU	5-methoxycarbonylmethyl-2'-O-methyluridine		
MIU	5-(isopentenylaminomethyl)-2'-O-methyluridine		
MMU	5,2'-O-dimethyluridine	2MU	1FIR
MRU	2'-O-methyluridine		
MSU	2-thio-2'-O-methyluridine		
OAU	uridine 5-oxyacetic acid		
OCU	5-methoxycarbonylmethyluridine		
OEU	uridine 5-oxyacetic acid methyl ester		
OMU	5-methoxyuridine		
SAU	5-aminomethyl-2-thiouridine		
SCU	5-carboxymethylaminomethyl-2-thiouridine		
SEU	5-methylaminomethyl-2-selenouridine		
SMU	5-methoxycarbonylmethyl-2-thiouridine		
STU	5-taurinomethyl-2-thiouridine		
PSU	pseudouridine		1EHZ

13P	1-methyl-3-(3-amino-3-carboxypropyl)pseudouridine		
1MP	1-methylpseudouridine		
3MP	3-methylpseudouridine		
MRP	2'-O-methylpseudouridine		
INO	inosine		
1MI	1-methylinosine		
MMI	1,2'-O-dimethylinosine		
MRI	2'-O-methylinosine		

DNA Modifications

3-letter code	Name	Common Name/ Alternate Codes	Source
2EG	1,N2-etheno-dG		
2FG	8-(2-aminofluorene)-dG		
2PG	1,N2-propano-dG		
3EA	3-ethyl-dA		
3EC	3,N4-etheno-dC		
3MA	3-methyl-dA		
4ET	O4-ethyl-dT		
4MT	O4-methyl-dT		
5CC	5-methyl-dC		
5FU	5-fluoro-dU		
5GC	5,6-dihydroxy-5-methyl-dC		
5HC	5-hydroxymethyl-dC		
6EA	1,N6-etheno-dA		
6EG	O6-ethyl-dG		
6MG	O6-methyl-dG		
6TG	6-thio-dG		
8HG	8-hydroxy-dG		
8OG	8-oxo-dG		
ACG	8-(1,2-dihydrodiol-6-aminochrysene)-dG		
AFG	8-(N-acetyl-2-aminofluorene)-dG		
ATG	7-(aflatoxin-B1)-dG	Aflatoxin-B1	
BPG	8-(2,3-dimethyl-4-aminobiphenyl)-dG		
CCA	N2-(7,12-dimethyl-2,3,4-trihydroxy-		
CTA	benzo[a]anthracene)-dA		
CCG	N2-(7,12-dimethyl-2,3,4-trihydroxy-		

CTG	benzo[a]anthracene)-dG		
DPT	6-pyrimidine-dT	6,4-pyrimidine dimer	
DTT	5,6-(5,6-deoxythymidine)-dT	5,6-pyrimidine dimer	
FCA FTA	N6-(2,3,4-trihydroxy- benzo[c]phenanthrene)-dA		
FCG FTG	N6-(2,3,4-trihydroxy- benzo[c]phenanthrene)-dG		
HMU	5-hydroxymethyl-deoxyuridine		
IQG	8-(2-amino-3-methylimidazo[4,5- f]quinoline)-dG		
IXG	8-(2-amino-3,8-dimethylimidazo[4,5- f]quinoxaline)-dG		
NMA	N6-methyl-dA		
NMC	N4-methyl-dC		
P2G	1,N2-propeno-dG	Malonaldehyde-dG	
PAG	N2-(6-aminopyrene)-dG		
PCA PTA	N2-(7,8,9-trihydroxy-benzo[a]pyrene)-dA	B[a]PDE	
PCG PTG	N2-(7,8,9-trihydroxy-benzo[a]pyrene)-dG	B[a]PDE	
PNG	N2-(6-nitropyrene)-dG		
PPG	8-(2-amino-1-methyl-6-phenylimidazo[4,5- b]pyridine)-dG		
TGT	5R,6R-dihydroxy-dT	Thymine glycol	
YCA YTA	N2-(11,12,13-trihydroxy- dibenzo[a,l]pyrene)-dA		
YCG YTG	N2-(11,12,13-trihydroxy- dibenzo[a,l]pyrene)-dG		

^a The PDB reference is given for nucleosides where available. GaussView was used for generating the starting geometry wherever the PDB source is not mentioned.

Table 6.5 Multi-Orientation Fitting effects on the Calculated Pseudouridine Charges Using the R.E.D. Program

PSU	RED_1	RED_4	RED_8	RED_12	RED_20
O5'	-0.6384	-0.6408	-0.6371	-0.6357	-0.6364
C5'	0.0761	0.1142	0.0997	0.0936	0.0955
C4'	0.0921	0.1363	0.1405	0.1397	0.1374
O4'	-0.4004	-0.4154	-0.4129	-0.4127	-0.4119
C3'	0.2068	0.2368	0.2433	0.2422	0.2420
O3'	-0.6732	-0.6849	-0.6864	-0.6866	-0.6862
C2'	0.0832	0.0725	0.0725	0.0736	0.0686
O2'	-0.6166	-0.6227	-0.6217	-0.6208	-0.6202
C1'	0.0094	0.0285	0.0239	0.0236	0.0244
N1	-0.2797	-0.3035	-0.2998	-0.2936	-0.2958
C2	0.5110	0.5062	0.5060	0.5054	0.5100
O2	-0.5620	-0.5579	-0.5591	-0.5599	-0.5608
N3	-0.2787	-0.2647	-0.2593	-0.2599	-0.2650
C4	0.4133	0.4001	0.4003	0.4062	0.4068
O4	-0.5136	-0.5080	-0.5084	-0.5109	-0.5105
C5	-0.0076	-0.0185	-0.0215	-0.0229	-0.0215
C6	-0.1123	-0.0997	-0.0959	-0.0980	-0.0996
H5'	0.0624	0.0463	0.0495	0.0515	0.0512
H5''	0.0624	0.0463	0.0495	0.0515	0.0512
H4'	0.1207	0.0993	0.0987	0.0998	0.1004
H3'	0.0519	0.0339	0.0312	0.0313	0.0326
H2'	0.0898	0.0918	0.0908	0.0904	0.0922
H1'	0.1824	0.1791	0.1800	0.1798	0.1799
HO2'	0.4239	0.4268	0.4258	0.4251	0.4256
HO3'	0.4454	0.4459	0.4462	0.4467	0.4466
HO5'	0.4337	0.4291	0.4299	0.4299	0.4300
H6	0.2164	0.2115	0.2082	0.2080	0.2088
N3H	0.2934	0.2903	0.2876	0.2867	0.2884
N1H	0.3085	0.3209	0.3183	0.3158	0.3164
S.D. ^a		0.0166	0.0164	0.0153	0.0149
M.A.D. ^b	0.0111	0.0033	0.0019	0.0013	

^a Standard deviation of the charge values with respect to single orientation. ^b Mean absolute deviation of the charge values with respect to the RED_20 charges.

Table 6.6 Population Analysis effects on the Calculated Charges of the Thymine Nucleobase^a

Atom	MK	MK 4,4	MK 8,4	MK 8,8	ChelpG	ChelpG 8,8
N1	-0.5972	-0.5861	-0.5854	-0.5799	-0.5956	-0.6062
C2	0.8904	0.8898	0.8806	0.8734	0.9355	0.9554
N3	-0.7229	-0.7284	-0.7202	-0.7128	-0.7506	-0.7693
C4	0.8174	0.8290	0.8210	0.8103	0.8655	0.8766
C5	-0.1005	-0.1241	-0.1152	-0.1029	-0.2019	-0.2042
C6	0.0390	0.0183	0.0169	0.0117	0.0630	0.0703
O4	-0.6381	-0.6377	-0.6339	-0.6325	-0.6559	-0.6617
O2	-0.6004	-0.6011	-0.5984	-0.5962	-0.6160	-0.6182
H6	0.1778	0.1901	0.1906	0.1901	0.1708	0.1693
N3H	0.3886	0.3911	0.3895	0.3885	0.3870	0.3909
N1H	0.3795	0.3792	0.3797	0.3790	0.3688	0.3700
M.A.D. ^b	0.0075	0.0093	0.0044		0.0069	

^a The notation and description of the population analysis is discussed in the original paper.⁴³ ^b Mean deviation with respect to the most accurate method of collecting ESP points pertinent to similar techniques.

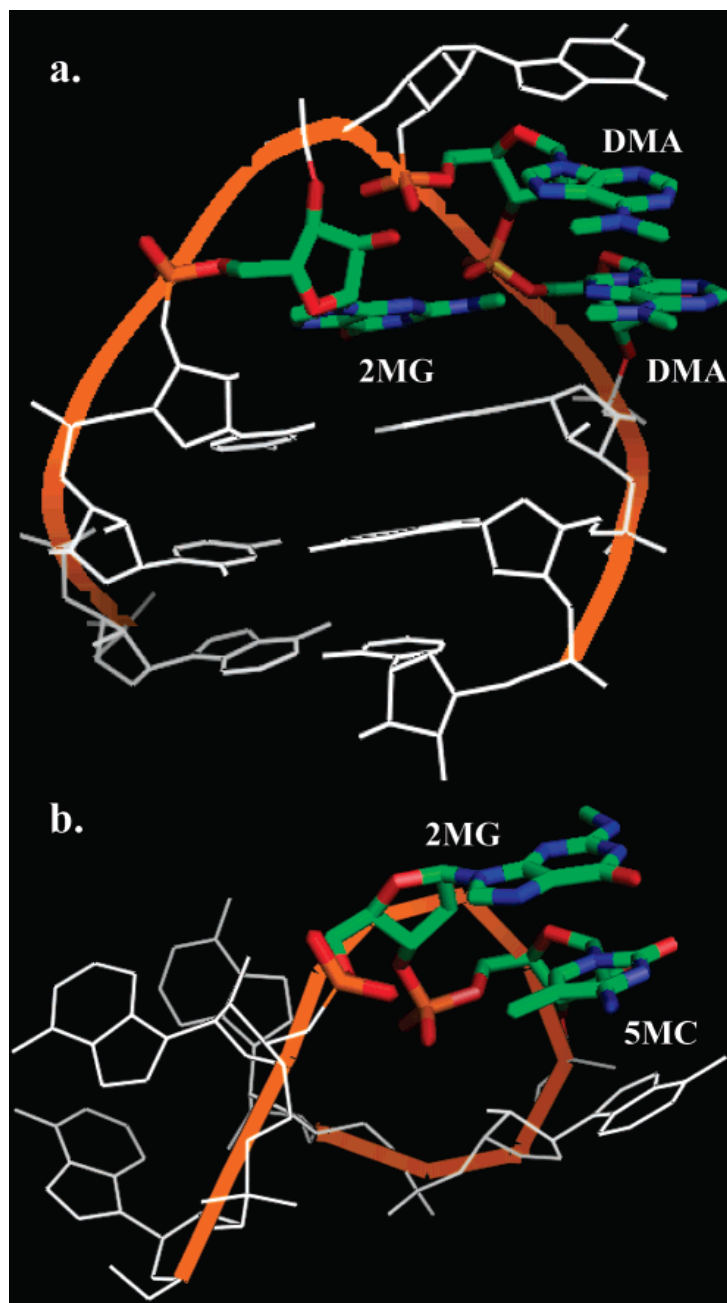


Figure 6.5 The effect of modifications in the stability and functioning of 16S rRNA of 30S ribosome (1J5E). (a) The dimethylated adenines (DMA) in the "dimethyl A loop" of 16S rRNA help in the stabilization of the loop through stacking interactions and forms a hydrophobic pocket with 2MG. (b) The methylated 966 and 967 positions of 16S rRNA increase the surface area for stacking and also form a van der Waals contact with the hydrophobic portion of Arg-128 of S9 protein (not shown).

6.7 References

1. Noller, H. F. RNA Structure: Reading the Ribosome. *Science* **2005**, 309, 1508-1514.
2. Sen, G. L.; Blau, H. M. A Brief History of RNAi: the Silence of the Genes. *Faseb J.* **2006**, 20, 1293-1299.
3. Krutzfeldt, J.; Stoffel, M. MicroRNAs: A New Class of Regulatory Genes Affecting Metabolism. *Cell Metab.* **2006**, 4, 9-12.
4. Rozenski, J.; Crain, P. F.; McCloskey, J. A. The RNA Modification Database: 1999 Update. *Nucleic Acids Res.* **1999**, 27, 196-197.
5. Grosjean, H. *Modification and Editing of RNA*. ASM Press: 1998.
6. Murphy, F. V.; Ramakrishnan, V.; Malkiewicz, A.; Agris, P. F. The Role of Modifications in Codon Discrimination by tRNA(Lys) UUU. *Nat. Struct. Mol. Biol.* **2004**, 11, 1186-1191.
7. Agris, P. F. Decoding the Genome: A Modified View. *Nucleic Acids Res.* **2004**, 32, 223-238.
8. Sumita, M.; Desaulniers, J. P.; Chang, Y. C.; Chui, H. M. P.; Clos, L.; Chow, C. S. Effects of Nucleotide Substitution and Modification on the Stability and Structure of Helix 69 from 28S rRNA. *RNA* **2005**, 11, 1420-1429.
9. Blount, K. E.; Uhlenbeck, O. C. The Structure-Function Dilemma of the Hammer Head Ribozyme. *Annu. Rev. Bioph. Biom.* **2005**, 34, 415-440.
10. Bruno, L. *Conserved Ribosomal RNA Modification and their Putative Roles in Ribosome Biogenesis and Translation*. Springer: Berlin/Heidelberg, 2005; Vol. 12.

11. Alexandrov, A.; Chernyakov, I.; Gu, W. F.; Hiley, S. L.; Hughes, T. R.; Grayhack, E. J.; Phizicky, E. M. Rapid tRNA Decay can Result from Lack of Nonessential Modifications. *Mol. Cell* **2006**, *21*, 87-96.
12. Lane, B. G.; Ofengand, J.; Gray, M. W. Pseudouridine and O-2'-Methylated Nucleosides - Significance of Their Selective Occurrence in Ribosomal-RNA Domains That Function in Ribosome-Catalyzed Synthesis of the Peptide-Bonds in Proteins. *Biochimie* **1995**, *77*, 7-15.
13. Ames, B. N.; Shigenaga, M. K.; Hagen, T. M. Oxidants, Antioxidants, and the Degenerative Diseases of Aging. *Proc. Natl. Acad. Sci.* **1993**, *90*, 7915-7922.
14. Cadet, J.; Berger, M.; Douki, T.; Morin, B.; Raoul, S.; Ravanat, J. L.; Spinelli, S. Effects of UV and visible radiation on DNA - Final base damage. *Biol. Chem.* **1997**, *378*, 1275-1286.
15. Lindahl, T. Instability and Decay of the Primary Structure of DNA. *Nature* **1993**, *362*, 709-715.
16. Shimada, T.; Hayes, C. L.; Yamazaki, H.; Amin, S.; Hecht, S. S.; Guengerich, F. P.; Sutter, T. R. Activation of chemically diverse procarcinogens by human cytochrome P-450 1B1. *Cancer Res.* **1996**, *56*, 2979-2984.
17. Jernstrom, B.; Graslund, A. Covalent Binding of Benzo[a]Pyrene 7,8-Dihydrodiol 9,10-Epoxides to DNA - Molecular-Structures, Induced Mutations and Biological Consequences. *Biophys. Chem.* **1994**, *49*, 185-199.
18. Ferguson, L. R.; Denny, W. A. Genotoxicity of non-covalent interactions: DNA intercalators. *Mutat. Res.-Fundam. Mol. Mech. Mutagen.* **2007**, *623*, 14-23.

19. Auffinger, P.; Westhof, E. RNA Solvation: A Molecular Dynamics Simulation Perspective. *Biopolymers* **2000**, *56*, 266-274.
20. MacKerell, A. D.; Bashford, D.; Bellott, M.; Dunbrack, R. L.; Evanseck, J. D.; Field, M. J.; Fischer, S.; Gao, J.; Guo, H.; Ha, S.; Joseph-McCarthy, D.; Kuchnir, L.; Kuczera, K.; Lau, F. T. K.; Mattos, C.; Michnick, S.; Ngo, T.; Nguyen, D. T.; Prodhom, B.; Reiher, W. E.; Roux, B.; Schlenkrich, M.; Smith, J. C.; Stote, R.; Straub, J.; Watanabe, M.; Wiorkiewicz-Kuczera, J.; Yin, D.; Karplus, M. All-Atom Empirical Potential for Molecular Modeling and Dynamics Studies of Proteins. *J. Phys. Chem. B* **1998**, *102*, 3586-3616.
21. Case, D. A.; Cheatham, T. E.; Darden, T.; Gohlke, H.; Luo, R.; Merz, K. M.; Onufriev, A.; Simmerling, C.; Wang, B.; Woods, R. J. The AMBER Biomolecular Simulation Programs. *J. Comput. Chem.* **2005**, *26*, 1668-1688.
22. Brunger, A. T.; Adams, P. D.; Clore, G. M.; DeLano, W. L.; Gros, P.; Grosse-Kunstleve, R. W.; Jiang, J. S.; Kuszewski, J.; Nilges, M.; Pannu, N. S.; Read, R. J.; Rice, L. M.; Simonson, T.; Warren, G. L. Crystallography & NMR System: A New Software Suite for Macromolecular Structure Determination. *Acta Crystallogr. D* **1998**, *54*, 905-921.
23. Scott, W. R. P.; Hunenberger, P. H.; Tironi, I. G.; Mark, A. E.; Billeter, S. R.; Fennen, J.; Torda, A. E.; Huber, T.; Kruger, P.; van Gunsteren, W. F. The GROMOS Biomolecular Simulation Program Package. *J. Phys. Chem. A* **1999**, *103*, 3596-3607.
24. Kaminski, G. A.; Stern, H. A.; Berne, B. J.; Friesner, R. A.; Cao, Y. X. X.; Murphy, R. B.; Zhou, R. H.; Halgren, T. A. Development of a Polarizable Force Field for

- Proteins via Ab Initio Quantum Chemistry: First Generation Model and Gas Phase Tests. *J. Comput. Chem.* **2002**, 23, 1515-1531.
25. Halgren, T. A.; Damm, W. Polarizable Force Fields. *Curr. Opin. Struc. Biol.* **2001**, 11, 236-242.
 26. Lind, K. E.; Sherlin, L. D.; Mohan, V.; Griffey, R. H.; Ferguson, D. M. *Parameterization and simulation of the physical properties of phosphorothioate nucleic acids*. 1998; Vol. 682.
 27. Meagher, K. L.; Redman, L. T.; Carlson, H. A. Development of Polyphosphate Parameters for Use with the AMBER Force Field. *J. Comput. Chem.* **2003**, 24, 1016-1025.
 28. http://pharmacy.man.ac.uk/amber/nuc/tRNA_inf.html.
 29. Lind, K. E.; Mohan, V.; Manoharan, M.; Ferguson, D. M. Structural Characteristics of 2'-O-(2-methoxyethyl)-Modified Nucleic Acids from Molecular Dynamics Simulations. *Nucleic Acids Res.* **1998**, 26, 3694-3699.
 30. Auffinger, P.; Louise-May, S.; Westhof, E. Molecular Dynamics Simulations of Solvated Yeast tRNA(Asp). *Biophys. J.* **1999**, 76, 50-64.
 31. Stuart, J. W.; Koshlap, K. M.; Guenther, R.; Agris, P. F. Naturally-Occurring Modification Restricts the Anticodon Domain Conformational Space of tRNA(Phe). *J. Mol. Biol.* **2003**, 334, 901-918.
 32. McCrate, N. E.; Varner, M. E.; Kim, K. I.; Nagan, M. C. Molecular Dynamics Simulations of Human tRNA (Lys,3)(UUU) : the Role of Modified Bases in mRNA Recognition. *Nucleic Acids Res.* **2006**, 34, 5361-5368.

33. Cornell, W. D.; Cieplak, P.; Bayly, C. I.; Gould, I. R.; Merz, K. M.; Ferguson, D. M.; Spellmeyer, D. C.; Fox, T.; Caldwell, J. W.; Kollman, P. A. A 2nd Generation Force-Field for the Simulation of Proteins, Nucleic-Acids, and Organic-Molecules. *J. Am. Chem. Soc.* **1995**, *117*, 5179-5197.
34. Frisch, M. J.; Trucks, G. W.; Schlegel, H. B.; Scuseria, G. E.; Robb, M. A.; Cheeseman, J. R.; Montgomery, J. A.; Vreven, T.; Kudin, K. N.; Burant, J. C.; Millam, J. M.; Iyengar, S.; Tomasi, J.; Barone, V.; Mennucci, B.; Cossi, M.; Scalmani, G.; Rega, N.; Petersson, G. A.; Nakatsuji, H.; Hada, M.; Ehara, M.; Toyota, K.; Fukuda, R.; Hasegawa, J.; Ishida, M.; Nakajima, T.; Honda, Y.; Kitao, O.; Nakai, H.; Klene, M.; Li, X.; Knox, J. E.; Hratchian, H. P.; Cross, J. B.; Adamo, C.; Jaramillo, J.; Gomperts, R.; Stratmann, R. E.; Yazyev, O.; Austin, A. J.; Cammi, R.; Pomelli, C.; Ochterski, J.; Ayala, P. Y.; Morokuma, K.; Voth, G. A.; Salvador, P.; Dannenberg, J. J.; Zakrzewski, V. G.; Dapprich, S.; Daniels, A. D.; Strain, M. C.; Farkas, Ö.; Malick, D. K.; Rabuck, A. D.; Raghavachari, K.; Foresman, J. B.; Ortiz, J. V.; Cui, Q.; Baboul, A. G.; Clifford, S.; Cioslowski, J.; Stefanov, B. B.; Liu, G.; Liashenko, A.; Piskorz, P.; Komaromi, I.; Martin, R. L.; Fox, D. J.; Keith, T.; Al-Laham, M. A.; Peng, C. Y.; Nanayakkara, A.; Challacombe, M.; Gill, P. M. W.; Johnson, B.; Chen, W.; Wong, M. W.; Andres, J. L.; Gonzalez, C.; Replogle, E. S.; Pople, J. A. *Gaussian 03*, ver.D01; Gaussian, Inc.: Pittsburgh, PA, 2003.
35. Steenken, S. Purine-Bases, Nucleosides, and Nucleotides - Aqueous-Solution Redox Chemistry and Transformation Reactions of Their Radical Cations and E- and OH Adducts. *Chem. Rev.* **1989**, *89*, 503-520.

36. Besler, B. H.; Merz, K. M.; Kollman, P. A. Atomic Charges Derived from Semiempirical Methods. *J. Comput. Chem.* **1990**, *11*, 431-439.
37. Singh, U. C.; Kollman, P. A. An Approach to Computing Electrostatic Charges for Molecules. *J. Comput. Chem.* **1984**, *5*, 129-145.
38. Bayly, C. I.; Cieplak, P.; Cornell, W. D.; Kollman, P. A. A Well-Behaved Electrostatic Potential Based Method Using Charge Restraints for Deriving Atomic Charges - the Resp Model. *J. Phys. Chem.* **1993**, *97*, 10269-10280.
39. Wang, J. M.; Wang, W.; Kollman, P. A.; Case, D. A. Automatic Atom Type and Bond Type Perception in Molecular Mechanical Calculations. *J. Mol. Graph Model* **2006**, *25*, 247-260.
40. Cieplak, P.; Cornell, W. D.; Bayly, C.; Kollman, P. A. Application of the Multimolecule and Multiconformational Resp Methodology to Biopolymers - Charge Derivation for DNA, RNA, and Proteins. *J. Comput. Chem.* **1995**, *16*, 1357-1377.
41. Sierzputowskagracz, H.; Sochacka, E.; Malkiewicz, A.; Kuo, K.; Gehrke, C. W.; Agris, P. F. Chemistry and Structure of Modified Uridines in the Anticodon, Wobble Position of Transfer-Rna Are Determined by Thiolation. *J. Am. Chem. Soc.* **1987**, *109*, 7171-7177.
42. Durant, P. C.; Bajji, A. C.; Sundaram, M.; Kumar, R. K.; Davis, D. R. Structural Effects of Hypermodified Nucleosides in the Escherichia Coli and Human tRNA(Lys) Anticodon Loop: The Effect of Nucleosides s(2)U, mcm(5)U, mcm(5)s(2)U, mnm(5)s(2)U, t(6)A, and ms(2)t(6)A. *Biochemistry* **2005**, *44*, 8078-8089.

43. Aduri, R.; Psciuk, B. T.; Saro, P.; Taniga, H.; Schlegel, H. B.; SantaLucia, J. AMBER force field parameters for the naturally occurring modified nucleosides in RNA. *J. Chem. Theory Comput.* **2007**, *3*, 1464-1475.
44. Wang, J. M.; Cieplak, P.; Kollman, P. A. How well does a restrained electrostatic potential (RESP) model perform in calculating conformational energies of organic and biological molecules? *J. Comput. Chem.* **2000**, *21*, 1049-1074.
45. Wang, J. M.; Wolf, R. M.; Caldwell, J. W.; Kollman, P. A.; Case, D. A. Development and Testing of a General Amber Force Field. *J. Comput. Chem.* **2004**, *25*, 1157-1174.
46. Woods, R. J.; Khalil, M.; Pell, W.; Moffat, S. H.; Smith, V. H. Derivation of Net Atomic Charges from Molecular Electrostatic Potentials. *J. Comput. Chem.* **1990**, *11*, 297-310.
47. Pigache, A.; Cieplak, P.; Dupradeau, F. Y. In *Automatic and Highly Reproducible RESP and ESP Charge Derivation: Application to the Development of Programs RED and X RED.*, Abstracts of Papers of the American Chemical Society, Mar 28; 2004; pp U1011-U1011.
48. Breneman, C. M.; Wiberg, K. B. Determining Atom-Centered Monopoles from Molecular Electrostatic Potentials - the Need for High Sampling Density in Formamide Conformational-Analysis. *J. Comput. Chem.* **1990**, *11*, 361-373.
49. Shi, H. J.; Moore, P. B. The Crystal Structure of Yeast Phenylalanine tRNA at 1.93 Angstrom Resolution: A Classic Structure Revisited. *RNA* **2000**, *6*, 1091-1105.

50. Still, W. C.; Tempczyk, A.; Hawley, R. C.; Hendrickson, T. Semianalytical Treatment of Solvation for Molecular Mechanics and Dynamics. *J. Am. Chem. Soc.* **1990**, *112*, 6127-6129.
51. Darden, T.; York, D.; Pedersen, L. Particle Mesh Ewald - an N.Log(N) Method for Ewald Sums in Large Systems. *J. Chem. Phys.* **1993**, *98*, 10089-10092.
52. York, D. M.; Darden, T. A.; Pedersen, L. G. The Effect of Long-Range Electrostatic Interactions in Simulations of Macromolecular Crystals - a Comparison of the Ewald and Truncated List Methods. *J. Chem. Phys.* **1993**, *99*, 8345-8348.

CHAPTER 7

THEORETICAL DETERMINATION OF ONE-ELECTRON OXIDATION POTENTIALS FOR NUCLEIC ACID BASES

Reproduced with permission from J. Chem. Theory Comput., **2012**, 8, 5107
Copyright 2012, American Chemical Society

7.1 Introduction

In biological systems, DNA is persistently exposed to harmful oxidizing agents. Most biological systems possess mechanisms for repairing oxidative damage to DNA. Although these repair mechanisms tend to be highly successful, they cannot repair all damaged DNA. Unrepaired oxidative damage to DNA can lead to mutations that are associated with carcinogenesis, cellular aging, and cellular death.¹⁻⁶ Determining the most probable sites for DNA damage is very important for understanding the mechanisms and reaction pathways leading to permanent mutations. It is known that guanine has the lowest oxidation potential among the common nucleobases. There is also a consensus concerning the qualitative trend in oxidation potentials of the common nucleobases.⁷ Due to electron transfer processes in DNA, the specific site where oxidative damage takes place may be different from the site of chemical mutation. The electrochemical properties of individual nucleosides are important for the understanding of oxidative damage to DNA. In the present paper, we have used electronic structure calculations and a polarizable continuum solvation model to calculate the electrochemical potentials of some nucleosides.

The one-electron oxidation potentials of nucleosides have been measured by a number of experimental groups in different solvents and at various pH levels in aqueous

solution.⁸⁻¹² Unfortunately, there is not yet a consensus set of redox potentials for the standard nucleic acids guanine, adenine, cytosine, thymine, and uracil. The various measured values have been discussed extensively, and concerns have been raised such as cyclic voltammetry measurements that involve irreversible redox reactions, solubility issues with specific nucleobases, and inaccurate reference compound potentials.^{10,12,13}

The experimental studies by Steenken and coworkers^{8,9} and by Seidel et al.¹³ have attracted the most attention concerning nucleoside oxidation potentials. The measurements by Steenken and Jovanovic were made in aqueous solution at near physiological pH using chemical oxidation and kinetic rate measurements of reference compounds reacting with the nucleobases. They determined half-cell potentials for guanine at pH 7 ($E_7 = 1.29$ V) and adenine at pH 3 and pH 5 ($E_3 = 1.64$ V and $E_5 = 1.56$ V). Standard potentials (E°) were also derived by Steenken and Jovanovic. However, numerous tautomeric and acid-base equilibria control the composition of the reactants and products for redox reactions in aqueous solution. For a redox reaction in aqueous solution at a given pH, the acid dissociation constants (K_a) are needed to relate the measured potentials to E° , and the derived E° becomes very sensitive to the K_a values of the oxidized and reduced species. The measurements made by Seidel et al. were performed using cyclic voltammetry in acetonitrile solution. By measuring the one-electron oxidation potentials in an aprotic solvent, they eliminated the complications of acid-base equilibria. However, the cyclic voltammetry measurements were made with a single voltammetric sweep due to the irreversibility of the redox reactions.

As computational power has increased over the years, sophisticated electronic structure calculations have become practical for larger systems and have provided an alternative way to obtain redox potentials.¹⁴⁻¹⁷ An excellent example of utilizing electronic structure calculations to determine potentials is the recent article by Coote and co-workers benchmarking the absolute reduction potential of the ferrocenium/ferrocene couple in nonaqueous solutions.¹⁵ Thermodynamic cycles similar to the one depicted in Scheme 7.1 are often used to compute the solution phase free energy difference (ΔG^*_{sol}) for a redox reaction. Similar approaches have yielded good results for computing pK_a 's.^{18,19}

Redox potentials calculated by electronic structure methods are not without issues. The computed solution phase electron attachment or detachment energy for a given species is considered to be an absolute potential, while a potential determined experimentally using electrochemical techniques is measured against a reference electrode and is therefore reported as a relative value. For a calculated absolute potential to be comparable to a measured potential, the absolute potential of the corresponding reference electrode must be subtracted from the calculated absolute potential. The absolute potential of the Standard Hydrogen Electrode (SHE or NHE) has been debated extensively in the literature.²⁰⁻²³ Deriving an accurate value of $E^{\text{abs}}(\text{SHE})$ requires careful consideration of the proper electron convention, standard state convention, and especially the free energy of a solvated proton.

The present study uses electronic structure calculations to obtain redox potentials and acid dissociation constants that are necessary for calculating pH dependent half-cell potentials for the nucleobases in aqueous solution. Thermodynamic

cycles are utilized to obtain reaction free energies for deprotonation reactions and redox processes. Both highly accurate and efficient methods are employed for calculating gas phase free energies. Solvation free energies are estimated using the SMD polarizable continuum model (PCM) by Marenich, Cramer and Truhlar.²⁴ Adding explicit solvent molecules can improve the results for PCM calculations in aqueous solution. However this can cause some difficulties in comparing the pK_a 's and redox potentials of the nucleobases, since they have differing numbers of hydrogen bonding sites. As an alternative, we calibrate the PCM calculations by adjusting the cavity scaling factors to fit observed pK_a 's. The resulting scaling factors will be useful for closely related species, for example, in our next study which focuses on the prediction of pK_a 's and redox potentials of transient intermediates in the pathways for oxidative damage to DNA. These data would provide useful information toward a molecular level understanding of why certain DNA oxidation pathways are experimentally observed and others are not.

7.2 General Description of a Reduction Potential

A standard redox potential is related to the free energy difference of a redox reaction by eq (1)

$$E_{red(sol)}^{\circ} = \frac{-\Delta G_{red(sol)}^*}{nF} \quad (1)$$

where F is Faraday's constant, $\Delta G_{red(sol)}^*$ is the solution phase standard state free energy change, and n is the number of electrons in the redox process. For all equations shown in the present study, example reactions will be written as one-electron reductions

where $n = 1$ throughout. Using the thermodynamic cycle outlined in Scheme 7.1, $\Delta G^*_{\text{red(sol)}}$ is defined in eq (2) for a one-electron reduction of a given radical cation

$$\Delta G^*_{\text{red(sol)}} = G^*_{\text{(sol)}}(B) - G^*_{\text{(sol)}}(B^{+\bullet}) \quad (2)$$

The standard state free energy is expressed in eq (3)

$$G^*_{\text{(sol)}} = \left(G^\circ_{\text{(g)}} + G^{1\text{atm} \rightarrow 1\text{M}} \right) + \Delta G^*_{\text{solv}} \quad (3)$$

where $G^\circ_{\text{(g)}}$ is the standard state free energy in the gas phase and ΔG^*_{solv} is the standard state free energy of solvation. $\Delta G^{1\text{atm} \rightarrow 1\text{M}} = 1.89$ kcal/mol is the free energy difference for converting from the standard state concentration of 1 atm to the standard state concentration of 1 mol/L. The notation introduced by Ben-Naim et al.,²⁵ is used throughout this study, where a degree symbol ($^\circ$) denotes a standard state of 1 atm and an asterisk (*) denotes 1 mol/L. Substituting eq (3) into eq (2) yields $\Delta G^*_{\text{red(sol)}}$

$$\Delta G^*_{\text{red(sol)}} = \left(G^\circ_{\text{(g)}} + \Delta G^{1\text{atm} \rightarrow 1\text{M}} + \Delta G^*_{\text{solv}}(B) \right) - \left(G^\circ_{\text{(g)}} + \Delta G^{1\text{atm} \rightarrow 1\text{M}} + \Delta G^*_{\text{solv}}(B^{+\bullet}) \right) \quad (4)$$

and is represented in Scheme 7.1. A potential calculated using eq (1) yields an absolute potential. Experimental potentials are measured against a reference electrode and are reported as relative half-cell potentials. For comparison with experimental results, we must take the difference of the calculated potential and the absolute potential of the reference electrode. The absolute potential of the standard hydrogen electrode (SHE) in an aqueous solution is estimated to be 4.281 V.^{16,17,20,21}

7.3 Gas and Solution Phase Calculations

In terms of electronic structure calculations, $G^\circ_{(g)}$ is

$$G^\circ_{(g)} = E_{el} + ZPE + \Delta G_{0 \rightarrow 298K} \quad (5)$$

where E_{el} is the electronic energy (including nuclear repulsion), ZPE is the zero point vibrational energy, and $\Delta G_{0 \rightarrow 298K}$ is the calculated thermal free energy change going from 0 to 298 K. In the present study, the gas phase free energy for a given species is obtained by optimizing the structure at the B3LYP level of theory²⁶⁻³⁰ with the 6-31+G(d,p) basis set.³¹⁻³⁶ A vibrational frequency calculation is used to determine whether the structure is a minimum or saddle point on the potential energy surface and to compute the ZPE and $\Delta G_{0 \rightarrow 298K}$ terms. An additional single point calculation using the aug-cc-pVTZ basis set³⁷ is used to obtain a more accurate E_{el} . The gas phase free energy at the B3LYP level of theory is given by

$$G^\circ_{(g)} = E_{el}^{B3LYP/aug-cc-pVTZ/B3LYP/6-31+G(d,p)} + ZPE^{B3LYP/6-31+G(d,p)} + \Delta G_{0 \rightarrow 298K}^{B3LYP/6-31+G(d,p)} \quad (6)$$

An even more accurate method for computing gas phase free energies is the CBS-QB3 compound model chemistry^{38,39} which has been shown to predict gas phase thermodynamic properties at near chemical accuracy (MAE of 1.1 kcal/mol).

For a given molecule, Ben-Naim and Marcus²⁵ described the free energy of solvation (ΔG^*_{solv}) shown in eq (7)

$$\Delta G^*_{solv} = G^*_{(sol)}(R') - G^*_{(g)}(R) \quad (7)$$

as the difference between the solution phase free energy of the solution phase optimized molecule, R' , and the gas phase free energy of the gas phase optimized molecule, R . The solvation free energy is computed using the SMD implicit solvation

model²⁴ at the B3LYP/6-31+G(d,p) level of theory and includes the electrostatic, cavitation, and dispersion terms. The solution phase free energies are computed by combining the solvation free energies calculated at the B3LYP level of theory with the gas phase free energies calculated with the B3LYP method

$$G_{(sol)}^* = E_{el}^{B3LYP/aug-cc-pVTZ/B3LYP/6-31+G(d,p)} + ZPE^{B3LYP/6-31+G(d,p)} + \Delta G_{0K \rightarrow 298K}^{B3LYP/6-31+G(d,p)} + \Delta G^{1atm \rightarrow 1M} + \Delta G_{solv}^{*SMD/B3LYP/6-31+G(d,p)} \quad (8)$$

and the CBS-QB3 method

$$G_{(sol)}^* = G_{(g)}^{CBS-QB3} + G^{1atm \rightarrow 1M} + \Delta G_{solv}^{*SMD/B3LYP/6-31+G(d,p)} \quad (9)$$

All calculations in this study were carried out with a development version of Gaussian.⁴⁰ Solution phase calculations were performed using the SMD implicit solvation model.²⁴ The SMD solvation model uses the integral equation formalism of the polarizable continuum model (IEF-PCM)⁴¹⁻⁴⁴ with a parameterized set of atomic radii to calculate the bulk electrostatic energy contribution. The model calculates short-range interaction energies between solvent and solute by using a modified solvent-accessible surface area which incorporates parameters for atomic and molecular surface tensions and hydrogen-bond acidity and basicity. The tessellated solute-solvent boundary uses an average tesserae area of 0.2 Å².

The molecules studied here are canonical nucleobases and their derivatives. A nucleic acid base or nucleobase bonded to a ribose or deoxyribose sugar is a nucleoside. Nucleosides bonded to one or more phosphate groups are nucleotides. To compare better with the experimental measurements on nucleosides in solution,^{8,9,13} most of the nucleobases calculated in this study have been methylated at the position where the sugar moiety is attached in a nucleoside (for atom numbering see

Scheme 7.2). This avoids complications resulting from protic equilibria and solution phase modeling surrounding the glycosidic nitrogen atoms. The sugar moiety would affect protic equilibria primarily at high pH (>12) where hydroxyl groups of the sugar can be deprotonated. In a previous study investigating reaction pathways following guanine oxidation, replacing the sugar by methyl, hydroxymethyl, and methoxyethyl yielded relative enthalpies that compared well with one another.⁴⁵

7.4 Accounting for Multiple Tautomers

The methods discussed above yield redox potentials specific to a given protonation state of the oxidized (Ox_i) and reduced (Red_j) species. During a measurement in aqueous solution, equilibria exist between multiple tautomers (Scheme 7.3). Relative populations of each tautomer are given by a normalized Boltzmann distribution, f , based on the relative free energies of the tautomers

$$f_i = \frac{[Ox_i]}{[Ox]} = \frac{[Ox_i]}{\sum_n [Ox_n]} = \frac{\exp\left(\frac{-G_{1(sol)}^*}{RT}\right)}{\sum_n \exp\left(\frac{-G_{n(sol)}^*}{RT}\right)} \quad \sum f_n = 1 \quad (10)$$

The tautomer specific equilibrium constant, K_{red}^{ij} , can be related to the ensemble equilibrium constant, K_{red} , using the Boltzmann weighted populations for each species.

$$K_{red}^{ij} = \frac{[Red_j]}{[Ox_i]} = \frac{[Red] f'_j}{[Ox] f_i} = K_{red} \frac{f'_j}{f_i} \quad (11)$$

where f'_j is the population of the j th tautomer of the set of reduced species and f_i is the population of the i th tautomer of the oxidized species. From eq (11), the ensemble

equilibrium constant can now be generalized for all possible reductions between tautomers

$$K_{red} = K_{red}^{11} \frac{f_1}{f'_1} = K_{red}^{12} \frac{f_1}{f'_2} = K_{red}^{21} \frac{f_2}{f'_1} = \dots \frac{f_i}{f'_j} \quad (12)$$

The ensemble reduction potential is obtained by inserting the free energy $\Delta G^*_{red(sol)} = -R \cdot T \ln(K_{red})$ into the Nernst equation

$$E^{\circ}_{red(sol)} = \frac{RT}{F} \ln(K_{red}) \quad (13)$$

Substituting eq (12) into eq (13) yields the ensemble reduction potential expressed in terms of tautomer specific potentials

$$E^{\circ}_{red(sol)} = E^{\circ}_{red(sol)} + \frac{RT}{F} \ln(f_i) - \frac{RT}{F} \ln(f'_j) \quad (14)$$

7.5 Calculating pK_a and E_7

Experimental standard redox potentials are usually derived from potentials measured at a specific pH in aqueous solutions using the Nernst half-cell equation shown in eq (15)

$$E_{1/2} = E^{\circ} - \frac{RT}{F} \ln \left(\frac{[Red]}{[Ox]} \right) \quad (15)$$

Conversely, a pH dependent potential can be derived from a calculated standard redox potential using the equilibrium concentrations of the reduced and oxidized species. In protic solvents, the concentrations of alternate protonation states existing in solution within the applicable pH range need to be included for both the reduced and oxidized species. Assuming dilute concentrations (low ionic strength), a functional form can be

derived^{46,47} for calculating the pH dependent potentials for a nucleobase that has three K_a 's for the reduced form and two K_a 's for the oxidized form

$$E_{pH} = E^\circ(\text{X}^\bullet, \text{H}^+/\text{XH}) + \frac{RT}{F} \ln \left(\frac{K_{a1o}}{K_{a1r}} \right) + \frac{RT}{F} \ln \left(\frac{K_{a1r}K_{a2r}K_{a3r} + K_{a1r}K_{a2r}10^{-pH} + K_{a1r}10^{-2pH} + 10^{-3pH}}{K_{a1o}K_{a2o} + K_{a1o}10^{-pH} + 10^{-2pH}} \right) \quad (16)$$

Similar expressions can be obtained for cases with different numbers of K_a 's, e.g.

$$E_{pH} = E^\circ(\text{X}^\bullet, \text{H}^+/\text{XH}) + \frac{RT}{F} \ln \left(\frac{K_{a1o}}{K_{a1r}} \right) + \frac{RT}{F} \ln \left(\frac{K_{a1r}K_{a2r} + K_{a1r}10^{-pH} + 10^{-2pH}}{K_{a1o} + 10^{-pH}} \right) \quad (17)$$

"XH" signifies a specific nucleic acid species in the reduced or closed shell neutral state, and "X" is the corresponding oxidized species that has been deprotonated following the one-electron transfer comprising the predicted redox couple for processes occurring in aqueous solution at pH 7. "o" stands for the oxidized species K_a and "r" stands for the reduced species K_a . For a redox potential in aqueous solution, acid dissociation constants of the oxidized species (K_{ao}) and reduced species (K_{ar}) account for the concentrations of the relevant protonation states. For example, the experimental values needed for the pH dependent potential of guanosine are $pK_{a1r} = 1.9$, $pK_{a2r} = 9.3$, $pK_{a3r} \approx 12.5$, $pK_{a1o} = 3.9$, $pK_{a2o} = 10.9$, and $E^\circ = 1.58 \text{ V}$.^{9,48} Further discussions regarding the pH dependence of reduction potentials can be found in the literature.^{46,47}

Acid dissociation constants for short-lived radical species may be difficult to measure experimentally, and very few measured pK_a 's are available for radical nucleobase species. Additionally, discrepancies between experimentally measured pK_a 's of closed shell species are often larger than the reported measurement error.

where f'_j is the population of the j th tautomer of the set of deprotonated species and f_i is the population of the corresponding i th tautomer of the protonated species. The tautomer specific pK_a is

and $\Delta G^*_{\text{deprot(aq)}}$ is calculated using the thermodynamic cycle in Scheme 7.4. The aqueous free energy for the deprotonation reaction is given by

In this study, the literature value $\Delta G^*_{\text{solv}}(\text{H}^+) = -265.9 \text{ kcal/mol}^{22}$ is used for the aqueous solvation free energy of H^+ .

The gas phase energies for the proton and the electron at 0 K are zero. The gas phase free energy for H^+ at 298 K is $G^\circ_{(g)}(H^+) = -6.287$ kcal/mol and is derived from $G^\circ_{(g)} = H^\circ_{(g)} - T \cdot S^\circ_{(g)}$ where $E_{0K} = 0$ au, $H^\circ_{(g)} = 5/2 R \cdot T = 1.48$ kcal/mol and $S^\circ_{(g)} = 26.05$ cal/mol·K. Similarly, the gas phase free energy of the electron at 298 K is

$G^\circ_{(g)}(H^+) = -0.867 \text{ kcal/mol}$ using $H^\circ_{(g)}(H^+) = 0.752 \text{ kcal/mol}$ and $S^\circ_{(g)}(H^+) = 5.434 \text{ cal/mol}$ based on Fermi-Dirac statistics.^{52,53}

7.6 Results and Discussion

Redox potentials in solution include the intrinsic energy of adding or removing an electron along with the solvation energy of the oxidized and reduced species. For the nucleobases considered here, these are neutral, cationic, and anionic species depending on the experimental pH conditions and whether or not a proton transfer accompanies the electron transfer. To compare with experimentally observed values, the relative abundance of the various tautomers at each redox level must be taken into account. In aqueous solution, acid-base equilibria must also be included in the treatment. To assess the accuracy of the various levels of theory, we first compared the calculated ionization potential and gas phase basicity with experimental values. Then, we examined the suitability of the SMD solvation model by calculating the pK_a 's for the nucleobases. To obtain ensemble averaged pK_a 's, tautomeric equilibria are included for the different protonation states. Solvent cavity scaling parameters are adjusted to improve the agreement with experimental results. Next, redox potentials are calculated in acetonitrile, where acid-base equilibria are absent. Finally, redox potentials are calculated in aqueous solution as a function of the pH, taking into account both the tautomeric and acid-base equilibria.

7.7 Gas Phase Energies

For the gas phase reaction $A + H^+ \rightarrow AH^+$ (the upper part of Scheme 7.4), the proton affinity (PA) is the reaction enthalpy and the gas phase basicity (GB) is the reaction free energy. Table 7.1 compares computed and measured PA and GB energies for unsubstituted nucleobases and their anions. The results from a theoretical study by Moser, et al.⁵⁴ are also listed for comparison. The CBS-QB3^{38,39} and the G3B3⁵⁵ compound model chemistries are the most accurate calculations in the table. Compared to experimental results, the mean absolute errors (MAE) for CBS-QB3 and G3B3 are 0.7 – 1.3 kcal/mol, and are well within the estimated experimental error of 2 – 3 kcal/mol. Both York and co-workers⁵⁴ and Lee and co-workers⁵⁶ noted that their calculated values for proton affinities of neutral thymine and uracil disagreed with experimental results by as much as 4 kcal/mol. Calculations by Wolken and Turecek⁵⁷ showed that the most stable protonated isomer of uracil is the N1 deprotonated 2,4-dihydroxy form, rather than the expected N-1 protonated 2-oxo,4-hydroxy form (Scheme 7.5). The present B3LYP, G3B3, and CBS-QB3 calculations confirm that the N1 deprotonated 2,4-dihydroxy form is the most stable isomer for both thymine and uracil. The PA and GB for the neutrals and anions calculated with B3LYP/aug-cc-pVTZ are on average 1.7 and 2.1 kcal/mol higher than the experimental and CBS-QB3 values, respectively.

Table 7.2 compares the calculated vertical and adiabatic ionization energies with experimental values. The adiabatic ionization energy is the gas phase analogue of the one-electron oxidation potentials we are interested in, and systematic errors in the ionization energies should be reflected in the redox potentials. The best agreement with

experimental results is found for CBS-QB3 (MAE = 0.03 – 0.05 eV) and G3B3 (MAE = 0.05 – 0.08 eV). The MAE's are comparable to the estimated experimental error of ± 0.05 eV. The B3LYP/aug-cc-pVTZ values are systematically too low when compared to experimental results (MAE = 0.14 – 0.21 eV) and CBS-QB3 (MAE = 0.17 – 0.19 eV). The BP86/aug-cc-pVTZ calculations yield a slightly larger underestimation than B3LYP (MAE 0.19 – 0.29 eV versus experiment). This underestimation of ionization energies is known to be characteristic of the B3LYP and other DFT levels of theory as other studies have shown.^{54,58,59} The ionization energies calculated by Crespo-Hernandez et al.⁶⁰ at the PMP2 level of theory⁶¹ with a 6-31++G(d,p) basis have smaller MAE's than the DFT results, but the deviations are less systematic.

Experimental data show that methyl substitution of the nucleobases lowers the vertical ionization energy by 0.26 eV for 9-methylguanine,⁶² 0.09 eV for 9-methyladenine,⁶³ 0.24 eV for 1-methylcytosine,⁶⁴ 0.40 eV for 1-methylthymine,⁶⁵ and 0.39 eV for 1-methyluracil.⁶⁶ The calculated methyl substitution effects on the vertical ionization energy are in good agreement with experimental results (MAE = 0.05 eV for CBS-QB3 and G3B3). Although there are no experimental data, calculations show that replacing the methyl substituent with ribose lowers the ionization energy by an additional 0.1–0.4 eV. Calculations by Crespo-Hernandez et al.⁶⁷ find similar effects for methyl and 2'-deoxyribose substitution of the bases. As recommended by Crespo-Hernandez et al., the present calculations use the anti-orientation for the nucleosides since this conformation is more relevant for the geometries in solution and in DNA.

7.8 Solvent Scaling Parameters

Calculated solvation free energies for ionic species generally have larger errors than for neutral species. A relatively simple way of addressing this error is either to scale the individual atomic radii used to create the solvent cavity or scale the entire solvent cavity. In addition to compensating for different errors in solvation free energies for charged species and for specific hydrogen bonding between solvent and solute, this may also adjust for systematic errors in the calculated gas phase free energies of the molecular species. Other studies have incorporated cavity scaling techniques with success.^{14,49,68-72} Figure 7.1 shows the pK_a 's as a function of the cavity scaling parameter α for the cations and the anions (the solvent cavities for the neutrals were left unscaled, $\alpha = 1.00$). The scale factors were chosen by comparison with experimental results, minimizing the average error and rounding to the nearest 0.025. The optimal scale factors at the CBS-QB3 level of theory were found to be $\alpha = 0.975$ for the cations and $\alpha = 0.925$ for the anions. The corresponding values for the B3LYP calculations are $\alpha = 1.00$ for the cations and $\alpha = 0.90$ for the anions. A previous study by Verdolino et al.⁴⁹ found $\alpha = 0.91$ for the cations and $\alpha = 0.83$ for the anions for B3LYP calculations on a smaller set of comparisons for unoxidized nucleobases. Their study used an earlier version of the IEF-PCM solvation model with UFF atomic radii and a solvent excluding surface. The fact that the present scale factors are closer to unity reflects improvements in the solvation model.

7.9 Calculated pK_a Values

Table 7.3 summarizes the pK_a 's calculated for the methyl substituted nucleobases at the CBS-QB3 and B3LYP levels of theory with the optimal solvent cavity scaling factors. These values are compared with calculations by Baik et al.⁵⁹ and Verdolino et al.⁴⁹ Some pK_a 's have been measured for the methyl substituted bases, but more experimental data are available for the nucleosides (sugar substituted nucleobases). Where available, the experimental value for the methyl substituted base is used for comparison with the calculations. The difference between the experimental pK_a 's for the methyl- and sugar-substituted bases is usually less than 1 pK_a unit. Deprotonation of the sugar occurs at pH \sim 12.5 and above; therefore, pK_a values greater than 12 are not included in the comparisons. Figure 7.2 compares the experimental and calculated pK_a 's. The MAE is 0.9 for CBS-QB3 and 0.7 for B3LYP. The SMD method has an MAE of ca. 1 kcal/mol for the solvation free energy of neutral molecules and an MAE of ca. 4 kcal/mol for singly charged ionic molecules, translating to an MAE of roughly 3 pK_a units. The good MAE values achieved in the computed pK_a 's can be attributed in part to the solvent cavity scaling.

For the unoxidized bases, the present calculations agree quite well with the results obtained by Verdolino et al. and with calculations by Goddard and co-workers^{50,51} on guanine and 8-oxoguanine. For the oxidized bases, there is a larger spread in values between the present CBS-QB3 and B3LYP calculations and the PW91 calculations of Baik et al. Comparison with other calculations in the literature are hampered by the fact that they rely on linear regressions rather than direct calculations of the pK_a 's. The pK_a 's for deprotonation of the cations are typically less than 6, while

the pK_a 's for deprotonation of the neutrals are higher than 7 (9-methylxanthine is an exception). Consequently, oxidation of a neutral base makes it much more acidic, and oxidation at pH 7 will typically be accompanied by loss of a proton.

The calculated pK_a 's listed in Table 7.3 are ensemble averages. The tautomer specific pK_a 's and relative energies of the tautomers are shown in Figure 7.3 through Figure 7.9. In most cases, one tautomer dominates in solution (the anion of 9-methyl-8-oxoguanine is an exception). In almost all cases, the most stable tautomer of the oxidized and unoxidized species is the same, even though the relative energies of their higher lying tautomers differ. For 9-methylguanine, adenine, xanthine, and their oxidized forms, protonation occurs at N7, but for 9-methyl-8-oxoguanine, protonation occurs at N1. Deprotonation of N1 is preferred for neutral and oxidized 9-methylxanthine and oxidized 9-methyl-8-oxoguanine, but deprotonation of N3 and N7 are nearly equal in energy for 9-methyl-8-oxoguanine. For most of the remaining structures, protonation or deprotonation occurs at a ring nitrogen in preference to an NH_2 group. Deprotonation of an exocyclic NH_2 to form NH^- is strongly disfavored for the neutral species, but deprotonation of NH_2^+ is more facile in the corresponding oxidized species (e.g., pK_{a2r} versus pK_{a0} of 9-methyladenine and 1-methylcytosine). The enol tautomers of the oxidized species are 5–15 kcal/mol higher in energy than the keto forms.

7.10 Redox Potentials in Acetonitrile

Redox potentials in acetonitrile should be easier to compute than in aqueous solution because they are not complicated by acid-base equilibria, and the SMD

solvation model should be well suited for aprotic solvents. The $E^\circ(\text{XH}^{+}/\text{XH})$ redox potentials for the nucleobases listed in Table 7.4 were calculated without cavity scaling. To check the accuracy of the present approach, standard reduction potentials were calculated for a few compounds with well-established values (4-methyl aniline, anisole, and naphthalene). The MAE in the calculated reduction potentials is 0.02 V for CBS-QB3 and 0.25 V for B3LYP and is similar to the MAE's for their gas phase ionization potentials (shown in Table 7.5). For a much larger set of quinones and azacyclic compounds in aprotic solvents, Leszczynski and co-workers find MAE's in the range of 0.09–0.21 V, depending on the combination of density functional, basis set, and solvation model.¹⁴ For a diverse set of 270 organic molecules, Fu et al.⁷⁰ found that B3LYP/6-311++G(2df,2p) underestimated the ionization potential by 0.28 eV. Using PCM solvation with Bondi radii scaled by 1.20, and correcting the ionization potentials by 0.28 V, Fu et al. found a standard deviation of 0.17 V for the reduction potentials in acetonitrile. These data suggest that the inherent uncertainty in the calculated redox potentials in acetonitrile may be 0.1–0.2 V even after systematic errors are taken into account.

Table 7.4 compares the computed redox potentials in acetonitrile with the experimental values for the nucleosides in acetonitrile solution measured versus SCE by Seidel et al.¹³ The calculated values for the methyl substituted nucleobases are on average 0.21 V and 0.33 V too low for CBS-QB3 and B3LYP, while the values for nucleosides are 0.28 V too low for B3LYP. These deviations are somewhat larger than the MAE's for the corresponding ionization potentials in Table 7.2. The effect of the systematic errors in the ionization potentials and the solvation energies can be reduced

significantly by comparing the relative values of redox potentials as shown in lower half of Table 7.4. Using adenine as a reference, the calculated relative redox potentials are in much better agreement with experimental values (MAE = 0.10 V for CBS-QB3 and 0.07 V for B3LYP) and with each other (MAE = 0.04 V). Both the CBS-QB3 and B3LYP calculations yield a redox potential for 9-methylguanine that is 0.4–0.5 V lower than 9-methyladenine in agreement with Seidel et al. The calculations find the redox potentials of 1-methylcytidine, 1-methylthymine, and 9-methylxanthine are similar to 9-methyladenine, while 1-methyluracil is 0.3–0.4 V higher and 9-methyl-8-oxoguanine is 0.8 V lower. Replacing the methyl substituent with ribose increases the redox potentials relative to adenine by approximately 0.10 V.

7.11 Redox Potentials in Water

The determination of redox potentials of the nucleobases in aqueous solution is considerably more difficult than in acetonitrile. Experimental measurements are hampered by problems due to solubility and irreversibility. Calculations are complicated by acid-base equilibria and hydrogen bonding in aqueous solution. To help separate the effects of solvation from acid-base equilibria, we first compare the $E^\circ(\text{XH}^{+*}/\text{XH})$ redox potentials in water (Table 7.6) with the corresponding values in acetonitrile (Table 7.4). The calculated redox potentials of the nucleobases relative to adenine in water compare well with the results measured by Seidel et al. in acetonitrile (MAE = 0.13 V).¹³ The relative values of $E^\circ(\text{XH}^{+*}/\text{XH})$ calculated by CBS-QB3 and B3LYP in water are in very good agreement with each other (MAE = 0.04 V) and

compare well with the corresponding calculated values in acetonitrile (0.14 V and 0.11 V, respectively).

The present calculations as well as other calculations from the literature agree that $E^\circ(\text{XH}^{+}/\text{XH})$ in water for guanine is 0.3 – 0.4 V lower than for adenine. Likewise, $E^\circ(\text{XH}^{+}/\text{XH})$ for 8-oxoguanine is calculated to be ca. 0.62 V lower than adenine or ca. 0.3 V lower than guanine. The calculated relative redox potentials in water are 0.01 – 0.12 V higher than in acetonitrile. Most of the contributions from the solvation energies should cancel when relative redox potentials are compared. The remaining difference can be traced to changes in the radius used for oxygen in SMD; 2.168 Å is used in acetonitrile versus 1.52 Å in water, while the same radii are used for all other atoms. Adenine has no oxygen atoms, whereas the other nucleobases in the table have one or two oxygen atoms, thus affecting the differences in solvation energies between acetonitrile and water. For example, the calculated $E^\circ(\text{XH}^{+}/\text{XH})$ potential for guanine in water using the default oxygen radius of 1.52 Å is 1.20 V. By using an oxygen radius of 2.168 Å in water, the calculated $E^\circ(\text{XH}^{+}/\text{XH})$ potential for guanine is 1.13 V, thus matching the calculated $E^\circ(\text{XH}^{+}/\text{XH})$ potential for guanine in acetonitrile despite the difference in other solvation parameters.

Table 7.7 lists $E_7(\text{X}^{\bullet}, \text{H}^+/\text{XH})$ for the nucleobases in water. From the $\text{p}K_{\text{a}}$ values in Table 7.3, it is apparent that guanine, adenine, cytosine, thymine, and uracil exist primarily as neutral species at pH 7. Similarly, the oxidized forms of these bases are also neutral at pH 7. Hence, removal of an electron at pH 7 is accompanied by the loss of a proton. Implicit solvation models are generally more accurate for neutral molecules

than for ions.²⁴ In principle, solvent effects should be smaller for $E_7(X^{\bullet}, H^+/XH)$ than for $E^{\circ}(XH^{+\bullet}/XH)$.

Numerous measurements are available for guanosine in aqueous solution. The most widely quoted value is $E_7 = 1.29$ V versus SHE obtained by Steenken and Jovanovic from kinetic rate measurements.⁹ Langmaier et al. obtained $E_7 = 1.16$ V for guanosine and 1.18 V for 2'-deoxyguanosine from equilibria with $Ru(bpy)_3^{3+/2+}$.⁷³ Faraggi et al. reported $E_7 = 1.17$ V for deoxyguanosine by cyclic voltammetry.¹⁰ Several measurements are also available for guanosine monophosphate (GMP). Oliveira-Brett et al. reported E_p for nucleotides by differential pulsed voltammetry; however, the peak values for these irreversible oxidations would have to be corrected for scan rates etc. to estimate E_7 .⁷ Fukuzumi et al. determined $E_7 = 1.31$ V for GMP from the kinetics of thermal and photoinduced electron transfer.⁷⁴ Faraggi et al. obtained $E_7 = 1.25$ V for GMP by cyclic voltammetry.¹⁰ Weatherly et al. measured an E_7 potential of 1.28 V for 2'-deoxyguanosine-5'-triphosphate (GTP).⁷⁵ The values measured by Langmaier et al. and Xie et al. for GMP were the same as for guanosine.^{73,76} These three groups^{10,73,76} also obtained E_7 's for guanine that were 0.13, 0.15, and 0.21 V lower than guanosine. In summary, the reported measurements support $E_7 = 1.2$ –1.3 V for guanosine and guanosine monophosphate, with guanine ca. 0.16 V lower. Fewer measurements are available for adenine. A value of 1.42 V was obtained by Steenken et al. for adenosine⁹ and by Fukuzumi for the monophosphate,⁷⁴ while Faraggi reported 1.32 V for adenine.¹⁰ More experimental data are needed for the oxidation potentials of the pyrimidine nucleobases in water, but thymine appears to be the most readily oxidized of these bases.

The E_7 redox potentials of the methyl substituted bases calculated with CBS-QB3 and B3LYP are in good agreement with each other (MAE = 0.04 V) but have significantly larger differences with experimental values. Compared to the values measured by Steenken et al.⁹ for the nucleosides, the MAE's for the calculated redox potentials in water for the methyl substituted bases (0.19 and 0.21 V for CBS-QB3 and B3LYP, respectively) are like those obtained in acetonitrile. Comparable agreement is found with the results of Fukuzumi et al. and Faraggi et al. (MAE = 0.19 V). Li et al. calculated $E_7(X^{\bullet}, H^+/XH)$ for unsubstituted bases at the B3LYP/6-311++G(2df,2p) level with COSMO-RS solvation and obtained similar agreement with the experimental values listed in Table 7.7 (MAE = 0.16 V).⁷⁷

The relative redox potentials should be less sensitive to the solvent and the substituents. Potentials relative to adenine are shown in the bottom half of Table 7.7. The redox potential of guanine is lower than adenine, but the calculated difference is significantly larger than experimental results. Since the calculated differences in the ionization potentials (Table 7.2) and the differences in $E^{\circ}(XH^+/XH)$ in acetonitrile (Table 7.4) are in good agreement with experimental results, part of the discrepancy must arise from solvent effects in water. As noted above, the SMD model uses different radii for oxygen in acetonitrile and water to try to treat specific solvent interactions. Since guanine has a carbonyl oxygen and adenine does not, this may account for some of the difference in relative redox potentials. Replacing the N9 methyl substituent with ribose decreases the difference by 0.1 V at the B3LYP level. Langmaier found a decrease of 0.23 V at the RIMP2/cc-pVDZ level and traced it to opposing changes in the ionization potential and the proton affinity on going from guanine to guanosine.⁷³

This brings the calculated difference in the guanosine and adenosine redox potentials in better agreement with experimental results. The calculated redox potential of xanthine is in good agreement with the results of Faraggi et al.¹⁰ The computed values for 8-oxoguanine are too low, but the calculated difference between guanine and 8-oxoguanine (0.53 – 0.56 V) is in good agreement with the measurements of Steenken et al. (0.55 V).⁸

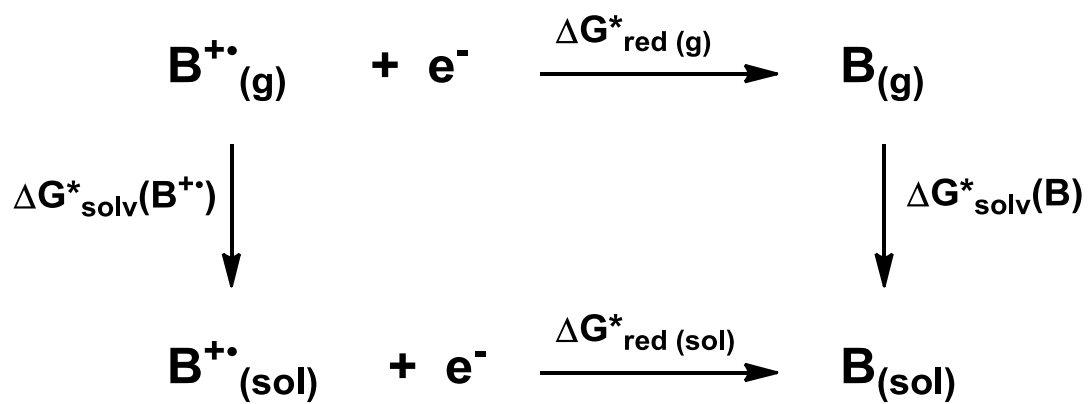
In agreement with measured values for the pyrimidine bases, calculations with the SMD solvation model indicate that redox potentials of cytosine and thymine are similar in acetonitrile, but thymine is oxidized more easily than cytosine in water at pH 7. The calculations also indicate that the redox potential of uracil is ca. 0.3 V higher than thymine in acetonitrile and in water. The experimental difference is 0.29 V in acetonitrile but only 0.05 V in water. While the calculated redox potentials of cytosine, thymine, and uracil relative to adenine are in good agreement with experimental results in acetonitrile, they are 0.1 – 0.5 V too high in water. This suggests that it may be necessary to go beyond the SMD model to treat specific solvent interactions that occur in water. Alternatively, inconsistencies among the few measured values that are available for these bases suggest that new experimental studies may be needed to clarify the situation.

7.12 Summary

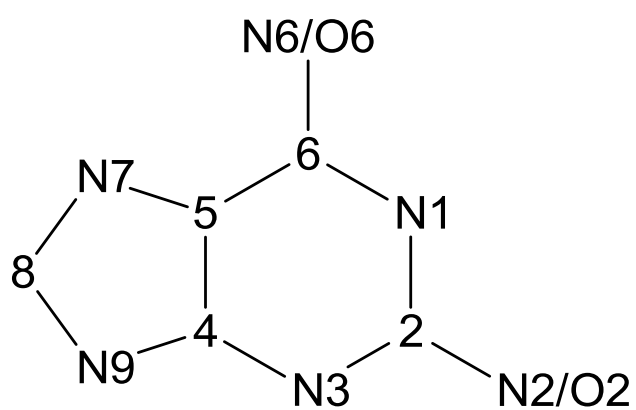
Using an appropriate thermodynamic cycle, pK_a 's and redox potentials can be calculated from gas phase basicities, adiabatic ionization potentials, and solvation energies. Equilibria between various tautomers must be taken into account when

determining the pK_a 's. In turn, the pK_a 's for the neutral and oxidized nucleobases are needed in the calculation of redox potentials at a given pH. With suitable choices of model chemistries, gas phase basicities and ionization potentials can be calculated to near chemical accuracy (MAE of 1 kcal/mol or 0.05 eV). However, implicit solvation models have greater uncertainties, especially for ions and protic solvents. The scaling of solvent cavities improves the calculation of solvation energies. After scaling, the calculated MAE's for the pK_a 's of the nucleobases are 0.7 for B3LYP and 0.9 for CBS-QB3. Nevertheless, there is still some uncertainty in the calculated and experimental pK_a 's for a number of the oxidized nucleobases. The calculated redox potentials in acetonitrile are lower than experimental results by 0.18 V for CBS-QB3 and 0.30 for B3LYP, indicating that there is still a systematic error (in part, because of the implicit solvation model). Much of this systematic error cancels if relative redox potentials are compared to experiment (MAE = 0.10 V for CBS-QB3 and 0.07 V for B3LYP for redox potentials in acetonitrile relative to adenine). For redox potentials in water, solubility problems, irreversible chemical reactions involving labile radical species, and somewhat conflicting measurements complicate the interpretation of the experimental data. Because of problems with irreversibility in electrochemical measurements of the nucleobases in water, redox potentials obtained from equilibria or kinetics measurements appear to be more reliable. For guanosine and guanosine monophosphate, $E_7 = 1.2\text{--}1.3$ V, while guanine is ca. 0.16 V lower. Adenosine and its monophosphate have $E_7 = 1.42$ V. Of the remaining standard bases, thymine seems to be the most readily oxidized in water, but there is no consensus on the measured oxidation potentials of the pyrimidine bases. The B3LYP and CBS-QB3 calculations

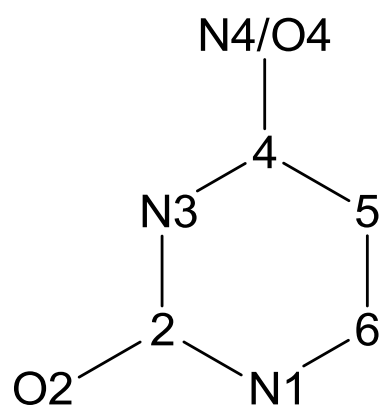
have MAE's of 0.21 and 0.19 V for $E_7(X^{\bullet}, H^+/XH)$. The larger MAE's reflect the difficulty in treating solvation effects in water with implicit models and also the greater uncertainty in the experimental values. The calculated difference between the guanine and 8-oxoguanine oxidation potentials is in good agreement with experimental values, but the calculated difference between guanine and adenine is too large. Replacing the methyl substituent with ribose changes the calculated E_7 potentials by 0.1–0.2 V. The fact that the MAE's for redox potentials in water are significantly larger than the MAE's in acetonitrile suggests that a better solvation model may be needed for water, perhaps including explicit solvent molecules. On the other hand, new measurements of the redox potentials for nucleobases, methylated nucleobases, and nucleosides in water using identical experimental conditions would help resolve some of the experimental data differences.



Scheme 7.1 Thermodynamic cycle used in the calculation of reduction potentials.

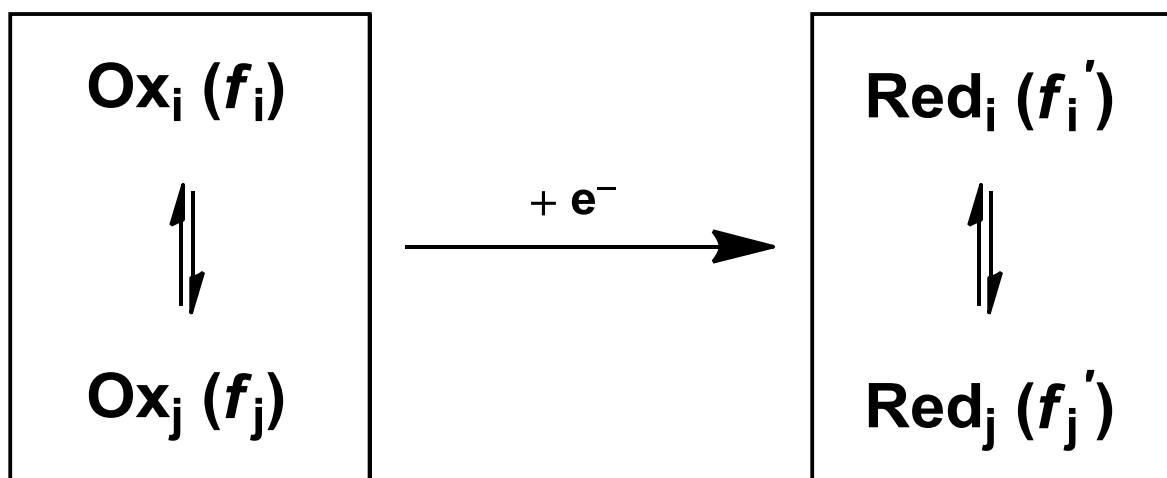


Purines

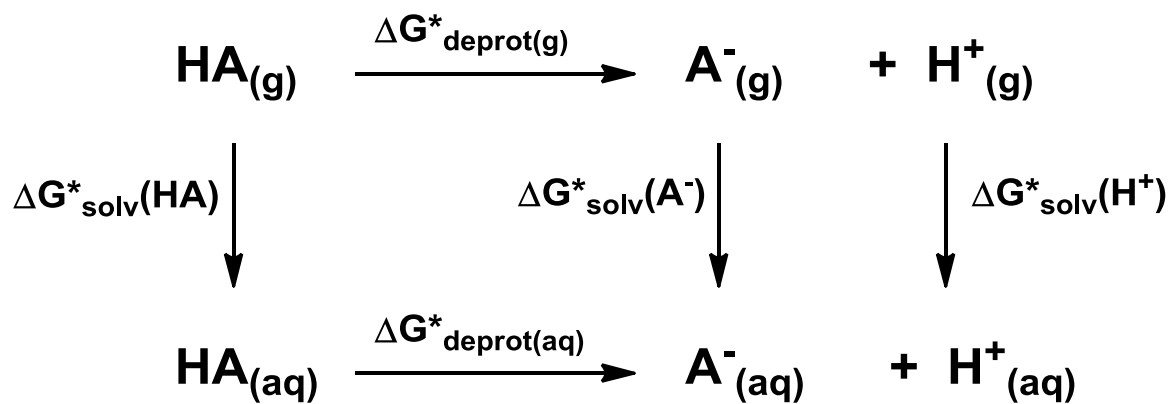


Pyrimidines

Scheme 7.2 Atomic numbering for purines and pyrimidine nucleobases. Charge, multiplicity and hydrogen atoms are not explicitly shown.



Scheme 7.3 Multiple tautomers contribute to the ensemble reduction potential.



Scheme 7.4 Thermodynamic cycle used in the calculation of pK_a 's

Table 7.1 Experimental and Calculated Gas Phase Basicities and Proton Affinities for Nucleic Acid Bases in kcal/mol

$A + H^+ \rightarrow AH^+$						
	H ⁺ site	exptl. ^a	CBS-QB3	G3B3	B3LYP ^c	B3LYP ^d
Proton Affinity						
guanine	N7	229.3	227.6 ^b	228.2 ^b	230.8	230.5 ^b
adenine	N1	225.3	223.6 ^b	224.9 ^b	227.1	226.7 ^b
cytosine	N3	227.0	226.9 ^b	227.6 ^b	229.2	228.9 ^b
1-methylcytosine	N3	230 ^e	230.1 ^c	230.9 ^c	232.7	232.4 ^c
thymine	O4	210.5	209.6 ^c	210.6 ^c	211.1	210.8 ^c
uracil	O4	208.6	206.8 ^c	207.7 ^c	208.2	207.8 ^c
<i>MAE to exptl.</i>			1.1	0.7	1.5	1.3
Gas Phase Basicity						
guanine	N7	221.7	220.2 ^b	220.9 ^b	223.3	223.0 ^b
adenine	N1	218.1	216.3 ^b	217.1 ^b	218.9	218.3 ^b
cytosine	N3	219.0	218.9 ^b	219.8 ^b	221.0	219.9 ^b
1-methylcytosine	N3	223 ^e	222.4 ^c	223.3 ^c	224.8	224.5 ^c
thymine	O4	203.2	201.7 ^c	202.6 ^c	203.2	202.8 ^c
uracil	O4	201.2	198.9 ^c	199.8 ^c	200.2	199.9 ^c
<i>MAE to exptl.</i>			1.3	0.8	1.2	0.9

$A^- + H^+ \rightarrow AH$						
	H ⁺ site	exptl. ^e	CBS-QB3	G3B3	B3LYP ^c	B3LYP ^d
Proton Affinity						
guanine	N1		337.7 ^b	338.2 ^b	340.1	339.9 ^b
guanine	N9	335	335.2 ^c	335.9 ^c	338.1	337.8 ^c
adenine	N9	335	335.3 ^c	335.9 ^c	338.5	338.2 ^c
cytosine	N1	342	344.8 ^c	345.3 ^c	347.1	346.8 ^c
thymine	N3	346	346.3 ^b	347.0 ^b	347.1	346.9 ^b
thymine	N1	335	335.4 ^c	336.2 ^c	335.9	336.6 ^c
uracil	N3	347	346.3 ^b	347.0 ^b	346.6	346.9 ^b
<i>MAE to exptl.</i>			0.8	1.2	2.4	2.2
Gas Phase Basicity						
guanine	N1		330.2 ^b	330.6 ^b	332.6	332.3 ^b
guanine	N9	328	327.7 ^c	328.4 ^c	330.6	330.3 ^c
adenine	N9	329	328.8 ^c	328.7 ^c	331.7	331.4 ^c
cytosine	N1	335	337.5 ^c	337.8 ^c	339.9	339.7 ^c
thymine	N3	339	338.5 ^b	339.1 ^b	339.3	339.0 ^b
thymine	N1	328	327.9 ^c	328.7 ^c	328.4	329.1 ^c
uracil	N3		338.1 ^b	338.6 ^b	338.7	338.4 ^b
<i>MAE to exptl.</i>			0.7	0.9	2.2	2.1

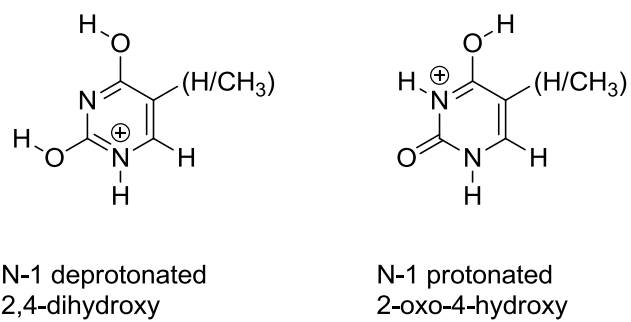
^a Ref.⁷⁸⁻⁸¹ Experimental error of ± 2 kcal/mol. ^b Ref.⁵⁴ ^c Present study. ^d Calculated using the B3LYP/6-311++(3df,2p)//B3LYP/6-31++G(d,p) level of theory.⁵⁴ ^e Experimental error of ± 3 kcal/mol.^{56,82,83}

Table 7.2 Experimental and Calculated Gas Phase Adiabatic (AIE) and Vertical Ionization Energies (VIE) for Nucleic Acid Bases in eV

	exptl. ^{a,b}	<i>adiabatic</i>				
		CBS-QB3	G3-B3	B3LYP ^c	BP86 ^c	PMP2 ^d
guanine	7.77	7.85	7.88	7.66	7.65	7.90
adenine	8.26	8.28	8.30	8.07	8.04	8.23
cytosine	8.68	8.71	8.83	8.56	8.50	8.78
thymine	8.87	8.91	8.93	8.72	8.64	8.74
uracil	9.32	9.32	9.35	9.21	9.14	9.36
<i>MAE to exptl.^e</i>		<i>0.03</i>	<i>0.08</i>	<i>0.14</i>	<i>0.19</i>	<i>0.08</i>
9-methylguanine		7.65		7.47		
9-methyladenine		8.10		7.89		
1-methylcytosine		8.35		8.27		
1-methylthymine		8.54		8.38		
1-methyluracil		8.92		8.81		
guanosine				7.24		
adenosine				7.84		
cytidine				8.05		
thymidine				7.96		
uridine				8.28		

	exptl.	<i>vertical</i>				
		CBS-QB3	G3-B3	B3LYP ^j	BP86 ^j	PMP2
guanine	8.28 ^e	8.33	8.29	8.10	8.41	8.33 ^d
adenine	8.48 ^f	8.51	8.47	8.25	8.21	8.62 ^d
cytosine	8.89 ^g	8.86	8.91	8.69	8.64	8.69 ^d
thymine	9.20 ^h	9.18	9.21	9.00	8.88	9.07 ^d
uracil	9.59 ⁱ	9.58	9.56	9.45	9.29	9.43 ^d
<i>MAE to exptl.</i>		<i>0.03</i>	<i>0.02</i>	<i>0.18</i>	<i>0.23</i>	<i>0.13</i>
9-methylguanine	8.02 ^e	8.03	8.08	7.81	7.76	8.17
9-methyladenine	8.39 ^f	8.37	8.30	8.09	8.03	8.45
1-methylcytosine	8.65 ^g	8.54	8.70	8.43	8.36	8.49
1-methylthymine	8.79	8.83	8.85	8.64	8.52	8.69
1-methyluracil	9.2	9.15	9.21	9.04	8.93	9.01
<i>MAE to exptl.</i>		<i>0.05</i>	<i>0.05</i>	<i>0.21</i>	<i>0.29</i>	<i>0.13</i>

^a Ref.⁸⁴ Estimated accuracy of ± 0.05 V. ^b A separate set of values is given by NIST: guanine 7.85 eV; adenine 8.3 ± 0.1 eV; cytosine 8.45 eV; thymine 9.0 ± 0.1 eV; uracil 9.2 ± 0.1 eV.⁷⁸ ^c For the given level of theory, the calculated AIE is the difference in energy between the radical cation and neutral species where the energy of each species is the sum of the $\Delta G_{0 \rightarrow 298K}$ correction using the 6-31+G(d,p) basis set and E_{0K} using the aug-cc-pVTZ basis set on the geometry optimized at the 6-31+G(d,p) basis set. ^d Crespo-Hernandez et al. study calculated at PMP2/6-31++G(d,p) level of theory where adiabatic energies are for ZPE at HF/6-31++G(d,p) level of theory.⁶⁰ ^e Ref.⁶² ^f Ref.⁶³ ^g Ref.⁶⁴ ^h Ref.⁶⁵ ⁱ Ref.⁶⁶ ^j For the given level of theory, the calculated VIE is the difference in E_{0K} using the aug-cc-pVTZ basis set between the radical cation and neutral species at the geometry of the neutral species optimized using the 6-31+G(d,p) basis set.



Scheme 7.5 Lowest energy gas phase tautomers of protonated uracil/thymine.

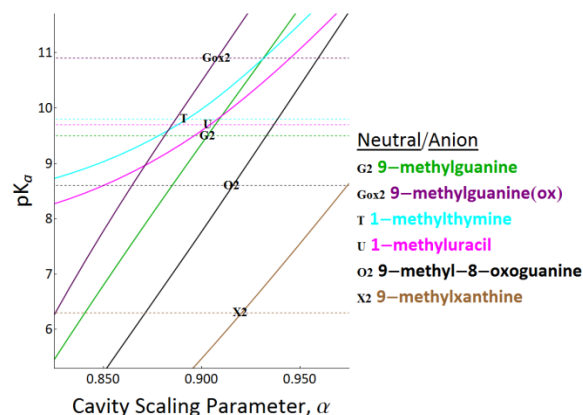
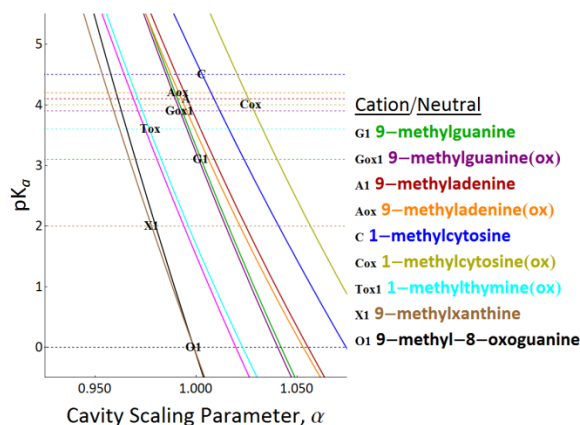
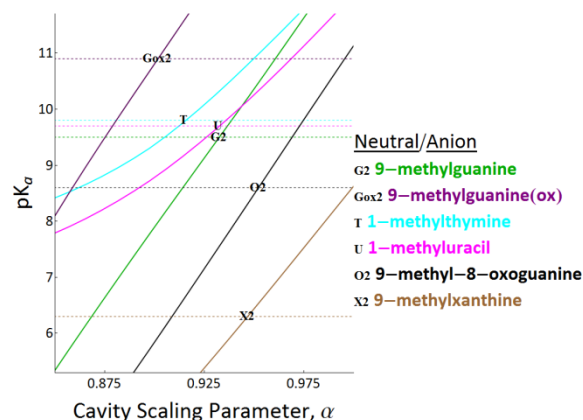
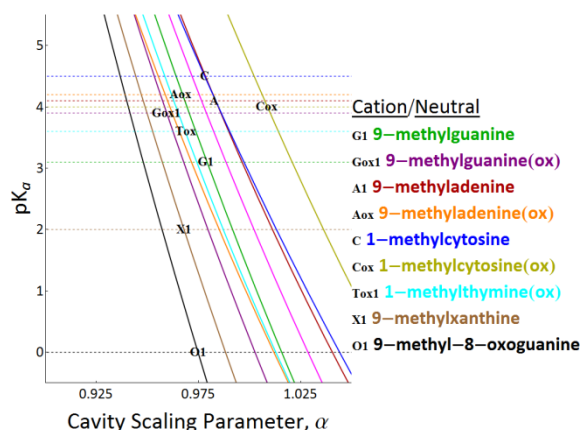
B3LYP**CBS-QB3**

Figure 7.1 Effect of changing the solvent cavity parameter on the calculated pK_a for the B3LYP and CBS-QB3 methodologies. Each solid curve represents a third order polynomial fit of calculated pK_a data points collected at scaled solvent cavities. For all neutral species shown, the solvent cavity was left unscaled ($\alpha=1.0$), while the solvent cavity scaling values for ionic species were varied. Horizontal dotted lines represent experimentally measured pK_a 's. The intersection of a calculated pK_a curve with an experimental pK_a (depicted by a symbol specific to the nucleobase) indicate the optimal solvent cavity scaling value for a given nucleobase. The optimal solvent cavity scaling parameters for B3LYP are 0.9, 1.0 and 1.0 for anionic, cationic and neutral species, respectively. The optimal scaling factors for CBS-QB3 are 0.925, 0.975 and 1.0 for anionic, cationic and neutral species, respectively.

Table 7.3 Experimental and Calculated pK_a Values

	exptl. <i>methyl</i> <i>subst.</i>	exptl. <i>ribose</i> <i>subst.</i>	CBS-QB3 <i>methyl</i> <i>subst.</i>	B3LYP <i>methyl</i> <i>subst.</i>	B3LYP ^j <i>ribose</i> <i>subst.</i>	other calcd. <i>unsubst.</i>
guanine						
pK_a 1	3.1 ^a	1.9 ^d	3.50	3.20	1.47	3.4 ^k , 3.15 ^m
pK_a 2	9.5 ^a	9.2 ^d	9.10	9.36		9.6 ^k , 9.60 ^m
pK_a 1 _{ox}		3.9 ^e	2.53	3.34	2.61	4.01 ^l
pK_a 2 _{ox}		10.9 ^e	11.88	10.32		
adenine						
pK_a 1	4.1 ^b	3.6 ^f	4.89	3.79	4.43	4.2 ^k
pK_a ox		4.2 ^g	2.82	3.90	3.18	2.01 ^l
cytosine						
pK_a 1	4.5	4.2 ^f	4.80	4.71	4.54	4.2 ^k
pK_a ox		~4 ^e	6.72	5.69	6.46	3.37 ^l
thymine						
pK_a		9.8 ^f	9.96	9.98		10.5 ^k
pK_a ox		3.6 ^e	3.04	1.69	2.88	6.40 ^l
uracil						
pK_a	9.7	9.2 ^f	9.33	9.59		
pK_a ox			4.06	1.52	1.61	
xanthine						
pK_a 1	2.0 ^c	1.1 ^c	1.31	0.44	-1.46	
pK_a 2	6.3 ^c	5.7 ^c	5.29	4.76		
pK_a 1 _{ox}			-4.03	-5.52	-5.98	
pK_a 2 _{ox}			7.54	6.98		
8-oxoguanine						
pK_a 1		0.1 ^h	-0.04	-0.12	-1.96	0.22 ^m
pK_a 2		8.6 ^h	7.09	8.13		8.0 ^k , 8.69 ^m
pK_a 1 _{ox}			0.06	-0.28	-0.54	6.83 ^l
pK_a 2 _{ox}		6.6 ⁱ	4.83	5.50		
MAE to exptl.			0.88	0.66	1.31	

a Ref.⁸⁵ b Ref.⁸⁶ c Ref.⁸⁷ d Ref.⁸⁸ e Ref.¹¹ f Ref.⁴⁸ g Value is for deoxyribose substituted species.⁸⁹ h Ref.⁹⁰ i Ref.⁸ j Computed using B3LYP gas phase free energies for nucleosides. Solvent cavities were not scaled for calculations involving nucleosides. ^k Verdolino et al. calculated ensemble pK_a 's for non-methylated nucleobases using Boltzmann-weighting for alternate tautomers at the B3LYP level of theory.⁴⁹ ^l Baik et al. calculated tautomer specific pK_a 's for nucleobases at PW91 level of theory.⁵⁹ ^m Goddard and coworkers calculated ensemble pK_a 's for non-methylated nucleobases using Boltzmann-weighting for alternate tautomers at the B3LYP level of theory.^{50,51}

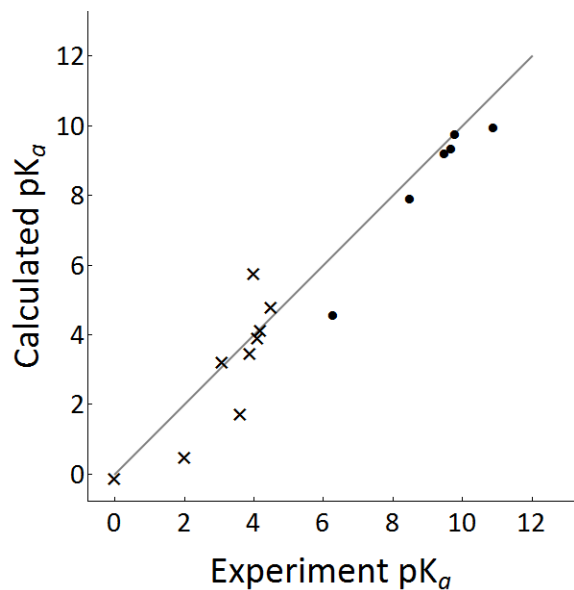
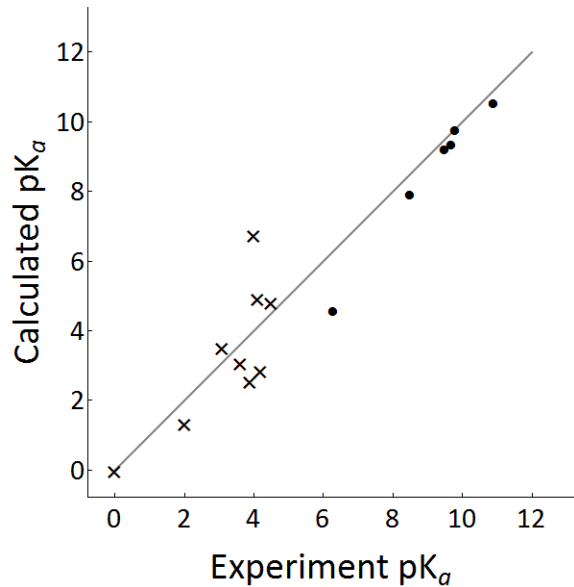
B3LYP**CBS-QB3**

Figure 7.2 Linear correlation plots of calculated pK_a 's versus experimental pK_a 's. Cation deprotonations are signified by a cross and neutral deprotonations are signified by a dot.

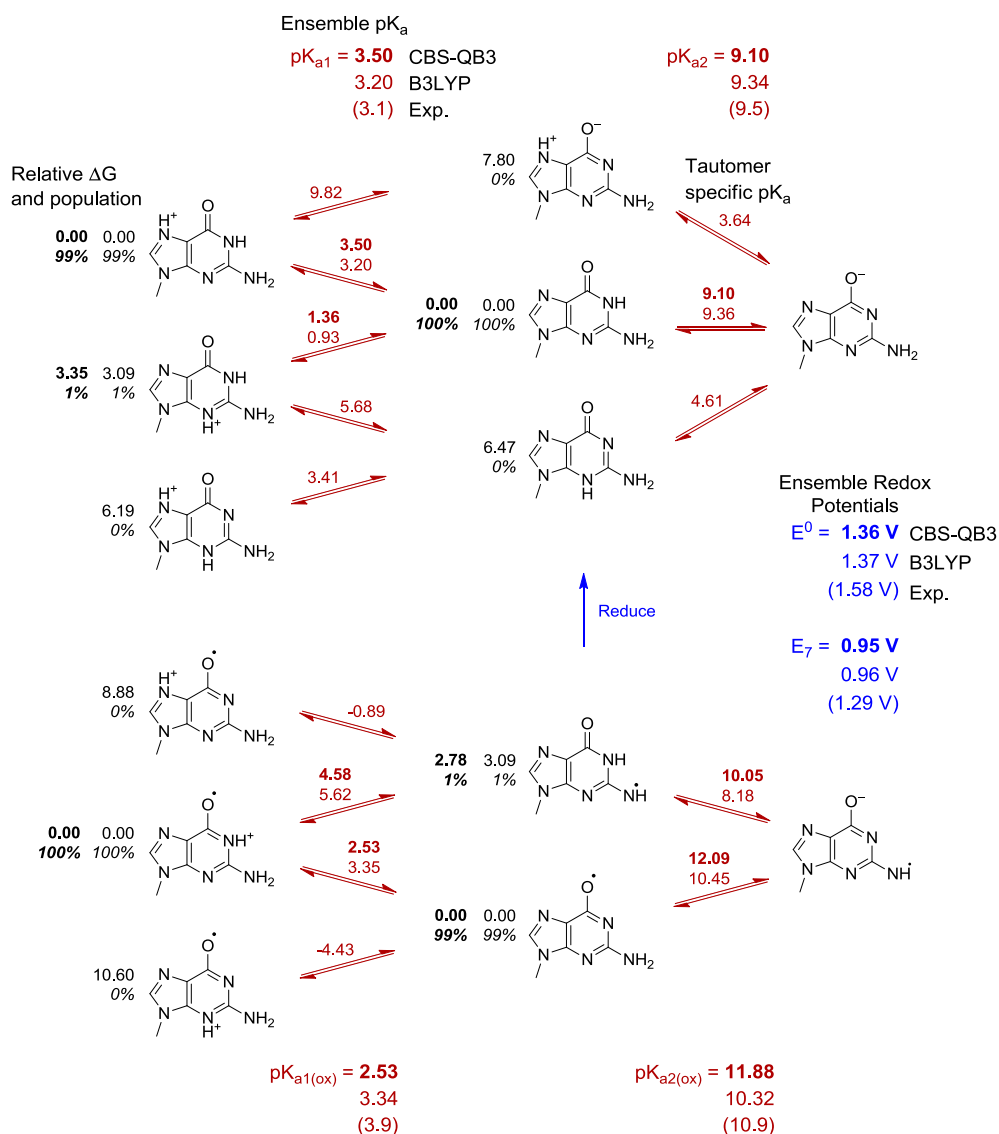


Figure 7.3 Calculated pK_a 's and oxidation potentials for 9-methylguanine. Experimentally measured values are shown in parenthesis. CBS-QB3 calculated values are shown in bold face text, while B3LYP calculated values are shown in regular text. Black numbers to the left of each isomer indicate the relative free energy in kcal/mol (regular font) and the population in percentage (italics). Red numbers shown in between isomers indicate calculated pK_a 's for the specific isomers, while red numbers on the top and bottom of the figure indicate the ensemble averaged pK_a for each acid/base equilibrium. Blue numbers shown between the reduced (top) and oxidized species (bottom) indicate calculated one-electron oxidation potentials E^0 and E_7 .

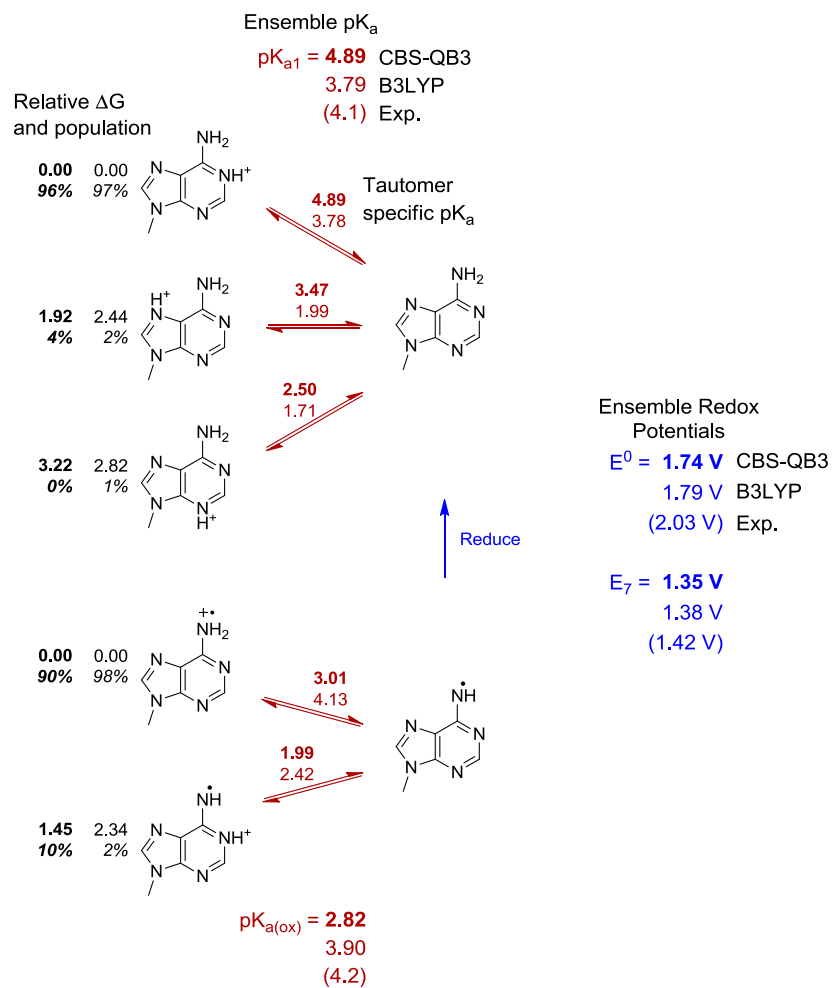


Figure 7.4 Calculated pK_a 's and oxidation potentials for 9-methyladenine. See Figure 7.3 caption for details.

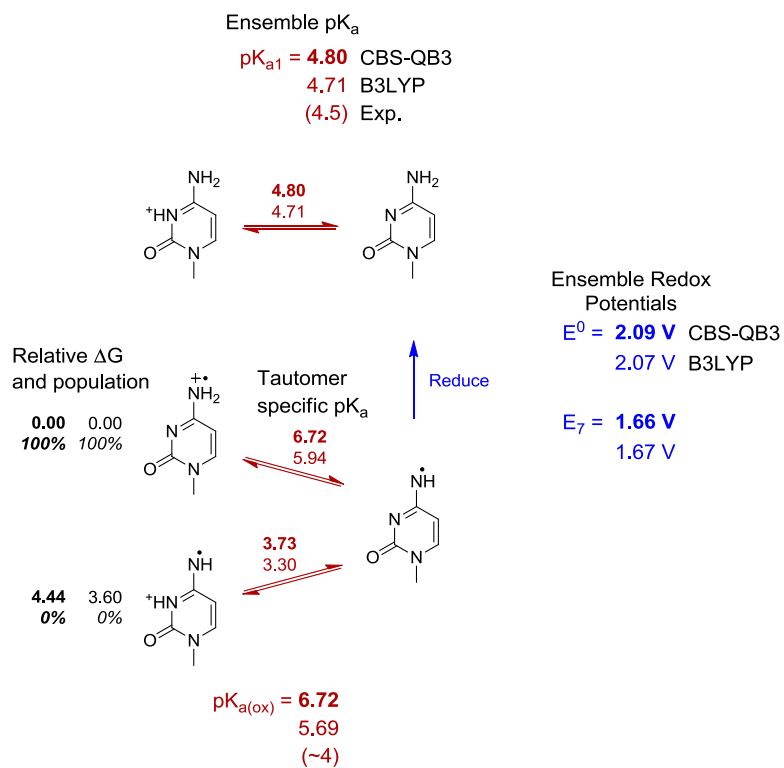


Figure 7.5 Calculated pK_a 's and oxidation potentials for 1-methylcytosine. See Figure 7.3 caption for details.

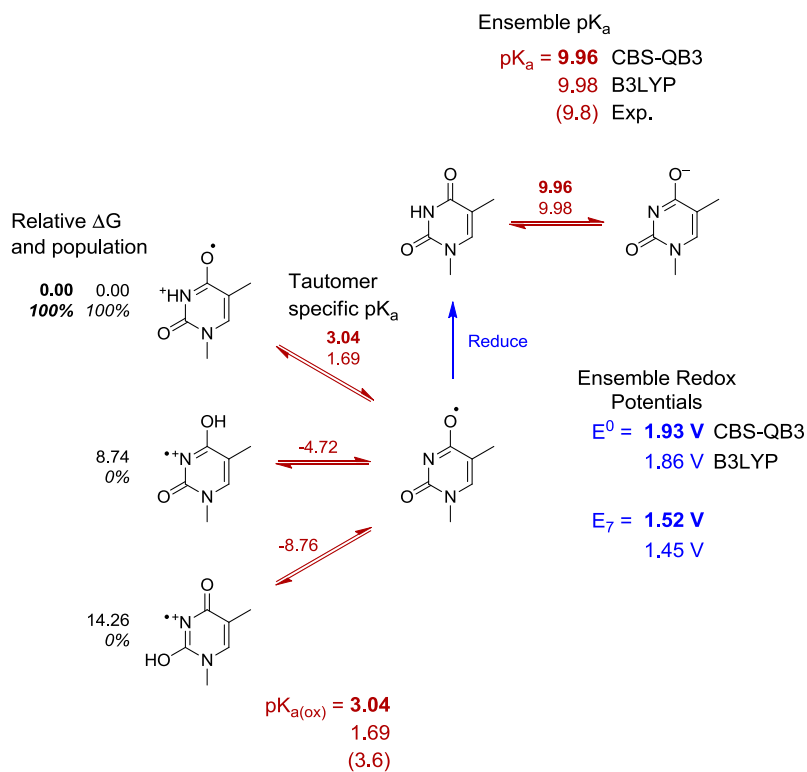


Figure 7.6 Calculated pK_a 's and oxidation potentials for 1-methylthymine. See Figure 7.3 caption for details.

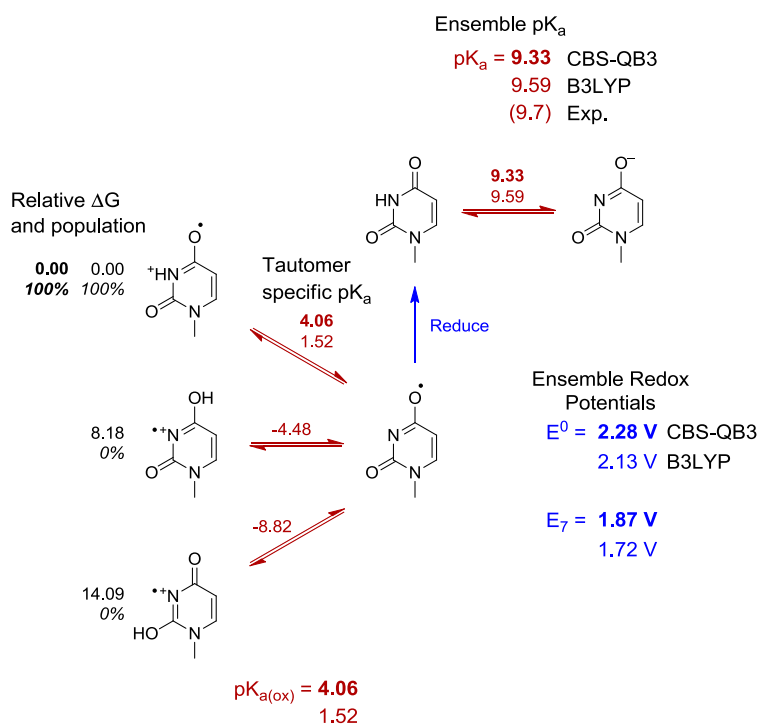


Figure 7.7 Calculated pK_a 's and oxidation potentials for 1-methyluracil. See Figure 7.3 caption for details.

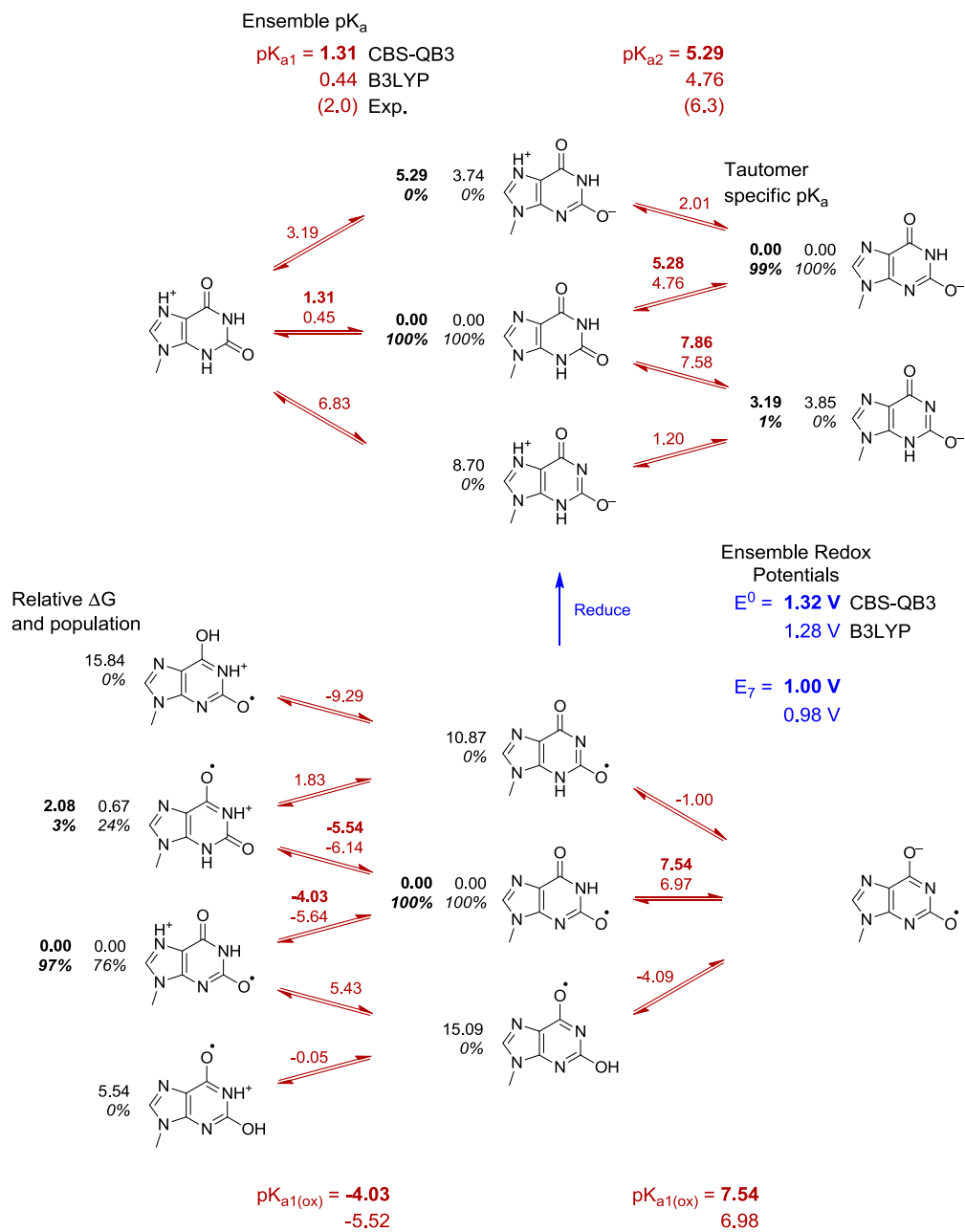


Figure 7.8 Calculated pK_a 's and oxidation potentials for 9-methylxanthine. See Figure 7.3 caption for details.

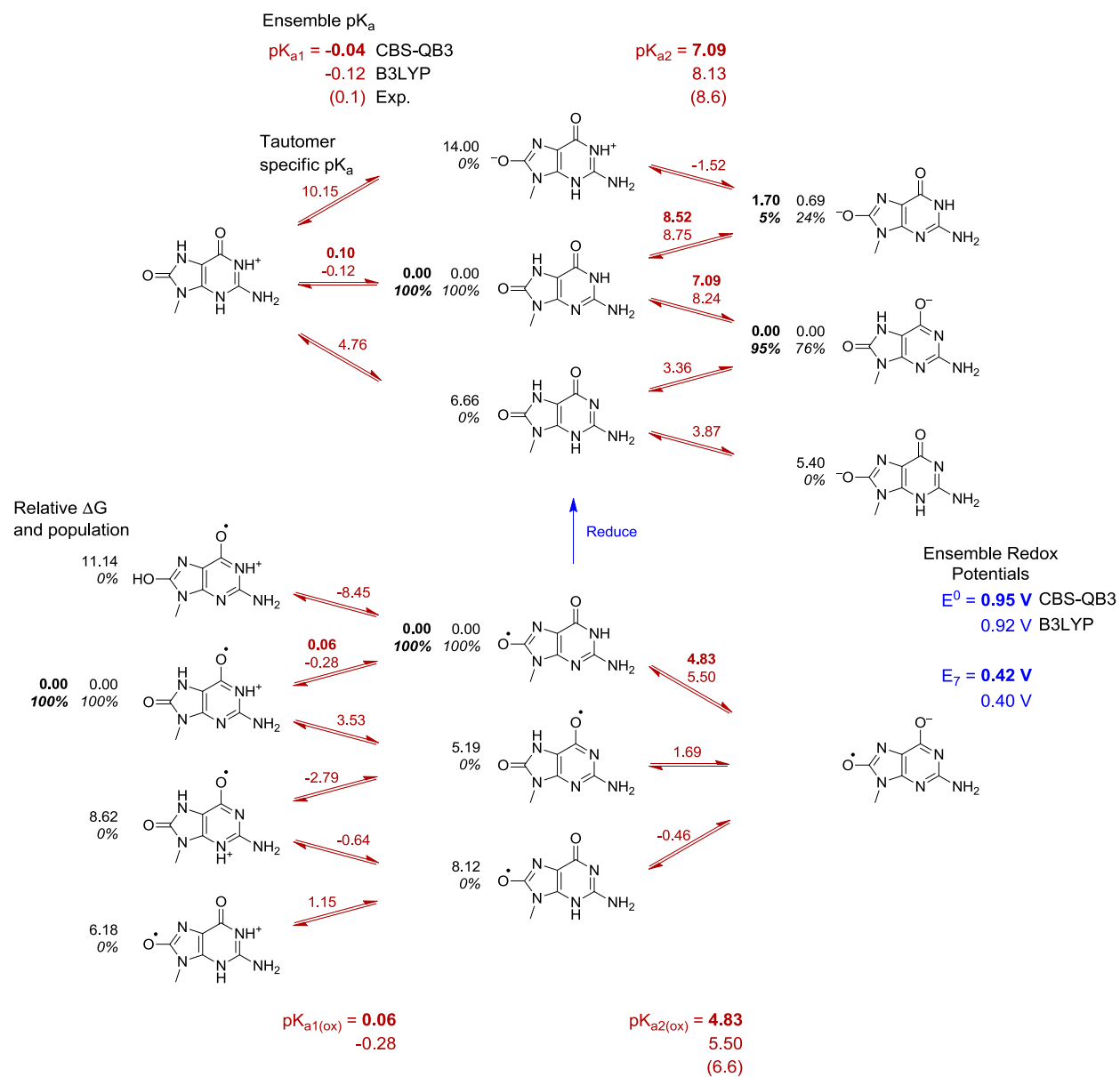


Figure 7.9 Calculated pK_a 's and oxidation potentials for 9-methyl-8-oxoguanine. See Figure 7.3 caption for details.

Table 7.4 Experimental and Calculated $E^\circ(\text{XH}+\bullet/\text{XH})$ Reduction Potentials in Acetonitrile Solution in eV

	exptl. ^b	CBS-QB3 ^c	B3LYP ^d	B3LYP ^e
	<i>deoxyribose</i> <i>subst.</i>	<i>methyl</i> <i>subst.</i>	<i>methyl</i> <i>subst.</i>	<i>ribose</i> <i>subst.</i>
<i>reduction potential versus SCE</i>				
guanine	1.25	1.14	0.96	1.04
adenine	1.72	1.58	1.44	1.41
cytosine	1.90	1.58	1.50	1.57
thymine	1.87	1.63	1.51	1.60
uracil	>2.15	1.91	1.81	1.88
xanthine		1.56	1.41	1.48
8-oxoguanine		0.80	0.64	0.68
<i>MAE to exptl.</i>		<i>0.21</i>	<i>0.33</i>	<i>0.28</i>
<i>reduction potential relative to adenine</i>				
guanine	−0.47	−0.44	−0.48	−0.37
adenine	0.00	0.00	0.00	0.00
cytosine	0.18	0.01	0.05	0.16
thymine	0.15	0.05	0.07	0.19
uracil	0.43	0.34	0.38	0.47
xanthine		−0.02	−0.04	0.07
8-oxoguanine		−0.77	−0.80	−0.73
<i>MAE to exptl.</i>		<i>0.10</i>	<i>0.07</i>	<i>0.05</i>

^a Potentials are reported against the absolute potential of SCE in acetonitrile solution (4.429 V).²⁰ ^b Seidel et al. study determined potentials for DNA nucleosides by cyclic voltammetry in acetonitrile solution.¹³ ^c Present study calculated values were obtained for N-methyl substituted bases using an unscaled solvent cavity and CBS-QB3 gas phase free energies. ^d Present study calculated values were obtained for N-methyl substituted bases using an unscaled solvent cavity and B3LYP gas phase free energies. ^e Present study calculated values were obtained for nucleosides using an unscaled solvent cavity and B3LYP gas phase free energies.

Table 7.5 Reference Compound Reduction Potentials in Aqueous and Acetonitrile Solution and Gas Phase Adiabatic Ionization Energies in eV

<i>Adiabatic Ionization Energies</i>			
	<i>exptl.</i>	CBS-QB3	B3LYP
1-methylindole	7.40 ^a	7.59	7.35
indole	7.76 ^a	7.80	7.56
phenol	8.51 ^b	8.54	8.30
thioanisole	7.93 ^c	7.96	7.70
<i>MAD to exptl.</i>		0.07	0.17
	<i>exptl.</i>	CBS-QB3	B3LYP
4-methylaniline	7.37 ^d	7.46	7.22
anisole	8.24 ^c	8.26	8.03
naphthalene	8.14 ^e	8.15	7.87
<i>MAD to exptl.</i>		0.04	0.21
<i>Standard Reduction Potentials</i> <i>E°(XH⁺/XH)</i>			
<i>Aqueous[†]</i>			
	<i>exptl.</i>	CBS-QB3	B3LYP
1-methylindole	1.23 ^g	1.21	0.97
indole	1.24 ^g	1.32	1.08
phenol ^h	1.35 ⁱ	1.26	1.19
thioanisole	1.45 ^j	1.54	1.29
<i>MAD to exptl.</i>		0.07	0.19
<i>Acetonitrile^k</i>			
	<i>exptl.</i>	CBS-QB3	B3LYP
4-methylaniline	0.78 ^l	0.81	0.58
anisole	1.62 ^m	1.62	1.35
naphthalene	1.54 ⁿ	1.57	1.26
<i>MAD to exptl.</i>		0.02	0.25

^a Ref.⁹¹ ^b Ref.⁹² ^c Ref.⁹³ ^d Ref.⁹⁴ ^e Ref.⁹⁵ ^f Potentials are reported against the absolute potential of SHE in aqueous solution (4.281 V).²¹ ^g Ref.⁹⁶ ^h Potentials shown for phenol are for the $E^\circ(X^+/XH)$ redox couple. ⁱ Ref.⁹⁷ ^j Ref.⁹⁸ ^k Potentials are reported against the absolute potential of SCE in acetonitrile solution (4.429 V).²⁰ ^l Ref.⁹⁹ ^m Ref.¹⁰⁰ ⁿ Ref.¹⁰¹

Table 7.6 Aqueous Solution Calculated $E^\circ(\text{XH}^{+}/\text{XH})$ Potential Relative to Adenine in eV

	<i>present study</i>			
	CBS-QB3	B3LYP	B3LYP	B3LYP
	<i>methyl subst.</i>	<i>methyl subst.</i>	<i>ribose subst.</i>	<i>unsubst.</i>
guanine	−0.36	−0.39	−0.29	−0.37
adenine	0.00	0.00	0.00	0.00
cytosine	0.11	0.23	0.22	0.32
thymine	0.18	0.19	0.28	0.27
uracil	0.47	0.49	0.53	0.57
xanthine	0.02	0.04	0.16	
8-oxoguanine	−0.62	−0.63	−0.62	
<i>other computational studies</i>				
	PW91 ^a	PMP2 ^b	M06-2X ^c	
	<i>unsubst.</i>	<i>unsubst.</i>	<i>unsubst.</i>	
guanine	−0.34	−0.39	−0.37	
adenine	0.00	0.00	0.00	
cytosine	0.44	0.10	0.33	
thymine	0.47	0.24	0.23	
uracil		0.46		
xanthine				
8-oxoguanine	−0.63			

^a Baik et al.⁵⁹ calculated potentials of nucleobases using PW91 level of theory with the COSMO solvation model. ^b Crespo-Hernandez et al.⁶⁰ calculated potentials of nucleobases using PMP2/6-31++G(d,p) level of theory with the PCM solvation model. Molecules were optimized in the gas phase only. ^c Paukku and Hill¹⁰² calculated potentials of nucleobases using the M06-2X/6-31++G(d,p) level of theory with the PCM solvation model.

Table 7.7 Experimental and Calculated E_7 Reduction Potentials in Aqueous Solution in eV

	<i>exptl.</i>	<i>exptl.</i>	<i>exptl.</i>	<i>Present Study</i>	<i>Present Study</i>	<i>Present Study</i>	<i>Li et al.</i>
	<i>Steenken et al.^b</i>	<i>Fukuzumi et al.^c</i>	<i>Faraggi et al.^d</i>	CBS-QB3 ^f	B3LYP ^f	B3LYP ^g	B3LYP ^h
	<i>ribose subst.</i>	<i>deoxyribose nucleotide</i>	<i>unsubst.</i>	<i>methyl subst.</i>	<i>methyl subst.</i>	<i>ribose subst.</i>	<i>unsubst.</i>
<i>Reduction potential versus SHE</i>							
guanine	1.29	1.31	1.04 ^e	0.95	0.96	1.03	1.06
adenine	1.42	1.42	1.32	1.35	1.38	1.35	1.34
cytosine	~ 1.6	1.50	1.44 ^e	1.66	1.67	1.77	1.72
thymine	~ 1.7	1.45	1.29	1.52	1.45	1.61	1.38
uracil			1.34 ^e	1.87	1.72	1.78	1.58
xanthine			0.93	1.00	0.98		
8-oxo guanine	0.74			0.42	0.40	0.50	0.83
<i>Reduction potential relative to adenine</i>							
guanine	-0.13	-0.11	-0.28	-0.40	-0.42	-0.32	-0.28
adenine	0.00	0.00	0.00	0.00	0.00	0.00	0.00
cytosine	~ 0.18	0.19	0.12	0.31	0.29	0.42	0.38
thymine	~ 0.28	0.14	-0.03	0.17	0.07	0.26	0.04
uracil			0.02	0.51	0.34	0.43	0.24
xanthine			-0.39	-0.35	-0.40		
8-oxo guanine	-0.68			-0.93	-0.98	-0.85	-0.51

^a Potentials are reported against the absolute potential of SHE in aqueous solution (4.281 V).

^b Steenken et al. measured nucleoside potentials using kinetic rate measurement in aqueous solution.^{8,9}

^c Fukuzumi et al. measured DNA nucleotide potentials by cyclic voltammetry in aqueous solution.⁷⁴

^d Faraggi et al. measured nucleobase potentials by cyclic voltammetry in aqueous solution.¹⁰ ^e Values are estimated based on an extrapolation of 0.06 V per pH from measured potentials at higher pH.¹⁰

^f Calculated for N-methylated nucleobases from the corresponding computed values for E° and pK_a using eq (16). ^g Calculated for nucleosides from the corresponding computed E° corrected by the hydrogen ion concentration, $\log[H^+]$. ^h Li et al. calculated values for non-methylated nucleobases at the B3LYP/6-311++G(2df,2p)/B3LYP/6-31+G(d) level of theory.⁷⁷ Potentials are reported against an absolute SHE potential of 4.43 V.

7.13 References

1. Pratviel, G.; Meunier, B. Guanine oxidation: One- and two-electron reactions. *Chem.-Eur. J.* **2006**, *12*, 6018-6030.
2. Gimisis, T.; Cismas, C. Isolation, characterization, and independent synthesis of guanine oxidation products. *Eur. J. Org. Chem.* **2006**, 1351-1378.
3. Burrows, C. J.; Muller, J. G. Oxidative nucleobase modifications leading to strand scission. *Chem. Rev.* **1998**, *98*, 1109-1151.
4. Cadet, J.; Berger, M.; Douki, T.; Morin, B.; Raoul, S.; Ravanat, J. L.; Spinelli, S. Effects of UV and visible radiation on DNA - Final base damage. *Biol. Chem.* **1997**, *378*, 1275-1286.
5. Breen, A. P.; Murphy, J. A. Reactions of oxyl radicals with DNA. *Free Radic. Biol. Med.* **1995**, *18*, 1033-1077.
6. Ames, B. N.; Shigenaga, M. K.; Hagen, T. M. Oxidants, antioxidants, and the degenerative diseases of aging. *Proc. Natl. Acad. Sci. U. S. A.* **1993**, *90*, 7915-7922.
7. Oliveira-Brett, A. M.; Piedade, J. A. P.; Silva, L. A.; Diculescu, V. C. Voltammetric determination of all DNA nucleotides. *Anal. Biochem.* **2004**, *332*, 321-329.
8. Steenken, S.; Jovanovic, S. V.; Bietti, M.; Bernhard, K. The trap depth (in DNA) of 8-oxo-7,8-dihydro-2'-deoxyguanosine as derived from electron-transfer equilibria in aqueous solution. *J. Am. Chem. Soc.* **2000**, *122*, 2373-2374.
9. Steenken, S.; Jovanovic, S. V. How easily oxidizable is DNA? One-electron reduction potentials of adenosine and guanosine radicals in aqueous solution. *J. Am. Chem. Soc.* **1997**, *119*, 617-618.

10. Faraggi, M.; Broitman, F.; Trent, J. B.; Klapper, M. H. One-electron oxidation reactions of some purine and pyrimidine bases in aqueous solutions. Electrochemical and pulse radiolysis studies. *J. Phys. Chem.* **1996**, *100*, 14751-14761.
11. Steenken, S. Purine-bases, nucleosides, and nucleotides - Aqueous-solution redox chemistry and transformation reactions of their radical cations and e- and OH adducts. *Chem. Rev.* **1989**, *89*, 503-520.
12. Jovanovic, S. V.; Simic, M. G. One-electron redox potentials of purines and pyrimidines. *J. Phys. Chem.* **1986**, *90*, 974-978.
13. Seidel, C. A. M.; Schulz, A.; Sauer, M. H. M. Nucleobase-specific quenching of fluorescent dyes. 1. Nucleobase one-electron redox potentials and their correlation with static and dynamic quenching efficiencies. *J. Phys. Chem.* **1996**, *100*, 5541-5553.
14. Sviatenko, L.; Isayev, O.; Gorb, L.; Hill, F.; Leszczynski, J. Toward Robust Computational Electrochemical Predicting the Environmental Fate of Organic Pollutants. *J. Comput. Chem.* **2011**, *32*, 2195-2203.
15. Namazian, M.; Lin, C. Y.; Coote, M. L. Benchmark Calculations of Absolute Reduction Potential of Ferricinium/Ferrocene Couple in Nonaqueous Solutions. *J. Chem. Theory Comput.* **2010**, *6*, 2721-2725.
16. Lewis, A.; Bumpus, J. A.; Truhlar, D. G.; Cramer, C. J. Molecular Modeling of environmentally important processes: Reduction potentials. *J. Chem. Educ.* **2004**, *81*, 596-604.

17. Lewis, A.; Bumpus, J. A.; Truhlar, D. G.; Cramer, C. J. Molecular modeling of environmentally important processes: Reduction potentials (vol 81, pg 596, 2004). *J. Chem. Educ.* **2007**, *84*, 934-934.
18. Ho, J. M.; Coote, M. L. A universal approach for continuum solvent pK(a) calculations: are we there yet? *Theor. Chem. Acc.* **2010**, *125*, 3-21.
19. Ho, J. M.; Coote, M. L. First-principles prediction of acidities in the gas and solution phase. *Wiley Interdiscip. Rev.-Comput. Mol. Sci.* **2011**, *1*, 649-660.
20. Isse, A. A.; Gennaro, A. Absolute Potential of the Standard Hydrogen Electrode and the Problem of Interconversion of Potentials in Different Solvents. *J. Phys. Chem. B* **2010**, *114*, 7894-7899.
21. Kelly, C. P.; Cramer, C. J.; Truhlar, D. G. Aqueous solvation free energies of ions and ion-water clusters based on an accurate value for the absolute aqueous solvation free energy of the proton. *J. Phys. Chem. B* **2006**, *110*, 16066-16081.
22. Camaioni, D. M.; Schwerdtfeger, C. A. Comment on "Accurate experimental values for the free energies of hydration of H^+ , OH^- , and H_3O^+ ". *J. Phys. Chem. A* **2005**, *109*, 10795-10797.
23. Roy, L. E.; Jakubikova, E.; Guthrie, M. G.; Batista, E. R. Calculation of One-Electron Redox Potentials Revisited. Is It Possible to Calculate Accurate Potentials with Density Functional Methods? *J. Phys. Chem. A* **2009**, *113*, 6745-6750.
24. Marenich, A. V.; Cramer, C. J.; Truhlar, D. G. Universal Solvation Model Based on Solute Electron Density and on a Continuum Model of the Solvent Defined by

- the Bulk Dielectric Constant and Atomic Surface Tensions. *J. Phys. Chem. B* **2009**, *113*, 6378-6396.
25. Bennaim, A.; Marcus, Y. Solvation thermodynamics of nonionic solutes. *J. Chem. Phys.* **1984**, *81*, 2016-2027.
 26. Stephens, P. J.; Devlin, F. J.; Chabalowski, C. F.; Frisch, M. J. Ab-initio calculations of vibrational absorption and circular-dichroism spectra using density-functional force-fields. *J. Phys. Chem.* **1994**, *98*, 11623-11627.
 27. Becke, A. D. Density-functional thermochemistry. 3. The role of exact exchange. *J. Chem. Phys.* **1993**, *98*, 5648-5652.
 28. Lee, C. T.; Yang, W. T.; Parr, R. G. Development of the Colle-Salvetti correlation-energy formula into a functional of the electron-density. *Phys. Rev. B* **1988**, *37*, 785-789.
 29. Becke, A. D. Density-functional exchange-energy approximation with correct asymptotic-behavior. *Phys. Rev. A* **1988**, *38*, 3098-3100.
 30. Vosko, S. H.; Wilk, L.; Nusair, M. Accurate spin-dependent electron liquid correlation energies for local spin-density calculations - A critical analysis. *Can. J. Phys.* **1980**, *58*, 1200-1211.
 31. Francel, M. M.; Pietro, W. J.; Hehre, W. J.; Binkley, J. S.; Gordon, M. S.; Defrees, D. J.; Pople, J. A. Self-consistent molecular-orbital methods. 23. A polarization-type basis set for 2nd-row elements. *J. Chem. Phys.* **1982**, *77*, 3654-3665.
 32. Gordon, M. S. The isomers of silacyclopropane. *Chem. Phys. Lett.* **1980**, *76*, 163-168.

33. Hariharan, P. C.; Pople, J. A. Accuracy of AH equilibrium geometries by single determinant molecular-orbital theory. *Mol. Phys.* **1974**, *27*, 209-214.
34. Hariharan, P. C.; Pople, J. A. Influence of polarization functions on molecular-orbital hydrogenation energies. *Theor. Chim. Acta* **1973**, *28*, 213-222.
35. Hehre, W. J.; Ditchfield, R.; Pople, J. A. Self-consistent molecular-orbital methods .12. Further extensions of gaussian-type basis sets for use in molecular-orbital studies of organic-molecules. *J. Chem. Phys.* **1972**, *56*, 2257.
36. Ditchfield, R.; Hehre, W. J.; Pople, J. A. Self-consistent molecular-orbital methods .9. Extended gaussian-type basis for molecular-orbital studies of organic molecules. *J. Chem. Phys.* **1971**, *54*, 724-728.
37. Kendall, R. A.; Dunning, T. H.; Harrison, R. J. Electron-affinities of the 1st-row atoms revisited - Systematic basis-sets and wave-functions. *J. Chem. Phys.* **1992**, *96*, 6796-6806.
38. Montgomery, J. A.; Frisch, M. J.; Ochterski, J. W.; Petersson, G. A. A complete basis set model chemistry. VII. Use of the minimum population localization method. *J. Chem. Phys.* **2000**, *112*, 6532-6542.
39. Montgomery, J. A.; Frisch, M. J.; Ochterski, J. W.; Petersson, G. A. A complete basis set model chemistry. VI. Use of density functional geometries and frequencies. *J. Chem. Phys.* **1999**, *110*, 2822-2827.
40. Frisch, M. J.; Trucks, G. W.; Schlegel, H. B.; Scuseria, G. E.; Robb, M. A.; al., e. *Gaussian Development Version* GDVRev. H20+; Gaussian, Inc.: Wallingford, CT, 2010.

41. Scalmani, G.; Frisch, M. J. Continuous surface charge polarizable continuum models of solvation. I. General formalism. *J. Chem. Phys.* **2010**, *132*, 114110.
42. Cossi, M.; Barone, V.; Mennucci, B.; Tomasi, J. Ab initio study of ionic solutions by a polarizable continuum dielectric model. *Chem. Phys. Lett.* **1998**, *286*, 253-260.
43. Mennucci, B.; Tomasi, J. Continuum solvation models: A new approach to the problem of solute's charge distribution and cavity boundaries. *J. Chem. Phys.* **1997**, *106*, 5151-5158.
44. Cances, E.; Mennucci, B.; Tomasi, J. A new integral equation formalism for the polarizable continuum model: Theoretical background and applications to isotropic and anisotropic dielectrics. *J. Chem. Phys.* **1997**, *107*, 3032-3041.
45. Munk, B. H.; Burrows, C. J.; Schlegel, H. B. Exploration of mechanisms for the transformation of 8-hydroxy guanine radical to FAPyG by density functional theory. *Chem. Res. Toxicol.* **2007**, *20*, 432-444.
46. Wardman, P. Reduction potentials of one-electron couples involving free-radicals in aqueous-solution. *J. Phys. Chem. Ref. Data* **1989**, *18*, 1637-1755.
47. Clark, W. M. *Oxidation-reduction potentials of organic systems*. Williams & Wilkins: Baltimore,, 1960; p 107-148.
48. Dawson, R. M. C. *Data for biochemical research*. 3rd ed.; Clarendon Press: Oxford, 1986; p 103-114.
49. Verdolino, V.; Cammi, R.; Munk, B. H.; Schlegel, H. B. Calculation of pK(a) Values of Nucleobases and the Guanine Oxidation Products Guanidinohydantoin

- and Spiroiminodihydantoin using Density Functional Theory and a Polarizable Continuum Model. *J. Phys. Chem. B* **2008**, *112*, 16860-16873.
50. Jang, Y. H.; Goddard, W. A.; Noyes, K. T.; Sowers, L. C.; Hwang, S.; Chung, D. S. pK(a) values of guanine in water: Density functional theory calculations combined with Poisson-Boltzmann continuum-solvation model. *J. Phys. Chem. B* **2003**, *107*, 344-357.
51. Jang, Y. H.; Goddard, W. A.; Noyes, K. T.; Sowers, L. C.; Hwang, S.; Chung, D. S. First principles calculations of the tautomers and pK(a) values of 8-oxoguanine: Implications for mutagenicity and repair. *Chem. Res. Toxicol.* **2002**, *15*, 1023-1035.
52. Bartmess, J. E. Thermodynamics of the electron and the proton. *J. Phys. Chem.* **1994**, *98*, 6420-6424.
53. Bartmess, J. E. Thermodynamics of the electron and the proton (vol 98, pg 6423, 1994). *J. Phys. Chem.* **1995**, *99*, 6755-6755.
54. Moser, A.; Range, K.; York, D. M. Accurate Proton Affinity and Gas-Phase Basicity Values for Molecules Important in Biocatalysis. *J. Phys. Chem. B* **2010**, *114*, 13911-13921.
55. Baboul, A. G.; Curtiss, L. A.; Redfern, P. C.; Raghavachari, K. Gaussian-3 theory using density functional geometries and zero-point energies. *J. Chem. Phys.* **1999**, *110*, 7650-7657.
56. Liu, M.; Li, T. T.; Amegayibor, F. S.; Cardoso, D. S.; Fu, Y. L.; Lee, J. K. Gas-Phase Thermochemical Properties of Pyrimidine Nucleobases. *J. Org. Chem.* **2008**, *73*, 9283-9291.

57. Wolken, J. K.; Turecek, F. Proton affinity of uracil. A computational study of protonation sites. *J. Am. Soc. Mass Spectrom.* **2000**, *11*, 1065-1071.
58. Close, D. M. Calculation of the ionization potentials of the DNA bases in aqueous medium. *J. Phys. Chem. A* **2004**, *108*, 10376-10379.
59. Baik, M. H.; Silverman, J. S.; Yang, I. V.; Ropp, P. A.; Szalai, V. A.; Yang, W. T.; Thorp, H. H. Using density functional theory to design DNA base analogues with low oxidation potentials. *J. Phys. Chem. B* **2001**, *105*, 6437-6444.
60. Crespo-Hernandez, C. E.; Arce, R.; Ishikawa, Y.; Gorb, L.; Leszczynski, J.; Close, D. M. Ab initio ionization energy thresholds of DNA and RNA bases in gas phase and in aqueous solution. *J. Phys. Chem. A* **2004**, *108*, 6373-6377.
61. Schlegel, H. B. Potential-energy curves using unrestricted Moller-Plesset perturbation-theory with spin annihilation. *J. Chem. Phys.* **1986**, *84*, 4530-4534.
62. Lin, J.; Yu, C.; Peng, S.; Akiyama, I.; Li, K.; Lee, L. K.; Lebreton, P. R. Ultraviolet photoelectron studies of the ground-state electronic-structure and gas-phase tautomerism of hypoxanthine and guanine. *J. Phys. Chem.* **1980**, *84*, 1006-1012.
63. Lin, J.; Yu, C.; Peng, S.; Akiyama, I.; Li, K.; Lee, L. K.; Lebreton, P. R. Ultraviolet photoelectron studies of the ground-state electronic-structure and gas-phase tautomerism of purine and adenine. *J. Am. Chem. Soc.* **1980**, *102*, 4627-4631.
64. Yu, C.; Peng, S.; Akiyama, I.; Lin, J.; Lebreton, P. R. Ultraviolet photoelectron studies of biological pyrimidines - Valence electronic-structure of cytosine. *J. Am. Chem. Soc.* **1978**, *100*, 2303-2307.

65. Dougherty, D.; Wittel, K.; Meeks, J.; McGlynn, S. P. Photoelectron-spectroscopy of carbonyls - ureas, uracils, and thymine. *J. Am. Chem. Soc.* **1976**, *98*, 3815-3820.
66. Denifl, S.; Sonnweber, B.; Hanel, G.; Scheier, P.; Mark, T. D. Threshold electron impact ionization studies of uracil. *Int. J. Mass Spectrom.* **2004**, *238*, 47-53.
67. Crespo-Hernandez, C. E.; Close, D. M.; Gorb, L.; Leszczynski, J. Determination of redox potentials for the Watson-Crick base pairs, DNA nucleosides, and relevant nucleoside analogues. *J. Phys. Chem. B* **2007**, *111*, 5386-5395.
68. Ginovska, B.; Camaioni, D. M.; Dupuis, M. The $\text{H}_2\text{O}_2 + \text{OH} \rightarrow \text{HO}_2 + \text{H}_2\text{O}$ reaction in aqueous solution from a charge-dependent continuum model of solvation. *J. Chem. Phys.* **2008**, *129*, 014506.
69. Caricato, M.; Mennucci, B.; Tomasi, J. Solvent polarity scales revisited: a ZINDO-PCM study of the solvatochromism of betaine-30. *Mol. Phys.* **2006**, *104*, 875-887.
70. Fu, Y.; Liu, L.; Yu, H. Z.; Wang, Y. M.; Guo, Q. X. Quantum-chemical predictions of absolute standard redox potentials of diverse organic molecules and free radicals in acetonitrile. *J. Am. Chem. Soc.* **2005**, *127*, 7227-7234.
71. Orozco, M.; Luque, F. J. Optimization of the cavity size for ab-initio MST-SCRF calculations of monovalent ions. *Chem. Phys.* **1994**, *182*, 237-248.
72. Bachs, M.; Luque, F. J.; Orozco, M. Optimization of solute cavities and van-der-Waals parameters in ab-initio MST-SCRF calculations of neutral molecules. *J. Comput. Chem.* **1994**, *15*, 446-454.

73. Langmaier, J.; Samec, Z.; Samcova, E.; Hobza, P.; Reha, D. Origin of difference between one-electron redox potentials of guanosine and guanine: Electrochemical and quantum chemical study. *J. Phys. Chem. B* **2004**, *108*, 15896-15899.
74. Fukuzumi, S.; Miyao, H.; Ohkubo, K.; Suenobu, T. Electron-transfer oxidation properties of DNA bases and DNA oligomers. *J. Phys. Chem. A* **2005**, *109*, 3285-3294.
75. Weatherly, S. C.; Yang, I. V.; Thorp, H. H. Proton-coupled electron transfer in duplex DNA: Driving force dependence and isotope effects on electrocatalytic oxidation of guanine. *J. Am. Chem. Soc.* **2001**, *123*, 1236-1237.
76. Xie, H.; Yang, D. W.; Heller, A.; Gao, Z. Q. Electrocatalytic oxidation of guanine, guanosine, and guanosine monophosphate. *Biophys. J.* **2007**, *92*, L70-L72.
77. Li, M. J.; Liu, W. X.; Peng, C. R.; Lu, W. C. A First-Principles Method for Predicting Redox Potentials of Nucleobases and the Metabolites in Aqueous Solution. *Acta Phys.-Chim. Sin.* **2011**, *27*, 595-603.
78. Hunter, E. P. L.; Lias, S. G. Evaluated gas phase basicities and proton affinities of molecules: An update. *J. Phys. Chem. Ref. Data* **1998**, *27*, 413-656.
79. Greco, F.; Liguori, A.; Sindona, G.; Uccella, N. Gas-phase proton affinity of deoxyribonucleosides and related nucleobases by fast-atom-bombardment tandem mass-spectrometry. *J. Am. Chem. Soc.* **1990**, *112*, 9092-9096.
80. Meotner, M. Ion thermochemistry of low-volatility compounds in the gas-phase .2. Intrinsic basicities and hydrogen-bonded dimers of nitrogen heterocyclics and nucleic bases. *J. Am. Chem. Soc.* **1979**, *101*, 2396-2403.

81. Wilson, M. S.; McCloskey, J. A. Chemical ionization mass-spectrometry of nucleosides - Mechanisms of ion formation and estimations of proton affinity. *J. Am. Chem. Soc.* **1975**, *97*, 3436-3444.
82. Zhachkina, A.; Liu, M.; Sun, X. J.; Amegayibor, F. S.; Lee, J. K. Gas-Phase Thermochemical Properties of the Damaged Base O(6)-Methylguanine versus Adenine and Guanine. *J. Org. Chem.* **2009**, *74*, 7429-7440.
83. Chen, E. C. M.; Herder, C.; Chen, E. S. The experimental and theoretical gas phase acidities of adenine, guanine, cytosine, uracil, thymine and halouracils. *J. Mol. Struct.* **2006**, *798*, 126-133.
84. Orlov, V. M.; Smirnov, A. N.; Varshavsky, Y. M. Ionization-potentials and electron-donor ability of nucleic-acid bases and their analogs. *Tetrahedron Lett.* **1976**, 4377-4378.
85. Song, B.; Zhao, J.; Griesser, R.; Meiser, C.; Sigel, H.; Lippert, B. Effects of (N7)-coordinated nickel(II), copper(II), or platinum(II) on the acid-base properties of guanine derivatives and other related purines. *Chem.-Eur. J.* **1999**, *5*, 2374-2387.
86. Kampf, G.; Kapinos, L. E.; Griesser, R.; Lippert, B.; Sigel, H. Comparison of the acid-base properties of purine derivatives in aqueous solution. Determination of intrinsic proton affinities of various basic sites. *J. Chem. Soc.-Perkin Trans. 2* **2002**, 1320-1327.
87. Kulikowska, E.; Kierdaszuk, B.; Shugar, D. Xanthine, xanthosine and its nucleotides: solution structures of neutral and ionic forms, and relevance to substrate properties in various enzyme systems and metabolic pathways. *Acta Biochim. Pol.* **2004**, *51*, 493-531.

88. Christensen, J. J.; Rytting, J. H.; Izatt, R. M. Thermodynamic pK, delta degrees, delta degrees, and delta Cp degrees values for proton dissociation from several purines and their nucleosides in aqueous solution. *Biochemistry* **1970**, *9*, 4907-4913.
89. Kobayashi, K. Evidence of Formation of Adenine Dimer Cation Radical in DNA: The Importance of Adenine Base Stacking. *J. Phys. Chem. B* **2010**, *114*, 5600-5604.
90. Cho, B. P. Structure of oxidatively damaged nucleic-acid adducts - pH-dependence of the C-13 NMR-spectra of 8-oxoguanosine and 8-oxoadenosine. *Magn. Reson. Chem.* **1993**, *31*, 1048-1053.
91. Hager, J. W.; Wallace, S. C. 2-laser photoionization supersonic jet mass-spectrometry of aromatic-molecules. *Anal. Chem.* **1988**, *60*, 5-10.
92. Lipert, R. J.; Colson, S. D. Accurate ionization-potentials of phenol and phenol-(H₂O) from the electric-field dependence of the pump probe photoionization threshold. *J. Chem. Phys.* **1990**, *92*, 3240-3241.
93. Behan, J. M.; Johnstone, R. A. W.; Bentley, T. W. Evaluation of empirical methods for calculating ionization-potentials of substituted benzenes. *Org. Mass Spectrom.* **1976**, *11*, 207-211.
94. Cowling, S. A.; Johnstone, R. A. W. Photoelectron spectroscopy: The effects of steric inhibition to resonance in anilines. *J. Electron Spectrosc. Relat. Phenom.* **1973**, *2*, 161-169.
95. Cockett, M. C. R.; Ozeki, H.; Okuyama, K.; Kimura, K. Vibronic coupling in the ground cationic state of naphthalene - A laser threshold photoelectron zero

- kinetic-energy (ZEKE)-photoelectron spectroscopic study. *J. Chem. Phys.* **1993**, *98*, 7763-7772.
96. Merenyi, G.; Lind, J.; Shen, X. H. Electron-transfer from indoles, phenol, and sulfite SO_3^{2-} to chlorine dioxide ClO_2 . *J. Phys. Chem.* **1988**, *92*, 134-137.
97. Surdhar, P. S.; Armstrong, D. A. Reduction potentials and exchange-reactions of thiyl radicals and disulfide anion radicals. *J. Phys. Chem.* **1987**, *91*, 6532-6537.
98. Jonsson, M.; Lind, J.; Merenyi, G.; Eriksen, T. E. Redox properties of 4-substituted aryl methyl chalcogenides in water. *J. Chem. Soc.-Perkin Trans. 2* **1995**, 67-70.
99. Weinberg, N. L.; Tilak, B. V. Technique of electroorganic synthesis. In *Techniques of chemistry*, Wiley: New York, 1974; p 667.
100. Jonsson, M.; Lind, J.; Reitberger, T.; Eriksen, T. E.; Merenyi, G. Redox chemistry of substituted benzenes - The one-electron reduction potentials of methoxy-substituted benzene radical cations. *J. Phys. Chem.* **1993**, *97*, 11278-11282.
101. Murov, S. L.; Hug, G. L.; Carmichael, I. *Handbook of photochemistry*. 2nd ed.; M. Dekker: New York, 1993; p 271.
102. Paukku, Y.; Hill, G. Theoretical Determination of One-Electron Redox Potentials for DNA Bases, Base Pairs, and Stacks. *J. Phys. Chem. A* **2011**, *115*, 6738-6738.

CHAPTER 8

COMPUTATIONAL PREDICTION OF ONE-ELECTRON REDUCTION POTENTIALS AND ACID DISSOCIATION CONSTANTS FOR GUANINE OXIDATION PRODUCTS AND INTERMEDIATES

8.1 Introduction

Ionizing radiation and reactive oxygen species are nearly constant sources of oxidative stress to the DNA of living organisms. Oxidative damage to DNA has been implicated in the process of aging, neurological diseases, carcinogenesis, and cellular death.¹⁻⁹ Among the canonical nucleobases, guanine is well known to be the most susceptible to oxidative damage.¹⁰ Extensive research has been carried out over the last few decades to map the reaction pathways following guanine oxidation and to identify the major intermediates and products both experimentally^{4,7,11-17} and theoretically.¹⁸⁻²¹ The key intermediate and product species examined in this chapter are based on these experimental and theoretical findings. Figure 8.1 shows three significant reaction pathways that are available after the initial oxidation of guanine.

Determining the reduction potentials for nucleobase species has been a specific area of research interest to investigators studying oxidative damage to DNA. While there have been numerous experimental studies attempting to accurately measure a set of absolute reduction potentials for the canonical nucleic acid residues,^{10,22-28} the studies by Seidel et al.²⁴ and Steenken et al.^{25,26} are the most widely cited. Standard potentials (E°) for the canonical nucleosides were measured by Seidel et al. using cyclic voltammetry measurements in acetonitrile solution. By measuring the potentials in

acetonitrile, the possibilities for protonation/deprotonation events were eliminated and the redox pair was strictly between the reduced neutral and the oxidized radical cation. Steenken et al. used chemical oxidation and kinetic rate measurements of reference compounds reacting with the adenosine, guanosine, and 8-oxoguanosine nucleosides. Measurements were made in aqueous solution at a specific buffered pH to obtain reduction potentials at a constant pH of 7 (E_7).

In Chapter 7, we constructed a computational methodology²⁹ that reliably reproduced the relative trends in the E° potentials measured by Seidel et al. and the E_7 potentials measured by Steenken et al. E° potentials were obtained from calculated solution phase free energies for the redox reactions. E_7 potentials were computed using the Nernst half-cell equation, which takes into account the physiologically relevant acid dissociation constants (K_a) for each species in addition to the E° potentials. Since measured pK_a 's were unavailable for many of the one-electron oxidized nucleic acid species, we calculated all of the pK_a 's needed for the reduced and oxidized species. Using the SMD implicit solvation model with solvent cavity scaling, we achieved good agreement between calculated and measured pK_a 's and used the same solvent scaling parameters to reproduce the experimental trends for the E° and E_7 potentials of nucleosides. For this chapter, we employ the same methodology to predict unknown pK_a 's and E_7 reduction potentials for key intermediate and product species in the reaction pathways following guanine oxidation. These intermediate and product species may be transient and difficult to isolate experimentally. The thermodynamic properties of many of these species are currently unknown. Accurate prediction of these unknown

values could help to provide experimentalists with very useful information needed for a better understanding of the reaction pathways and mechanisms of oxidative damage.

8.2 Methods

A reduction potential under standard conditions is directly proportional to free energy of the reaction under the same standard conditions. For an arbitrary nucleic acid base (or nucleobase) in solution, given the free energy for a one-electron reduction of the radical cation species



the standard reduction potential can be computed using

$$E_{\text{red}(\text{sol})}^{\circ} = \frac{-\Delta G_{\text{red}(\text{sol})}^*}{F} \quad (2)$$

where F is Faraday's constant (23.06 kcal/mol). The free energy of reducing the radical cation species in solution

$$\Delta G_{\text{red}(\text{sol})}^* = G_{(\text{sol})}^*(B) - G_{(\text{sol})}^*(B^{+\bullet}) - G_{(\text{g})}^{\circ} \quad (3)$$

is calculated with the aid of a thermodynamic cycle shown in Scheme 8.1. The standard state free energy in solution

$$G_{(\text{sol})}^* = \left(G_{(\text{g})}^{\circ} + \Delta G^{\text{1atm} \rightarrow \text{1M}} \right) + G_{\text{solv}}^* \quad (4)$$

is the sum of the standard state free energy in the gas phase $G_{(\text{g})}^{\circ}$ and the standard state free energy of solvation G_{solv}^* with an additional term $\Delta G^{\text{1atm} \rightarrow \text{1M}} = 1.89$ kcal/mol representing the free energy difference for converting from the standard state concentration of 1 atm in the gas phase to the standard state concentration of 1 mol/L in the solution phase. Using the notation introduced by Ben-Naim and Marcus,³⁰ the

standard state at 1 atm is denoted by a degree symbol ($^\circ$) and the standard state at 1 mol/L is denoted by an asterisk (*). The equation for calculating a reduction potential as outlined in Scheme 8.1 is obtained by substituting eq (4) into eq (3)

$$\begin{aligned} \Delta G_{\text{red(sol)}}^* = & \left(G_{(\text{g})}^\circ + \Delta G^{\text{1atm} \rightarrow \text{1M}} + \Delta G_{\text{solv}}^*(B) \right) \\ & - \left(G_{(\text{g})}^\circ + \Delta G^{\text{1atm} \rightarrow \text{1M}} + \Delta G_{\text{solv}}^*(B^{+\bullet}) \right) \\ & - G_{(\text{g})}^\circ \end{aligned} \quad (5)$$

Our goal for this chapter is to not only predict the absolute reduction potentials for the nucleic acid species following guanine oxidation, but to make predictions that are comparable to potentials that could be measured in a laboratory setting. Experimental potentials are measured or referenced against a standard electrode and reported as relative half-cell potentials. To convert absolute reduction potentials to standard reduction potentials, the estimated absolute potential of the Standard Hydrogen Electrode (SHE = 4.281 V)³¹⁻³⁴ is subtracted from the computed potential calculated by eq (2). In Chapter 7, we found that there were still systematic differences in the calculated potentials relative to SHE compared with the measured potentials. In this chapter, all calculated potentials will be reported relative to the calculated guanine potential.

The calculated gas phase free energy is the sum of three values

$$G_{(\text{g})}^\circ = E_{\text{el}} + \text{ZPE} + \Delta G_{0 \rightarrow 298\text{K}}^\circ \quad (6)$$

where E_{el} is the computed electronic energy including nuclear repulsion, ZPE is the zero point vibrational energy, and $\Delta G_{0 \rightarrow 298\text{K}}^\circ$ is the calculated thermal free energy increase from 0 to 298 K based on ideal gas approximations. Every gas phase structure is geometry optimized using the B3LYP hybrid density functional³⁵⁻³⁹ with the 6-31+G(d,p)

basis set.⁴⁰⁻⁴⁵ Subsequent vibrational frequency calculations are used to compute the ZPE and $\Delta G^\circ_{0 \rightarrow 298K}$ energies. Using the gas phase optimized geometry, the accuracy of the E_{el} is enhanced by performing a single point calculation with the larger aug-cc-pVTZ basis set.⁴⁶ The computational procedure for obtaining the gas phase free energy is shown explicitly in eq (7).

$$G^\circ_{(g)} = E_{el}^{B3LYP/aug-cc-pVTZ/B3LYP/6-31+G(d,p)} + ZPE^{B3LYP/6-31+G(d,p)} + \Delta G^\circ_{0 \rightarrow 298K}^{B3LYP/6-31+G(d,p)} \quad (7)$$

A more accurate approach for computing gas phase free energies is also employed by using the CBS-QB3 compound model chemistry,^{47,48} which has been shown to produce nearly chemically accurate gas phase thermodynamic energies (MAE of 1.1 kcal/mol).

The free energy of solvation for a given molecule, R ,

$$\Delta G^*_{solv} = G^*_{(sol)}(R') - G^*_{(g)}(R) \quad (8)$$

is described by Ben-Naim and Marcus³⁰ as the difference between the solution phase free energy of a solution phase optimized molecule (R') and the gas phase free energy of a gas phase optimized molecule (R). Solution phase free energies are computed at the B3LYP/6-31+G(d,p) level of theory using the SMD implicit solvation model.⁴⁹ Finally, two accurate methods for determining solution phase free energies are constructed by combining the B3LYP and CBS-QB3 gas phase free energy methods with the calculated solvation free energy yielding the B3LYP method

$$G^*_{(sol)} = E_{el}^{B3LYP/aug-cc-pVTZ/B3LYP/6-31+G(d,p)} + ZPE^{B3LYP/6-31+G(d,p)} + \Delta G^\circ_{0 \rightarrow 298K}^{B3LYP/6-31+G(d,p)} + \Delta G^{1atm \rightarrow 1M} + \Delta G^*_{solv}^{SMD/B3LYP/6-31+G(d,p)} \quad (9)$$

and the CBS-QB3 method

$$G_{(\text{sol})}^* = G_{(\text{g})}^{\text{CBS-QB3}} + \Delta G^{\text{1atm} \rightarrow \text{1M}} + \Delta G_{\text{solv}}^* \text{ SMD/B3LYP/6-31+G(d,p)} \quad (10)$$

In this chapter, all calculations are performed using a development version of the Gaussian software.⁵⁰ The SMD implicit solvation model⁴⁹ includes electrostatic, cavitation, and dispersion energies. SMD uses the integral equation formalism of the polarizable continuum model (IEF-PCM)⁵¹⁻⁵⁴ with a parameterized set of atomic radii to calculate the bulk electrostatic energy contribution. Solute-solvent short range interactions are calculated by using a modified solvent-accessible area with parameters for atomic and molecular surface tensions and hydrogen bond acidity and basicity. An average tesserae area of 0.2 Å² is used for the tessellated solute-solvent boundary.

In Chapter 7, it was found that reliable relative reduction potentials and pK_a values could be computed using N-methylated nucleobase as a model for nucleoside and nucleotide species.²⁹ A nucleotide is a nucleic acid residue that contains the base, sugar, and phosphate groups, whereas nucleosides contain only the base and sugar groups. Nucleobases are nucleic acid residues that do not include the ribose/deoxyribose sugar or phosphate moiety. By methylating the nucleobase at the location where the sugar moiety would coordinate (N9 for pyrimidines and N1 for purines shown in Scheme 8.2), we were able to reliably simulate the necessary features of the nucleobase coordination environment without disturbing the intrinsic thermodynamic properties. The overall effect of the sugar moiety on the absolute reduction potential for the nucleic acid species is debatable. However, the relative reduction potentials should remain unaffected from a standard sugar moiety as the highest occupied molecular orbitals are expected to be heavily localized on the nucleobase subunit. Since we are interested in modeling nucleobase behavior near

physiological pH conditions, we do not need to be concerned about the effect of the sugar subunit on the protic equilibria, because the hydroxyl groups are expected to deprotonate only under very basic conditions ($\text{pH} > 12$).

The biologically relevant environment for nucleic acid species is in aqueous solution in a narrow pH range. Therefore, the more important reduction potentials are not the ones that would occur under standard conditions at pH 0, but the reduction potentials under physiological conditions where the pH of the solution is 7. The Nernst half-cell equation

$$E_{1/2} = E^\circ - \frac{RT}{F} \ln \left(\frac{[\text{Red}]}{[\text{Ox}]} \right) \quad (11)$$

can convert standard potentials to potentials under nonstandard conditions and vice versa. In order to calculate a potential that would be measured at pH 7, the equilibrium concentrations of the physiologically relevant protonation states must be included in eq (11). The ratio of equilibrium concentrations of protonation states are governed by acid dissociation constants (K_a). Using K_a 's and assuming dilute concentrations of solute (low ionic strength), an example equation of a pH dependent potential

$$E_{\text{pH}} = E^\circ_{\text{X}^\bullet/\text{XH}} + \frac{RT}{F} \ln \left(\frac{K_{\text{a1o}}}{K_{\text{a1r}}} \right) + \frac{RT}{F} \ln \left(\frac{K_{\text{a1r}}K_{\text{a2r}} + K_{\text{a1r}}10^{-\text{pH}} + 10^{-2\text{pH}}}{K_{\text{a1o}} + 10^{-\text{pH}}} \right) \quad (12)$$

can be calculated from a derived form of eq (11). In eq (12), the standard redox pair involves an one-electron redox event and a change in protonation state where “XH” is the reduced neutral form of the nucleobase species and “X” is the oxidized neutral radical that has one less proton than the reduced neutral species. In a physiological

environment where the pH of the aqueous solution is near 7, the neutral forms of the reduced and oxidized nucleobases tend to be the most dominant; therefore, the redox pair used in the calculation of E° models a one-electron reduction immediately followed by a proton transfer. The acid dissociation constants for the reduced and oxidized species are identified by an “o” for an oxidized species and a “r” for a reduced species. The K_a subscript number indicates the ordering of the deprotonation events from acidic to basic; for example, the first physiologically relevant deprotonation event for the reduced species of a given nucleobase is signified by K_{a1r} . Further details in the derivation of eq (12) and additional discussions regarding pH dependent potentials can be found in the literature.^{55,56}

For most of the intermediate and product species along the guanine oxidation pathways, experimental measurements for pK_a 's do not exist, especially for oxidized species. These pK_a data are required for evaluating eq (12), therefore we decided to calculate relevant pK_a values for each of the intermediate and product species. Similar to calculating a reduction potential, a calculated pK_a is directly proportional to the free energy for the deprotonation reaction

$$pK_a = \frac{\Delta G_{\text{deprot (aq)}}^*}{2.303RT} \quad (13)$$

Scheme 8.3 describes the thermodynamic cycle used to calculate $\Delta G_{\text{deprot (aq)}}^*$. In the calculation of the free energy for aqueous deprotonation of a given species, HA,

$$\begin{aligned} \Delta G_{\text{deprot (aq)}}^* = & \left(G_{(g)}^\circ(\text{A}^-) + \Delta G^{\text{latm} \rightarrow \text{IM}} + \Delta G_{\text{solv}}^*(\text{A}^-) \right) \\ & + \left(G_{(g)}^\circ(\text{H}^+) + \Delta G^{\text{latm} \rightarrow \text{IM}} + \Delta G_{\text{solv}}^*(\text{H}^+) \right) \\ & - \left(G_{(g)}^\circ(\text{HA}) + \Delta G^{\text{latm} \rightarrow \text{IM}} + \Delta G_{\text{solv}}^*(\text{HA}) \right) \end{aligned} \quad (14)$$

the aqueous solvation free energy of a proton is given by the literature values $\Delta G^*_{\text{solv}}(\text{H}^+) = 265.9 \text{ kcal/mol}$.⁵⁷

Nucleobases contain multiple sites for protonation or deprotonation. In an aqueous solvent environment, multiple tautomers of a given nucleobase will be present in equilibrium concentrations for both the reduced and oxidized species (Scheme 8.4). In order to correctly model the outcome of an experimental measurement in aqueous solution, significantly populated tautomeric states must be taken into account. This can be done by using a normalized Boltzmann distribution (f) of weighted populations for each tautomer based on the relative free energies

$$f_1 = \frac{\exp\left(\frac{-G^*_{1(\text{sol})}}{RT}\right)}{\sum_n \exp\left(\frac{-G^*_{n(\text{sol})}}{RT}\right)} \quad \text{where} \quad \sum f_n = 1 \quad (15)$$

Skipping a more detailed derivation²⁹ shown in Chapter 7, the result is eq (16)

$$E^{\circ}_{\text{red(sol)}} - E^{\circ}_{\text{red(sol)}} = \frac{RT}{F} \ln(f_i) - \frac{RT}{F} \ln(f'_j) \quad (16)$$

where f_i is the population of the i -th tautomer of the oxidized species and f'_j is the j -th tautomer of the reduced species. Eq (16) implies that any calculated specific tautomeric potential can be equated to an ensemble potential when combined with the weighted populations of each tautomer. Using a very similar approach,⁵⁸⁻⁶⁰ an equation for calculating ensemble $\text{p}K_{\text{a}}$'s can be derived

$$\text{p}K_{\text{a}} = \text{p}K_{\text{a}}^{\text{xy}} - \log(f_x) + \log(f'_y) \quad (17)$$

where f_x is the population of the species that is protonated relative to the deprotonated species that has a population f'_y .

For the tautomeric sampling as many as four low-energy tautomers were examined per protonation state for each reduced and oxidized species; though in most cases, only one or two tautomers needed to be considered. Tautomers that included protonated amino groups (e.g. -NH_3^+) and enol forms of keto structures were typically found to be much higher in energy and were not included in the tautomeric sampling. Multiply charged species were not considered since they are unlikely to be relevant, but also result in larger errors in the PCM solvation energies.

Solution phase calculations for charged solutes were not producing sufficiently accurate results²⁹ in Chapter 7 due to specific interactions with solvent molecules and other issues known to be problematic for implicit solvent modeling. To overcome these inaccuracies in the solvation modeling we calibrated our calculated $\text{p}K_{\text{a}}$'s against well-established experimentally measured $\text{p}K_{\text{a}}$'s by uniformly scaling the solute cavity for charged species. Cavity scaling parameters were fit separately for the methodology and charge state as follows: B3LYP cations = 1.00, B3LYP anions = 0.90, CBS-QB3 cations = 0.975, and CBS-QB3 anions = 0.925. Since the guanine oxidation pathway intermediate and product species are sufficiently similar to the canonical nucleobases from Chapter 7, we used the same cavity scaling parameters for all of the species in this chapter.

8.3 Results and Discussion

In Chapter 7, we calculated the $\text{p}K_{\text{a}}$'s of the nucleobases and their oxidized forms.²⁹ Details of the present calculations of $\text{p}K_{\text{a}}$'s and reduction potentials of the intermediates and products along the guanine oxidation pathways are presented in

Figure 8.2 through Figure 8.15, and are summarized in Table 8.1. The calculated pK_a 's for guanine (pK_{a1} 3.20, pK_{a2} 9.34 at B3LYP and pK_{a1} 3.50, pK_{a2} 9.10 at CBS-QB3)²⁹ are in excellent agreement with other calculated values (pK_{a1} 3.4,⁶⁰ 3.15,⁵⁹ pK_{a2} 9.6,⁶⁰ 9.60⁵⁹) and experimental measurements (pK_{a1} 3.1, pK_{a2} 9.5).⁶¹ Similarly, our calculated pK_a 's for oxidized guanine ($pK_{a1 \text{ ox}}$ 3.34, $pK_{a2 \text{ ox}}$ 10.32) are also in excellent agreement with calculated ($pK_{a1 \text{ ox}}$ 4.01⁶²) and experimental values ($pK_{a1 \text{ ox}}$ 3.9,⁶³ $pK_{a2 \text{ ox}}$ 10.9⁶³). The contributing tautomers were also consistent with those found experimentally, where the pK_{a1} is a deprotonation at the N7 position, the pK_{a2} and $pK_{a1 \text{ ox}}$ are deprotonations from the N1 position, and the $pK_{a2 \text{ ox}}$ is a deprotonation from the N2 amino group.

Guanine is the easiest to oxidize of the canonical nucleobases. The most widely cited value for guanine is 1.29 V,²⁵ obtained by Steenken from chemical oxidation and kinetic rate measurements on the nucleoside. By contrast, Faraggi et al.²³ measured 1.06 V for 1-methylguanine by cyclic voltammetry. Our calculations on 9-methylguanine at the CBS-QB3 and B3LYP levels of theory yield 0.95 and 0.96 V. As discussed in our previous work, better agreement between computed and experimental values can be obtained for reduction potential differences between the nucleobases than for reduction potentials relative to SHE. The computations have difficulty in obtaining accurate estimates of solvation energies for ionic species; the experiments are hampered by problems with solubility and irreversibility. When differences are taken, many of the systematic biases cancel. For example, the calculated difference between the reduction potentials of guanine and 8-oxoguanine (−0.53 V at CBS-QB3 and −0.56 V at B3LYP) is in very good agreement with experiment (−0.55 V).^{25,26} Therefore, discussion of

reduction potentials in this chapter will be based on values relative to the reduction potential of guanine at pH 7, and are denoted as E_7 rel. Since all reduction potentials and pK_a 's were computed using two theoretical methods, the numbers are reported as a range of values in the discussion.

Following the initial oxidation of G, three significant reaction pathways are considered in this chapter, identified as A, B, and C in Figure 8.1. Key intermediate and product species were chosen based on pathways deduced from experimental investigations,^{4,7,11,13-17} and computational investigations of the energetics of the guanine oxidation reaction pathways (for leading computational references see work by Munk et al.¹⁸⁻²⁰ and Wetmore et al.²¹).

8.4 Pathway A

This pathway starts with 9-methyl-8-oxoguanine (8oxoG) which can be formed by the attack of a reactive oxygen species at the C8 position of guanine (G). As shown in Table 8.1 and Figure 8.3, the calculated pK_a 's of 8oxoG (pK_{a1} -0.12, pK_{a2} 8.13, $pK_{a1\text{ ox}}$ -0.28, and $pK_{a2\text{ ox}}$ 5.50)²⁹ are in good agreement with experimental measurements (pK_{a1} 0.1,⁶⁴ pK_{a2} 8.6,⁶⁴ and $pK_{a2\text{ ox}}$ 6.6²⁶) and other calculated results (pK_{a1} -0.4,⁶⁰ pK_{a2} 8.0,⁶⁰ pK_{a1} 0.22,⁵⁸ and pK_{a2} 8.69⁵⁸). Ring nitrogen atoms in cationic 8oxoG are all protonated and the first deprotonation occurs at the N3 position. The reduced neutral and radical cation species are identical isomers, but deprotonation for pK_{a2} occurs at N1 while deprotonation for $pK_{a1\text{ ox}}$ occurs at N7. The $pK_{a2\text{ ox}}$ involves the deprotonation of the last protonated ring nitrogen at N1. Our calculated E_7 potential for 8oxoG is 0.53 – 0.56 V lower than for G,²⁹ in very good agreement with the

experimental difference in reduction potentials (0.55 V).^{25,26} Although 8oxoG is a stable intermediate along the path, its low reduction potential relative to G indicates that 8oxoG can easily undergo further oxidation. At pH7, the oxidation of the canonical nucleobases is accompanied by the loss of a proton. The calculated pK_a 's for oxidized 8oxoG show that it will lose not just one proton but also a second proton to form the radical anion at physiological pH. Loss of an additional electron from oxidized 8oxoG yields 2-amino-6,8-dioxo-9-methylpurine (8oxoP). The calculated reduction potential of oxidized 8oxoG is 0.35 – 0.44 V lower than G. This indicates the oxidation of 8oxoG to 8oxoP can occur readily by the removal of an electron, followed by the loss of two protons and then removal of one more electron.

The pK_a 's for 8oxoP (Figure 8.4) are very similar to those of 8oxoG: pK_{a1} is 0 – 1, pK_{a2} is ca. 8, and $pK_{a1\text{ ox}}$ is ca. –2. However, the protonation sites of 8oxoP differ from 8oxoG: for pK_{a1} deprotonation takes place at N1 while for pK_{a2} and $pK_{a1\text{ ox}}$ it occurs at the exocyclic N2 amine position. The CBS-QB3 calculation of $pK_{a1\text{ ox}}$ is unreliable because of severe spin contamination. Since 8oxoP has already been oxidized twice from 8oxoG, the reduction potential is expected to be comparatively high and further oxidation is unlikely. The calculated E_7 potential of 8oxoP is 1.1 V higher than guanine and 0.4 V higher than the calculated E_7 of uracil,²⁹ which has the highest reduction potential of the canonical nucleobases. . The next step on the reaction pathway involves the addition of water across the C4–N7 bond of 8oxoP leading to the 5-hydroxy-9-methyl-8-oxoguanine (5OH8OG) intermediate. This step is calculated to have a reaction free energy of ca. –5 to +1 kcal/mol.

5OH8OG is a key intermediate step along Pathway A for guanine oxidation where a pH dependent bifurcation of the reaction path takes place. A recent study by Burrows and coworkers⁶⁵ investigating the environmental effects on the guanine oxidation pathway inferred a pK_a of ca. 5.7 for the 5OH8OG nucleoside based on product yield ratios. This pK_a is the critical factor in determining that the reaction proceeds to guanidinohydantoin (Gh) under acidic conditions ($pH < 5.7$) and to spiroiminodihydantoin (Sp) under neutral to basic conditions ($pH > 5.7$). In a theoretical study detailing the energetics of guanine oxidation pathways, Munk et al.¹⁹ found that the lowest energy route for converting 8oxoG to Sp involved an initial deprotonation of neutral 5OH8OG followed by the migration the C6–O6 acyl group from C5 to C4. Figure 8.5 shows that 5OH8OG protonates at N1 with a pK_{a1} of 2.56 – 3.75, which is similar to the first protonation of guanine. The computed pK_{a2} of 6.05 – 6.69 for deprotonation supports both the experimental and calculated results that the conversion of 5OH8OG to Sp occurs under neutral to basic conditions. Acyl migration converts deprotonated 5OH8OG to deprotonated Sp and is exothermic by ca. 24 – 25 kcal/mol. Under mildly acidic conditions, 5OH8OG is uncharged. The addition of water to the C6 carbonyl generates the *gem*-diol intermediate on the pathway toward Gh. The formation of the *gem*-diol from 5OH8OG is endothermic by ca. 12 – 22 kcal/mol for the neutral case, and ca. 6 – 15 kcal/mol for the N1 protonated case.

The estimation of E_7 of 5OH8OG requires the pK_a 's of the oxidized species. Two tautomers of the radical cation of 5OH8OG are within 3 kcal/mol energetically for each level of theory (however, B3LYP and CBS-QB3 differ in the preferred site of protonation). Only zwitterion structures could be optimized for the neutral radical and

both levels of theory agree that N1 is protonated (optimization of non-zwitterionic structures of the neutral radical in the gas phase resulted in ring opening at the C5–C6 bond). The B3LYP level of theory predicts a $pK_{a1\text{ ox}}$ of 2.31 – 5.80 which is similar to the $pK_{a1\text{ ox}}$ of guanine. The calculated E_7 potential for 5OH8OG is 0.83 – 1.15 V higher than guanine, and thus 5OH8OG is not susceptible to further oxidation.

Addition of water to the C6–O6 carbonyl of 5OH8OG is endothermic by ca. 12 – 22 kcal/mol and yields the *gem*-diol intermediate (Figure 8.6). The *gem*-diol intermediate prefers a cationic state as reflected by the unusually high pK_{a1} of 7.40 – 8.33 involving an N1 deprotonation. The calculated pK_{a2} is 6.69 – 7.89 and predicted to be lower than the calculated pK_{a1} . The deprotonation associated with pK_{a2} leads to four tautomers that are very similar in energy. The calculated pK_a 's for the oxidized *gem*-diol are $pK_{a1\text{ ox}}$ of 1.48 – 5.53 and $pK_{a2\text{ ox}}$ of 5.07 – 5.85. The *gem*-diol has a calculated E_7 which is 0.48 – 0.78 V higher than that of guanine, indicating further oxidation is unlikely.

The next step on Pathway A toward Gh is a ring opening and proton transfer, converting the *gem*-diol to the 4-carboxy-9-methylguanidinohydantoin (4carboxyGh) intermediate. This step is 15 – 23 kcal/mol exothermic for the neutral species. Neutral 4carboxyGh (Figure 8.7) is a zwitterion with a negatively charged carboxylate and a positively charged guanidine group. Protonation occurs at the carboxyl group with a calculated pK_{a1} of –0.44 to –2.59. Deprotonation occurs at N7 of the neutral with a pK_{a2} of 6.07 – 6.66 and the guanidine group is predicted to remain positively charged. Deprotonation of the radical cation at the 4-hydroxyl group has a $pK_{a1\text{ ox}}$ of 3.88 – 7.61, and deprotonation of the neutral radical at the guanidine group has a $pK_{a2\text{ ox}}$ of

7.81 – 9.11. This leads to a nominal value of E_7 that is ca. 1.11 – 1.23 V higher than guanine. However, deprotonation of the carboxyl group in any of the 4carboxyGh radical species leads to decarboxylation. The E_7 for the oxidative process including decarboxylation to give oxidized neutral Gh is 0.01 – 0.10 V lower than E_7 for G.

Decarboxylation of 4carboxyGh and tautomerization produces guanidinohydantoin (Gh), and is exothermic by ca. 30 kcal/mol. For neutral Gh (Figure 8.8), the zwitterion is 3.6 – 5.1 kcal/mol more stable than the other tautomers. Deprotonation of the guanidine group has a pK_{a1} of 6.11 – 7.77 and deprotonation of the hydantoin group has a pK_{a2} of 9.14 – 9.58. There is no mention of any experimental measurements for the pK_a 's of Gh in the literature. The pK_a 's of guanidines can vary significantly with substituents (e.g. guanidine pK_a 13.7,⁶⁶ acetylguanidine pK_a 8.3 (exp.⁶⁷) versus 8.5 (present calc.)) but the pK_a 's of substituted hydantoins fall in a much narrower range (pK_a 8 – 10).⁶⁸⁻⁷⁰ The calculated $pK_{a1\text{ ox}}$ of 0.70 – 2.29 is similar to $pK_{a1\text{ ox}}$ values computed for guanine (2.53 – 3.34), 4carboxyGh (3.88 – 7.61), and 5OH8OG (2.31 – 5.23). Oxidized Gh is predicted to be neutral at pH 7 and E_7 is calculated to be 0.32 – 0.49 V higher than guanine.

As summarized in Figure 8.9, Sp is readily deprotonated, with pK_{a1} –0.06 to 1.32 and pK_{a2} 2.64 – 3.30. The values are in agreement with those calculated by Verdolino et al. (pK_{a1} 0.5 and pK_{a2} 4.8).⁶⁰ However, they pointed out that a pK_{a2} of 4.8 is “... surprisingly low for a substituted hydantoin...”.⁶⁰ They attribute the low value of pK_{a2} to through-space interactions of the C6 carbonyl group (confirmed by replacing C6=O6 with C=CH₂ and CH₂) and greater solvent stabilization of the N7 anion (tautomers with a N7 anion have a dipole moment of 15 – 20 debye compared to 5 – 15 debye for other

tautomers).⁶⁰ The present calculations may underestimate pK_{a2} and a better treatment of solvent effects may be needed. Verdolino et al. have estimated the pK_{a2} of Sp to be around 7. The calculated pK_a 's of oxidized Sp are probably also too low due to similar effects described above for the pK_{a2} . Oxidized Sp is most likely an anion at pH 7 and E_7 is calculated to be 0.39 – 0.78 V higher than guanine.

8.5 Pathway B

A key intermediate on the pathway to FAPyG is 2-amino-8-hydroxy-9-methyl-1,7,8-trihydropurin-6-one (hemiaminal), shown in Figure 8.10. The pK_a 's of the hemiaminal (pK_{a1} 2.49 – 2.62, pK_{a2} 7.92 – 9.53) are similar to the pK_a 's of guanine (pK_{a1} 3.20 – 3.50, pK_{a2} 9.10 – 9.34). All of the ring nitrogens are protonated in the cation species and the pK_{a1} corresponds to a deprotonation at N3. The next deprotonation for the pK_{a2} occurs at N1. The $pK_{a1\text{ ox}}$ of the radical cation involves a deprotonation at the N7 position. Under very basic conditions the radical neutral is predicted to deprotonate at the N1 position. The hemiaminal intermediate is very readily oxidized and its E_7 reduction potential is 0.75 – 0.84 V lower than guanine. The hemiaminal intermediate is even more susceptible to oxidation than 8oxoG. Tautomers with the C8-hydroxyl species deprotonated were difficult to obtain as many of the optimizations progressed toward ring opening. Ring opening at the C8–N9 bond of the hemiaminal and tautomerism leads to 2,6-diamino-(N-methyl)-5-formamido-4-hydroxypyrimidine (FAPyG) and is exothermic by ca. 9 – 11 kcal/mol. Breaking the N7–C8 bond followed by tautomerism yields to 2,5-diamino-(N-methyl)-6-formamido-4-hydroxypyrimidine (2,5FAPyG) and is exothermic by ca. 4 – 6 kcal/mol.

The pK_a 's for FAPyG (Figure 8.11) and 2,5FAPyG (Figure 8.12) are similar to one another in addition to being similar to the pK_a 's of guanine. FAPyG and 2,5FAPyG are protonated under acidic conditions on the N1 position of the pyrimidine ring with calculated pK_{a1} 's of 3.29 – 3.66 and 2.77 – 3.10, respectively. Neutral FAPyG and 2,5FAPyG deprotonate from the N3 position with calculated pK_{a2} 's of 8.40 – 9.06 and 7.04 – 7.40, respectively. The calculated 2,5FAPyG pK_{a2} of 7.04 – 7.40 indicates a significant concentration of the anion should be present under physiological conditions. The radical cation species for FAPyG and 2,5FAPyG deprotonate at the N3 position with $pK_{a1\text{ ox}}$'s of 5.41 – 6.58 and 4.11 – 4.43, which are slightly more basic than the radical cations of other guanine species (ca. 3 – 4). The oxidized neutral FAPyG deprotonates from the formamide group at a $pK_{a2\text{ ox}}$ of 8.08. The deprotonation of oxidized neutral 2,5FAPyG takes place at the same site (formerly the N7 nitrogen atom) with a very similar $pK_{a2\text{ ox}}$ 8.58 – 8.61 despite the fact that the site is an amino group rather than an amide. In agreement with the computational study by Munk et al.,¹⁸ FAPyG is the thermodynamically favored product by ca. 5.4 – 8.5 kcal/mol. E_7 reduction potentials of FAPyG and 2,5FAPyG are 0.25 – 0.32 V and 0.42 – 0.54 V lower than G, respectively. FAPyG has an E_7 that is 0.17 – 0.22 V higher than 2,5FAPyG, making it somewhat less susceptible to oxidation than 2,5FAPyG.

8.6 Pathway C

Pathway C starts with oxidative damage caused by a reactive oxygen species attacking the C5 position of guanine to yield the 5-hydroxy-9-methylguanine (5OHG) intermediate shown in Figure 8.13. While the calculated pK_a 's of 5OHG are similar in

value to those of G and many of the other intermediates, the sites of protonation / deprotonation differ. 5OHG is protonated at N3 with a pK_{a1} of 2.77 – 3.69; whereas, most of the other guanine oxidation intermediates are predominantly protonated at N1 or N7. The only acidic proton remaining in neutral 5OHG is the C5 hydroxyl which deprotonates at a pK_{a2} of 8.03 – 9.44. The oxidized radical cation prefers to be protonated at the N1 position and deprotonates with a $pK_{a1\text{ ox}}$ of 4.11 – 4.81. Additional tautomers of 5OHG radical cation (such as the isomer protonated at O5) could not be optimized due to ring opening at the C5–C6 bond. Similarly, attempts at optimizing a 5OHG radical anion failed due to ring opening for all structures considered. In the absence of ring opening, the calculated E_7 reduction potential is 0.81 – 1.05 V higher than G.

Similar to the 5OH8OG to Sp conversion, 5OHG can undergo an acyl migration to yield N-methyl-2-deoxospiroiminodihydantoin (i.e. reduced spiroiminodihydantoin or Sp_{red}). This reaction is exothermic by 20 – 21 kcal/mol. Sp_{red} has three ring nitrogen that are reasonable protonation sites under physiological conditions. Two of three combinations of two protons on the three ring nitrogen sites are calculated to be similar in energy (Figure 8.14). Sp_{red} protonates at the guanidine group with a pK_{a1} of 0.49 – 1.40. Neutral Sp_{red} deprotonates at the former N3 with a pK_{a2} of 7.12 – 7.40. An oxidized radical cation isomer of Sp_{red} could not be optimized due to the instabilities in the rings leading to ring opening. Oxidation coupled with loss of a proton leads to the neutral radical of Sp_{red}, which can be optimized. The calculated $pK_{a2\text{ ox}}$ for the radical neutral is 6.02 – 6.72 indicating that it would lose another proton at physiological

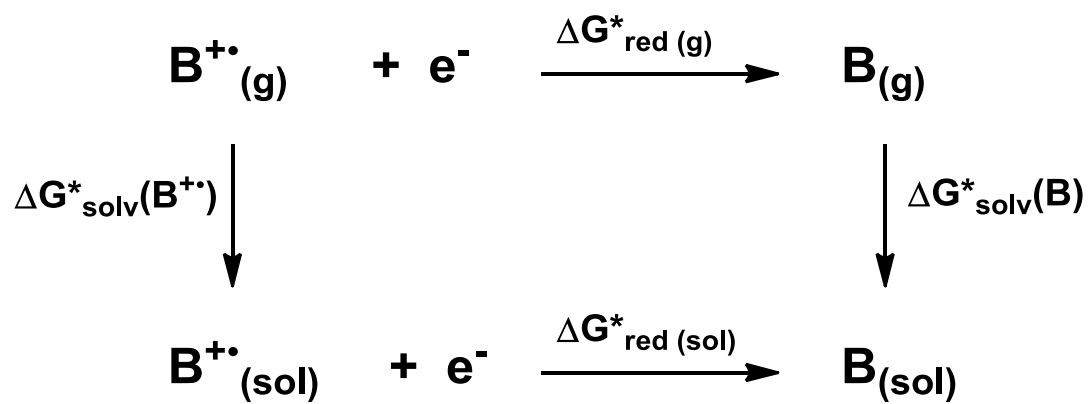
conditions yielding the radical anion species. The calculated E_7 reduction potential for Sp_{red} is 0.45 – 0.62 V higher than the calculated potential for G.

The final product in Pathway C involves a water addition across the C2–N3 bond of the deaminated hydantoin ring followed by proton transfer and ring opening to the 5-carboxamido-5-formamido-(N-methyl)-2-iminohydantoin (2Ih) product. This reaction is calculated to be endothermic by 3 – 6 kcal/mol. Similar to Sp and Sp_{red} , the predicted $\text{p}K_{\text{a}1}$ of 2Ih is acidic with a calculated value of 0.95 – 2.40 and is predicted to deprotonate from the former N1 position (Figure 8.15). 2Ih deprotonates from the former N3 position with a calculated $\text{p}K_{\text{a}2}$ of 8.18 – 8.49. The oxidized radical cation also has a predicted acidic $\text{p}K_{\text{a}1 \text{ ox}}$ of –4.58 to –2.35 for deprotonation at the former N3 position. The neutral 2Ih radical species can deprotonate from either of the exocyclic amino groups with almost equal energy. The calculated $\text{p}K_{\text{a}2 \text{ ox}}$ is 5.55 – 5.85 and is similar to the calculated $\text{p}K_{\text{a}2 \text{ ox}}$ of Sp_{red} . The calculated E_7 reduction potential of 2Ih is also very similar to the Sp_{red} species and is 0.58 – 0.69 V higher than guanine, indicating that further oxidation of 2Ih is unlikely.

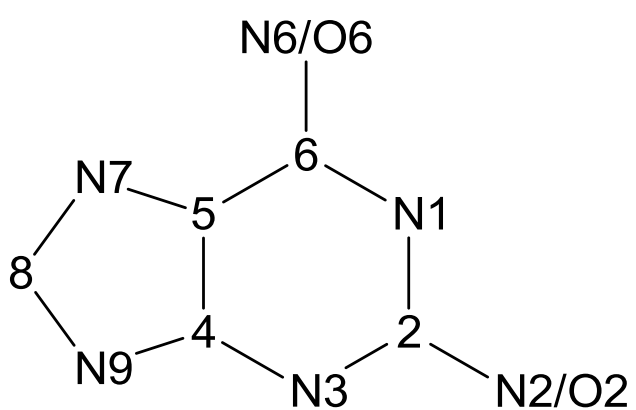
8.7 Conclusion

Three major reaction pathways resulting from the initial oxidation of guanine were investigated computationally. Previously unknown reduction potentials and $\text{p}K_{\text{a}}$'s of transient intermediate and product species along the reaction paths were predicted using the computational methodology developed in our earlier paper. The approach uses an implicit solvation model with cavity scaling and incorporates computed tautomerization energies to calculate E° and $\text{p}K_{\text{a}}$'s and obtain E_7 potentials that can be

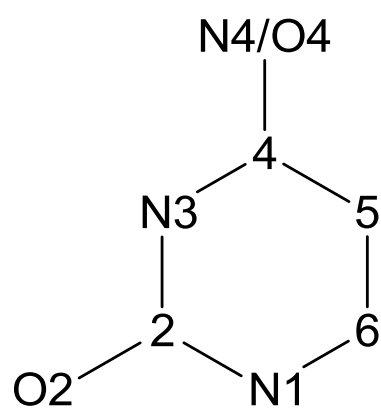
compared directly with experimental measurements in aqueous solution. Pathway A starts at the 8-oxoguanine intermediate (8oxoG) and includes 2-amino-6,8-dioxopurine (8oxoP), 5-hydroxy-8-oxoguanine (5OH8OG), 4-carboxy-guanidinohydantoin (4carboxyGh), a *gem*-diol intermediate and the product species guanidinohydantoin (Gh) and spiroiminodihydantoin (Sp). Pathway B leads to two formamidopyrimidine isomers (FAPyG and 2,5FAPyG), through a hemiaminal intermediate. Pathway C starts with 5-hydroxyguanine, goes through the reduced spiroiminodihydantoin intermediate (Sp_{red}) and ends at the 5-carboxamido-5-formamido-2-iminohydantoin product (2lh). Calculated pK_a 's appear to be reasonable based on chemical intuition in addition to some limited experimental evidence. The calculations show that 8-oxoguanine can easily lose an electron followed by the loss of two protons and the loss of another electron to produce 8-oxopurine. Calculated reduction potentials for intermediates and products along Pathway A after 8-oxopurine are more than 0.38 V higher than guanine. This indicates that these species along Pathway A are unlikely to undergo further oxidation even in an oxidatively stressful environment. Similar behavior is seen in the calculated reduction potentials for intermediate and product species along Pathway C, where the computed E_7 potentials are higher than guanine by at least 0.45 V. Species along Pathway B are predicted to be much easier to oxidize than guanine with relative calculated E_7 potentials that are between 0.25 V and 0.85 V lower than guanine. The results of Pathway B are in agreement with experimental observations of FAPyG products occurring only in an anaerobic environment.



Scheme 8.1 Thermodynamic cycle used in the calculation of reduction potentials.

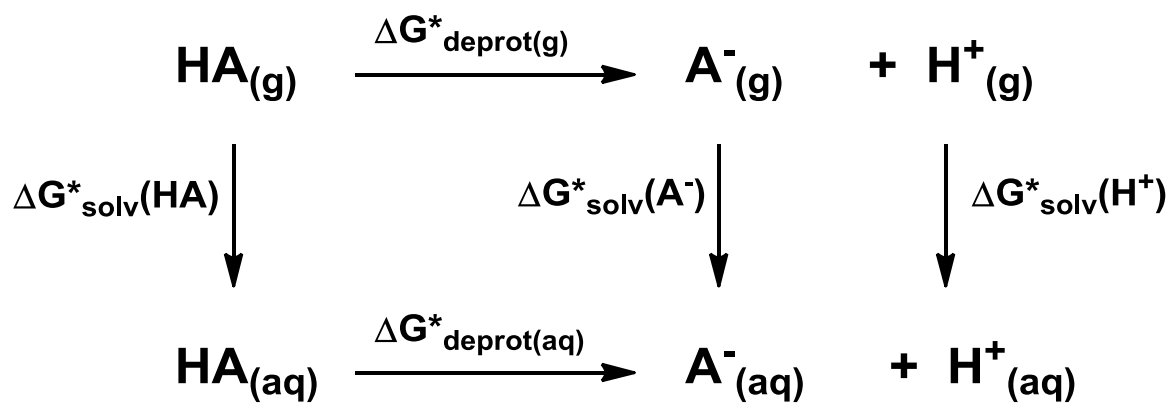


Purines

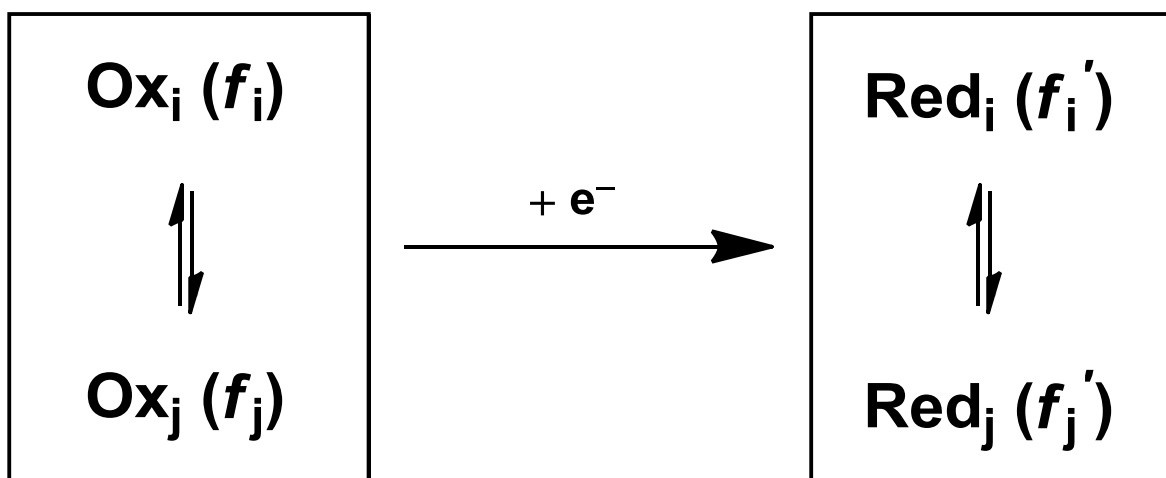


Pyrimidines

Scheme 8.2 Atomic numbering for purines and pyrimidine nucleobases. Charge, multiplicity and hydrogen atoms are not explicitly shown.



Scheme 8.3 Thermodynamic cycle used in the calculation of $\text{p}K_{\text{a}}$'s



Scheme 8.4 Multiple tautomers contribute to the ensemble reduction potential.

Table 8.1 Calculated Reduction Potentials and pK_a 's for Reactant, Intermediate, and Product Species using B3LYP and CBS-QB3 Methodologies

Species	pK_{a1}	pK_{a2}	$pK_{a1\text{ ox}}$	$pK_{a2\text{ ox}}$	E°_{rel}	$E_{7\text{ rel}}$
G						
B3LYP	3.20	9.34	3.34	10.32	0.00 (1.37) ^b	0.00 (0.96) ^b
CBS-QB3	3.50	9.10	2.53	11.88	0.00 (1.36) ^b	0.00 (0.95) ^b
8oxoG						
B3LYP	-0.12	8.13	-0.28	5.50	-0.45	-0.56
CBS-QB3	-0.04	7.09	0.06	4.83	-0.41	-0.53
8oxoP						
B3LYP	-0.04	7.52	-1.92		+1.13	+1.13
CBS-QB3	1.21	8.25	-8.59 ^a		+1.07	+1.07
5OH8OG						
B3LYP	2.56	6.05	2.31	1.17	+0.77	+0.83
CBS-QB3	3.75	6.69	5.23	0.69	+1.13	+1.15
gemdiol						
B3LYP	7.40	6.69	1.48	5.07	+0.44	+0.48
CBS-QB3	8.33	7.89	5.53	5.85	+0.70	+0.78
4carboxyGh						
B3LYP	-2.59	6.07	3.88	9.11	+1.06	+1.11
CBS-QB3	-0.44	6.66	7.61	7.81	+1.25	+1.23
Gh						
B3LYP	6.11	9.58	2.29	7.60	+0.38	+0.38
CBS-QB3	7.77	9.14	0.70	9.89	+0.44	+0.49
Sp						
B3LYP	-0.06	2.64	-4.26	0.53	+0.53	+0.78
CBS-QB3	1.32	3.30	-9.74	-0.32	+0.18	+0.39
hemiaminal						
B3LYP	2.62	9.53	5.45	13.59	-0.84	-0.84
CBS-QB3	2.49	7.92	6.16	11.02	-0.75	-0.75
FAPyG						
B3LYP	3.29	9.06	5.41	8.08	-0.32	-0.32
CBS-QB3	3.66	8.40	6.58	8.08	-0.24	-0.25
2,5FAPyG						
B3LYP	2.77	7.40	4.11	8.61	-0.54	-0.54
CBS-QB3	3.10	7.04	4.43	8.58	-0.43	-0.42
5OHG						
B3LYP	2.77	8.03	4.11		+0.81	+0.81
CBS-QB3	3.69	9.44	4.81		+1.05	+1.05
Sp _{red}						
B3LYP	0.49	7.40		6.72	+0.45	+0.45
CBS-QB3	1.40	7.12		6.02	+0.61	+0.62
2lh						
B3LYP	0.95	8.49	-2.35	5.85	+0.58	+0.58
CBS-QB3	2.40	8.18	-4.58	5.55	+0.69	+0.69

^a Calculation contains a significant amount of spin contamination ($S^2 = \sim 1.8$).^b Numbers in parenthesis are for the absolute reduction potentials.

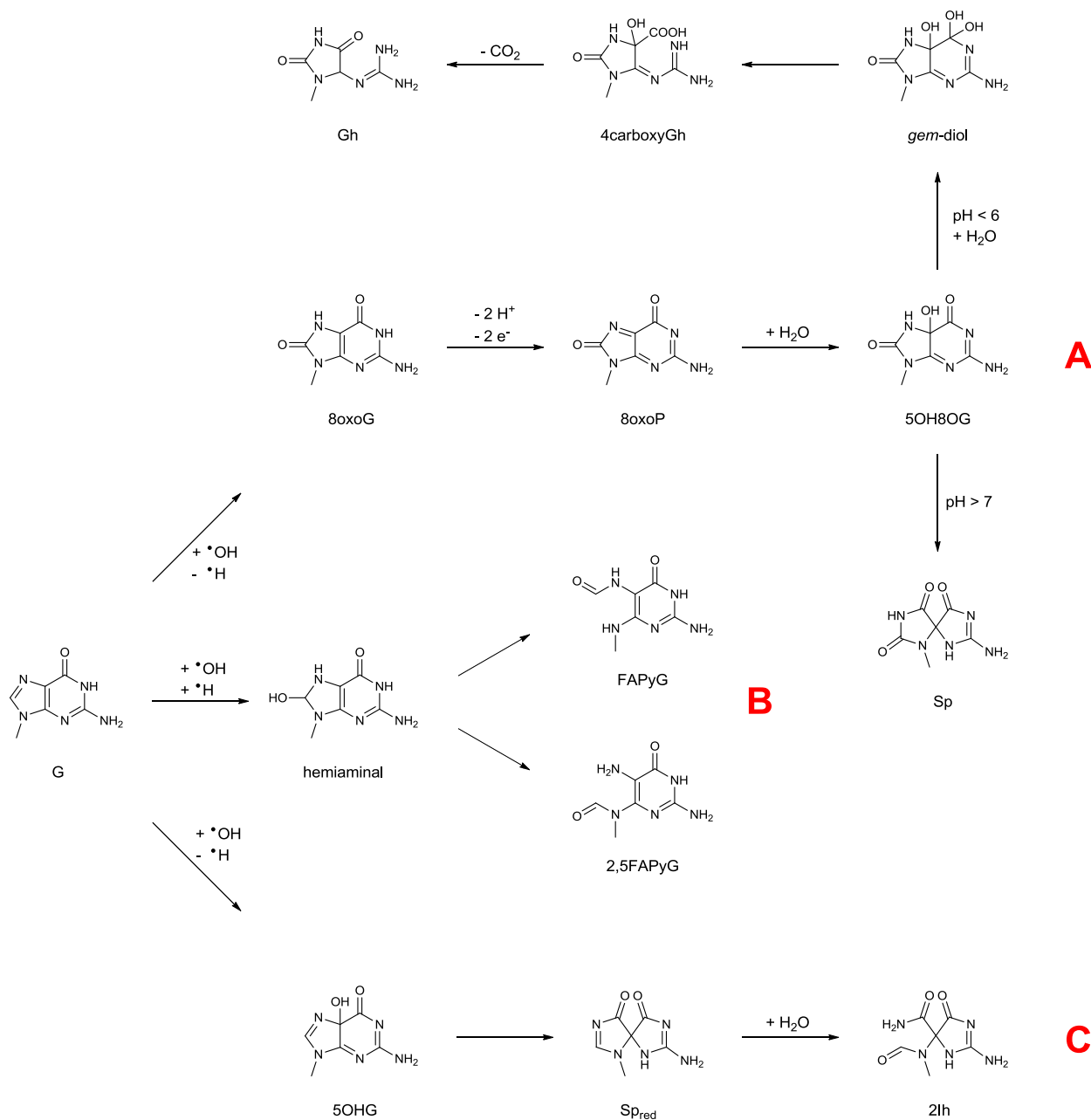


Figure 8.1 Key intermediates and products along three significant reaction pathways following guanine oxidation. Pathway A starts with the 9-methyl-8-oxoguanine (8oxoG) intermediate structure and leads to the spiroiminodihydantoin (Sp) and guanidinohydantoin (Gh) products. Pathway B goes through the hemiaminal intermediate and produces the formamidopyrimidine (FAPyG) products. Pathway C starts at the 5-hydroxy-9-methylguanine (5OHG) and goes through the N-methyl-2-deoxy-spiroiminodihydantoin (Sp_{red}) intermediate and ends at the 5-carboxamido-5-formamido-(N-methyl)-2-iminohydantoin (2lh) product.

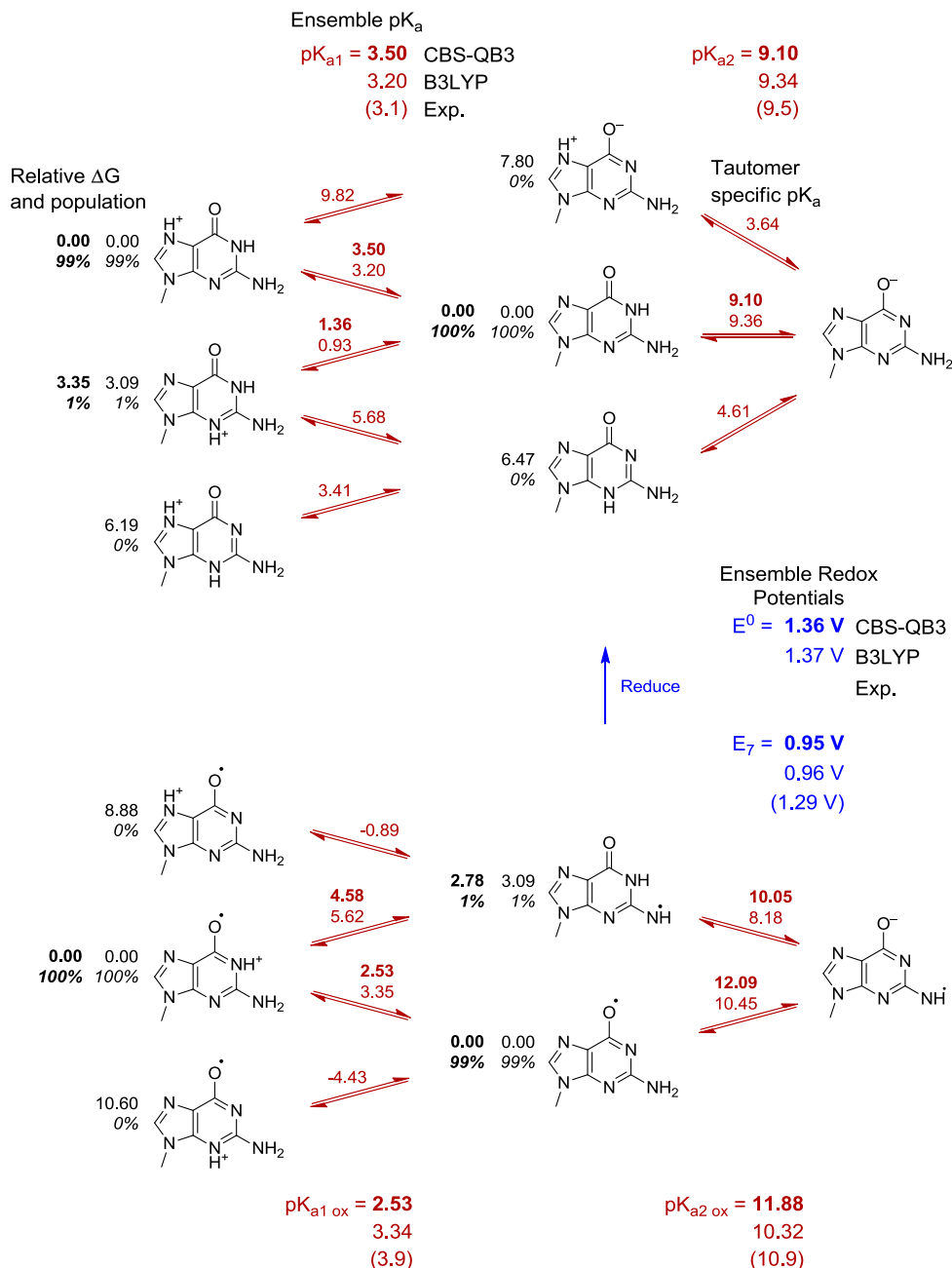


Figure 8.2 Calculated pK_a 's and reduction potentials for 9-methylguanine (G). Where applicable, relative free energy differences in kcal/mol (black) with the tautomer populations (black italics) are shown near individual tautomers. Tautomer specific pK_a 's (red) are shown between individual isomers. Ensemble averaged pK_a 's (red) are shown at the top and bottom of the figure. Ensemble oxidation potentials E^0 and E_7 (blue) are shown between the reduced and oxidized species on the right. Figure 8.3 through Figure 8.15 report oxidation potentials relative to guanine (E_{rel}^0 and $E_{7\text{ rel}}^0$). Experimentally measured values are shown in parenthesis.

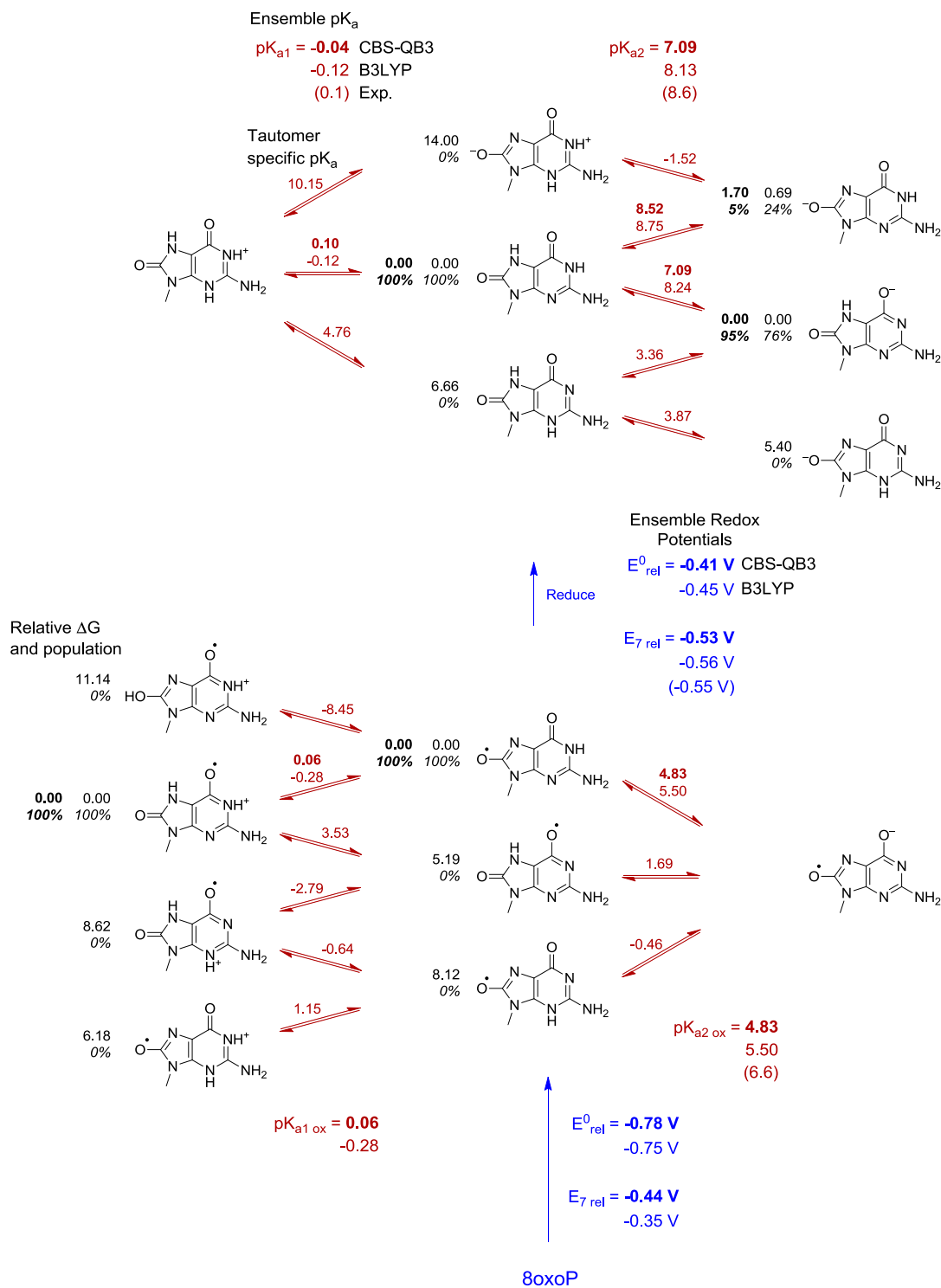


Figure 8.3 Calculated pK_a 's and relative reduction potentials for 9-methyl-8-oxoguanine (8oxoG). See Figure 8.2 caption for details. Blue values at the bottom of the figure are the relative E_7 reduction potentials for the oxidized 8oxoG and reduced 8oxoP one-electron redox pair.

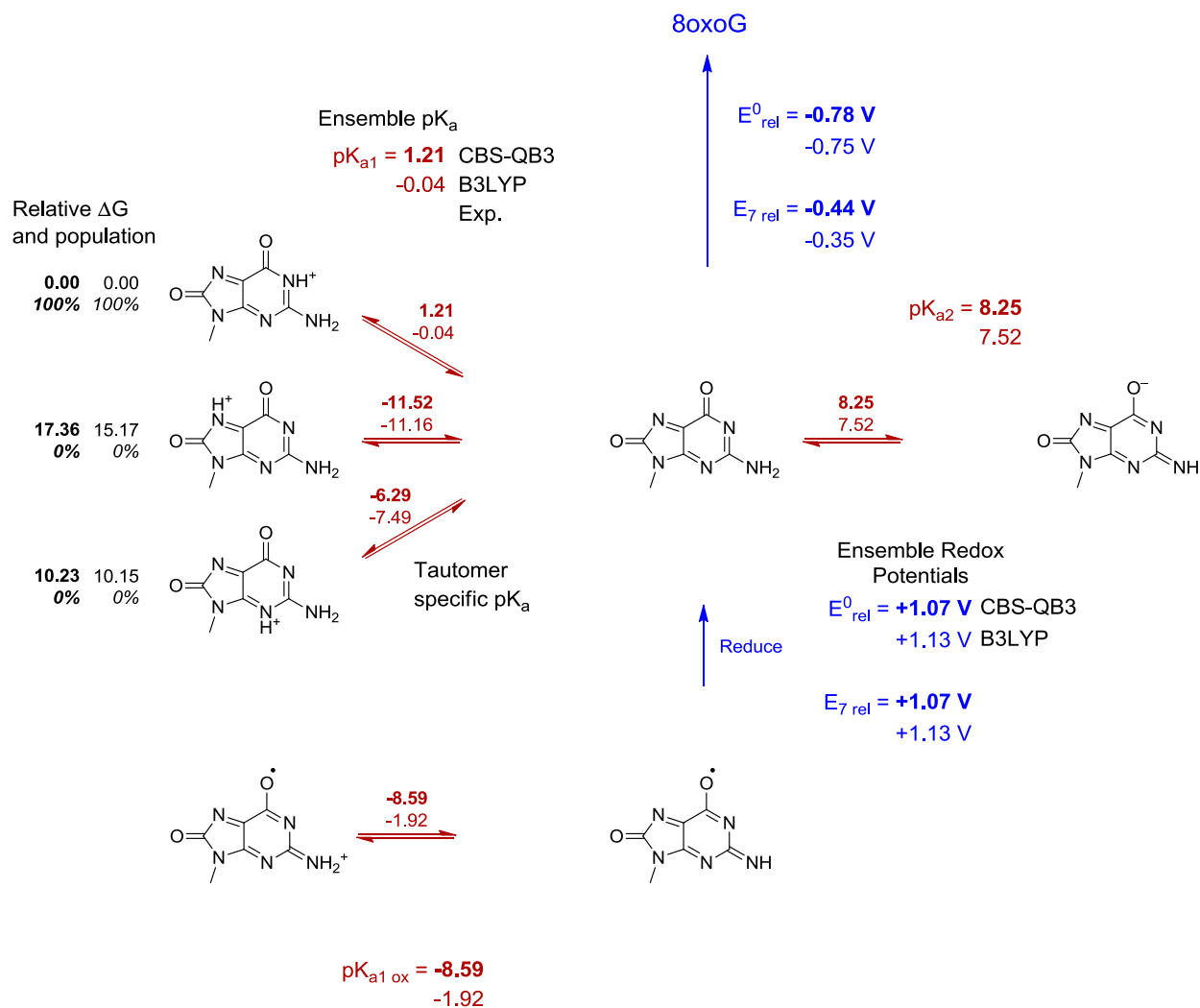


Figure 8.4 Calculated pK_a 's and relative reduction potentials for 2-amino-6,8-dioxo-9-methylpurine (8oxoP). See Figure 8.2 caption for details. Blue values at the top of the figure are the relative E_7 reduction potentials for the oxidized 8oxoG and reduced 8oxoP one-electron redox pair.

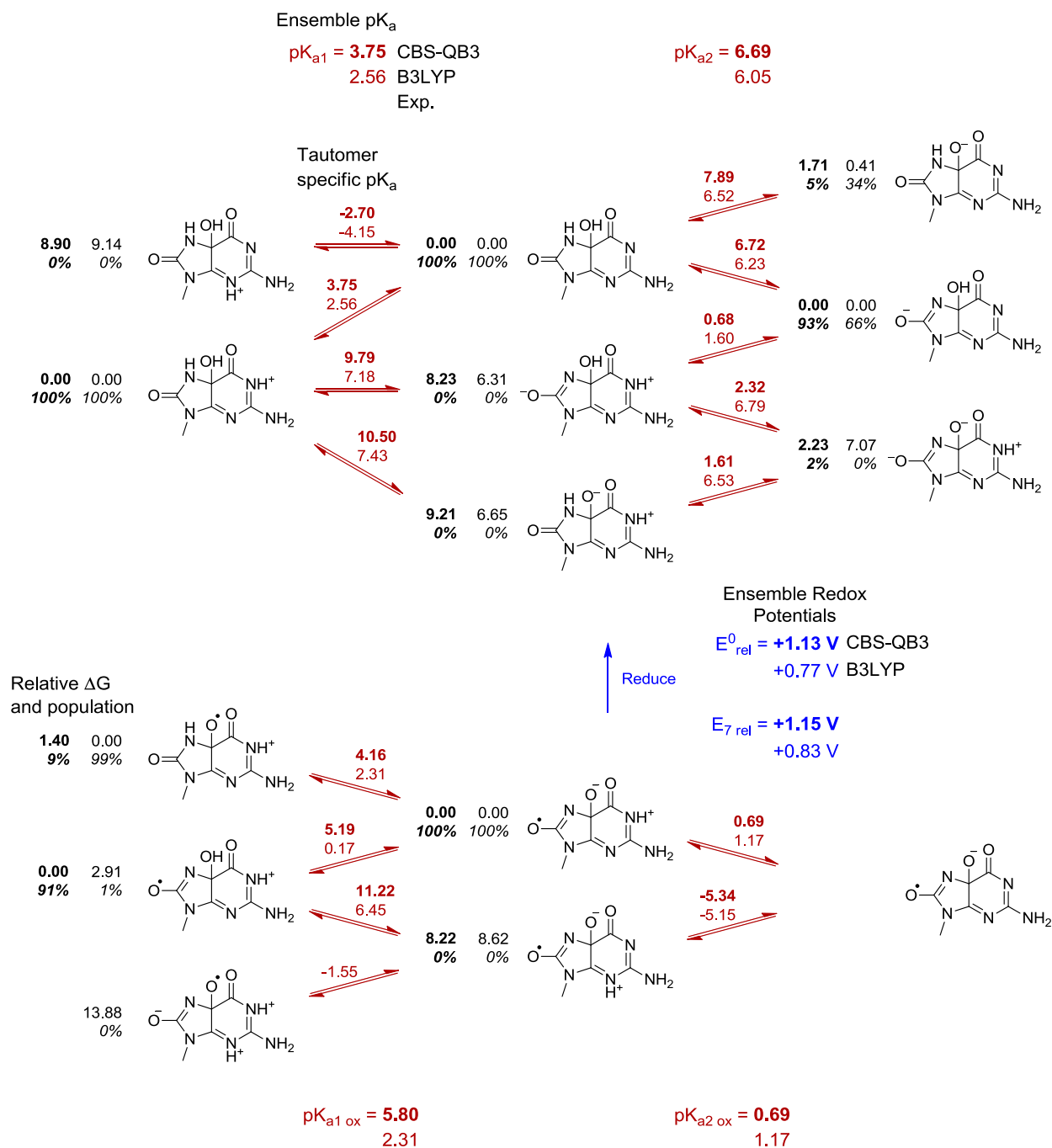


Figure 8.5 Calculated pK_a 's and relative reduction potentials for 5-hydroxy-9-methyl-8-oxoguanine (5OH8OG). See Figure 8.2 caption for details.

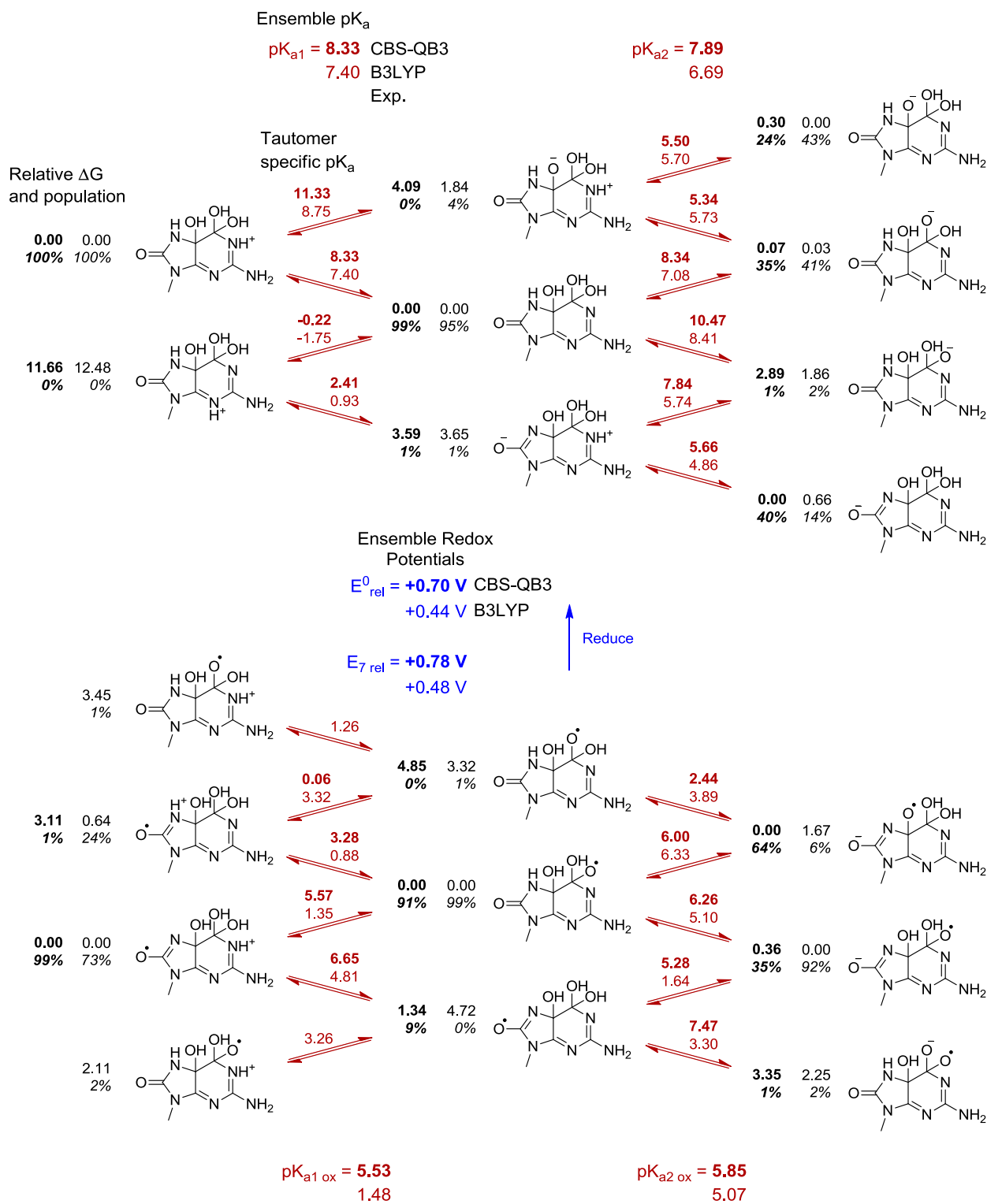


Figure 8.6 Calculated pK_a 's and relative reduction potentials for *gem*-diol. See Figure 8.2 caption for details.

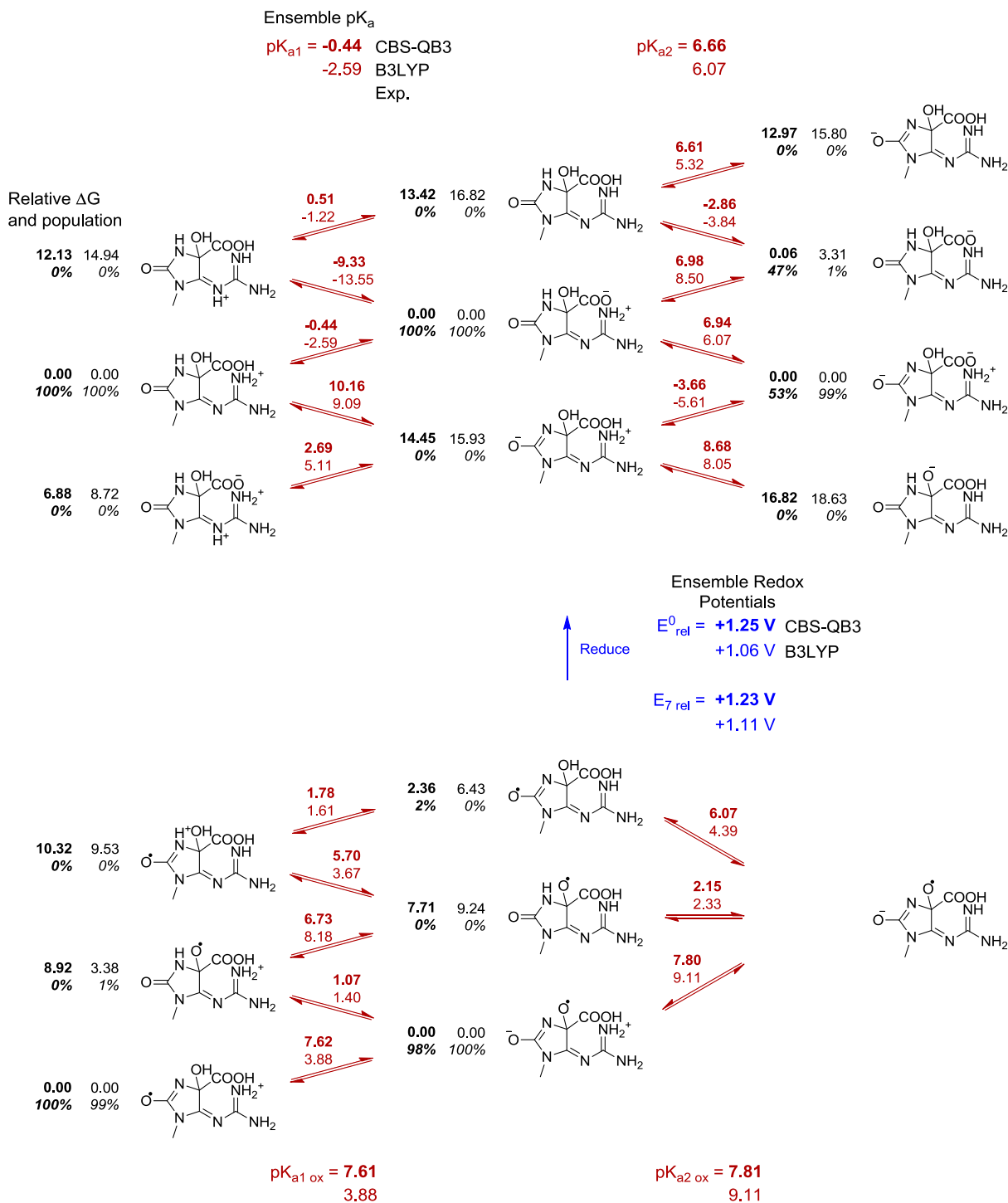


Figure 8.7 Calculated pK_a 's and relative reduction potentials for 4-carboxy-1-methylguanidinohydantoin (4carboxyGh). See Figure 8.2 caption for details. Calculations show that if the carboxylic acid of oxidized 4carboxyGh is deprotonated, the molecule will dissociate into carbon dioxide and Gh.

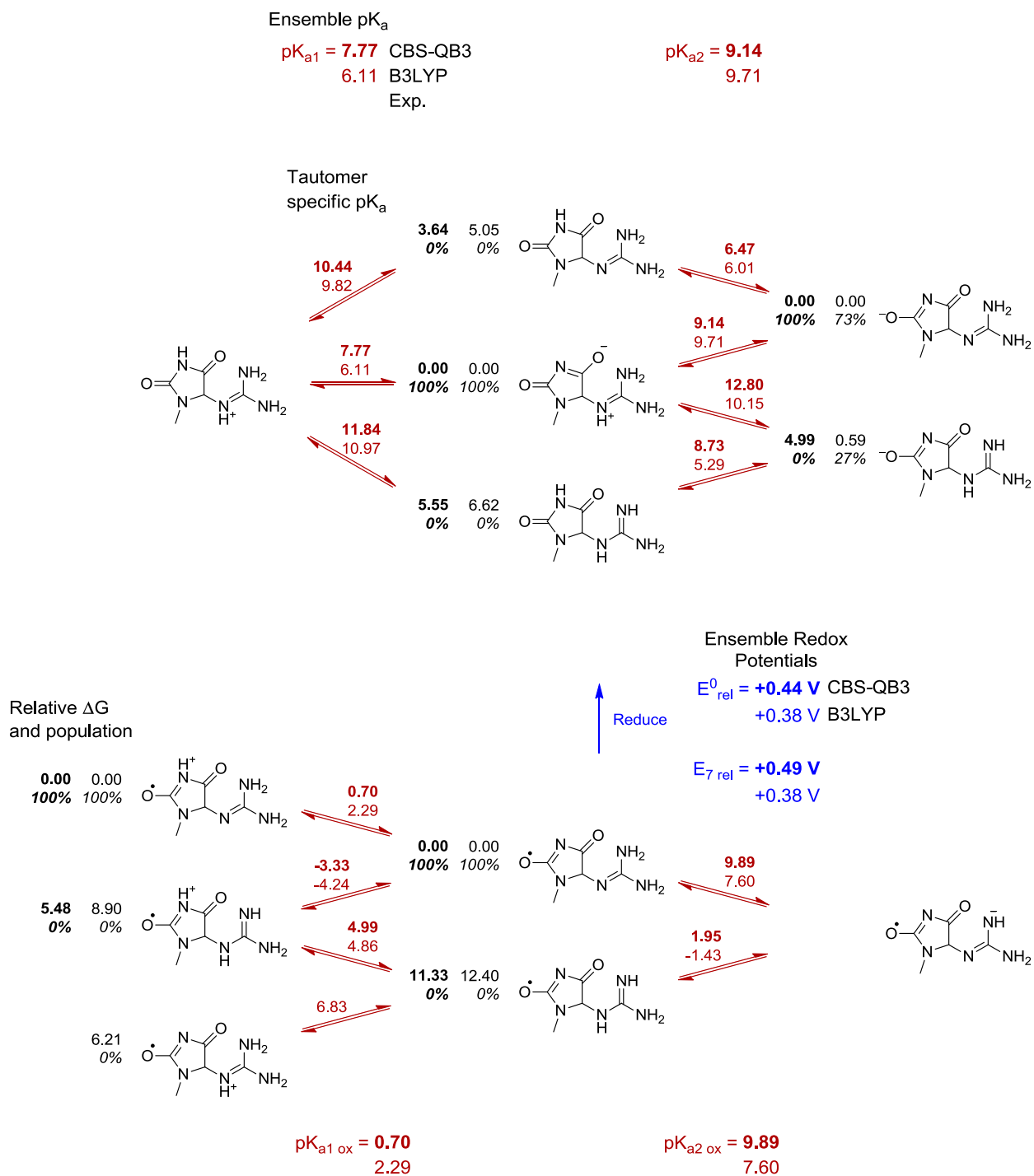


Figure 8.8 Calculated pK_a 's and relative reduction potentials for 1-methylguanidinohydantoin (Gh). See Figure 8.2 caption for details.

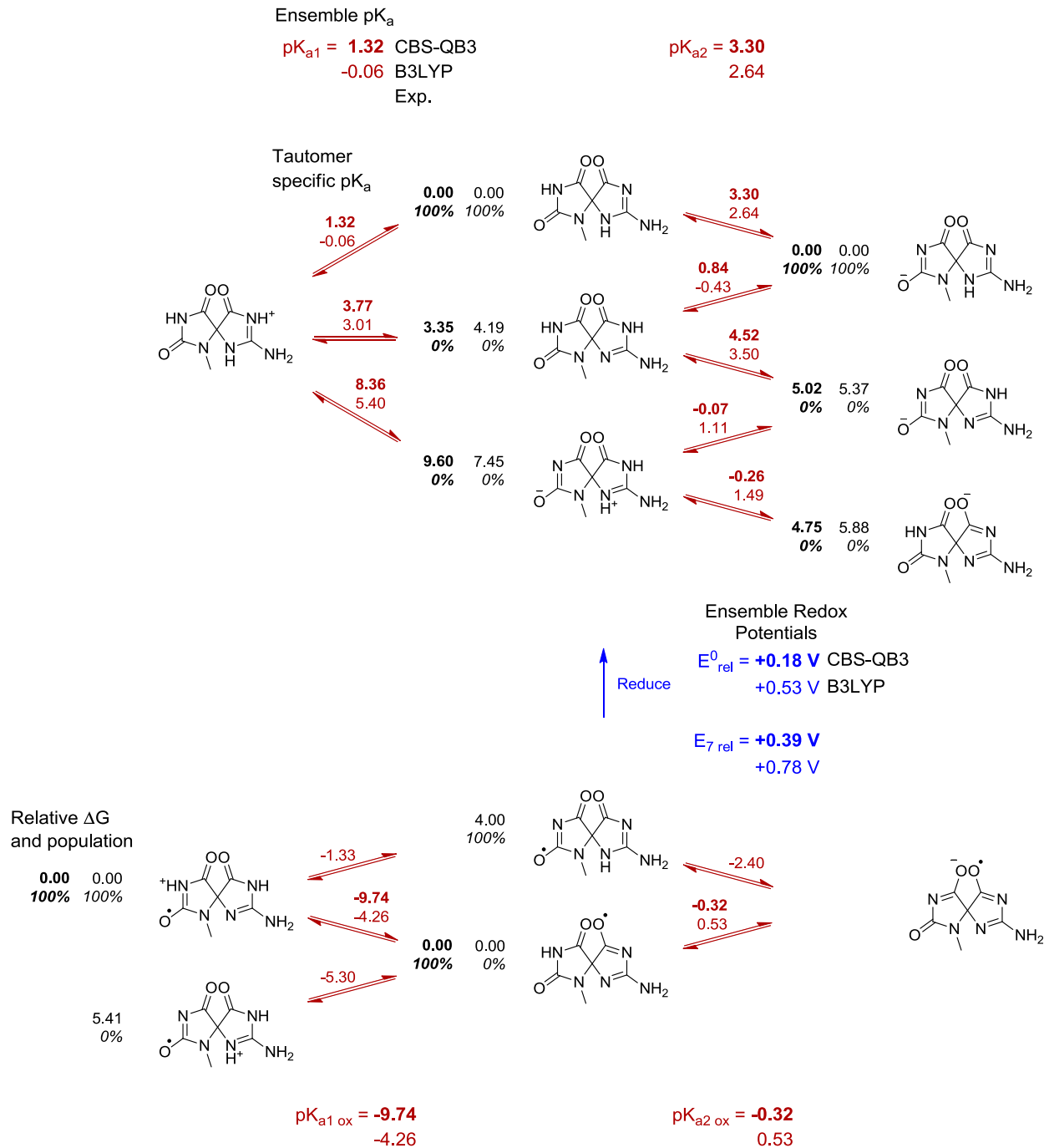


Figure 8.9 Calculated pK_a 's and relative reduction potentials for N-methylspiroiminodihydantoin (Sp). See Figure 8.2 caption for details.

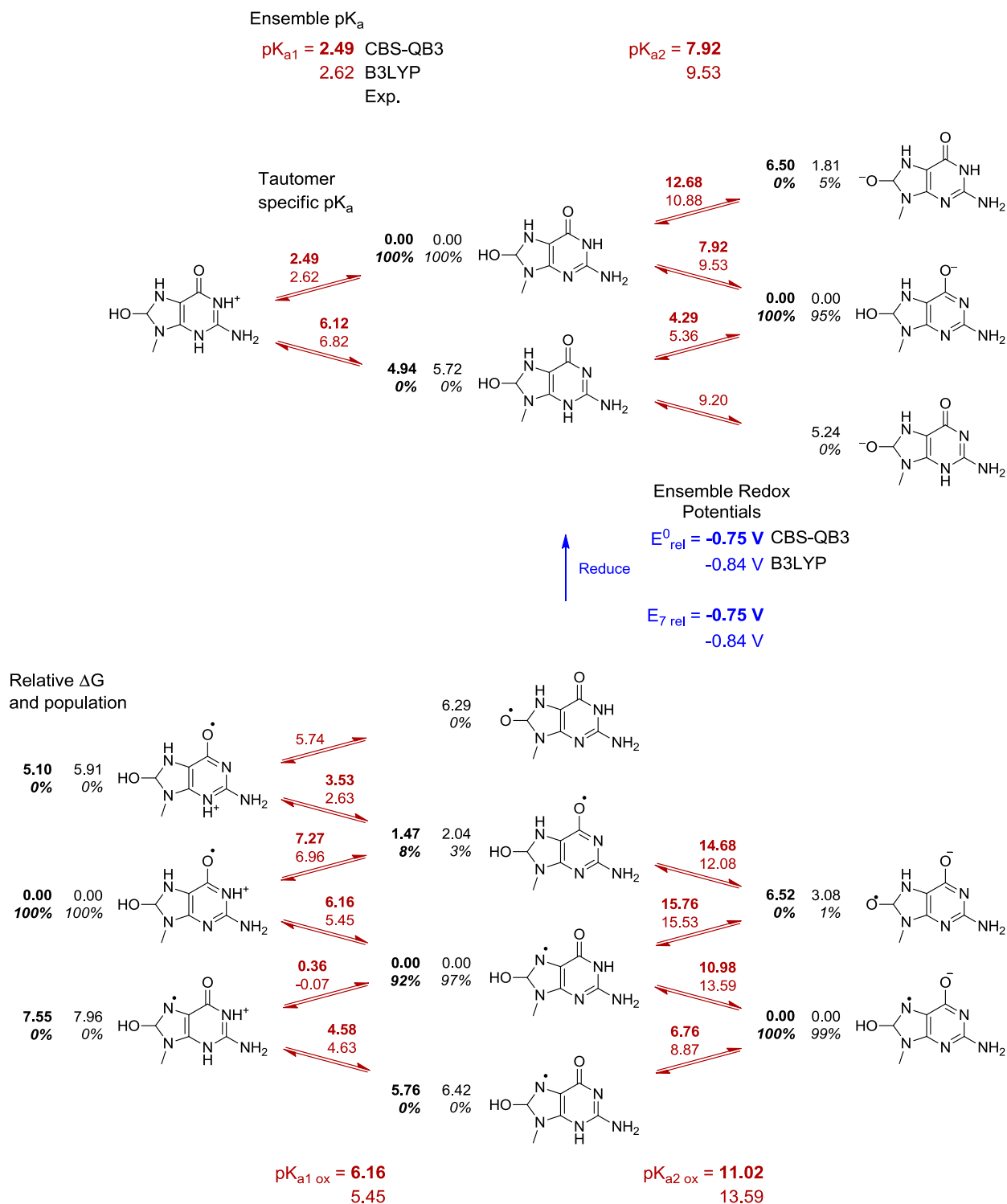


Figure 8.10 Calculated pK_a 's and relative reduction potentials for 2-amino-8-hydroxy-9-methyl-1,7,8-trihydropurin-6-one (hemiaminal). See Figure 8.2 caption for details.

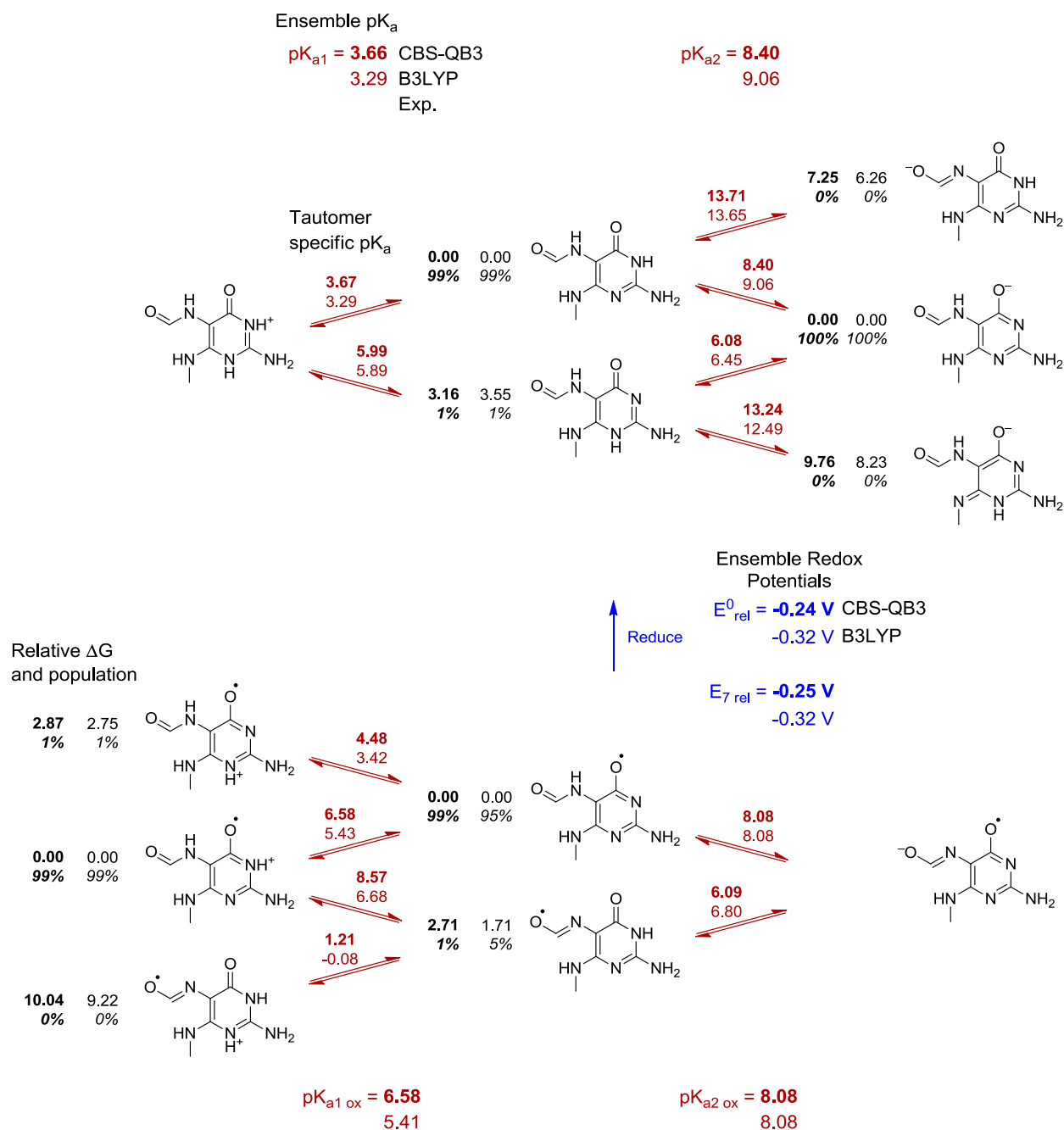


Figure 8.11 Calculated pK_a 's and relative reduction potentials for 2,6-diamino-(N-methyl)-5-formamido-4-hydroxypyrimidine (FAPyG). See Figure 8.2 caption for details.

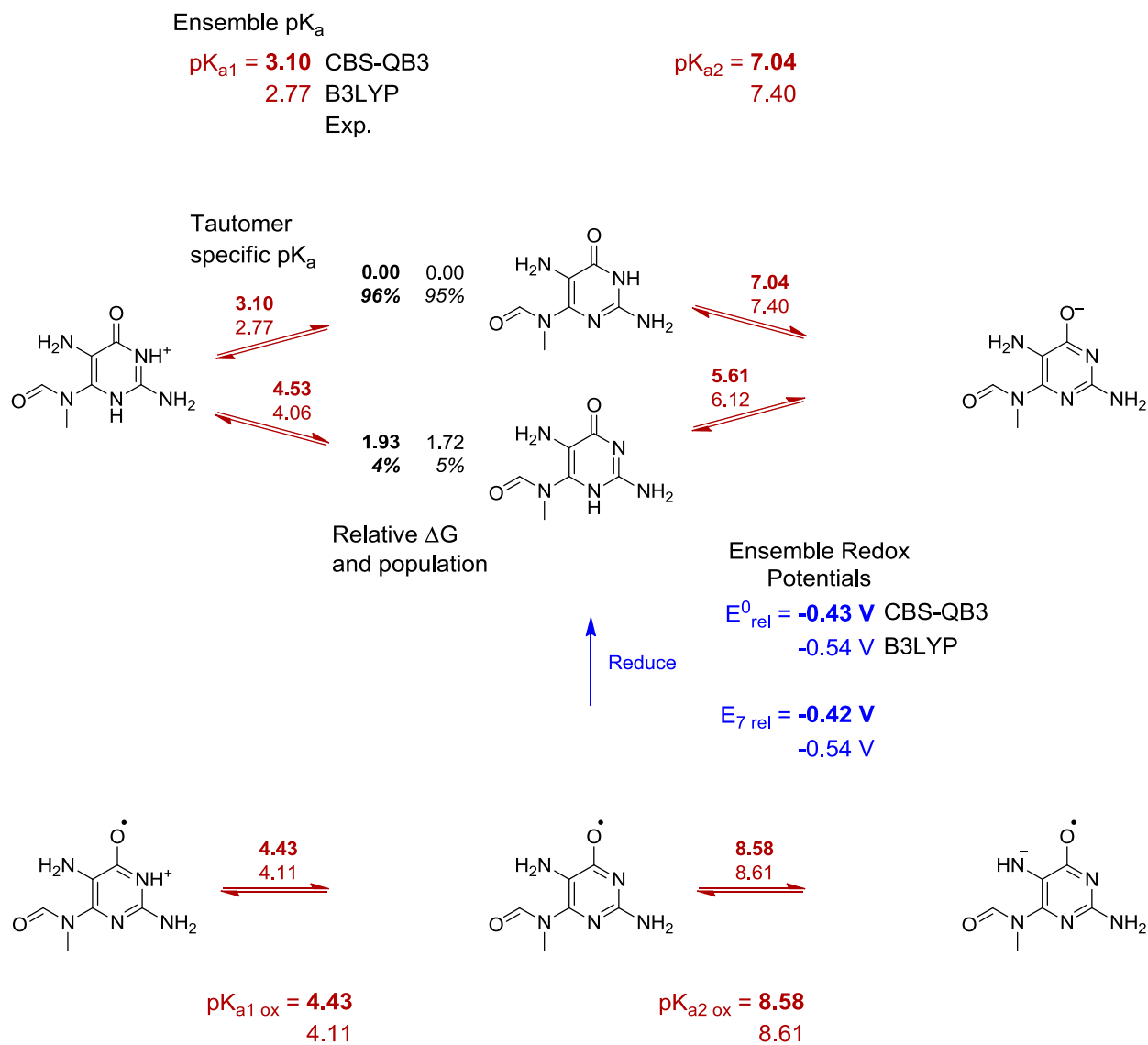


Figure 8.12 Calculated pK_a 's and relative reduction potentials for 2,5-diamino-(N-methyl)-6-formamido-4-hydroxypyrimidine (2,5FAPyG). See Figure 8.2 caption for details.

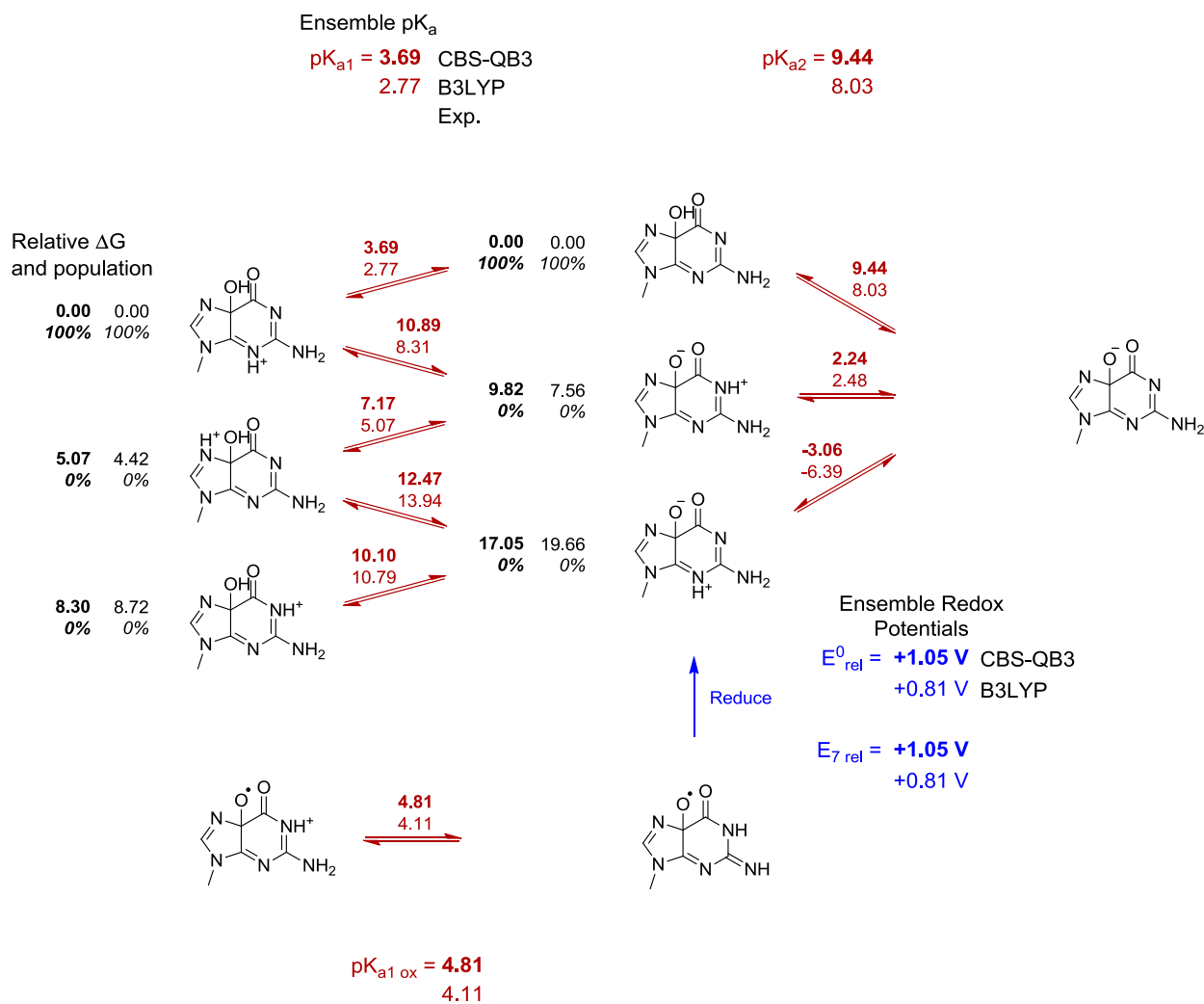


Figure 8.13 Calculated pK_a 's and relative reduction potentials for 5-hydroxy-9-methylguanine (5OHG). See Figure 8.2 caption for details.

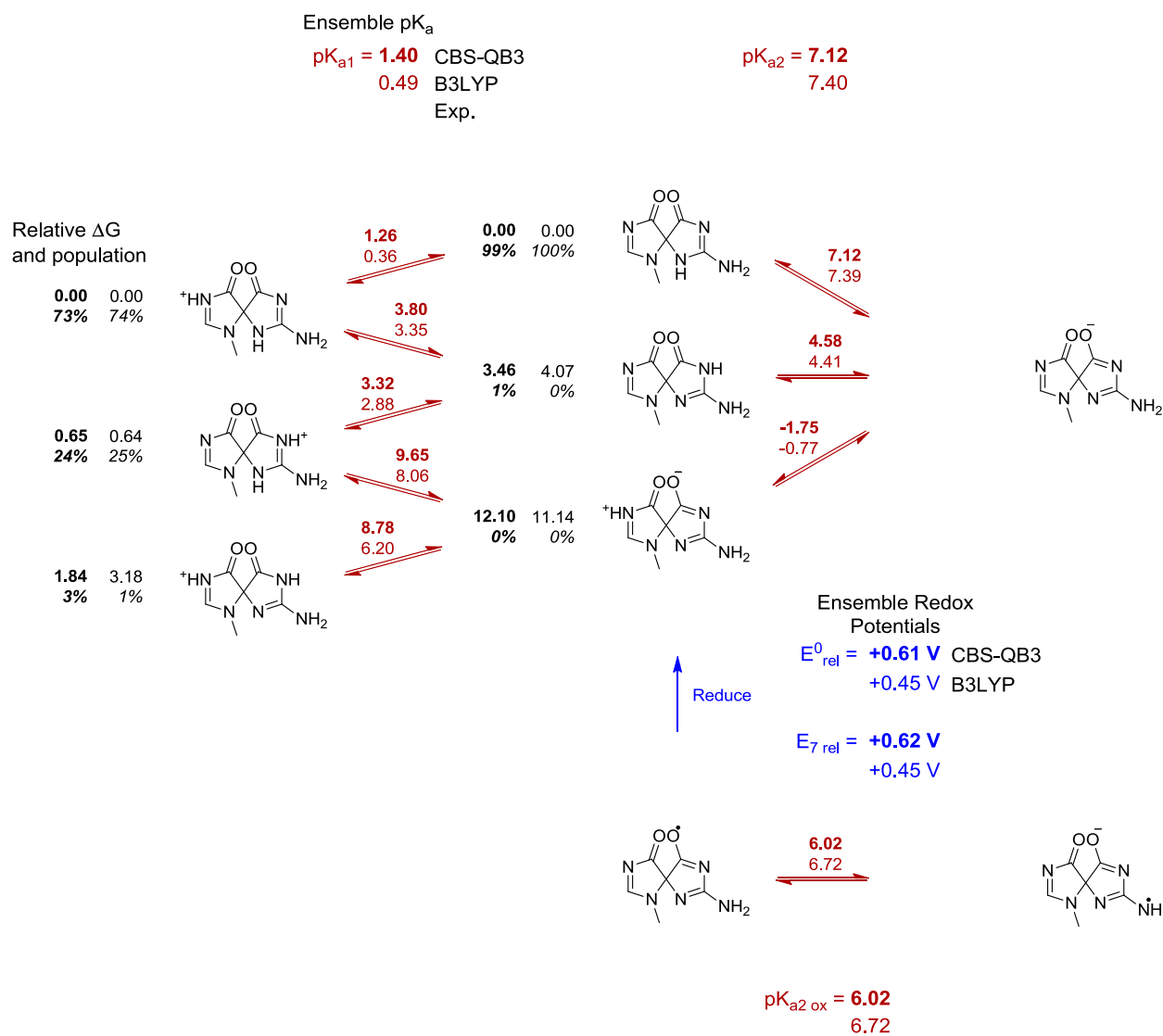


Figure 8.14 Calculated pK_a 's and relative reduction potentials for N-methyl-2-deoxo-spiroiminodihydantoin (Sp_{red}). See Figure 8.2 caption for details.

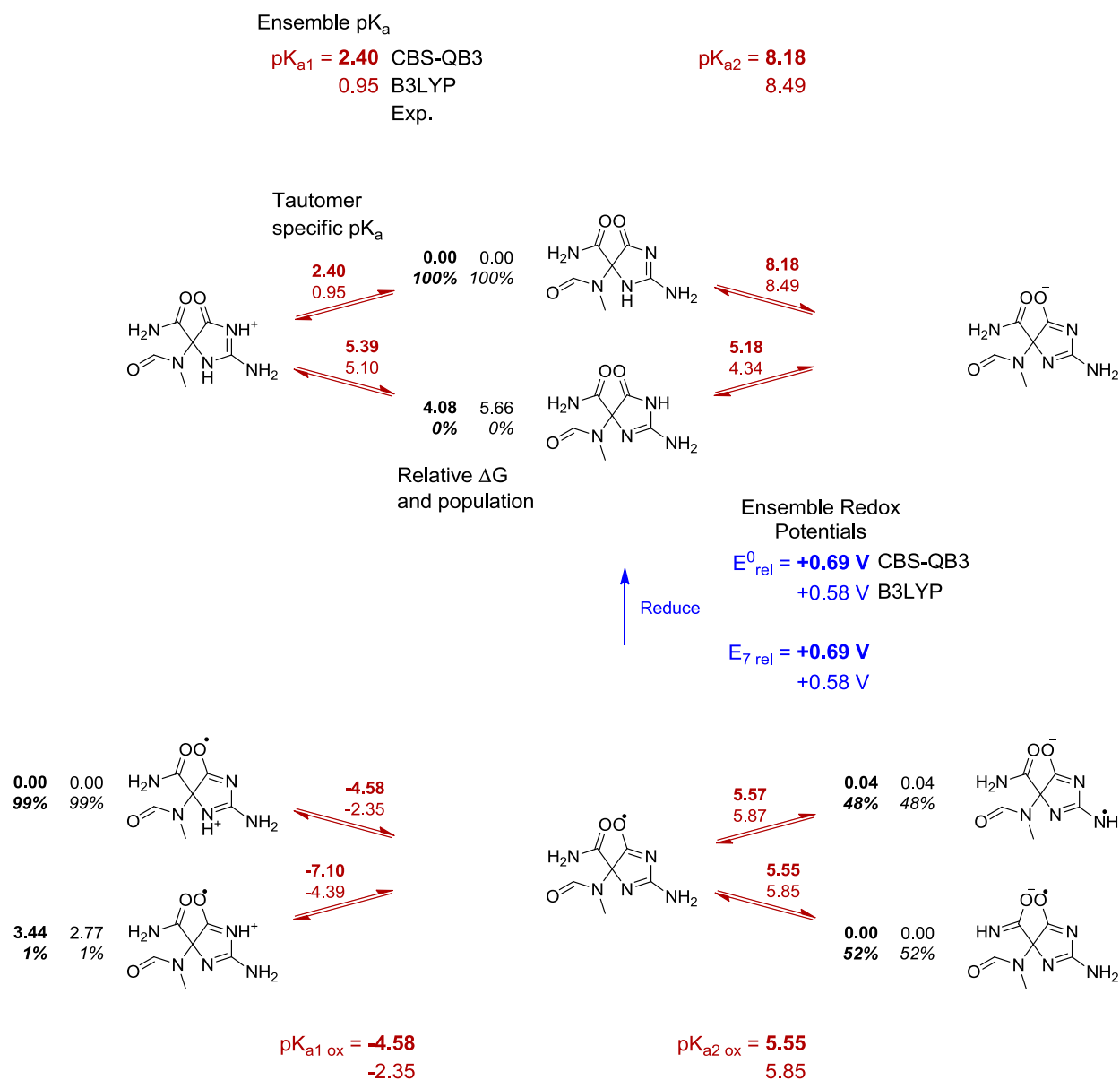


Figure 8.15 Calculated pK_a 's and relative reduction potentials for 5-carboxamido-5-formamido-(N-methyl)-2-iminohydantoin (2lh). See Figure 8.2 caption for details.

8.8 References

1. Ames, B. N.; Shigenaga, M. K.; Hagen, T. M. Oxidants, antioxidants, and the degenerative diseases of aging. *Proc. Natl. Acad. Sci. U. S. A.* **1993**, *90*, 7915-7922.
2. Breen, A. P.; Murphy, J. A. Reactions of oxyl radicals with DNA. *Free Radic. Biol. Med.* **1995**, *18*, 1033-1077.
3. Cadet, J.; Berger, M.; Douki, T.; Morin, B.; Raoul, S.; Ravanat, J. L.; Spinelli, S. Effects of UV and visible radiation on DNA - Final base damage. *Biol. Chem.* **1997**, *378*, 1275-1286.
4. Burrows, C. J.; Muller, J. G. Oxidative nucleobase modifications leading to strand scission. *Chem. Rev.* **1998**, *98*, 1109-1151.
5. Cooke, M. S.; Olinski, R.; Evans, M. D. Does measurement of oxidative damage to DNA have clinical significance? *Clin. Chim. Acta* **2006**, *365*, 30-49.
6. Gimisis, T.; Cismas, C. Isolation, characterization, and independent synthesis of guanine oxidation products. *Eur. J. Org. Chem.* **2006**, 1351-1378.
7. Pratviel, G.; Meunier, B. Guanine oxidation: One- and two-electron reactions. *Chem.-Eur. J.* **2006**, *12*, 6018-6030.
8. Son, J.; Pang, B.; McFaline, J. L.; Taghizadeh, K.; Dedon, P. C. Surveying the damage: the challenges of developing nucleic acid biomarkers of inflammation. *Mol. Biosyst.* **2008**, *4*, 902-908.
9. Lonkar, P.; Dedon, P. C. Reactive species and DNA damage in chronic inflammation: reconciling chemical mechanisms and biological fates. *Int. J. Cancer* **2011**, *128*, 1999-2009.

10. Steenken, S. Purine-bases, nucleosides, and nucleotides - Aqueous-solution redox chemistry and transformation reactions of their radical cations and e⁻ and OH adducts. *Chem. Rev.* **1989**, *89*, 503-520.
11. Candeias, L. P.; Steenken, S. Reaction of HO center dot with guanine derivatives in aqueous solution: Formation of two different redox-active OH-Adduct radicals and their unimolecular transformation reactions. Properties of G(-H)(center dot). *Chem.-Eur. J.* **2000**, *6*, 475-484.
12. Luo, W. C.; Muller, J. G.; Rachlin, E. M.; Burrows, C. J. Characterization of spiroiminodihydantoin as a product of one-electron oxidation of 8-oxo-7,8-dihydroguanosine. *Org. Lett.* **2000**, *2*, 613-616.
13. Llano, J.; Eriksson, L. A. Oxidation pathways of adenine and guanine in aqueous solution from first principles electrochemistry. *Phys. Chem. Chem. Phys.* **2004**, *6*, 4707-4713.
14. Crean, C.; Geacintov, N. E.; Shafirovich, V. Oxidation of guanine and 8-oxo-7,8-dihydroguanine by carbonate radical anions: Insight from oxygen-18 labeling experiments. *Angew. Chem.-Int. Edit.* **2005**, *44*, 5057-5060.
15. Fleming, A. M.; Muller, J. G.; Ji, I. S.; Burrows, C. J. Characterization of 2'-deoxyguanosine oxidation products observed in the Fenton-like system Cu(II)/H₂O₂/reductant in nucleoside and oligodeoxynucleotide contexts. *Org. Biomol. Chem.* **2011**, *9*, 3338-3348.
16. Delaney, S.; Jarem, D. A.; Volle, C. B.; Yennie, C. J. Chemical and biological consequences of oxidatively damaged guanine in DNA. *Free Radic. Res.* **2012**, *46*, 420-441.

17. Jena, N. R.; Mishra, P. C. Formation of ring-opened and rearranged products of guanine: Mechanisms and biological significance. *Free Radic. Biol. Med.* **2012**, *53*, 81-94.
18. Munk, B. H.; Burrows, C. J.; Schlegel, H. B. Exploration of mechanisms for the transformation of 8-hydroxy guanine radical to FAPyG by density functional theory. *Chem. Res. Toxicol.* **2007**, *20*, 432-444.
19. Munk, B. H.; Burrows, C. J.; Schlegel, H. B. An exploration of mechanisms for the transformation of 8-oxoguanine to guanidinohydantoin and spiroiminodihydantoin by density functional theory. *J. Am. Chem. Soc.* **2008**, *130*, 5245-5256.
20. Ye, Y.; Munk, B. H.; Muller, J. G.; Cogbill, A.; Burrows, C. J.; Schlegel, H. B. Mechanistic Aspects of the Formation of Guanidinohydantoin from Spiroiminodihydantoin under Acidic Conditions. *Chem. Res. Toxicol.* **2009**, *22*, 526-535.
21. Wetmore, S. D.; Boyd, R. J.; Llano, J.; Lundqvist, M. J.; Eriksson, L. A. Hydroxyl radical reactions in biological media. In *Recent Advances in Density Functional Methods*, Barone, V.; Bencini, A.; Fantucci, P., Eds. World Scientific: Singapore, 2000; Vol. 3, pp 387-415.
22. Jovanovic, S. V.; Simic, M. G. One-electron redox potentials of purines and pyrimidines. *J. Phys. Chem.* **1986**, *90*, 974-978.
23. Faraggi, M.; Broitman, F.; Trent, J. B.; Klapper, M. H. One-electron oxidation reactions of some purine and pyrimidine bases in aqueous solutions.

- Electrochemical and pulse radiolysis studies. *J. Phys. Chem.* **1996**, *100*, 14751-14761.
24. Seidel, C. A. M.; Schulz, A.; Sauer, M. H. M. Nucleobase-specific quenching of fluorescent dyes. 1. Nucleobase one-electron redox potentials and their correlation with static and dynamic quenching efficiencies. *J. Phys. Chem.* **1996**, *100*, 5541-5553.
25. Steenken, S.; Jovanovic, S. V. How easily oxidizable is DNA? One-electron reduction potentials of adenosine and guanosine radicals in aqueous solution. *J. Am. Chem. Soc.* **1997**, *119*, 617-618.
26. Steenken, S.; Jovanovic, S. V.; Bietti, M.; Bernhard, K. The trap depth (in DNA) of 8-oxo-7,8-dihydro-2'-deoxyguanosine as derived from electron-transfer equilibria in aqueous solution. *J. Am. Chem. Soc.* **2000**, *122*, 2373-2374.
27. Oliveira-Brett, A. M.; Piedade, J. A. P.; Silva, L. A.; Diculescu, V. C. Voltammetric determination of all DNA nucleotides. *Anal. Biochem.* **2004**, *332*, 321-329.
28. Fukuzumi, S.; Miyao, H.; Ohkubo, K.; Suenobu, T. Electron-transfer oxidation properties of DNA bases and DNA oligomers. *J. Phys. Chem. A* **2005**, *109*, 3285-3294.
29. Psciuk, B. T.; Lord, R. L.; Munk, B. H.; Schlegel, H. B. Theoretical Determination of One-Electron Oxidation Potentials for Nucleic Acid Bases. *J. Chem. Theory Comput.* **2012**, *8*, 5107-5123.
30. Bennaim, A.; Marcus, Y. Solvation thermodynamics of nonionic solutes. *J. Chem. Phys.* **1984**, *81*, 2016-2027.

31. Lewis, A.; Bumpus, J. A.; Truhlar, D. G.; Cramer, C. J. Molecular Modeling of environmentally important processes: Reduction potentials. *J. Chem. Educ.* **2004**, *81*, 596-604.
32. Lewis, A.; Bumpus, J. A.; Truhlar, D. G.; Cramer, C. J. Molecular modeling of environmentally important processes: Reduction potentials (vol 81, pg 596, 2004). *J. Chem. Educ.* **2007**, *84*, 934-934.
33. Kelly, C. P.; Cramer, C. J.; Truhlar, D. G. Aqueous solvation free energies of ions and ion-water clusters based on an accurate value for the absolute aqueous solvation free energy of the proton. *J. Phys. Chem. B* **2006**, *110*, 16066-16081.
34. Isse, A. A.; Gennaro, A. Absolute Potential of the Standard Hydrogen Electrode and the Problem of Interconversion of Potentials in Different Solvents. *J. Phys. Chem. B* **2010**, *114*, 7894-7899.
35. Vosko, S. H.; Wilk, L.; Nusair, M. Accurate spin-dependent electron liquid correlation energies for local spin-density calculations - A critical analysis. *Can. J. Phys.* **1980**, *58*, 1200-1211.
36. Becke, A. D. Density-functional exchange-energy approximation with correct asymptotic-behavior. *Phys. Rev. A* **1988**, *38*, 3098-3100.
37. Lee, C. T.; Yang, W. T.; Parr, R. G. Development of the Colle-Salvetti correlation-energy formula into a functional of the electron-density. *Phys. Rev. B* **1988**, *37*, 785-789.
38. Becke, A. D. Density-functional thermochemistry. 3. The role of exact exchange. *J. Chem. Phys.* **1993**, *98*, 5648-5652.

39. Stephens, P. J.; Devlin, F. J.; Chabalowski, C. F.; Frisch, M. J. Ab-initio calculations of vibrational absorption and circular-dichroism spectra using density-functional force-fields. *J. Phys. Chem.* **1994**, *98*, 11623-11627.
40. Ditchfield, R.; Hehre, W. J.; Pople, J. A. Self-consistent molecular-orbital methods .9. Extended gaussian-type basis for molecular-orbital studies of organic molecules. *J. Chem. Phys.* **1971**, *54*, 724-728.
41. Hehre, W. J.; Ditchfield, R.; Pople, J. A. Self-consistent molecular-orbital methods .12. Further extensions of gaussian-type basis sets for use in molecular-orbital studies of organic-molecules. *J. Chem. Phys.* **1972**, *56*, 2257.
42. Hariharan, P. C.; Pople, J. A. Influence of polarization functions on molecular-orbital hydrogenation energies. *Theor. Chim. Acta* **1973**, *28*, 213-222.
43. Hariharan, P. C.; Pople, J. A. Accuracy of AH equilibrium geometries by single determinant molecular-orbital theory. *Mol. Phys.* **1974**, *27*, 209-214.
44. Gordon, M. S. The isomers of silacyclopropane. *Chem. Phys. Lett.* **1980**, *76*, 163-168.
45. Francl, M. M.; Pietro, W. J.; Hehre, W. J.; Binkley, J. S.; Gordon, M. S.; Defrees, D. J.; Pople, J. A. Self-consistent molecular-orbital methods. 23. A polarization-type basis set for 2nd-row elements. *J. Chem. Phys.* **1982**, *77*, 3654-3665.
46. Kendall, R. A.; Dunning, T. H.; Harrison, R. J. Electron-affinities of the 1st-row atoms revisited - Systematic basis-sets and wave-functions. *J. Chem. Phys.* **1992**, *96*, 6796-6806.

47. Montgomery, J. A.; Frisch, M. J.; Ochterski, J. W.; Petersson, G. A. A complete basis set model chemistry. VI. Use of density functional geometries and frequencies. *J. Chem. Phys.* **1999**, *110*, 2822-2827.
48. Montgomery, J. A.; Frisch, M. J.; Ochterski, J. W.; Petersson, G. A. A complete basis set model chemistry. VII. Use of the minimum population localization method. *J. Chem. Phys.* **2000**, *112*, 6532-6542.
49. Marenich, A. V.; Cramer, C. J.; Truhlar, D. G. Universal Solvation Model Based on Solute Electron Density and on a Continuum Model of the Solvent Defined by the Bulk Dielectric Constant and Atomic Surface Tensions. *J. Phys. Chem. B* **2009**, *113*, 6378-6396.
50. Frisch, M. J.; Trucks, G. W.; Schlegel, H. B.; Scuseria, G. E.; Robb, M. A.; Cheeseman, J. R.; Scalmani, G.; Barone, V.; Mennucci, B.; Petersson, G. A.; Nakatsuji, H.; Caricato, M.; Li, X.; Hratchian, H. P.; Izmaylov, A. F.; Bloino, J.; Zheng, G.; Sonnenberg, J. L.; Liang, W.; Hada, M.; Ehara, M.; Toyota, K.; Fukuda, R.; Hasegawa, J.; Ishida, M.; Nakajima, T.; Honda, Y.; Kitao, O.; Nakai, H.; Vreven, T.; Montgomery, J., J. A.; Peralta, J. E.; Ogliaro, F.; Bearpark, M.; Heyd, J. J.; Brothers, E.; Kudin, K. N.; Staroverov, V. N.; Keith, T.; Kobayashi, R.; Normand, J.; Raghavachari, K.; Rendell, A.; Burant, J. C.; Iyengar, S. S.; Tomasi, J.; Cossi, M.; Rega, N.; Millam, J. M.; Klene, M.; Knox, J. E.; Cross, J. B.; Bakken, V.; Adamo, C.; Jaramillo, J.; Gomperts, R.; Stratmann, R. E.; Yazyev, O.; Austin, A. J.; Cammi, R.; Pomelli, C.; Ochterski, J. W.; Martin, J. M. L.; Morokuma, K.; Zakrzewski, V. G.; Voth, G. A.; Salvador, P.; Dannenberg, J. J.; Dapprich, S.; Parandekar, P. V.; Mayhall, N. J.; Daniels, A. D.; Farkas, O.;

- Foresman, J. B.; Ortiz, J. V.; Cioslowski, J.; Fox, D. J. *Gaussian Development Version, Revision H.20+*, Wallingford, CT, 2010.
51. Cancès, E.; Mennucci, B.; Tomasi, J. A new integral equation formalism for the polarizable continuum model: Theoretical background and applications to isotropic and anisotropic dielectrics. *J. Chem. Phys.* **1997**, *107*, 3032-3041.
 52. Mennucci, B.; Tomasi, J. Continuum solvation models: A new approach to the problem of solute's charge distribution and cavity boundaries. *J. Chem. Phys.* **1997**, *106*, 5151-5158.
 53. Cossi, M.; Barone, V.; Mennucci, B.; Tomasi, J. Ab initio study of ionic solutions by a polarizable continuum dielectric model. *Chem. Phys. Lett.* **1998**, *286*, 253-260.
 54. Scalmani, G.; Frisch, M. J. Continuous surface charge polarizable continuum models of solvation. I. General formalism. *J. Chem. Phys.* **2010**, *132*, 114110.
 55. Clark, W. M. *Oxidation-reduction potentials of organic systems*. Williams & Wilkins: Baltimore, MD, 1960.
 56. Wardman, P. Reduction potentials of one-electron couples involving free-radicals in aqueous-solution. *J. Phys. Chem. Ref. Data* **1989**, *18*, 1637-1755.
 57. Camaioni, D. M.; Schwerdtfeger, C. A. Comment on "Accurate experimental values for the free energies of hydration of H^+ , OH^- , and H_3O^+ ". *J. Phys. Chem. A* **2005**, *109*, 10795-10797.
 58. Jang, Y. H.; Goddard, W. A.; Noyes, K. T.; Sowers, L. C.; Hwang, S.; Chung, D. S. First principles calculations of the tautomers and $pK(a)$ values of 8-

- oxoguanine: Implications for mutagenicity and repair. *Chem. Res. Toxicol.* **2002**, *15*, 1023-1035.
59. Jang, Y. H.; Goddard, W. A.; Noyes, K. T.; Sowers, L. C.; Hwang, S.; Chung, D. S. pK(a) values of guanine in water: Density functional theory calculations combined with Poisson-Boltzmann continuum-solvation model. *J. Phys. Chem. B* **2003**, *107*, 344-357.
60. Verdolino, V.; Cammi, R.; Munk, B. H.; Schlegel, H. B. Calculation of pK(a) Values of Nucleobases and the Guanine Oxidation Products Guanidinohydantoin and Spiroiminodihydantoin using Density Functional Theory and a Polarizable Continuum Model. *J. Phys. Chem. B* **2008**, *112*, 16860-16873.
61. Song, B.; Zhao, J.; Griesser, R.; Meiser, C.; Sigel, H.; Lippert, B. Effects of (N7)-coordinated nickel(II), copper(II), or platinum(II) on the acid-base properties of guanine derivatives and other related purines. *Chem.-Eur. J.* **1999**, *5*, 2374-2387.
62. Baik, M. H.; Silverman, J. S.; Yang, I. V.; Ropp, P. A.; Szalai, V. A.; Yang, W. T.; Thorp, H. H. Using density functional theory to design DNA base analogues with low oxidation potentials. *J. Phys. Chem. B* **2001**, *105*, 6437-6444.
63. Christensen, J. J.; Rytting, J. H.; Izatt, R. M. Thermodynamic pK, delta degrees, delta degrees, and delta Cp degrees values for proton dissociation from several purines and their nucleosides in aqueous solution. *Biochemistry* **1970**, *9*, 4907-4913.
64. Cho, B. P. Structure of oxidatively damaged nucleic-acid adducts - pH-dependence of the C-13 NMR-spectra of 8-oxoguanosine and 8-oxoadenosine. *Magn. Reson. Chem.* **1993**, *31*, 1048-1053.

65. Fleming, A. M.; Muller, J. G.; Dlouhy, A. C.; Burrows, C. J. Structural Context Effects in the Oxidation of 8-Oxo-7,8-dihydro-2'-deoxyguanosine to Hydantoin Products: Electrostatics, Base Stacking, and Base Pairing. *J. Am. Chem. Soc.* **2012**, *134*, 15091-15102.
66. Shugar, D.; Fox, J. J. Spectrophotometric studies of nucleic acid derivatives and related compounds as a function of pH. I. Pyrimidines. *Biochimica Et Biophysica Acta* **1952**, *9*, 199-218.
67. Albert, A.; Goldacre, R.; Phillips, J. The strength of heterocyclic bases. *J. Chem. Soc.* **1948**, 2240-2249.
68. Edward, J. T.; Nielsen, S. Thiohydantoins. I. Ionization and ultraviolet absorption. *J. Chem. Soc.* **1957**, 5075-5079.
69. Budavari, S. *The Merck Index*. 12th ed.; Merck: Whitehouse Station, NJ, 1996.
70. Nosheen, E.; Shah, A.; Badshah, A.; Zia ur, R.; Hussain, H.; Qureshi, R.; Ali, S.; Siddiq, M.; Khan, A. M. Electrochemical oxidation of hydantoins at glassy carbon electrode. *Electrochim. Acta* **2012**, *80*, 108-117.

CHAPTER 9

CONCLUSIONS

The chapters of this thesis describe a number of computational studies covering a variety of chemical topics. These topics range from the chemical physics of small molecule dynamics in intense laser fields to the aromatic properties of a novel set of inorganic metallacycle complexes to the prediction of electrochemical properties of oxidatively damaged nucleic acid residues.

In an intense laser field (ca. 10^{14} W/cm²), the valence electrons of molecules are easily torn from the system and a Coulomb explosion will result. If a sufficient number of electrons remain the system, dissociation may not be spontaneous and the dynamics of the energetically excited system likely determine the fragmentation products. In Chapter 2, we used ab initio classical trajectory calculations to investigate the fragmentation patterns of highly energetic C₃H₄ dications following exposure to an intense laser pulse on the singlet and triplet state potential surfaces. Density functional theory and compound model chemistries were used to calculate the energies of key isomers, fragmentation products, and barriers to isomerization and dissociation for C₃H₄²⁺ on the singlet and triplet energy surfaces. Trajectories were started from the allene, propyne, and cyclopropene structures on the singlet and triplet energy surfaces with ca. 240 kcal/mol of excess energy to simulate the vertical double ionization of C₃H₄²⁺. The initial excess energy was distributed randomly as momentum vectors of the nuclei in the system. A total of 200 classical trajectories were calculated for each starting condition. Proton dissociation was the dominant product fragment occurring with a frequency of 50 – 75 % within each set of trajectories. In approximately one-third

of all trajectories, extensive rearrangement was observed prior to dissociation. Despite the many trajectories that underwent rearrangement, the H_3^+ product fragment was not observed for allene due to the large amount of initial kinetic energy. However, other product channels were in agreement with experimental observations confirming that extensive isomerization occurs in $\text{C}_3\text{H}_4^{2+}$ prior to dissociation. Future directions for this work can include classical trajectory calculations with an electric field modeling the intense laser field to study the effects and dynamics of the system during the pulse of the laser.

In Chapter 3, we assessed the performance of some Time-Dependent Density Functional Theory (TD-DFT) methods for calculating excitation energies and intensities of charge transfer bands of inorganic complexes. An initial study of how basis sets and theoretical methods affect the calculated electronic spectra of small organic molecules was helpful in identifying reasonable model chemistries to be used in calculating accurate electronic spectra for inorganic complexes. A set of small inorganic complexes, TiCl_4 , $\text{Ni}(\text{CO})_4$, and $\text{Cr}(\text{CO})_6$, with relatively simple electronic structure characteristics was used for the initial survey. Results showed that the choice of a basis set has only a small effect on the calculated electronic spectra. Problems arose when using the normally accurate EOM-CCSD method as a benchmark for inorganic complexes due to complications from the poor quality of the Hartree-Fock reference wavefunction. Upon analyzing the overall performance of the theoretical methods we determined that wavefunction and pure density functional methods performed poorly for inorganic complexes. However, hybrid and long-range corrected functionals performed reasonably well. Computationally efficient and accurate methods for predicting energies

and intensities of charge transfer bands in inorganic complexes will be useful for future studies related to solar energy conversion. Results of EOM-CC calculations may be improved by using Bruckner or Kohn-Sham orbitals rather than canonical Hartree-Fock orbitals.

A surprise result from an experiment in the Winter laboratory lead to an identification of a novel metallapyrimidine complex. An ensuing theoretical investigation into the aromaticity of the newly isolated niobapyrimidine and niobapyrimidinium complexes concluded that the metallapyrimidine rings were weakly aromatic. A more detailed investigation into the aromaticity of metallapyrimidine complexes containing 2nd row transition metals was described in Chapter 4. Aromaticity was measured by calculating the isotropic chemical shift at Nucleus Independent Chemical Shifts (NICS) points located one angstrom above and below the plane of the metallacycle ring. Calculated chemical shifts were further broken down into orbital contributions of diamagnetic (field-free) and paramagnetic (field-induced) components. For comparison purposes, benzene and pyrimidine were used as classic examples of aromatic systems, while cyclobutadiene was used as a classic counter example of an anti-aromatic system. Two series of 2nd row transition metals containing metallapyrimidine complexes were studied, an isoelectronic d⁰ series having no valence d electrons with metal centers Y^{III}, Zr^{IV}, Nb^V, Mo^{VI}, and Tc^{VII} and a dⁿ series having a varying number of valence d electrons with metal centers Nb^V, Mo^V, Tc^V, Ru^V, and Rh^V. NICS(1)_{zz} chemical shifts of the d⁰ series appeared to have an increasing amount of aromaticity with increasing metal oxidation state. However, the d⁰ metallapyrimidines lacked a strong total paramagnetic (field-induced) contribution that was a signature of the

aromaticity present in benzene and pyrimidine. The d^n metallapyrimidine species had NICS(1)_{zz} chemical shifts that indicated strong aromaticity, but more importantly, showed very strong paramagnetic contributions to the NICS(1)_{zz} chemical shift that were comparable to benzene and pyrimidine. We concluded that using NICS(1)_{zz} chemical shifts as a stand-alone measurement to evaluate the aromaticity of metallacycle complexes may not be reliable. A strong paramagnetic or field-induced contribution to the total chemical shift may be a better indication of aromaticity. Finally, the d^0 metallapyrimidine species were judged as weak to non-aromatic, while the d^n species gave strong indications of being aromatic.

The aromaticity of metallapyrimidines was studied further in Chapter 5 where attention was focused on metallapyrimidine ring substituents such as protonation/methylation and the effect they had on the aromaticity. Two series of 2nd row transition metal containing metallapyrimidine complexes were examined: a d^0 series of Nb^V, Mo^{VI}, and Tc^{VII} and a d^n series of Nb^V, Tc^V, and Rh^V. Substituents were coordinated to the ring nitrogen atoms. The M–N bond lengths for the substituted species were elongated, while all other ring bonds lengths were relatively unaffected. Double protonation/methylation caused the d^0 metallapyrimidine species to severely pucker making interpretation of the NICS(1) chemical shifts problematic. The d^n species maintained planar metallacycles upon single or double substitution. Calculated chemical shifts revealed that substitutions generally reduced the aromaticity of the metallapyrimidine systems. The geometry changes resulting from protonation were largely responsible for reducing the aromaticity of the system. In the doubly protonated Tc^V system, we found that the lowest energy optimized geometry showed a switch in

the occupancy of the valence d orbital. A non-interacting d orbital in the plane of the metallacycle ring became occupied while the d- δ orbital became unoccupied. The unoccupied d- δ orbital interacted favorably with the pyrazolate ligands leading to η^2 coordination. The aromaticity of the system was greatly diminished as indicated by a very small paramagnetic component. This result reinforced a previous hypothesis that the d- δ orbital plays an important role in the degree of aromaticity for these metallapyrimidine systems. In future work, other measures of aromaticity will need to be examined for these metallapyrimidine systems. Further investigations will also study the properties of 3rd row transition metal containing metallapyrimidine and related metallacycle complexes.

The force field parameterization of naturally occurring modified ribonucleic acids (RNA) and modified deoxyribonucleic acids (DNA) nucleosides was described in Chapter 6. The AMBER force field has all of the necessary parameters for a given modified nucleobase except for the atom-centered partial charge parameters needed to describe nonbonding interactions. Ab initio molecular orbital calculations are used to determine these partial charges by a restrained fitting procedure. Using a modular approach to the fitting, atom-centered partial charges were obtained for 107 modified RNA and 42 modified DNA residues. Along with these parameters, a new 3-letter code naming convention was introduced to aid the biochemistry community in the identification of modified bases. Since the parameters were produced for nucleobase and sugar moiety fragments separately, newly discovered sugar modifications can be easily combined with existing base parameters, and vice versa, to produce parameters for many more modified nucleoside combinations. These parameters allow AMBER

users to easily use modified nucleosides in their molecular dynamics studies. Using the fitting techniques described in the chapter and the newly created parameters, future work could involve producing parameters for systems that include peptide nucleic acids (PNA) and DNA-protein hybrid structures.

The development of a computational methodology for calculating pK_a 's and solution phase reduction potentials for the canonical nucleosides is described in Chapter 7. Accurate electrochemical properties of DNA are important to many scientific areas. However, there is no consensus for the absolute or relative potentials of the canonical nucleic acid residues. Calculated standard redox potentials and pK_a 's are used in the Nernst half-cell equation to derive a calculated pH dependent potential that can be directly compared to experiment. Solvent cavity scaling parameters were fitted to correct for some known inaccuracies of using implicit solvent to model charged species. We were able to successfully reproduce experimentally measured pK_a 's and the relative trends of aqueous oxidation potentials of the canonical nucleobases, guanine, adenine, cytosine, thymine, and uracil, and modified nucleobases, xanthine and 8-oxogaunine using the same solvent parameters.

In Chapter 8, the computational methodology developed in Chapter 7 was used to predict pK_a 's and relative aqueous oxidation potentials of some key intermediates and products along the guanine oxidation reaction pathways. Three reaction pathways were studied. Pathway A starts at the 8-oxoguanine intermediate and reacts further to reach the final products guanidinohydantoin and spiroiminodihydantoin. Pathway B proceeds through a hemiaminal intermediate and yields FAPyG products. Along Pathway C, hydroxyl radical attack leads to 5-hydroxyguanine which reacts further to

give reduced spiroiminodihydantoin and eventually a 2-iminohydantoin product. The calculated properties of the species along the pathway are consistent with other measured and predicted properties available from theory and experiment. In future investigations will be needed to study the effects of base pairing, base stacking and other environmental factors on the predicted pK_a 's and relative aqueous reduction potentials. The inclusion of explicit waters in solution phase modeling calculations will be required to produce more accurate pK_a 's and aqueous reduction potentials.

ABSTRACT**EXPLORING MOLECULAR SYSTEMS FROM CHEMICAL PHYSICS TO
BIOCHEMISTRY USING CLASSICAL AND QUANTUM MECHANICS**

by

BRIAN THOMAS PSCIUK

May 2013

Advisor: Professor H. Bernhard Schlegel**Major:** Chemistry (Physical)**Degree:** Doctor of Philosophy

Six topics are considered in this dissertation. Chapter 2 is an investigation into the role of ultra-fast hydrogen dynamics in determining fragmentation products of C_3H_4 following exposure to intense laser fields. Classical dynamics simulations were performed starting from C_3H_4 isomers with 190 – 240 kcal/mol excess energy distributed randomly as nuclear momenta. Deprotonation events were seen in ca. 50 – 75 % of all trajectories. Roughly one third of all trajectories showed fragmentation involving internal isomerization prior to dissociation. Chapter 3 is a survey of currently popular density functional methods and their ability to calculate accurate excitation energies and intensities of some organic molecules and simple first row transition metal complexes. Choice of a reasonable basis set seemed to have little effect on the calculated electronic spectra of the inorganic complexes. Long-range corrected functionals and hybrid density functionals seemed to perform relatively well with only slight underestimations in either energies or intensities. Chapters 4 and 5 probe the structural and aromatic properties for a novel class of second row transition metal

metallapyrimidine compounds. Aromaticity was gauged using Nucleus Independent Chemical Shift calculations and Natural Chemical Shielding analysis by obtaining ring π orbital contributions to the calculated chemical shift. The paramagnetic contribution to the chemical shift was used as an enhanced metric for determining aromaticity in metallacycle compounds. Metallapyrimidines containing metals with no valence d orbitals were found to be no better than weakly aromatic, while metals with valence d orbitals can be quite aromatic. Chapter 6 documents the force field parameterization for 50 modified DNA and 107 naturally occurring modified RNA nucleosides. Hartree-Fock calculations were used with a restraining procedure to generate atom-centered partial charges for use in molecular dynamics simulations using the AMBER force field. The parameters will allow AMBER and other similar force fields method users to incorporate modified nucleosides into their classical simulations. Chapters 7 and 8 detail the development of a computational method for computing accurate acid dissociation constants and solution phase oxidation potentials of canonical nucleic acid residues in addition to intermediates and products of guanine oxidation. Using implicit solvent modeling and accounting for relevant tautomers and protonation states present in aqueous solution, the trends in the calculated oxidation potentials were found to be in relatively good agreement with the trends in experimentally measured potentials. The methodology was then used to map out the pK_a 's and redox potentials of pathways for guanine oxidation.

AUTOBIOGRAPHICAL STATEMENT

Brian Thomas Psciuk

Born on December 15th, 1981 in Marquette, Michigan, USA

EDUCATION

- Doctorate of Philosophy in Physical Chemistry, March 2013
Wayne State University, Detroit, Michigan
Advisor: Professor H. Bernhard Schlegel
- Baccalaureate of Science in Chemistry, December 2006
Northern Michigan University, Marquette, Michigan

EXPERIENCE

- Pfizer Intern – Chemical Technologies, May 2006 – August 2006
Pfizer Global Research and Development, Ann Arbor, Michigan
Advisor: Lakshmi Narasimhan Ph.D.
- Undergraduate Research Assistant, May 2005 – August 2005
Wayne State University, Detroit, Michigan
Advisor: Professor H. Bernhard Schlegel

FUTURE

- Post-Doctoral Associate, starting April 2013
Yale University, New Haven, CT
Advisor: Professor Victor S. Batista

AWARDS AND HONORS

- Summer Dissertation Fellowship, WSU 2012
- The Paul A. and Carol Schaap Graduate Research Fellowship, WSU 2007 – 2011
- The Thomas C. Rumble Graduate Research Fellowship, WSU 2007
- Pfizer Personal Achievement Award, Pfizer 2006

PEER-REVIEWED PUBLICATIONS

- **Psciuk, B. T.**, Lord, R. L., Winter, C. H., Schlegel, H. B., Can metallapyrimidines be aromatic? A computational study into a new class of metallacycles. *J. Chem. Theory Comput.* **2012**, 8, 5107-5123.
- **Psciuk, B. T.**, Lord, R. L., Munk, B. H. and Schlegel, H. B., Theoretical Determination of One-Electron Oxidation Potentials of Nucleic Acid Bases *J. Chem. Theory Comput.* **2012**, 8, 4950-4959.
- **Psciuk, B. T.**, Tao, P. and Schlegel, H. B., Ab Initio Classical Trajectory Study of the Fragmentation of C₃H₄ Dications on the Singlet and Triplet Surfaces *J. Phys. Chem. A* **2010**, 114, 7653-7660.
- **Psciuk, B. T.**, Benderskii, V. A., Schlegel, H. B., Protonated Acetylene Revisited *Theor. Chem. Acc.*, **2007**, 118, 75-80.
- Aduri, R., **Psciuk, B. T.**, Saro, P., Taniga, H., Schlegel, H. B. and SantaLucia, J., AMBER Force Field Parameters for the Naturally Occurring Modified Nucleosides in RNA *J. Chem. Theory Comput.* **2007**, 3, 1464-1475.